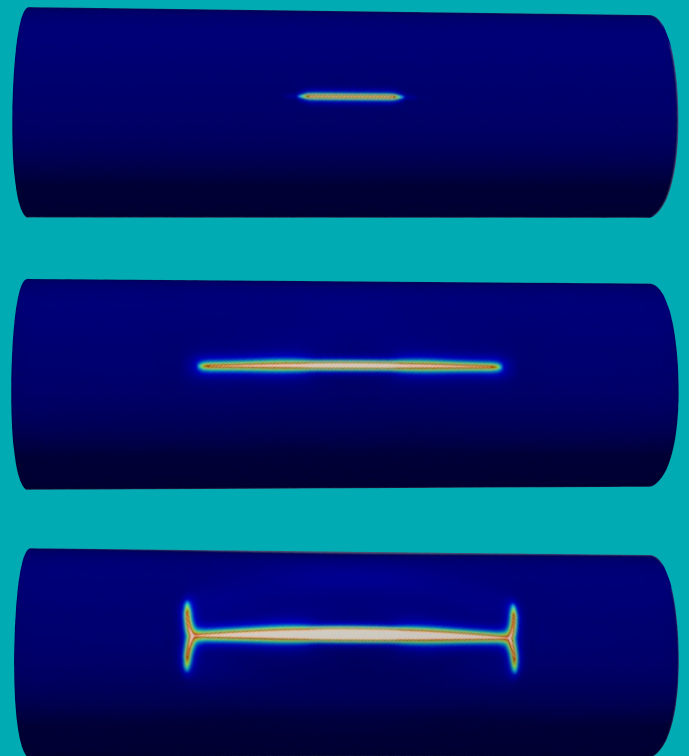
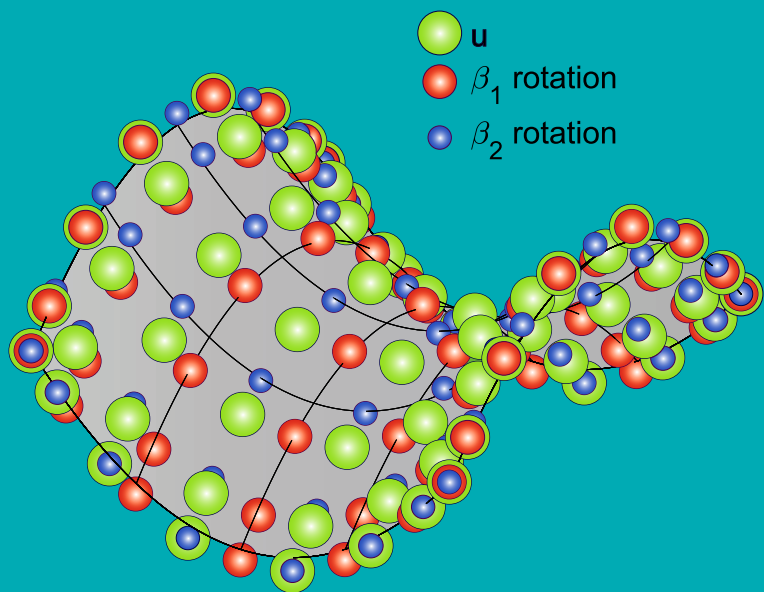




Locking and Brittle Fracture in Isogeometric Reissner–Mindlin Plate and Shell Analysis

Georgia Kikis



Locking and Brittle Fracture in Isogeometric Reissner-Mindlin Plate and Shell Analysis

Von der Fakultät für Bauingenieurwesen
der Rheinisch-Westfälischen Technischen Hochschule Aachen
zur Erlangung des akademischen Grades einer Doktorin der Ingenieurwissenschaften
genehmigte Dissertation

vorgelegt von

Georgia Kikis

aus Kozani - Griechenland

Berichter: Universitätsprofessor Dr.-Ing. habil. Sven Klinkel
Universitätsprofessorin Dr. Laura De Lorenzis
Universitätsprofessor Dr.-Ing. Wolfgang Dornisch
Tag der mündlichen Prüfung: 25. Februar 2022

Diese Dissertation ist auf den Internetseiten der Universitätsbibliothek online verfügbar.

Veröffentlicht als Heft 15 (2022) in der Schriftenreihe
des Lehrstuhls für Baustatik und Baudynamik
der RWTH Aachen

Herausgeber:

Universitätsprofessor Dr.-Ing. habil. Sven Klinkel

Organisation und Verwaltung:

Rheinisch-Westfälische Technische Hochschule Aachen
Fakultät für Bauingenieurwesen
Lehrstuhl für Baustatik und Baudynamik
Mies-van-der-Rohe-Str. 1
52074 Aachen

Telefon: +49 241 80 25088

Telefax: +49 241 80 22303

E-mail: sekretariat@lbb.rwth-aachen.de

© 2022 Georgia Kikis

D 82 (Diss. RWTH Aachen University, 2022)

Alle Rechte, insbesondere das der Übersetzung in fremde Sprachen, vorbehalten. Ohne Genehmigung des Autors ist es nicht gestattet, dieses Heft ganz oder teilweise auf fotomechanischem Wege (Fotokopie, Mikrokopie) zu vervielfältigen oder in elektronischen Medien zu speichern.

ISSN 1437-0840

ISBN 978-3-946090-14-4

Vorwort

Die vorliegende Arbeit entstand während meiner Tätigkeit als wissenschaftliche Mitarbeiterin am Lehrstuhl für Baustatik und Baudynamik der Rheinisch-Westfälischen Technischen Hochschule Aachen im Rahmen des DFG Forschungsvorhabens KL1345/7-1 „Angepasste Approximationsräume und Mehrfeldfunktionale zur Eliminierung von Versteifungseffekten für isogeometrische Schalenelemente“ sowie des SFB/Transregio 280 „Konstruktionsstrategien für materialminimierte Carbonbetonstrukturen - Grundlagen für eine neue Art zu bauen“. In diesem Kontext möchte ich mich für die finanzielle Unterstützung meiner Promotion bedanken. Außerdem möchte ich mich bei Herrn Prof. Dr.-Ing. Dr.-Ing E.h. Curbach und Herrn Prof. Dr.-Ing. Josef Hegger bedanken, die mir die Möglichkeit geboten haben im Sonderforschungsbereich Transregio 280 mitzuwirken. Letzterem danke ich auch für die Übernahme des Prüfungsvorsitzes.

Mein ganz besonderer Dank gilt Herrn Prof. Dr.-Ing. habil. Sven Klinkel für die in jeder Hinsicht hervorragende Betreuung und Unterstützung meiner wissenschaftlichen Arbeit und die Möglichkeiten, die er mir an seinem Institut eröffnet hat. Sein stetiges Interesse, sein Vertrauen und seine Ratschläge hatten einen wesentlichen Anteil am Gelingen dieser Promotion.

Des Weiteren danke ich Frau Prof. Dr. Laura De Lorenzis für die Möglichkeit die Sie mir eröffnet hat im Bereich Bruchmechanik zu arbeiten und für die Übernahme des Korreferates. Herrn Prof. Dr.-Ing. Wolfgang Dornisch möchte ich ebenfalls für die Übernahme des Korreferates danken und für die äußerst lehrreichen fachlichen Diskussionen. Ihr Interesse an meiner Forschungsarbeit ist eine große Ehre für mich.

Herzlich bedanke ich mich auch bei Marreddy Ambati für die sehr gute Zusammenarbeit und die zahlreichen wissenschaftlichen Diskussionen, die meinen Wissenshorizont stetig erweitert haben. Meinen Kollegen, Studenten und Hiwis am Lehrstuhl für Baustatik und Baudynamik danke ich für die freundschaftliche Zusammenarbeit. Besonders hervorzuheben ist mein Kollege Arturo Méndez Salas, der auch ein guter Freund geworden ist.

Von ganzem Herzen danke ich meinem Vater, der mich inspiriert hat in die Forschung zu gehen, meiner Mutter und Schwester für den Rückhalt und meinem Ehemann Daniel für die Unterstützung und die Geduld während der Zeit meiner Promotion. Bedanken möchte ich mich auch bei meinen zwei guten Freundinnen Rania und Stamatia, die während meiner Promotion für die nötige Ablenkung und Entspannung sorgten.

Aachen, im Mai 2022

Georgia Kikis

Kurzfassung

Die vorliegende Arbeit befasst sich mit zwei zentralen Themen, der Behandlung von Versteifungseffekten im Rahmen einer isogeometrischen Reissner-Mindlin-Schalenformulierung und der korrekten Beschreibung des spröden Bruches in Reissner-Mindlin Platten und Schalen mit Hilfe eines Phasen-Feld Modells. In beiden Fällen wird die Geometrie durch die Mittelfläche der Struktur repräsentiert und mit Non-Uniform Rational B-Splines (NURBS) Funktionen interpoliert, die im Bereich des CAD sehr verbreitet sind. Ein Direktor-Vektor-Feld wird benutzt, um die Dickenrichtung zu beschreiben. Da nur kleine Verformungen betrachtet werden, wird der Direktor-Vektor durch eine Differenzvektorformulierung berechnet. Zusätzlich zu den drei Verschiebungen werden zwei Rotationsfreiheitsgrade, die die Querschubeffekte erfassen, definiert.

Bezüglich des ersten Ziels der Behandlung von Versteifungseffekten im Rahmen der isogeometrischen Analyse liegt der Fokus auf den zwei Versteifungseffekten die in der vorliegenden Reissner-Mindlin-Schalenformulierung auftreten, nämlich den Querschubversteifungen und Membranversteifungen. Diese unerwünschten Effekte führen zu einer überhöhten Systemsteifigkeit, einer Unterschätzung der Verformung und Oszillationen in den Spannungsergebnissen. Sie werden ausgeprägter mit abnehmender Dicke, beziehungsweise im Kirchhoff-Limit. In einem ersten Schritt wird eine Methode zur Eliminierung von Querschubversteifungen in Platten und Schalen vorgestellt. Die Methode basiert auf der Tatsache, dass Querschubversteifungen durch eine Unstimmigkeit der Approximationsräume der Verschiebungen und Rotationen in der Kompatibilitätsbedingung der Schubverzerrungen entstehen. Daher werden für die zwei Rotationen angepasste Approximationsräume definiert, und zwar sind ihre Basisfunktionen in Richtung der relevanten Rotation um einen Polynomgrad niedriger als für die Verschiebungen. Die drei unterschiedlichen Kontrollnetze werden aus der gleichen Ausgangsgeometrie mit unterschiedlicher Polynomgrad-Erhöhung erzeugt. Das bedeutet, dass das isogeometrische Konzept immer noch erfüllt ist. Die Netze haben die gleiche Anzahl an Elementen und zusammen formen sie das globale Netz, das für die schwache Form des Gleichgewichts eingesetzt wird. Die Effizienz und Genauigkeit der Methode wird anhand von numerischen Beispielen untersucht. Die Ergebnisse unterstreichen die Überlegenheit der Methode gegenüber der herkömmlichen Reissner-Mindlin-Schalenformulierung die keine Maßnahmen gegen Versteifungseffekte enthält. Oszillationen in den Spannungsergebnissen werden eliminiert und es zeigt sich, dass die Methode konkurrenzfähig zu anderen Methoden ist, die in der isogeometrischen Analyse gegen Versteifungseffekte eingesetzt werden. Die Methode ist außerdem allgemein für jeden Polynomgrad anwendbar und führt im Vergleich zu der herkömmlichen Schalenformulierung zu weniger Freiheitsgraden im Gleichungssystem.

In einem zweiten Schritt wird eine gemischte Verschiebungs-Spannungs-Methode basierend auf dem Hellinger-Reissner Variationsprinzip vorgestellt, um sowohl die Mem-

branversteifungen als auch die Querschubversteifungen in Platten und Schalen zu reduzieren. Die Spannungsergebnisse, die mit diesen Versteifungseffekten zusammenhängen werden als zusätzliche Unbekannte berücksichtigt und müssen mit speziell gewählten Basisfunktionen interpoliert werden. In den entsprechenden Richtungen der Spannungskomponenten werden Ansatzfunktionen gewählt, die um ein Grad niedriger sind als bei den Verschiebungen und Rotationen. Die zusätzlichen Unbekannten, die für die gemischten Formulierungen benutzt werden, werden im Allgemeinen durch statische Kondensation aus dem resultierenden Gleichungssystem eliminiert. Im Gegensatz zu der klassischen Finite Elemente Methode, in der C^0 kontinuierliche Ansatzfunktionen benutzt werden, und in der die statische Kondensation auf Elementebene durchgeführt wird, ist das in der isogeometrischen Analyse durch die hohe Kontinuität der Funktionen nicht mehr möglich. Die statische Kondensation muss nun auf Patchebene erfolgen, was die Inversion einer Matrix auf Patchebene beinhaltet und zu einer vollbesetzten Steifigkeitsmatrix führt. Dies wiederum erhöht den Berechnungsaufwand und daher werden zwei lokale Methoden vorgestellt, die statische Kondensation auf Elementebene ermöglichen. Die erste Methode enthält Spannungsergebnisse, die diskontinuierlich (C^{-1}) über die Elementgrenzen definiert sind. Sie führt zu einer dünnbesetzten Steifigkeitsmatrix mit der gleichen Bandbreite wie die herkömmliche verschiebungsbasierte Schalenformulierung. Es zeigt sich, dass diese Methode die Ergebnisse für niedrige Polynomgrade verbessert und durch den niedrigen Berechnungsaufwand besonders attraktiv ist. Aufgrund der Diskontinuität der Spannungsergebnisse werden die Versteifungseffekte jedoch nicht ganz eliminiert und die Ergebnisse werden für höhere Polynomgrade nicht erheblich verbessert. In der zweiten lokalen Methode wird der in Greco et al. (2017, 2018) für \bar{B} Formulierungen vorgestellte Rekonstruktionsalgorithmus benutzt und die lokalen Kontrollvariablen werden gewichtet, um die verschmierten globalen Variablen zu ermitteln. In den numerischen Beispielen wird gezeigt, dass diese Methode fast die gleiche Genauigkeit wie die globale Methode auf Patchebene besitzt, jedoch führt sie im Gegensatz zu dieser zu einer Bandmatrix als Steifigkeitsmatrix und dadurch, dass sie teilweise auf Elementebene definiert ist reduziert sie die Gesamtberechnungskosten. Die gemischte kontinuierliche Methode auf Patchebene und die gemischte rekonstruierte Methode sind konkurrenzfähig gegenüber anderen Methoden, die gegen Versteifungseffekte eingesetzt werden.

Das zweite wesentliche Ziel dieser Arbeit ist die Entwicklung eines Phasen-Feld Modells zur Beschreibung des spröden Bruches bei isogeometrischen Reissner-Mindlin Platten und Schalen. Ein kontinuierliches Riss-Phasen-Feld, das auf der Schalenmittelfläche definiert ist und mit NURBS Basisfunktionen interpoliert wird, wird benutzt, um den Übergang zwischen gerissenem und ungerissenem Material zu beschreiben. Da Reissner-Mindlin Formulierungen sowohl für dünne als auch für dicke Strukturen benutzt werden, ist ein Bruchversagen aufgrund von Querschubverformungen möglich. Daher liegt ein besonderer Fokus auf der Einbindung der Querschubverzerrung in das Phasen-Feld Modell. Die spektrale Zerlegung für die Zug-Druck Aufteilung wird auf den gesamten Verzerrungstensor angewandt, der über die Dicke variiert, um ein unphysikalisches Bruchverhalten in Druckbereichen zu vermeiden. Der ebene Spannungs-

zustand kann nicht mehr durch eine einfache Eliminierung der Normalverzerrungen und Normalspannungen in Dickenrichtung aus dem Materialmodell erfolgen, sondern muss numerisch erzwungen werden. In jedem Integrationspunkt über die Dicke wird die Normalverzerrung in Dickenrichtung durch einen lokalen Algorithmus mit quadratischer Konvergenz bestimmt, um die Normalspannung in Dickenrichtung auf null zu bringen. Die Fähigkeit des Phasen-Feld Modells für spröden Bruch die Rissbildung, das Risswachstum und die Rissverschmelzung in Platten und Schalen korrekt darzustellen wird anhand von verschiedenen Beispielen untersucht. Ein Vergleich mit zwei bestehenden Formulierungen, einem 3D Solid und einer Kirchhoff-Love Schale, wird durchgeführt. Es wird gezeigt, dass im Falle von dünnen Platten und Schalen eine gute Übereinstimmung zwischen den drei unterschiedlichen Elementarten zu beobachten ist. In den Fällen jedoch wo Scherung eine entscheidende Rolle spielt, unterscheiden sich die Ergebnisse der Kirchhoff-Love Schale von den anderen zwei da die erstere keine Querschubverformungen berücksichtigt.

Abstract

The present work focuses on two main topics, the treatment of locking effects in the framework of an isogeometric Reissner-Mindlin shell formulation and the correct description of brittle fracture in Reissner-Mindlin plates and shells using a phase-field model. In both cases the geometry is described by the mid-surface of the structure with Non-Uniform Rational B-Spline (NURBS) basis functions that are common in CAD tools and a director vector field is used for the description of the thickness direction. Since only small deformations are considered, the director vector is updated using a difference vector formulation. In addition to the three displacements, two rotational degrees of freedom that account for the transverse shear effects are defined.

Regarding the first objective of treating locking in the framework of isogeometric analysis, the focus lies on the two main locking effects that occur in the present Reissner-Mindlin shell formulation, namely, transverse shear locking and membrane locking. These undesirable effects lead to an artificial stiffening of the system, an underestimation of the deformation and oscillations in the stress resultants. They are intensified with a decreasing thickness, i.e. in the Kirchhoff limit. In a first step, a method to eliminate transverse shear locking in plates and shells is introduced. The method is based on the fact that transverse shear locking occurs due to a mismatch of the approximation spaces of the displacements and rotations in the strain formulation. Thus, adjusted approximation spaces are defined for the two rotations, namely, their basis functions are in the relevant direction one order lower than the ones of the displacements. The three different control meshes are created using the same starting geometry and applying different degrees of refinement. This way, the isogeometric concept still holds. The meshes have the same number of elements and together they form the global mesh which is used in the weak formulation. The efficiency and accuracy of the method is assessed with the help of numerical examples. The results highlight the superior behavior of the method compared to the standard Reissner-Mindlin shell formulation without any anti-locking measures. Oscillations in the stress resultants are eliminated and the method is shown to be competitive with other methods used in isogeometric analysis against locking. It is generally applicable for any polynomial degree and leads to less degrees of freedom in the system of equations compared to the standard shell formulation.

In a second step, a displacement-stress mixed method based on the Hellinger-Reissner variational principle is proposed in order to alleviate both membrane and transverse shear locking in plates and shells. The stress resultants that are related to these locking effects are considered to be additional unknowns and have to be interpolated with carefully chosen shape functions. Namely, in the relevant direction, one order lower splines are chosen for the stress resultants than for the displacements and rotations. The additional unknowns that are used in mixed formulations are in general eliminated from the resulting system of equations using static condensation. In contrast to the classical finite element method where C^0 -continuous shape functions are used

and static condensation is performed on the element level, in isogeometric analysis the high continuity of splines does not allow that anymore. Static condensation has to be performed on the patch level, which includes the inversion of a matrix on the patch level and leads to a fully populated stiffness matrix. This on the other hand increases the computational cost and thus, two local approaches are proposed that enable static condensation on the element level. The first one includes stress resultants that are defined discontinuously (C^{-1}) across the element boundaries and leads to a sparse matrix that has the same bandwidth as the standard displacement-based shell formulation. It is shown that this method improves the results for low polynomial degrees and is attractive due to its low computational cost. However, because of the discontinuity of the stress resultant fields locking is not completely eliminated and the results are not greatly improved for higher polynomial degrees. In the second local approach, the reconstruction algorithm proposed in Greco et al. (2017, 2018) for \bar{B} formulations is used and the local control variables are weighted in order to compute blended global variables. In the numerical examples it is shown that this method has almost the same accuracy as the global approach on the patch level, however, in contrast to that it leads to a banded stiffness matrix and is computed partly on the element level, thus, reducing the overall computational cost. The mixed continuous approach on the patch level and the mixed reconstructed approach are competitive compared to other methods used against locking.

The second main objective of this work is the development of a phase-field model for the description of brittle fracture in isogeometric Reissner-Mindlin plates and shells. A continuous crack phase-field which is defined on the shell mid-surface and interpolated with NURBS basis functions is used to describe the transition between cracked and uncracked material. Since Reissner-Mindlin formulations are used for both thin and thick structures, fracture due to transverse shear deformations is possible. Thus, a special focus lies on the incorporation of the transverse shear strains in the phase-field model. The spectral decomposition for the tension-compression split is applied on the total strain tensor, which varies through the thickness, in order to avoid unphysical fracture in compressive areas. The plane stress condition cannot be applied by a simple elimination of the thickness normal strain and thickness normal stress from the constitutive law but has to be enforced numerically. In each integration point through the thickness, the thickness normal strain is computed using a local algorithm with quadratic convergence in order to achieve a zero thickness normal stress. The ability of the phase-field model of brittle fracture to correctly describe crack initiation, propagation and merging in plates and shells is assessed with the help of various numerical examples. A comparison to two existing formulations, namely, a 3D solid and a Kirchhoff-Love shell is carried out. It is shown that in the cases of thin plates and shells a good agreement between the three different element types is observed. However, in cases where shearing plays a crucial role, the results of the Kirchhoff-Love shell differ from the other two since it does not consider transverse shear deformations.

Contents

1	Introduction	1
1.1	Motivation	1
1.2	State of the art	5
1.3	Scope and objective	10
1.4	Overview	12
2	NURBS-based isogeometric analysis	15
2.1	Preliminaries	15
2.2	B-splines	17
2.3	NURBS curves and surfaces	18
2.4	Refinement	21
2.4.1	Knot insertion	21
2.4.2	Order elevation	23
2.4.3	k -refinement	25
2.5	Continuity	26
3	Adjusted approximation spaces for the treatment of transverse shear locking in isogeometric Reissner-Mindlin shell analysis	29
3.1	Abstract	29
3.2	Introduction	30
3.3	Reissner-Mindlin shell formulation	33
3.3.1	Kinematics and basis systems	33
3.3.2	Strains and stresses	35
3.3.3	Variational formulation	36

3.4	Standard NURBS-based isogeometric shell formulation	37
3.5	Adjusted approximation spaces against transverse shear locking . . .	39
3.6	Numerical examples	43
3.6.1	Simply supported plate with biaxial bending	43
3.6.2	Razzaque's skew plate	47
3.6.3	Fully hard clamped square plate	48
3.6.4	Choice of shell examples	50
3.7	Conclusions	56
4	Two-field formulations for isogeometric Reissner-Mindlin plates and shells with global and local condensation	59
4.1	Abstract	59
4.2	Introduction	60
4.3	Reissner-Mindlin shell formulation	63
4.3.1	Kinematics and basis systems	63
4.3.2	Strains and stresses	65
4.4	Isogeometric displacement-stress mixed method for alleviating membrane and shear locking	66
4.4.1	Hellinger-Reissner variational formulation	66
4.4.2	Continuous approach	71
4.4.3	Discontinuous approach	73
4.4.4	Reconstructed approach	74
4.4.5	Computational time	78
4.5	Numerical examples	81
4.5.1	Cook's membrane	81
4.5.2	Clamped plate with point load	84
4.5.3	Cylindrical shell strip	86
4.5.4	Pinched Cylinder	89
4.5.5	Partly clamped hyperbolic paraboloid	95
4.6	Conclusion	97

5	Phase-field model of brittle fracture in Reissner-Mindlin plates and shells	99
5.1	Abstract	99
5.2	Introduction	100
5.3	Reissner-Mindlin shell formulation	103
5.3.1	Kinematics and basis systems	103
5.3.2	Total strains	105
5.3.3	Strain energy density and stress resultants	106
5.4	Phase-field model of brittle fracture	108
5.5	Phase-field fracture models combined with plate and shell formulations	110
5.5.1	Existing approaches	110
5.5.2	Phase-field model of brittle fracture for the Reissner-Mindlin shell formulation	112
5.6	Numerical examples	115
5.6.1	Beam with transverse loading and different boundary conditions	116
5.6.2	Square plate with changing surface load	119
5.6.3	Annular plate	123
5.6.4	Pressurized cylinder with initial crack	126
5.7	Conclusion	130
6	Outlook and conclusion	133
6.1	Summary and concluding points	133
6.2	Outlook	135
A	Local plane stress algorithm	137
	References	138

Chapter 1

Introduction

1.1 Motivation

In engineering, inspiration for the development of new structures and mechanisms is often drawn from nature. Plates and shells, which are found in various forms and shapes in plants and animals, such as leaves, seashells and skulls have been adopted to numerous engineering fields, including architectural and civil engineering (bridge deck, storage tank, domes), mechanical engineering (wing skin, car body) and marine engineering (ship hull), see Fig. 1.1. Both plates and shells lead to lightweight structures and thus are economical solutions. In particular shells offer many advantages due to their geometrical form, i.e. their curvature. They have an optimal load-carrying behavior and a high stiffness. Thus, they are able to span wide areas without the need of any additional support. Furthermore, since they can take various forms they are often used for a more aesthetic design. Plates can be considered as special cases of shells with no curvature.



Figure 1.1: Shells in nature and engineering (Daderot (2014), Sydney (2017), NASA (2002))

A main characteristic of plates and shells is that their thickness is small compared with their other dimensions. Depending on how small the thickness is, they are further

classified into thick and thin plates/shells. In engineering, a shell is regarded as thin if the thickness to radius ratio is less than $1/20$. In other cases the shell is considered to be thick. For plates the limit between the thin and thick range is indicated by a thickness to the average side ratio of $1/10$. If the ratio gets smaller than $1/100$, flexural rigidity is almost non-existent and the structure is referred to as a membrane, see Ventsel and Krauthammer (2001). A plate or shell can be defined as a three-dimensional continuum and described using a three-dimensional constitutive law. However, a much simpler approach is to represent the geometry of the structure only by its mid-surface while the thickness direction is described by the normal of the surface or the director vector. The two main plate/shell theories are the Kirchhoff-Love and the Reissner-Mindlin theory. Kirchhoff (1850) made an important contribution to the analysis of thin plates in which he formulated the well-known Kirchhoff-hypotheses. Based on these, Love (1888) later presented a shell theory for thin elastic shells. In the Kirchhoff-Love theory transverse shear effects are neglected and the normal to the middle surface is considered to remain normal after deformation. This applies for thin shells where shear deformation is so small that it can be considered as non-existent. However, with increasing thickness the shear strains have a greater influence on the deformation and thus, new theories had to be introduced for the correct analysis of thick plates/shells. Reissner (1944) and Mindlin (1951) developed a shell theory where transverse shear effects are taken into account and which is applicable to both thin and thick plates and shells. Here, in addition to the displacements, the rotations of the normal or the transverse shear strains are considered as additional unknowns.

With increasingly complex structures, Computer-Aided Engineering (CAE) has become indispensable for the efficient and accurate determination of the load-bearing and deformation behavior. In this context, finite element procedures have played a crucial role in engineering analysis and have found wide application in various engineering fields. Nevertheless, the design process is still carried out separately from the analysis process. A model is first generated with the help of Computer Aided Design (CAD) tools and then converted to a geometry which can be used for the Finite Element Analysis (FEA). Thus, Hughes et al. (2005) introduced isogeometric analysis (IGA) in an attempt to unify the design and analysis process by using for both the same higher order basis functions that are common in CAD tools, e.g. Non-Uniform Rational B-Splines (NURBS). Especially in the context of shell structures, isogeometric analysis offers many advantages. First, the higher continuity of splines enables a straightforward implementation of Kirchhoff-Love formulations, which include second derivatives of the displacements and thus require C^1 -continuous basis functions. In the standard finite element method C^0 -continuous shape functions are used, which is not sufficient. Furthermore, the high continuity of splines throughout a patch allows for an exact computation of the shell curvature, tangent and normal vectors. Free

form shell structures are now computable with much less computational effort than with the classical finite element method. In addition, shells can be described by their mid-surface which is in accordance with the approach used in most CAD tools for thin structures.

In the standard finite element method it was soon noticed that the classical displacement-based formulations led under certain conditions to incorrect results. This undesired phenomenon was named locking. Since then a lot of research effort has been put into the development of methods that eliminate locking. Depending on their critical parameter, the different existing locking effects can be divided into two main categories, namely, the geometrical and the material locking effects, see Bischoff (1999). Geometrical locking effects include transverse shear locking, membrane locking, in-plane shear locking and curvature thickness locking. These effects strongly depend on the slenderness of the structure that includes the critical parameter, in this case the thickness. On the other hand, material locking effects like volumetric locking depend on critical material parameters such as the Poisson's ratio ν . In the context of plate and shell formulations in which the geometry is described only by the mid-surface and where the thickness is assumed to remain constant, the main locking effects that occur are transverse shear and membrane locking. Transverse shear locking, which results from the use of equal-order shape functions for the interpolation of the displacements and rotations (or difference vectors), affects both plates and shells. On the other hand, membrane locking, which is yielded by a coupling of the membrane strains and curvatures, only arises in shells due to their curved surface. These locking effects lead to an artificial stiffening of the system, thus, an underestimation of the deformation and in addition to parasitic oscillations in the stress resultants. This behavior is intensified with decreasing thickness.

Despite their favorable features in many aspects, splines suffer from the same locking effects as Lagrange shape functions, see Echter and Bischoff (2010). The higher order of splines may reduce locking, for instance transverse shear locking, however, it does not eliminate it completely and leads to a higher computational cost. Furthermore, membrane locking is even intensified when using higher order polynomials with high continuity, see Cardoso and Cesar de Sa (2014). Thus, the introduction of other approaches for the treatment of locking in the context of isogeometric analysis is necessary. In the past years, different methods have been proposed that either try to solve the problem on the theoretical level by using special formulations or that adopt approaches that have been valuable in the classical finite element analysis by modifying them for the isogeometric analysis.

Apart from the numerical aspects for the correct representation of shell structures, their material behavior, for instance in the case of fracture is of great interest. Fracture can lead to the complete failure of a structure, putting human lives at risk and

leading to financial losses. Especially in the case of brittle fracture, where failure occurs abruptly without any visible indication, the correct description of crack initiation and propagation is of great importance. A well-known incident that demonstrates the catastrophic results of brittle fracture is the case of the Liberty ships, see Kobayashi and Onoue (1943) and Fig. 1.2. Fracture models and their numerical implementation play a key role in the prediction and prevention of fracture, since experimental testing is not always possible due to the high cost. Griffith and Taylor (1921) described the propagation of cracks as the counteract of a structure's bulk energy and surface energy. In other words, a crack will only grow if the released strain energy exceeds a critical value, necessary to form a new crack surface. In the context of shell structures, the correct description of the fracture behavior is not an easy task due to the complex interaction of shell geometry, shell kinematics and material constitutive law. Fracture processes are either described discontinuously by discrete crack surfaces or continuously, i.e. the cracked medium is still considered as a continuum. An approach that has become quite popular due to its useful mathematical properties is the phase-field method, where a continuous crack phase-field is used that defines the transition between cracked and uncracked material. Phase-field models have the advantage of naturally describing crack initiation, propagation, merging and branching without the need of remeshing or additional criteria. These properties in addition to the continuous description of the cracked material make phase-field models a very promising option for the description of brittle fracture in isogeometric plate and shell formulations.

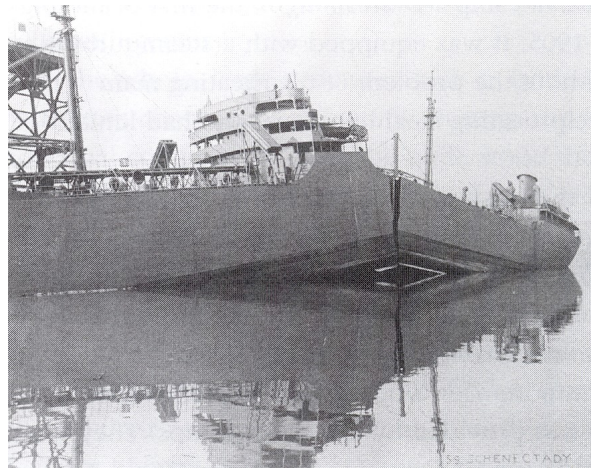


Figure 1.2: Cargo ship 'Schenectady' broke in two while lying at the outfitting dock in the constructors yard (U.S. GPO (1947))

1.2 State of the art

In the context of the numerical analysis of shells, isogeometric analysis (IGA) has attracted a lot of attention in recent years. It was introduced in Hughes et al. (2005) in order to unify the design and analysis process by using higher order basis functions from CAD tools, such as NURBS functions. Thus, a structure which is designed in the CAD tools can be directly used for the analysis process (isogeometric concept). The first notable steps for the structural analysis of shells with isogeometric analysis were done in the context of the Kirchhoff-Love theory in Kiendl et al. (2009) where a geometrically nonlinear shell element is introduced with only displacements as degrees of freedom. However, clamped edges, external moments and a coupling of patches, that are all related to the rotational degrees of freedom can only be applied using special measures. In Kiendl et al. (2010) a bending strip method is employed for the treatment of patch interfaces. Still, these formulations do not include measures against membrane locking. Benson et al. (2011) introduced a rotation-free isogeometric shell using a lifting operator for the correct definition of the shell normal vector. These Kirchhoff-Love shell formulations were later enriched and extended for instance in Nguyen-Thanh et al. (2011) in combination with PHT-splines, in Kiendl et al. (2015c) for hyperelastic materials and in Duong et al. (2017) where a penalty and Lagrange multiplier approach are used to achieve continuity between patch interfaces.

In the framework of Reissner-Mindlin shell formulations, where transverse shear effects are taken into account, the first isogeometric shells were introduced in Uhm and Youn (2009) for T-splines and in Benson et al. (2010b) for NURBS. In the latter formulation, the director vectors are only approximated by closest point projections of the normal vectors, which reduces the quality of the results for higher order NURBS basis functions. Thus, Dornisch et al. (2013) presented an isogeometric Reissner-Mindlin shell with exactly calculated director vectors which was later extended to shells with kinks in Dornisch and Klinkel (2014). In Kiendl et al. (2017) a Reissner-Mindlin shell formulation based on the isogeometric collocation method is presented. Blended shells, which combine the Kirchhoff-Love and the Reissner-Mindlin shell kinematics, were introduced in Benson et al. (2013). Hosseini et al. (2013, 2014b) presented an isogeometric solid-like shell and an isogeometric continuum shell for nonlinear analysis. In both formulations the shell is represented by its mid-surface, however, in the first case linear Lagrange shape functions are used for the thickness direction while in the second case they are replaced by higher order B-splines.

Despite their favorable features, splines suffer from the same locking effects as Lagrange shape functions, see Echter and Bischoff (2010). Locking leads to an artificial stiffening of the system, an underestimation of the deformation and oscillations in the stress resultants. All the aforementioned first shell formulations in the framework of

isogeometric analysis did not include any measures against locking. Some of them used higher order shape functions in order to reduce locking. Even though this approach is easy, it does not eliminate locking completely and at the same time increases the computational cost, see Benson et al. (2010b), Echter and Bischoff (2010) and Bouclier et al. (2013b). Only in the case of isogeometric collocation methods the computational time is not highly affected by the increase of the polynomial degree, see Kiendl et al. (2015a) for plates and Kiendl et al. (2017) for shells.

In the past years, various new methods have been proposed in order to eliminate the undesirable locking effects in the framework of isogeometric analysis. An attempt to overcome locking on the theoretical level was made by using hierarchic formulations. Echter et al. (2013) applied a hierarchic difference vector on the rotated Kirchhoff-Love type director of the deformed configuration in order to consider shear deformations. This formulation avoids transverse shear locking *ab initio*. However, it still exhibits some oscillatory behavior in certain stress resultants when using lower order shape functions. Thus, Oesterle et al. (2016) proposed a hierarchic shell formulation where two hierarchic displacements are used that describe the transverse shear deformation. Later, this formulation was extended to geometrically nonlinear problems in Oesterle et al. (2017). Even though these formulations were able to avoid transverse shear and curvature thickness locking *ab initio*, additional methods had to be implemented for the elimination of membrane locking. Similar approaches to these hierarchic formulations were presented in Long et al. (2012) for subdivision shells and in combination with NURBS and triangular NURPS in Beirão Da Veiga et al. (2015). In Kiendl et al. (2015b, 2018) the classical Timoshenko beam problem was reformulated to a single differential equation with only one primal variable in order to avoid shear locking by construction. A mixed displacement method that avoids the geometrical locking effects *ab initio* was presented in Bieber et al. (2018).

In addition to these formulations, methods that have been valuable in the classical finite element analysis for the elimination of locking effects have been extended to isogeometric analysis, like the Assumed Natural Strain (ANS) method in Caseiro et al. (2014, 2015), where the strain components are interpolated at carefully chosen tying points instead of the standard quadrature points. The Discrete Shear Gap (DSG) approach, which is closely related to the ANS method and the \bar{B} method, was implemented in Echter and Bischoff (2010) and Echter et al. (2013) in order to treat membrane locking. In Cardoso and Cesar de Sa (2012) the Enhanced Assumed Strain (EAS) method was used to alleviate volumetric locking. Non-uniform integration techniques were implemented for isogeometric Reissner-Mindlin shells in Dornisch et al. (2016) and Adam et al. (2015) in order to overcome locking and increase the efficiency of the formulations. However, the latter method fails for general non-uniform knot vectors and is thus not relevant for industrial applications. Reduced integrated fields were applied

for a solid-shell in Cardoso and Cesar de Sa (2014) in combination with a moving least square approach to project them back onto the fully integrated space and later in Leonetti et al. (2018) for composite multi-layered shells. The use of adjusted approximation spaces for the displacements and the rotations in Reissner-Mindlin plates was able to eliminate transverse shear locking, see Beirão da Veiga et al. (2012a). Thai et al. (2011) proposed a stabilization technique to overcome shear locking in laminated composite Reissner-Mindlin plates. The method consists of a small modification in the material matrix related to the shear terms, however, it only alleviates locking and does not eliminate it.

The \bar{B} method, one of the most popular methods in the finite element analysis, was introduced for isogeometric analysis in Elguedj et al. (2008) along with an \bar{F} projection in order to alleviate locking in nearly incompressible linear and nonlinear elasticity and plasticity problems. Later, it was extended to straight and curved Timoshenko beams in Bouclier et al. (2012) and to plane curved Kirchhoff rods in Greco et al. (2017). A first attempt to apply the \bar{B} method to isogeometric 2D solid shells was made in Bouclier et al. (2013b). As it was often stated in these works, the \bar{B} method within the framework of isogeometric analysis leads to a linear system where a matrix defined on the patch level has to be inverted and the resulting stiffness matrix is fully populated, which increases the computational cost. This led to the introduction of local \bar{B} formulations, where the \bar{B} -projection is applied locally and the global variables are obtained from the local ones using reconstruction algorithms. Such a local \bar{B} formulation was first introduced in Bouclier et al. (2013a) for a NURBS-based solid-shell. A local \bar{B} formulation based on the Bézier projection proposed by Thomas et al. (2015) was presented in Miao et al. (2018) to alleviate transverse shear locking in Timoshenko beams and volumetric locking in nearly incompressible elastic solids. In addition, Miao et al. (2018) presented a non-symmetric Bézier \bar{B} projection, where the variation of the assumed variables is discretized with dual basis functions. This way, the assumed variables are directly condensed out without the need of an inversion and lead to a sparse stiffness matrix with a slightly higher bandwidth. This method was later applied to geometrically nonlinear Reissner-Mindlin shells in Zou et al. (2020). A much simpler reconstruction algorithm which is also based on the work of Thomas et al. (2015) can be found in Greco et al. (2017, 2018) for plane curved Kirchhoff rods and Kirchhoff-Love shells. There, the local variables are directly interpolated with local B-spline functions without a Bézier projection and transformation to the Bernstein basis. Local \bar{B} formulations where the locking strains or stresses are projected onto interpolation spaces with the lowest possible order for each element leading to different projection spaces for the inner, corner and boundary elements are presented in Hu et al. (2016, 2020). Antolin et al. (2017, 2020) used discontinuous polynomial spaces for the projection of the strains.

Mixed formulations, which are equivalent to the \bar{B} formulations for linear cases as stated in Bouclier et al. (2013a) and Simo and Hughes (1986), were implemented in the context of isogeometric analysis for a solid-shell in order to eliminate membrane, shear and thickness locking in linear, see Bouclier et al. (2013a), and geometrically nonlinear cases, see Bouclier et al. (2015). Echter et al. (2013), Oesterle et al. (2016) and Rafetseder and Zulehner (2019) used a mixed formulation to overcome membrane locking in hierarchic shells and Kirchhoff-Love shells. Mixed variational formulations for nearly incompressible solids were implemented in Taylor (2011) and Fahrenndorf et al. (2020). However, as it is for the \bar{B} method, mixed methods involve static condensation on the patch level due to the high continuity of the shape functions in isogeometric analysis.

Griffith is considered to be the founder of fracture mechanics with his work on brittle fracture, see Griffith and Taylor (1921). Since then a lot of progress has been made in this field with the development of new fracture models and their numerical implementation. There exist two main ways to describe fracture processes, the discrete approaches where discrete crack surfaces are used and the continuum approaches in which the cracked medium is still considered as a continuum. One of the discrete approaches is the cohesive zone modeling approach in which interface or generalized contact cohesive elements are implemented, either from the beginning or adaptively. It has been widely used due its simplicity, especially in cases where the crack path is known. In the framework of shells, many applications of this method can be found e.g. in Cirak et al. (2005), Zavattieri (2006), Rabczuk and Areias (2008) and Becker et al. (2011) and in later years in combination with isogeometric analysis, e.g. in Dimitri et al. (2014).

Another discrete approach is the extended finite element method (XFEM) which was developed based on the partition of unity method in order to allow for arbitrary crack paths, independent of the mesh. XFEM describes discontinuities using additional approximation fields for the displacements and if needed for the director. This method has been applied to Kirchhoff-Love type shells in Areias et al. (2006), Song and Belytschko (2009) and Areias and Belytschko (2006), to solid-like shell formulations for modeling through-the-thickness cracks in Areias and Belytschko (2005), Larsson et al. (2011) and Mostofizadeh et al. (2013) and to a Reissner-Mindlin based plate in Dolbow et al. (2000). In the framework of isogeometric analysis, a Kirchhoff-Love based and a Reissner-Mindlin based extended isogeometric element formulation were introduced for modeling fracture in shells, see Nguyen-Thanh et al. (2015) and Benson et al. (2010a), respectively.

An approach which is very similar to XFEM and is able to compute mesh-independent crack propagation is the phantom node method. This method uses overlapping elements at the cracked regions, which are employed by the so-called phantom nodes.

Applications of this method can be found in Chau-Dinh et al. (2012), Lua et al. (2016) and Ahmed et al. (2012). Budarapu et al. (2017) created an adaptive multiscale method for solid shells by combining a continuum-based phantom node method with a molecular statics model. Multi-level models have also been used in the framework of debonding between the levels of composite structures in Kocaman et al. (2020). The main disadvantage of discrete approaches is that diffuse ductile damage, as it is encountered e.g. in metals, cannot be computed and thus they have mainly been applied to brittle fracture.

Continuum approaches do not describe the crack as a discontinuity in the structure. Instead the material is still seen as a continuum with weakened mechanical properties at the cracked areas. Various approaches of this type have been introduced, among others in Areias et al. (2011), Woelke and Abboud (2012), in connection with meshfree formulations in Ren and Li (2012), Caleyron et al. (2012) and based on the gradient-enhanced damage approach in Hosseini et al. (2014a), Nguyen et al. (2012) and Pigazzini et al. (2019). The disadvantage of continuum approaches is that they may have difficulties in properly describing surface decohesion and crack propagation after the softening and damage localization phase.

A method with especially useful mathematical properties that can be regarded as a gradient damage model is the phase-field method. Since its introduction in Bourdin et al. (2000, 2008) it has been extensively investigated for brittle and ductile fracture for the case of solids, see Ambati et al. (2015b) and Alessi et al. (2018), respectively. In the phase-field method the transition between cracked and uncracked material is defined using a continuous crack phase-field. This leads to a regularized representation of the crack. The model has been proven to converge (in the Γ -convergence sense) to the variational formulation of the classical Griffith's theory of brittle fracture, see Griffith and Taylor (1921) and Francfort and Marigo (1998). The advantage of using phase-field models is that crack initiation, propagation, merging and branching can be described naturally without the need of remeshing or additional criteria. A degradation function which is defined by the phase-field is used to reduce the elastic strain energy density. In general, the degradation function is either applied on the entire elastic strain energy density or only on the part that corresponds to tension. In the latter case, the elastic strain energy density has to be split first into its tensile and compressive parts.

In the framework of plates and shells, a first attempt to combine the phase-field method with Kirchhoff-Love shell formulations was conducted in Ulmer et al. (2012). There, the elastic strain energy density is separated into its membrane and bending parts. Afterwards the membrane part is split with a spectral decomposition into its tensile and compressive parts. The membrane tensile part and the entire bending part is then degraded. This formulation, however, can lead to unphysical crack behavior in certain loading conditions, see Kiendl et al. (2016). An alternative approach in which the

total strain energy density is degraded by the phase-field was proposed in Amiri et al. (2014). However, in this case fracture is going to occur in both tensile and compressive areas, which is unphysical. In order to overcome these deficiencies of the previous two approaches, Kiendl et al. (2016) suggested to apply the spectral decomposition on the total strain energy, without any classification in the different strain terms. In the framework of solid-shell formulations, Ambati and De Lorenzis (2016) used a phase-field model for the description of brittle and ductile fracture in shells with small rotations and displacements. Reinoso et al. (2017) used a phase-field model for brittle fracture in shells with large deformations in combination with a monolithic approach. Furthermore, Areias et al. (2016) used two independent phase-fields, one for the lower and one for the upper face of the shell, in order to describe correctly bending-dominated problems.

More recent works on phase-field models for plates and shells include the works of Raghu et al. (2020) and Raghu et al. (2021), where hybrid phase-field models were used for the analysis of brittle fracture in thick plates. Furthermore, Paul et al. (2020) presented an adaptive space-time phase-field model for the analysis of dynamic fracture of brittle shells using Locally Refinable (LR) NURBS. Multipatch shell problems were examined in the framework of a phase-field model of brittle fracture, see Proserpio et al. (2020), and ductile fracture, see Proserpio et al. (2021), using an isogeometric Kirchhoff-Love shell formulation. Combining the phase-field fracture approach with a Reissner-Mindlin shell formulation has not been attempted so far.

1.3 Scope and objective

One main objective of this thesis is the development of an efficient and robust shell formulation for the description of thin and thick plate and shell structures through the successful treatment of locking effects. The shell formulation is based on the isogeometric Reissner-Mindlin shell introduced in Dornisch et al. (2013), where the shell structure is described by its mid-surface and for the thickness direction a director vector is used. NURBS basis functions, which are common in Computer Aided Design (CAD) tools are used for the geometry description. The focus lies on the elimination of transverse shear and membrane locking that are pronounced in the Kirchhoff limit, i.e. for thin plate and shell structures. Two different approaches are implemented. The first one is using a displacement-based shell formulation and is concerned with the treatment of transverse shear locking in Reissner-Mindlin plates and shells. Transverse shear locking occurs due to a mismatch of the approximation spaces of the displacements and rotations in the strain formulation. Thus, in this approach adjusted approximation spaces are defined, i.e. the basis functions of the two rotations are chosen to be in

the relevant direction one order lower than the ones for the displacements. The idea of solving the problem of transverse shear locking at its roots by using adjusted approximation spaces is already known from the finite element method, see e.g. Babu and Prathap (1986), Babu et al. (1987) and Ishaquddin et al. (2012). It was first implemented in isogeometric analysis in Beirão da Veiga et al. (2012a). Using this approach, three separate control meshes are created that have in common the number of elements. The starting geometry is the same for all three meshes and only the degree of the subsequent refinement is different. Thus, the isogeometric concept, namely, the direct use of the surface design model in analysis, still holds. A global mesh, which is needed for the implementation of the weak formulation, is constructed through a combination of the three meshes. It includes the control points of all three meshes with varying degrees of freedom depending on which meshes they belong to. The resulting total number of degrees of freedom is less than for the corresponding standard Reissner-Mindlin shell formulation without any anti-locking mechanism. Thus, the computational cost for the solution of the linear equation is reduced. The method is generally applicable for any polynomial degree and no additional variables have to be introduced, i.e. the unknowns in the variational formulation are still the three displacements and two rotations.

The second approach is based on the two-field Hellinger-Reissner variational principle with the stress resultants being the additional unknowns. This time the aim is to eliminate both membrane and transverse shear locking by using appropriate approximation spaces for the interpolation of the corresponding stress resultants. In the framework of isogeometric analysis, the best choice for the basis functions of the stress resultants is to use, in the relevant direction, one order lower splines than the ones used for the interpolation of the displacements/rotations. All approximation spaces have the same number of elements and Gauss points as the displacement/rotation mesh. However, the location and the number of control points varies from approximation space to approximation space. Due to the high continuity of splines in isogeometric analysis, mixed formulations, as the one presented here, involve static condensation on the patch level, which includes the inversion of a matrix on the patch level and leads to a fully populated stiffness matrix. In order to overcome these issues and reduce the computational cost, in addition to the global approach (on the patch level), two local approaches are presented that enable static condensation on the element level. The first one includes stress resultants that are defined discontinuously (C^{-1}) across the element boundaries. This leads to a sparse stiffness matrix that has the same bandwidth as the standard displacement-based shell, reducing the computational cost. The second local approach is based on the reconstruction algorithm used for the \bar{B} method in Greco et al. (2017, 2018). In this work, it is reformulated for the mixed formulation with stress resultants as additional unknowns and extended to the case of Reissner-Mindlin plates and shells. The resulting stiffness matrix of this method has a slightly higher bandwidth than the

standard displacement-based shell. The two local approaches as well as the global approach are in general applicable for any polynomial degree.

The second main objective of this thesis is the development of a phase-field model for the correct description of brittle fracture in isogeometric Reissner-Mindlin plates and shells. The applied phase-field approach is an extension of the work of Kiendl et al. (2016), where brittle fracture was modeled for Kirchhoff-Love shells. A continuous crack phase-field is defined on the shell mid-surface in order to describe the cracked and uncracked material. In contrast to the phase-field model of Kiendl et al. (2016), here, a special focus lies on the incorporation of the transverse shear strains in the phase-field model, since Reissner-Mindlin plates and shells are considered. This way, fracture due to transverse shear deformations is computable. In order to avoid any fracture in compressive areas, a spectral decomposition is applied on the total strain energy which depends on the total strain tensor. Afterwards the tensile part of the strain energy surface density is degraded, leading to a physically correct behavior of fracture in the tensile and compressive regions. Since the total strain has to be considered for the spectral decomposition, the plane stress condition can not be applied by a simple elimination of the thickness normal strain and thickness normal stress from the constitutive law. Instead, it has to be enforced numerically. For this reason, a local algorithm with quadratic convergence presented in the work of Klinkel and Govindjee (2002) and Ambati et al. (2018) is implemented. The integration through the thickness is performed numerically and in each integration point the thickness normal strain is computed for which the thickness normal stress is zero.

1.4 Overview

The present cumulative dissertation consists of three peer-reviewed articles in international scientific journals and is organized as follows:

In Chapter 2, an introduction to isogeometric analysis is given. First, the concepts of knot vectors, control points and patches is explained. Furthermore, B-splines which are needed for the definition of Non-Uniform Rational B-splines (NURBS) are described. NURBS curves and NURBS surfaces are detailed. A special focus lies on the different refinement techniques and continuity of splines.

In Chapter 3, the first peer-reviewed article is presented which focuses on the elimination of transverse shear locking in isogeometric Reissner-Mindlin plates and shells. Since transverse shear locking occurs due to a mismatch of the approximation spaces of the displacements and rotations in the strain formulation, adjusted approximation spaces are defined for the rotations. Three separate control meshes are created from which the global mesh for the solution of the weak formulation is formed.

The second peer-reviewed article is included in Chapter 4. It is concerned with the alleviation of both transverse shear and membrane locking in the framework of the isogeometric Reissner-Mindlin shell formulation. A displacement-stress mixed method is derived using the Hellinger-Reissner functional. Appropriate approximation spaces are chosen for the stress resultants that are related to locking. The main focus lies on the performance of the static condensation. Three different approaches are presented, including a continuous approach that performs static condensation on the patch level, a discontinuous approach that performs the static condensation on the element level and a reconstructed approach that uses weights for the local control variables in order to get blended global ones.

Chapter 5 includes the third peer-reviewed article. A phase-field model for the description of brittle fracture in isogeometric Reissner-Mindlin plates and shells is presented. The transverse shear strains are incorporated in the model in order to allow for fracture due to transverse shear deformations. The spectral decomposition for the tension-compression split is applied on the total strain. The plane stress condition is enforced numerically using a local algorithm with quadratic convergence.

Chapter 6 provides a summary of this thesis and suggestions for future work.

In Appendix A the local algorithm for the enforcement of the plane stress condition described in Chapter 5 is presented.

Chapter 2

NURBS-based isogeometric analysis

In this chapter a brief summary of the basic terms and properties in isogeometric analysis is given based on the works of Piegl and Tiller (1997), Cottrell et al. (2009) and Rogers (2001). The isogeometric concept, namely, the direct use of the design model in the analysis, implies that the same basis functions are used for the description of the geometry in these two processes. The isoparametric concept, namely, the approximation of the unknown variables with the same basis functions as the geometry, is also included in isogeometric analysis. The most common basis functions that are used in Computer-Aided Design and Modeling are the Non-Uniform Rational B-splines (NURBS). The isogeometric Reissner-Mindlin shell formulation which is going to be investigated in the context of locking and brittle fracture in this thesis is developed using NURBS basis functions. Furthermore, regarding brittle fracture, the phase-field, which is used to describe cracked and uncracked material is also discretized using NURBS basis functions. With regard to the development of the mixed formulation in Chapter 4, a special focus is laid in this chapter on the different refinement techniques common in isogeometric analysis and the continuity properties of splines.

2.1 Preliminaries

In isogeometric analysis the geometry is defined using the control points and the corresponding basis functions. The control points include the degrees-of-freedom of the structure. They define the control mesh which does not have to coincide with the actual geometry and consists of multilinear elements. On the other hand, the physical mesh consists of the actual geometry and is divided into patches. Each patch should have the same material and physical properties and it can be seen as a type of subdomain. A patch can be represented in the physical space as well as in the parameter space. The basis functions map the entire patch from the parameter space to the physical space.

Each patch is decomposed into elements which are defined using the knot vector Ξ . The knot vector for curves has in general the following form

$$\Xi = \{\xi_1, \xi_2, \dots, \xi_{n+p+1}\} \quad (2.1)$$

where n is the number of control points, p the polynomial degree of the basis function and ξ_i the knots which are non-decreasing values. For surfaces two knot vectors Ξ^1, Ξ^2 are necessary, while for solids three knot vectors Ξ^1, Ξ^2, Ξ^3 are used. Knot values can be repeated more than once, i.e. can have a multiplicity $\tilde{m} \geq 1$. The multiplicity of a knot value determines the continuity of the basis functions at this point. This property is going to be discussed in more detail in Sections 2.4 and 2.5. The intervals $[\xi_i, \xi_{i+1}]$ with $i = 1, \dots, n + p$ are the so-called knot spans. Only knot spans with non-zero length, i.e. $\xi_i \neq \xi_{i+1}$ define an element. Knot vectors in which the knot spans have the same length are referred to as uniform knot vectors. Non-uniform knot vectors consists of knot spans with different lengths or knot values that have a multiplicity greater than one. If the first and last entry of the knot vector is repeated $p + 1$ times, the vector is referred to as open knot vector and the basis functions are interpolatory at the endpoints. An example for the definition of a spherical surface in the physical and parameter space is given in Fig. 2.1.

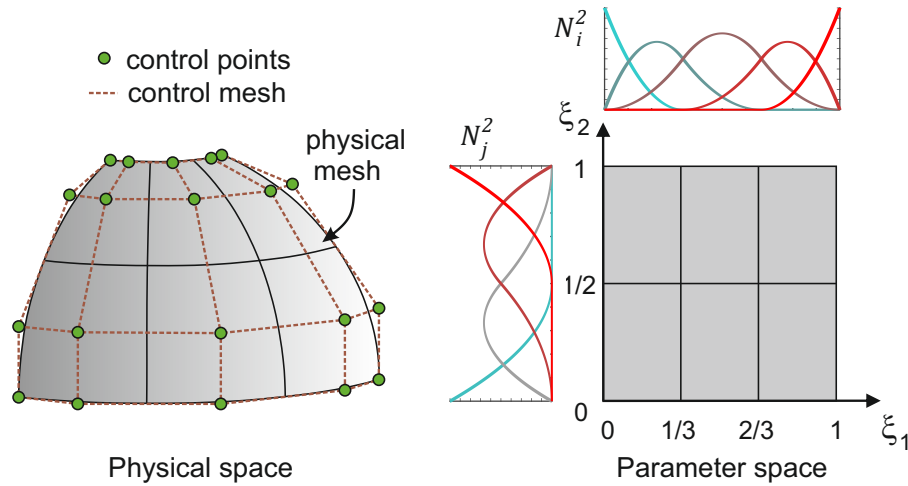


Figure 2.1: Physical and parameter space for a spherical surface. The knot vectors are defined as $\Xi^1 = \{0, 0, 0, 1/3, 2/3, 1, 1, 1\}$ and $\Xi^2 = \{0, 0, 0, 1/2, 1, 1, 1\}$ and the polynomial degrees of the basis functions are $p = q = 2$.

2.2 B-splines

B-splines build the basis for the definition of the Non-Uniform Rational B-splines (NURBS). They are piecewise polynomials and are infinitely differentiable within a knot span $[\xi_i, \xi_{i+1})$ while at knots they are $p - \tilde{m}$ times continuously differentiable, where \tilde{m} is the multiplicity of the knot value. B-splines are defined using the knot vector Ξ and the Cox-de Boor recursion formula. Starting from the polynomial degree $p = 0$, where

$$\bar{N}_i^0(\xi) = \begin{cases} 1 & \text{if } \xi_i \leq \xi < \xi_{i+1}, \\ 0 & \text{otherwise} \end{cases} \quad (2.2)$$

basis functions with higher polynomial degrees are defined as

$$\bar{N}_i^p(\xi) = \frac{\xi - \xi_i}{\xi_{i+p} - \xi_i} \bar{N}_i^{p-1}(\xi) + \frac{\xi_{i+p+1} - \xi}{\xi_{i+p+1} - \xi_{i+1}} \bar{N}_{i+1}^{p-1}(\xi). \quad (2.3)$$

The number of basis functions is at the same time the number of control points, i.e. $i = 1, \dots, n$. In contrast to higher order Lagrange shape functions, B-splines are positive in the entire parametric domain. Another important property of B-splines is the partition of unity, i.e.

$$\sum_{i=1}^n \bar{N}_i^p(\xi) = 1 \quad \forall \xi \in \Xi. \quad (2.4)$$

Furthermore, B-splines have only one maximum when $p \geq 1$. The support of a B-spline of order p is local and includes $p + 1$ knot spans, i.e. $\bar{N}_i^p(\xi) \neq 0$ for $\xi \in [\xi_i, \xi_{i+p+1})$. On the other hand, the number of B-spline functions that have an influence on a given knot span, i.e. are non-zero, is $n_{en} = p + 1$. More details on the properties of B-splines are given in Piegl and Tiller (1997).

The $k - th$ derivative of a B-spline basis function with polynomial degree p depends on the derivatives of lower order basis functions and is defined as

$$\frac{\partial^k}{\partial \xi^k} \bar{N}_i^p(\xi) = \frac{p}{\xi_{i+p} - \xi_i} \frac{\partial^{k-1} \bar{N}_i^{p-1}(\xi)}{\partial \xi^{k-1}} - \frac{p}{\xi_{i+p+1} - \xi_{i+1}} \frac{\partial^{k-1} \bar{N}_{i+1}^{p-1}(\xi)}{\partial \xi^{k-1}}. \quad (2.5)$$

An example for B-spline basis functions of $p = 2$ and their corresponding (in the same color) first and second derivatives is given in Fig. 2.2.

B-spline geometries are a linear combination of B-spline basis functions and the corresponding control points. Here, only the definition of B-spline curves is going to be presented, however, the extension to B-spline surfaces and solids is straightforward and is provided in Cottrell et al. (2009). A B-spline curve is defined as

$$\mathbf{X}(\xi) = \sum_{i=1}^n \bar{N}_i^p(\xi) \mathbf{B}_i \quad \xi_1 \leq \xi \leq \xi_{n+p+1} \quad (2.6)$$

where $\mathbf{B}_i = [x_i, y_i, z_i]^T$ is the set of n control points. Affine transformations of the curve such as rotations, shearings and translations can be applied directly to the control points. This important property is known as affine covariance. Furthermore, due to the convex hull property of B-splines, the curve is contained in the union of convex hulls defined by $p + 1$ successive control points, see Cottrell et al. (2009). B-splines can describe a respectable range of geometries, however they lack the ability to exactly represent geometries like conic sections and circles, see Piegl and Tiller (1997). Thus, Non-Uniform Rational B-splines are introduced.

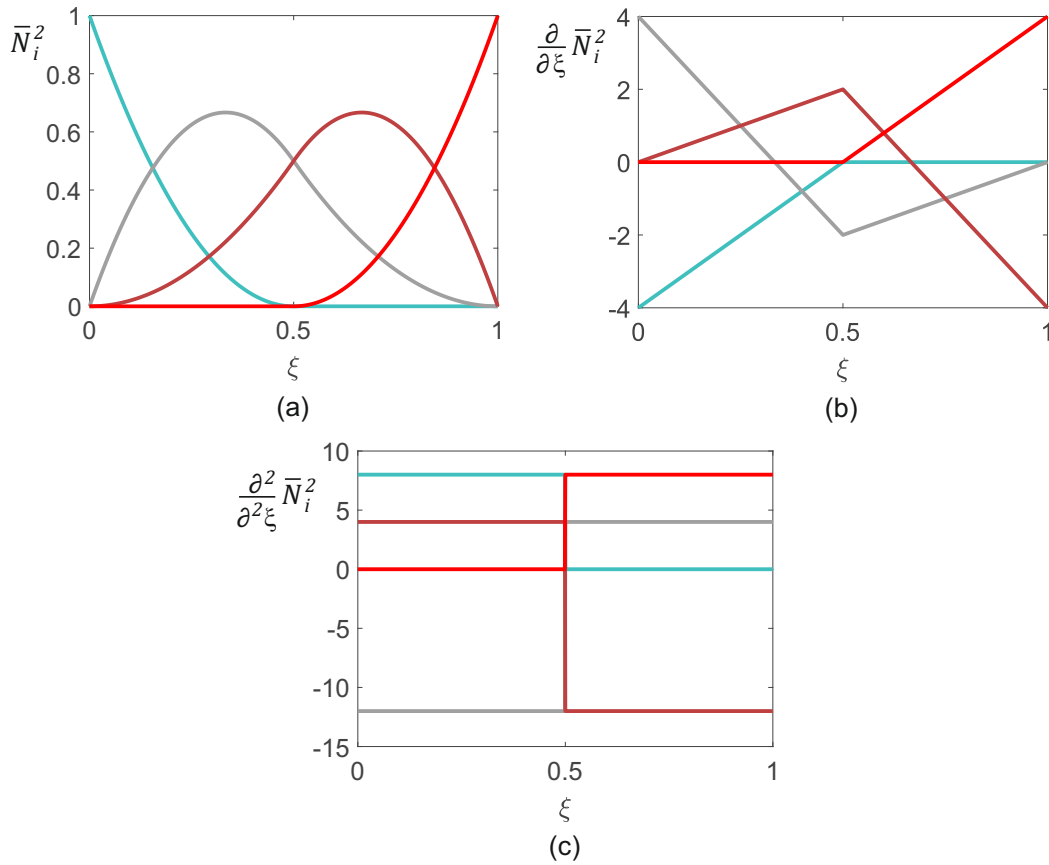


Figure 2.2: B-splines of $p = 2$ (a) and their corresponding first (b) and second (c) derivatives. The knot vector is defined as $\Xi = \{0, 0, 0, 1/2, 1, 1, 1\}$.

2.3 NURBS curves and surfaces

Non-Uniform Rational B-Splines (NURBS) are obtained from the B-splines by using a weight factor w_i , which indicates the influence of a control point on the geometry.

Each control point \mathbf{B}_i has its own weight w_i which is included in the definition of the control point along with the spatial coordinates \mathbf{X}_i

$$\mathbf{B}_i = [\mathbf{X}_i^T, w_i]^T = [x_i, y_i, z_i, w_i]^T \quad (2.7)$$

where $i = 1, 2, \dots, n$. NURBS basis functions have the same properties as the B-splines, including the partition of unity, nonnegativity, convex hull property, the continuity and support of the functions. In the case of affine transformations, the changes are directly applied to the control points while the weights remain the same.

From a geometric point of view, NURBS objects in \mathbb{R}^d are constructed by a projective transformation of a corresponding B-spline object in \mathbb{R}^{d+1} using the weights w_i . From a mathematical point of view, NURBS surface basis functions are constructed from the corresponding B-spline functions in combination with the weights w_i and the weighting function $W(\xi)$ resulting in

$$N_i^p(\xi) = \frac{\bar{N}_i^p(\xi)w_i}{W(\xi)}. \quad (2.8)$$

The definition of the weighting function $W(\xi)$ is given as follows

$$W(\xi) = \sum_{i=1}^n \bar{N}_i^p(\xi)w_i. \quad (2.9)$$

B-splines can be seen as a special case of NURBS where the weights have the same value for all control points.

A NURBS curve is computed analogously to a B-spline curve, see Eq. (2.6), as follows

$$\mathbf{X}(\xi) = \sum_{i=1}^n N_i^p(\xi) \mathbf{X}_i \quad \xi_1 \leq \xi \leq \xi_{n+p+1} \quad (2.10)$$

In the case of a surface in \mathbb{R}^3 , the parametric domain is described by two knot vectors $\Xi^1 = \{\xi_1^1, \xi_2^1, \dots, \xi_{n+p+1}^1\}$ and $\Xi^2 = \{\xi_1^2, \xi_2^2, \dots, \xi_{m+q+1}^2\}$, where n, m are the number of control points and p, q the polynomial degrees in the respective direction. The number of control points, the number of elements, the polynomial degree and the continuity can be chosen differently for each direction. The control points

$$\mathbf{B}_{ij} = [\mathbf{X}_{ij}^T, w_{ij}]^T = [x_{ij}, y_{ij}, z_{ij}, w_{ij}]^T \quad (2.11)$$

are identified in this case by a double index (ij) which corresponds to the ξ^1 and ξ^2 direction respectively, i.e. $i \in \{1, 2, \dots, n\}$ and $j \in \{1, 2, \dots, m\}$. The total number of control points is defined as $n_{cp} = n \cdot m$. Instead of the double index (ij) , a single

node index I can be used which includes only the non-zero basis functions $n_{en} = (p+1)(q+1)$ per element e . This is achieved by the use of a bijective function

$$f^e : \{1, \dots, n\} \times \{1, \dots, m\} \times \{1, \dots, numel\} \rightarrow \{1, \dots, n_{en}\} \quad (2.12)$$

where $numel$ is the number of elements. Thus, the node index I is defined as $I = f^e(i, j, e)$. In the case where multiple patches are considered the definition of f^e in Eq. (2.12) and I would have to be extended by the number of patches $k = 1, \dots, n_p$, see Dornisch (2015). This single index notation is going to be adopted in all following chapters.

In this sense, a NURBS surface is defined as

$$\mathbf{X}(\xi^1, \xi^2) = \sum_{I=1}^{n_{en}} N_I(\xi^1, \xi^2) \mathbf{X}_I. \quad (2.13)$$

The basis functions N_I are computed using B-spline basis functions in both parametric directions

$$N_I(\xi^1, \xi^2) = \frac{\bar{N}_i^p(\xi^1) \bar{N}_j^q(\xi^2) w_{ij}}{W(\xi^1, \xi^2)}. \quad (2.14)$$

The weighting function $W(\xi^1, \xi^2)$ which depends on the two parametric directions is defined as

$$W(\xi^1, \xi^2) = \sum_{I=1}^{n_{en}} \bar{N}_i^p(\xi^1) \bar{N}_j^q(\xi^2) w_{ij}. \quad (2.15)$$

The first derivatives of the NURBS surface basis functions with respect to the parametric coordinates ξ^α are given as follows

$$\frac{\partial N_I(\xi^1, \xi^2)}{\partial \xi^1} = w_{ij} \bar{N}_j^q(\xi^2) \frac{W(\xi^1, \xi^2) \frac{\partial \bar{N}_i^p(\xi^1)}{\partial \xi^1} - \frac{\partial W(\xi^1, \xi^2)}{\partial \xi^1} \bar{N}_i^p(\xi^1)}{(W(\xi^1, \xi^2))^2} \quad (2.16)$$

and

$$\frac{\partial N_I(\xi^1, \xi^2)}{\partial \xi^2} = w_{ij} \bar{N}_i^p(\xi^1) \frac{W(\xi^1, \xi^2) \frac{\partial \bar{N}_j^q(\xi^2)}{\partial \xi^2} - \frac{\partial W(\xi^1, \xi^2)}{\partial \xi^2} \bar{N}_j^q(\xi^2)}{(W(\xi^1, \xi^2))^2}. \quad (2.17)$$

The definition of higher partial derivatives is achieved by a subsequent differentiation of these two equations. More details on this topic can be found in Piegl and Tiller (1997).

2.4 Refinement

In this section the different refinement techniques which are commonly used in isogeometric analysis are presented and demonstrated for the simple case of B-spline curves. However, these techniques are applicable in the same manner to NURBS basis functions.

2.4.1 Knot insertion

Knot insertion involves the insertion of \hat{m} new knots in the knot vector $\Xi = \{\xi_1, \xi_2, \dots, \xi_{n+p+1}\}$ in order to create an extended knot vector $\bar{\Xi} = \{\bar{\xi}_1, \bar{\xi}_2, \dots, \bar{\xi}_{n+\hat{m}+p+1}\}$, where $\bar{\xi}_1 = \xi_1$ and $\xi_{n+p+1} = \bar{\xi}_{n+\hat{m}+p+1}$. This refinement mechanism has two main effects, it increases the number of elements in the parametric space when new knot values are inserted and it changes the continuity of the basis when the multiplicity of existing knot values is increased. In the first case, knot insertion shows similarities to the h -refinement from the classical finite element method. However, new control points are computed using linear combinations of the initial control points. In addition, the same number of new basis functions is formed while the polynomial degree of the basis is not changing. For a single new knot value, p new control points have to be computed, where p is the polynomial degree of the basis function, see Pieg and Tiller (1997). This way, a larger solution space is created and more accurate results are achieved. On the other hand, the use of knot insertion to change the continuity of the basis is very useful when discontinuities are expected to form in the geometry. In both cases, the curve remains the same geometrically and parametrically.

In Fig. 2.3, knot insertion is demonstrated for a curve $\mathbf{X}(\xi)$. The initial knot vector has the value $\Xi = \{0, 0, 0, 0, \frac{1}{3}, \frac{2}{3}, 1, 1, 1, 1\}$ and the polynomial degree is $p = 3$. An extended knot vector $\bar{\Xi} = \{0, 0, 0, 0, \frac{1}{3}, \frac{1}{2}, \frac{2}{3}, 1, 1, 1, 1\}$ is created by the insertion of a new knot $\bar{\xi} = \frac{1}{2}$. As it is seen, the new resulting curve $\bar{\mathbf{X}}(\xi)$ is identical to the initial one. Since only one new knot value has been inserted, $p = 3$ control points \mathbf{B}_i have to be recomputed as it is visible in Fig. 2.3. The first two and last two control points remain the same while the other three control points have either new positions or have been newly introduced. The corresponding basis functions N_i^3 are depicted in Figs. 2.4(a) and (b). The polynomial order and continuity have not changed. The green and yellow squares in Fig. 2.3 denote the split of the curve into three and four elements, respectively.

In Fig. 2.5 knot insertion is used in order to change the continuity of the basis functions. In this case the multiplicity of the knots in the knot vector Ξ is increased and the new knot vector $\bar{\Xi} = \{0, 0, 0, 0, \frac{1}{3}, \frac{1}{3}, \frac{2}{3}, \frac{2}{3}, \frac{2}{3}, 1, 1, 1, 1\}$ is formed. This way, the continuity of the basis functions, which was initially C^2 , is now reduced in certain areas to C^1 .

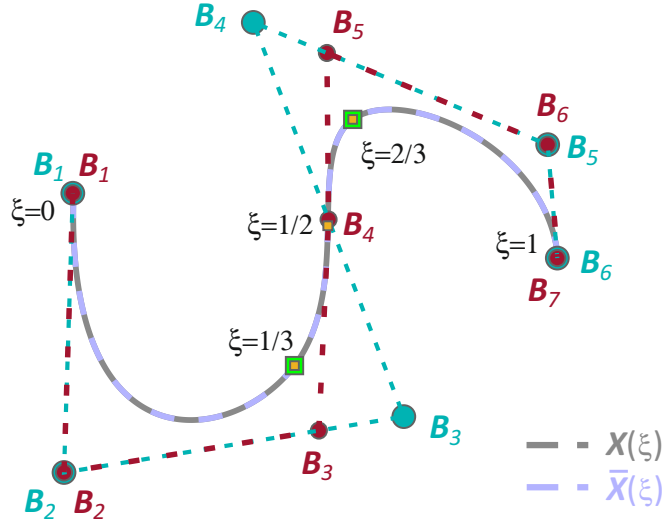


Figure 2.3: Knot insertion. Control polygon and element split of curves $\mathbf{X}(\xi)$ and $\bar{\mathbf{X}}(\xi)$. The original control points are depicted in blue and the new ones in red.

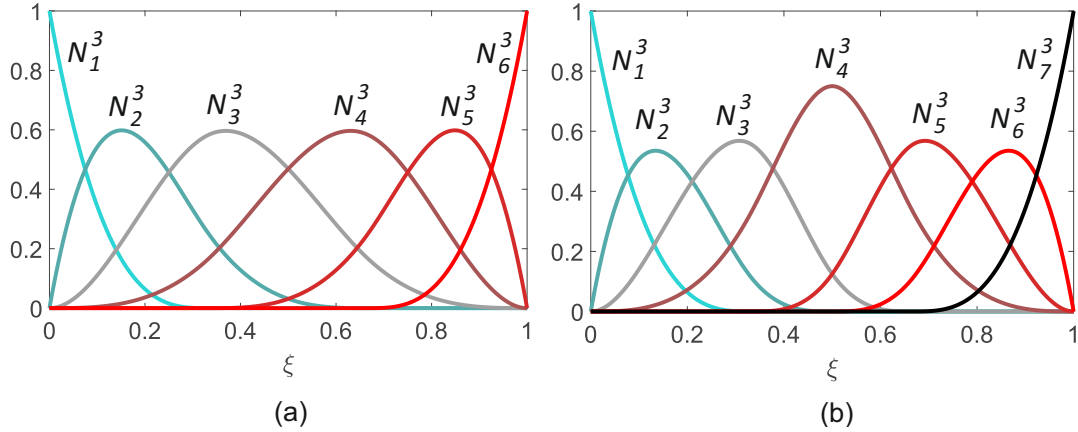


Figure 2.4: Basis functions for the curves (a) $\mathbf{X}(\xi)$ and (b) $\bar{\mathbf{X}}(\xi)$ displayed in Fig. 2.3.

and C^0 . In the case of C^0 -continuity the control point B_6 is located on the physical curve. The new resulting curve $\bar{\mathbf{X}}(\xi)$ coincides again with the original one $\mathbf{X}(\xi)$. New control points are introduced with their corresponding basis functions N_i^3 depicted in Fig. 2.6. The polynomial order remains the same and in this case no new elements are formed.

In the two examples presented here, knot insertion was demonstrated separately for the increase of elements and the reduction of continuity in order to highlight the effect of each option. However, both versions of knot insertion can be applied at the same time.

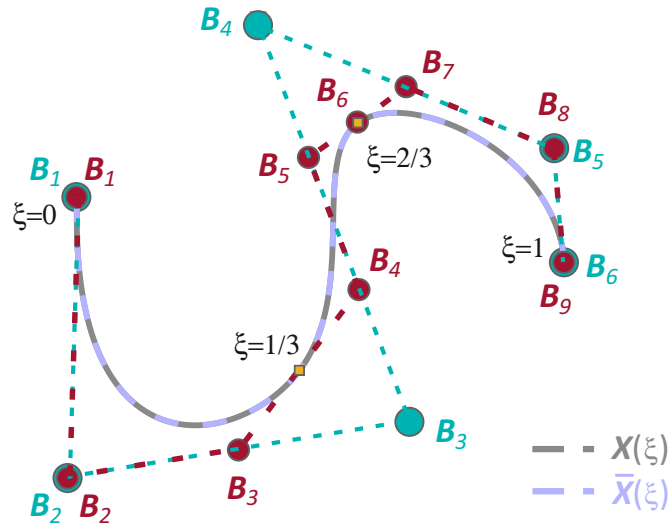


Figure 2.5: Knot insertion with change of continuity. Control polygon and element split of curves $X(\xi)$ and $\bar{X}(\xi)$. The original control points are depicted in blue and the new ones in red.

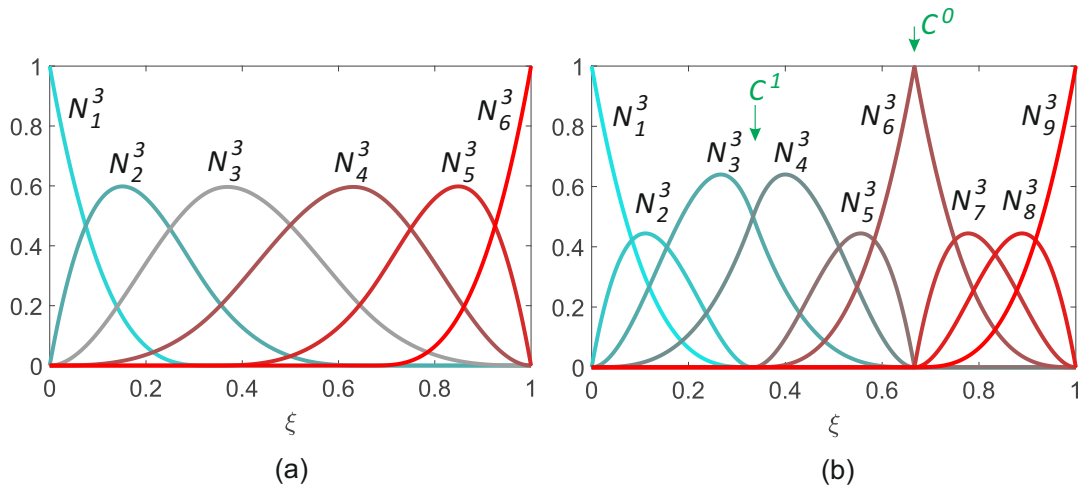


Figure 2.6: Basis functions for the curves (a) $X(\xi)$ and (b) $\bar{X}(\xi)$ displayed in Fig. 2.5.

2.4.2 Order elevation

Order elevation includes an increase of the polynomial degree of the basis function that describes the geometry. This refinement strategy is similar to the p -refinement of the classical finite element analysis. The basis function is enriched and the accuracy of the solution is increased. However, the geometry is not changing geometrically or parametrically. An interesting aspect of order elevation is that the initial continuity of the basis functions remains the same. This is important in order to preserve discontinuities

of the initial geometry. It is achieved by an increase of the knots' multiplicity. However, no new knot values are inserted, thus, the number of elements stays the same. For each increase of the polynomial degree by one, the multiplicity of the knots has to be increased by one as well. In the case of surfaces, order elevation is applied separately to the two parametric directions. Efficient algorithms for order elevation are included in Piegl and Tiller (1997).

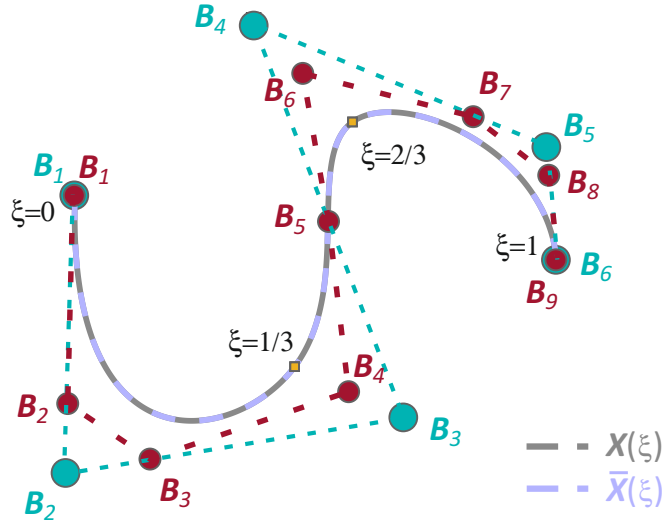


Figure 2.7: Order elevation. Control polygon and element split of curves $X(\xi)$ and $\bar{X}(\xi)$. The original control points are depicted in blue and the new ones in red.

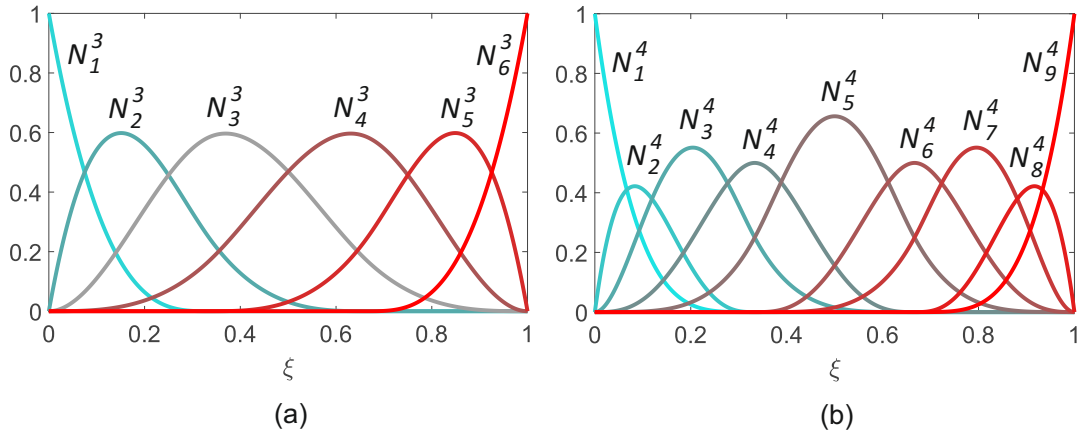


Figure 2.8: Basis functions for the curves (a) $X(\xi)$ and (b) $\bar{X}(\xi)$ displayed in Fig. 2.7.

The example which was previously examined for the case of knot insertion is now used to demonstrate order elevation. The polynomial degree of the curve which was initially

$p = 3$ is now increased to $\tilde{p} = 4$. In order to preserve the C^2 -continuity of the basis functions the initial knot vector $\Xi = \{0, 0, 0, 0, \frac{1}{3}, \frac{2}{3}, 1, 1, 1, 1\}$ is adjusted and the new knot vector reads $\bar{\Xi} = \{0, 0, 0, 0, 0, \frac{1}{3}, \frac{1}{3}, \frac{2}{3}, \frac{2}{3}, 1, 1, 1, 1, 1\}$. As it was stated before, the number of elements does not change. On the other hand, the number of control points is increased and existing control points have to be relocated, see Fig. 2.7. However, the initial curve $\mathbf{X}(\xi)$ and the new curve $\bar{\mathbf{X}}(\xi)$ are identical. The corresponding shape functions are depicted in Figs. 2.8 (a) and (b).

2.4.3 k -refinement

The refinement strategy denoted as k -refinement is a combination of order elevation and knot insertion. First, the polynomial degree is increased to \tilde{p} while the continuity at existing element boundaries remains the same. Afterwards, the number of elements is increased by inserting new knot values in the knot vector. The continuity at these new knots is the highest possible, i.e. $C^{\tilde{p}-1}$. Thus, the resulting basis functions have a higher order and continuity than the original ones and lead to a higher efficiency and robustness of the solution. New control points are introduced, however, their number is limited in comparison to e.g. the p -refinement strategy. The advantages of k -refinement are highlighted in Cottrell et al. (2009).

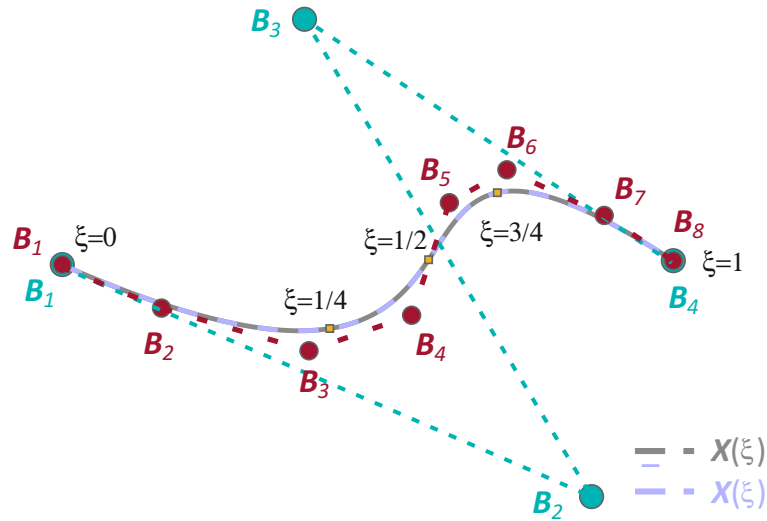


Figure 2.9: k -refinement. Control polygon and element split of curves $\mathbf{X}(\xi)$ and $\bar{\mathbf{X}}(\xi)$. The original control points are depicted in blue and the new ones in red.

In Fig. 2.9 an example for k -refinement is shown. The initial curve $\mathbf{X}(\xi)$ has a polynomial degree of $p = 3$, only one element and the knot vector reads $\Xi = \{0, 0, 0, 0, 1, 1, 1, 1\}$. First, the polynomial degree is increased to $\tilde{p} = 4$ and then

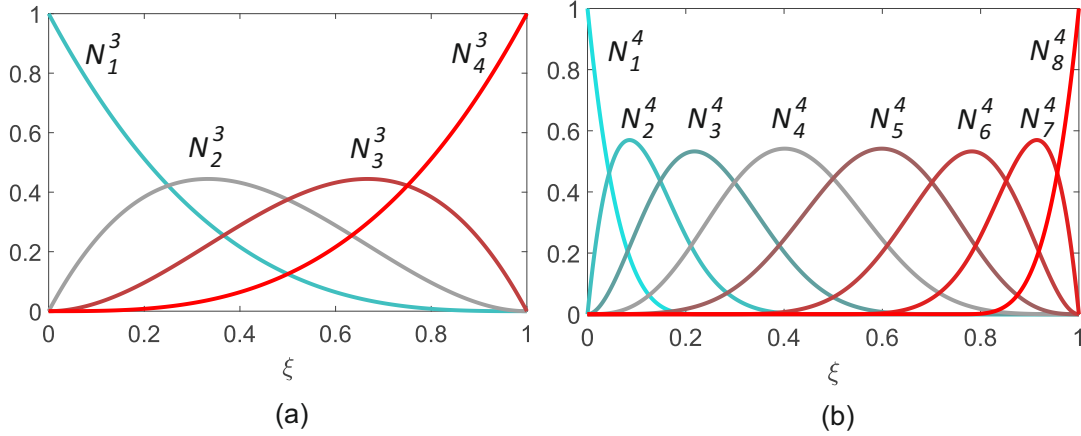


Figure 2.10: Basis functions for the curves (a) $\mathbf{X}(\xi)$ and (b) $\bar{\mathbf{X}}(\xi)$ displayed in Fig. 2.9.

new knot values are inserted until four elements are formed. The resulting knot vector reads $\bar{\Xi} = \{0, 0, 0, 0, 0, \frac{1}{4}, \frac{1}{2}, \frac{3}{4}, 1, 1, 1, 1, 1\}$. The new curve $\bar{\mathbf{X}}(\xi)$ coincides with the original one. The continuity across the element boundaries is C^3 which is the highest possible continuity. The corresponding shape functions are depicted in Figs. 2.10 (a) and (b). Here, a geometry was chosen that can be described by one element. This was done intentionally in order to demonstrate "pure" k -refinement. However, an initial geometry that includes more than one element, as the one shown in Fig. 2.3 could be used. In this case the continuity at the existing knots would be C^2 .

2.5 Continuity

The higher continuity of splines offers a lot of advantages. In contrast to the standard Lagrange-based finite element analysis, free form structures are now computable with a low computational effort. In addition, regarding shell structures, the shell's tangent, curvature and normal vectors can be exactly computed throughout the patch. Kirchhoff-Love type formulations, which require at least C^1 -continuity because of second order derivatives in their kinematics, can be implemented straightforwardly. Furthermore, the higher continuity leads in general to more accurate results, see Cottrell et al. (2009) and Echter (2013).

On the other hand, the high continuity across element boundaries is an obstacle in cases where discontinuities arise. Regarding the geometry, such discontinuities are for instance kinks and sharp bends in the structure. Furthermore, in non-smooth problems that include contact, material interfaces or boundary layers, the high continuity alters the solution since local effects are smeared over the domain. Finally, the use of splines with high continuity for the interpolation of stresses and strains hinders the straight-

forward implementation of standard methods against locking, such as mixed methods, the \bar{B} -method, the Enhanced Assumed Strain (EAS) method and the Assumed Natural Strain (ANS) method. In the case of mixed methods the high continuity of the stress resultants prohibits their elimination on the element level by static condensation. Thus, static condensation has to be performed on the patch level which increases the computational cost, see Section 4.4.

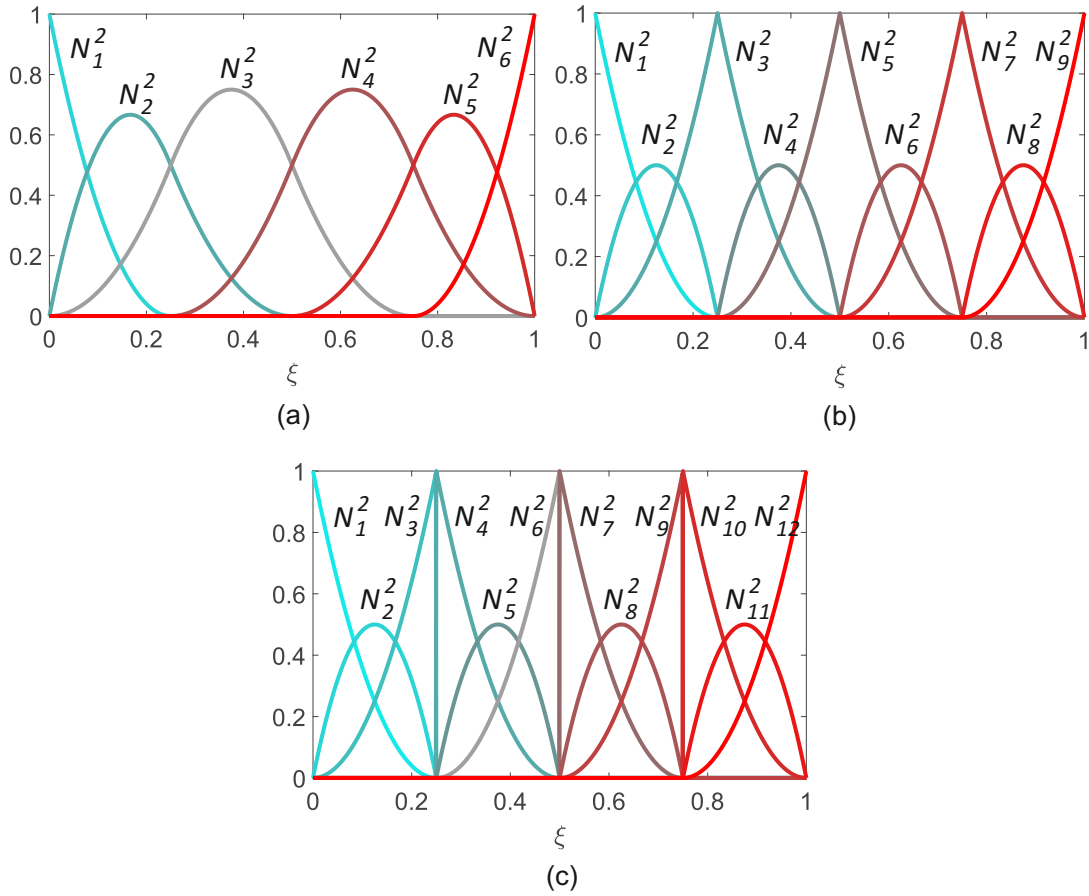


Figure 2.11: Basis functions with polynomial degree $p = 2$ and continuity (a) C^1 (b) C^0 (c) C^{-1} across the element boundaries.

However, as it was shown in Section 2.4.1, isogeometric analysis offers the possibility of controlling and changing the continuity of splines by repeating existing knot values in the knot vector. The continuity can even vary from knot to knot. This is a very special feature in comparison to standard Lagrange-based functions where the continuity is fixed to C^0 and can not be changed. In general, the continuity at a knot is defined as $C^{p-\tilde{m}}$, where p is the polynomial degree and \tilde{m} the multiplicity of the knot. Thus, the maximum achievable continuity is C^{p-1} . In the case of C^0 -continuity,

the basis becomes interpolatory at that knot. On the other hand, C^{-1} -continuity defines the boundary of a patch when open knot vectors are used. The basis functions of one patch are independent from other patches and discontinuous across the patch boundaries. The continuity additionally denotes in general the number of continuous derivatives across the element boundary. The support of a basis function, which is $p+1$ knot spans for a multiplicity $\tilde{m} = 1$ at the knot, is reduced when reducing the continuity between the elements. Note that the continuity referred to here is the parametric continuity. There also exist the geometric continuity, see Rogers (2001).

In Figs. 2.11(a-c) basis functions with polynomial degree $p = 2$ and different continuities across the element boundaries are depicted. In Fig. 2.11(a) the maximum possible continuity C^1 is chosen at the element boundaries and the corresponding knot vector reads $\Xi = \{0, 0, 0, \frac{1}{4}, \frac{1}{2}, \frac{3}{4}, 1, 1, 1\}$. In the second case, the continuity across the element boundaries is reduced to C^0 which corresponds to the standard Lagrange shape functions. The knot vector is then defined as $\bar{\Xi} = \{0, 0, 0, \frac{1}{4}, \frac{1}{4}, \frac{1}{2}, \frac{1}{2}, \frac{3}{4}, \frac{3}{4}, 1, 1, 1\}$. In the last case, C^{-1} continuity is chosen for the element boundaries and each element is independent, in terms of their basis functions, from the other elements. Thus, each element could be seen as a separate patch. The knot vector for this case is $\hat{\Xi} = \{0, 0, 0, \frac{1}{4}, \frac{1}{4}, \frac{1}{4}, \frac{1}{2}, \frac{1}{2}, \frac{1}{2}, \frac{3}{4}, \frac{3}{4}, \frac{3}{4}, 1, 1, 1\}$.

Chapter 3

Adjusted approximation spaces for the treatment of transverse shear locking in isogeometric Reissner-Mindlin shell analysis

This chapter was published as:

Kikis, G., Dornisch, W., and Klinkel, S. (2019). Adjusted approximation spaces for the treatment of transverse shear locking in isogeometric Reissner-Mindlin shell analysis. *Computer Methods in Applied Mechanics and Engineering*, 354:850-870.

Disclosure of the individual authors' contributions to the article:

G. Kikis reviewed the relevant existing literature, implemented the isogeometric Reissner-Mindlin plate and shell element with adjusted approximation spaces into the academic finite element software FEAP, performed all simulations, interpreted and compared the results and wrote the article. W. Dornisch and S. Klinkel gave conceptual advice, contributed to the discussion of the results, read the article and gave valuable suggestions for improvement. All authors approved the publication of the final version of the manuscript.

3.1 Abstract

Transverse shear locking is an issue that occurs in Reissner-Mindlin plate and shell elements. It leads to an artificial stiffening of the system and to oscillations in the stress resultants for thin structures. The thinner the structure is, the more pronounced are the effects. Since transverse shear locking is caused by a mismatch in the approximation

spaces of the displacements and the rotations, a field-consistent approach is proposed for an isogeometric degenerated Reissner-Mindlin shell formulation. The efficiency and accuracy of the method is investigated for benchmark plate and shell problems. A comparison to element formulations with locking alleviation methods from the literature is provided.

3.2 Introduction

Shells are very common in nature and are found in various forms and shapes in plants and animals. In engineering, shell structures have been of great interest due to their favorable mechanical features. They are lightweight structures coupled with a high stiffness and an optimal load-carrying behavior due to their geometrical form. They are able to span big areas without any additional support and also offer an aesthetic design. It is therefore not surprising that applications of shell structures are spread in numerous engineering fields, like architectural and civil engineering, mechanical engineering and marine engineering. In order to describe the mechanical behavior of a shell there exist two main theories, namely the Kirchhoff-Love theory and the Reissner-Mindlin theory. In the Kirchhoff-Love formulation, it is assumed that the normal to middle surface remains normal after deformation, which is sufficient for thin plates and shells where the shear deformations are neglectable. However, with increasing thickness, the shear strains are having a greater influence on the deformation. Thus, more realistic results can be obtained by considering the associated shear deformations in the shell theory. This can be done e.g. by employing two rotations of the normal as additional unknowns in the variational formulation, which is commonly known as Reissner-Mindlin formulation. This kind of shell formulation is applicable for both thin and thick shells.

In the context of the numerical analysis of shells, isogeometric analysis (IGA) has attracted a lot of attention in recent years. It was introduced in Hughes et al. (2005) in order to unify the design and analysis process by using higher order basis functions from CAD tools, such as NURBS functions. Thus, a model which is designed in the CAD tools can be directly used for the analysis process (isogeometric concept). In the framework of shells, the higher continuity of splines throughout a patch is very favorable for the correct computation of the curvature and the normal of the shell surface. Free form structures are computable with much less computational effort than with the classical finite element method. Furthermore, since CAD tools use surface representations and boundaries, isogeometric analysis is especially suitable for shell structures because they are described exclusively by their mid-surface. The first notable steps for the structural analysis of shells with isogeometric analysis were done in the context of

the Kirchhoff-Love theory in Kiendl et al. (2009, 2010) and Benson et al. (2011). In the framework of Reissner-Mindlin shells by Uhm and Youn (2009), Benson et al. (2010b) and Dornisch et al. (2013) and for solid-shells in the work of Hosseini et al. (2013) and Bouclier et al. (2013b,a). Blended shells, which combine the Kirchhoff-Love formulation with the Reissner-Mindlin formulation, were introduced in Benson et al. (2013), as well as a hierarchic family of shells in Echter et al. (2013). Later, these fields were enriched and extended e.g. for Kirchhoff-Love shells in Nguyen-Thanh et al. (2011), Kiendl et al. (2015c) and Duong et al. (2017), for Reissner-Mindlin shells in Dornisch and Klinkel (2014), Dornisch et al. (2016) and Kiendl et al. (2017) and for solid-shells in Hosseini et al. (2014b), Caseiro et al. (2014, 2015) and Bouclier et al. (2015). Furthermore, a shear deformable rotation free shell formulation was proposed in Oesterle et al. (2016).

Despite their favorable features in many aspects, splines suffer from the same locking phenomena as the Lagrange shape functions, see Echter and Bischoff (2010). In the past decade, various methods have been proposed to eliminate these undesirable effects for low order shape functions, most of them are direct extensions from methods that have been proven valuable in the classical finite element method. One of the first ideas and easiest ways to treat locking is to use higher order shape functions, see Echter and Bischoff (2010), however, this method only alleviates locking and increases the computational effort. In the context of plates and shells higher order functions have been investigated for Reissner-Mindlin shells in Benson et al. (2010b), 2D solid shell elements in Bouclier et al. (2013b) and recently, in the framework of an isogeometric collocation formulation for the Reissner-Mindlin shell problem in Kiendl et al. (2017). The use of non-uniform integration in order to alleviate locking and at the same time increase efficiency has been proposed in Adam et al. (2015) and Dornisch et al. (2016) for isogeometric Reissner-Mindlin shell elements. However, the method, which was originally proposed in Adam et al. (2014), does not work for general non-uniform knot vectors and is thus not relevant for industrial applications.

Mixed formulations were implemented in the context of collocation methods in Beirão da Veiga et al. (2012b) and Auricchio et al. (2013), without the need of compatibility conditions between the discrete approximation spaces of the unknown fields. However, collocation methods generally lead to non-symmetric linear systems that may cause difficulties for example in vibration analysis while computing the eigenvalues. Kiendl et al. (2015a) proposed a mixed formulation for Reissner-Mindlin plates and Bouclier et al. used it for solid-shell elements in linear, see Bouclier et al. (2013a) and geometrically nonlinear problems, see Bouclier et al. (2015). Furthermore, a three-field mixed variational formulation to handle nearly incompressible solids was presented in Taylor (2011). Thai et al. (2011) proposed a stabilization technique for the analysis of laminated composite Reissner-Mindlin plates with a small modification in

the material matrix related to the shear terms. First used by Elguedj et al. (2008) to alleviate volumetric locking, the \bar{B} projection method was extended by Bouclier et al. (2012) to a Timoshenko beam formulation. In the latter Bouclier et al. showed that for this case the \bar{B} method is equivalent to the mixed method. The idea of the approach is to project relevant strains onto a basis of lower dimension. However, as it is also for the mixed formulations and Discrete Shear Gap (DSG) approaches, this almost always leads to a linear system where the global matrix that has to be inverted is fully populated, increasing the computational cost. Attempts to overcome the problem are found e.g. in Greco and Cuomo (2016), Greco et al. (2017, 2018) and Antolin et al. (2017). A similar approach for the case of Timoshenko beams is given via the order reduction method in Hu et al. (2016). The \bar{B} projection method was extended to 2D, see Bouclier et al. (2013b) and 3D solid shells, see Bouclier et al. (2013a), where in the latter a local least-squares procedure is applied to each element of the mesh in order to produce a sparse global stiffness matrix. The Assumed Natural Strain (ANS) method, which uses carefully chosen tying points as integration points for the strain components, was used for a solid-shell formulation in Caseiro et al. (2014) and later for geometrically nonlinear problems of elasto-plastic shells, see Caseiro et al. (2015). The DSG method, which is closely related to the ANS method and the \bar{B} method, is implemented in Echter and Bischoff (2010) and Bouclier et al. (2012) for straight and curved Timoshenko beam problems. The Enhanced Assumed Strain (EAS) method was extended by Cardoso and Cesar de Sa (2012) to the NURBS-based isogeometric analysis in order to alleviate volumetric locking.

Echter et al. (2013) presented a family of hierarchic 3-, 5-, and 7-parameter NURBS-based shell formulations where shear and curvature thickness locking is avoided by construction. Membrane locking, is removed using the DSG method or a hybrid-mixed element formulation based on a two-field Hellinger-Reissner principle. However, in Oesterle et al. (2016) it is observed that certain stress resultants exhibit some oscillatory behavior for low order shape functions. Thus, a rotation-free shear deformable shell formulation is proposed in Oesterle et al. (2016) which includes five pure displacement degrees of freedom, which removes the artificial oscillations in the shear stress resultants. An extension to geometrically nonlinear problems was recently proposed in Oesterle et al. (2017). Analogous approaches were used for subdivision shells in Long et al. (2012) and for a Reissner-Mindlin plate formulation using NURBS and triangular NURPS in Beirão Da Veiga et al. (2015). Other approaches that avoid shear locking ab initio were proposed in Kiendl et al. (2015b) and Kiendl et al. (2018) where the classical Timoshenko beam problem is reformulated to a single differential equation with only one primal variable, namely, the bending displacement and the rotation, respectively. A mixed displacement method for removing geometrical locking effects was introduced firstly for straight Timoshenko beams, Reissner-Mindlin plates and

Kirchhoff-Love shells in Bieber et al. (2018).

This work is concerned with the treatment of transverse shear locking in the framework of Reissner-Mindlin shells. Shear locking occurs due to a mismatch of the approximation spaces of the displacement and the rotation terms in the strain formulation, which leads to an artificial stiffening of the system, an underestimation of the deformations and oscillations in the stress resultants. This behavior is intensified the thinner the structure gets, i.e. the more it approximates the Kirchhoff limit. The proposed approach attempts to solve the problem at its roots, by using adjusted approximation spaces for the displacements and the rotations. This method is already known from the finite element method, see e.g. Babu and Prathap (1986), Babu et al. (1987) and Ishaquddin et al. (2012). It was first implemented in isogeometric analysis by Beirão da Veiga et al. (2012a) in the framework of the Reissner-Mindlin plate bending problem. Here, it is extended to a Reissner-Mindlin shell formulation. The advantage of this method is that it is generally applicable for any polynomial degree and no additional variables have to be introduced, i.e. the unknowns in the variational formulation are as usual three displacements and two rotations. Furthermore, as it is shown in Section 3.5, the total number of degrees of freedom is actually reduced, decreasing the computational cost for the solution of the linear equation. Several numerical examples are carried out in order to verify the effectiveness of the method and to compare it with existing locking-free element formulations.

3.3 Reissner-Mindlin shell formulation

3.3.1 Kinematics and basis systems

The present element is a linear isogeometric Reissner-Mindlin shell element, based on the element proposed by Dornisch et al. (2013). In contrast to the Kirchhoff-Love shell formulation, the Reissner-Mindlin shell also considers the shear terms, making it a suitable formulation not only for thin but also for thick plates. The shell formulation from Dornisch et al. is derived from continuum mechanics using the direct approach from Simo and Fox (1989). The shell is represented only by its mid-surface reducing the computational effort. The thickness direction is described by the director vector leading to the definition of the reference position vector of an arbitrary point on the shell

$$\tilde{\mathbf{X}}(\xi^i) = \mathbf{X}(\xi^\alpha) + \xi^3 \mathbf{D}(\xi^\alpha), \quad (3.1)$$

where ξ^α with $\alpha = 1, 2$ are the parametric coordinates in the shell mid-surface and $-\frac{t}{2} \leq \xi^3 \leq \frac{t}{2}$ is the thickness coordinate. Parameters without (\sim) describe values on

the mid-surface. The reference director vector \mathbf{D} coincides with the normal vector of the shell surface and has the length $|\mathbf{D}(\xi^\alpha)| = 1$. Since the shell element is linear, a difference vector formulation can be applied for the definition of the deformed director vector

$$\mathbf{d} = \mathbf{D} + \mathbf{b}, \quad (3.2)$$

where

$$\mathbf{b} = \boldsymbol{\omega} \times \mathbf{D} = \mathbf{W}^T \cdot \boldsymbol{\omega} \quad \text{with} \quad \mathbf{W} = \text{skew}(\mathbf{D}) \quad (3.3)$$

is the difference vector, constructed by the vector cross product of the rotational parameter of the shell mid-surface $\boldsymbol{\omega}$ and the reference director vector. Its derivative with respect to the two parametric coordinates ξ^α is given as follows

$$\mathbf{b}_{,\alpha} = \boldsymbol{\omega}_{,\alpha} \times \mathbf{D} + \boldsymbol{\omega} \times \mathbf{D}_{,\alpha} = \mathbf{W}^T \cdot \boldsymbol{\omega}_{,\alpha} + \mathbf{W}_{,\alpha}^T \cdot \boldsymbol{\omega} \quad (3.4)$$

with $\mathbf{W}_{,\alpha} = \text{skew}(\mathbf{D}_{,\alpha})$.

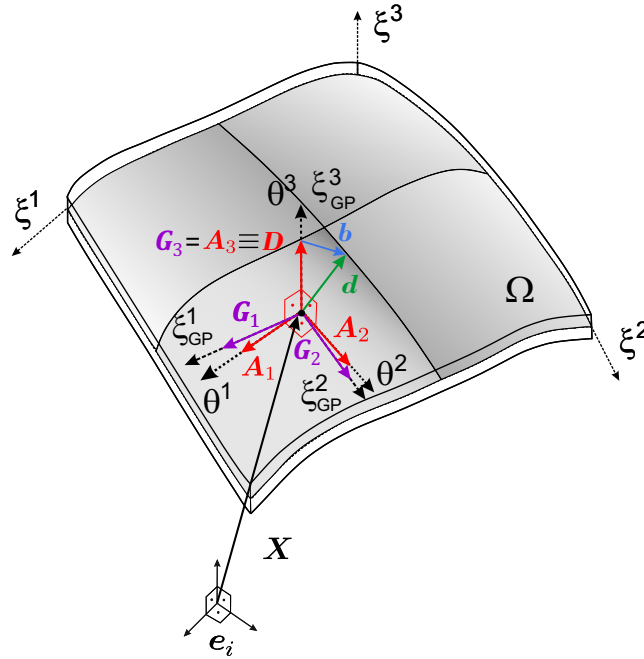


Figure 3.1: Basis systems and director vector at a Gauss point.

The inextensibility in thickness direction is ensured due to the condition $|\mathbf{d}| = |\mathbf{D}| = 1$. In this manner, the displacement vector $\tilde{\mathbf{u}}$ of an arbitrary point on the shell is described using the deformed director vector as follows

$$\tilde{\mathbf{u}}(\xi^i) = \mathbf{u}(\xi^\alpha) + \xi^3 \mathbf{d}(\xi^\alpha), \quad (3.5)$$

where $\mathbf{u}(\xi^\alpha)$ is the displacement vector of the mid-surface. The current position vector of an arbitrary point on the shell surface is obtained as

$$\tilde{\mathbf{x}}(\xi^i) = \mathbf{x}(\xi^\alpha) + \xi^3 \mathbf{d}(\xi^\alpha), \quad (3.6)$$

where $\mathbf{x}(\xi^\alpha)$ denotes the current position vector of a point on the shell mid-surface

$$\mathbf{x}(\xi^\alpha) = \mathbf{X}(\xi^\alpha) + \mathbf{u}(\xi^\alpha). \quad (3.7)$$

In this shell formulation there exist two different types of basis systems. The first one is the covariant basis system with its basis vectors defined as

$$\mathbf{G}_\alpha = \mathbf{X}_{,\alpha} + \xi^3 \mathbf{D}_{,\alpha}, \quad \mathbf{G}_3 = \mathbf{D}. \quad (3.8)$$

The corresponding contravariant basis vector is derived with the help of the Kronecker Delta, $\mathbf{G}_i \cdot \mathbf{G}^j = \delta_i^j$. In the constitutive relation an orthonormal basis system is needed, so a second local basis system \mathbf{A}_i is introduced, see Dornisch et al. (2013). The new basis system is computed at the Gauss points using the lamina coordinate system, see Hughes (2000), and is as close as possible to the convected basis system, see Fig. 3.1. The corresponding local Cartesian coordinate system for the basis vectors \mathbf{A}_i is θ_i . Since the stress and strain tensors are defined using \mathbf{A}_i , the displacement and position vectors, see Eq. (3.1), (3.5), (3.6), (3.7) and all differentiated values, e.g. Eq. (3.4), are now defined with respect to θ_i . As it is explained in more detail in Section 3.4, the nodal Cartesian system \mathbf{A}_{iI} at the control points is needed for the definition of the rotational parameter ω . A method for the calculation of the nodal basis systems is proposed in Dornisch et al. (2013). There, the nodal basis systems are defined so that their interpolated values at any point of the surface coincide as good as possible with the basis systems defined by the geometry.

3.3.2 Strains and stresses

As strain measure, the linearized Green-Lagrange strain tensor is used since only linear problems are considered

$$\mathbf{E} = E_{ij} \mathbf{G}^i \otimes \mathbf{G}^j \quad (3.9)$$

with the covariant components

$$E_{ij} = \frac{1}{2} (\mathbf{G}_i \cdot \tilde{\mathbf{u}}_{,j} + \mathbf{G}_j \cdot \tilde{\mathbf{u}}_{,i}). \quad (3.10)$$

The components E_{ij} are rearranged into in-plane and transverse shear strains

$$E_{\alpha\beta} = \varepsilon_{\alpha\beta} + \theta^3 \kappa_{\alpha\beta} + (\theta^3)^2 \rho_{\alpha\beta} \quad (3.11)$$

$$2E_{\alpha 3} = \gamma_\alpha \quad (3.12)$$

$$E_{33} = 0 \quad (\text{due to the inextensibility constraint}), \quad (3.13)$$

where $\varepsilon_{\alpha\beta}$ denote the membrane strains

$$\varepsilon_{\alpha\beta} = \frac{1}{2}(\mathbf{X}_{,\alpha} \cdot \mathbf{u}_{,\beta} + \mathbf{X}_{,\beta} \cdot \mathbf{u}_{,\alpha}), \quad (3.14)$$

$\kappa_{\alpha\beta}$ represent the curvatures of the shell

$$\kappa_{\alpha\beta} = \frac{1}{2}(\mathbf{X}_{,\alpha} \cdot \mathbf{b}_{,\beta} + \mathbf{X}_{,\beta} \cdot \mathbf{b}_{,\alpha} + \mathbf{D}_{,\alpha} \cdot \mathbf{u}_{,\beta} + \mathbf{D}_{,\beta} \cdot \mathbf{u}_{,\alpha}) \quad (3.15)$$

and γ_α are the shear strains

$$\gamma_\alpha = \mathbf{X}_{,\alpha} \cdot \mathbf{b} + \mathbf{u}_{,\alpha} \cdot \mathbf{D}. \quad (3.16)$$

The second-order curvatures $\rho_{\alpha\beta}$ are neglected. The resulting linear shell strains are arranged in Voigt notation in the strain vector

$$\boldsymbol{\varepsilon} = [\varepsilon_{11} \quad \varepsilon_{22} \quad 2\varepsilon_{12} \quad \kappa_{11} \quad \kappa_{22} \quad 2\kappa_{12} \quad \gamma_1 \quad \gamma_2]^T. \quad (3.17)$$

Analogously, the stress resultants are assembled into the stress tensor

$$\boldsymbol{\sigma} = [n^{11} \quad n^{22} \quad n^{12} \quad m^{11} \quad m^{22} \quad m^{12} \quad q^1 \quad q^2]^T, \quad (3.18)$$

where $n^{\alpha\beta}$ the membrane forces, $m^{\alpha\beta}$ the bending moments and q^α the shear forces.

3.3.3 Variational formulation

The weak form of equilibrium is derived from the strong form, which includes the static equilibrium and the Neumann and Dirichlet boundary conditions. After a scalar multiplication of the equations with a test function $\delta \mathbf{v}$, which represents a virtual deformation, the terms are integrated over the whole domain and, considering the present shell theory, rearranged in the following form

$$G(\mathbf{v}, \delta \mathbf{v}) = \int_{\Omega_0} \delta \boldsymbol{\varepsilon} \cdot \boldsymbol{\sigma} dA - \int_{\Omega_0} \delta \mathbf{v}^T \bar{\mathbf{p}}_0 dA - \int_{\Gamma_0^N} \delta \mathbf{v}^T \bar{\mathbf{t}}_0 ds = 0 \quad (3.19)$$

with $\bar{\mathbf{p}}_0$ the surface loads, $\bar{\mathbf{t}}_0$ the boundary tractions and $\mathbf{v} = \begin{bmatrix} \mathbf{u} \\ \boldsymbol{\beta} \end{bmatrix} = [u_1 \quad u_2 \quad u_3 \quad \beta_1 \quad \beta_2]^T$ the deformation vector. Only two rotations are taken into account because only smooth surfaces are being considered. In other cases, i.e. for surfaces with kinks, the third rotation is indispensable. The variation of the shell strain components reads

$$\begin{aligned} \delta \varepsilon_{\alpha\beta} &= \frac{1}{2}(\mathbf{X}_{,\alpha} \cdot \delta \mathbf{u}_{,\beta} + \mathbf{X}_{,\beta} \cdot \delta \mathbf{u}_{,\alpha}) \\ \delta \kappa_{\alpha\beta} &= \frac{1}{2}(\mathbf{X}_{,\alpha} \cdot \delta \mathbf{b}_{,\beta} + \mathbf{X}_{,\beta} \cdot \delta \mathbf{b}_{,\alpha} + \mathbf{D}_{,\alpha} \cdot \delta \mathbf{u}_{,\beta} + \mathbf{D}_{,\beta} \cdot \delta \mathbf{u}_{,\alpha}) \\ \delta \gamma_\alpha &= \mathbf{X}_{,\alpha} \cdot \delta \mathbf{b} + \delta \mathbf{u}_{,\alpha} \cdot \mathbf{D}. \end{aligned} \quad (3.20)$$

The relation between the stress resultants and the strains is very simple since only linear elastic materials are considered and is defined as $\boldsymbol{\sigma} = \mathbb{C} \cdot \boldsymbol{\varepsilon}$, where \mathbb{C} is the constitutive matrix, see Dornisch et al. (2016).

3.4 Standard NURBS-based isogeometric shell formulation

The Reissner-Mindlin shell theory described in Section 3.3 is now combined with the isogeometric analysis, see Piegl and Tiller (1997), Cottrell et al. (2009), for the numerical solution of the weak form of equilibrium, Eq. (3.19). As it was mentioned in Section 3.2, the main advantage of isogeometric analysis is that it uses the same basis functions for the design and analysis. This does not only reduce the computational cost but leads to an exact representation of the geometry. Thus, the interpolation of the mid-surface's position vector \mathbf{X} is not going to be an approximation but the exact value

$$\mathbf{X} = \sum_{I=1}^{n_{en}} N_I \mathbf{X}_I, \quad (3.21)$$

where N_I denotes the NURBS surface basis functions, see Piegl and Tiller (1997). The variable n_{en} defines the number of basis functions that have an influence on one element, i.e. their value is non zero. In general, it is specified by $n_{en} = (p+1) \cdot (q+1)$, where p, q are the chosen polynomial degrees for the basis functions in the first and in the second direction. The same holds for the reference director vector which coincides with the normal vector of the surface and is calculated using the given geometry

$$\mathbf{D} = \sum_{I=1}^{n_{en}} N_I \mathbf{D}_I. \quad (3.22)$$

The derivatives of \mathbf{X} and \mathbf{D} with respect to the local Cartesian basis system θ^α are consequently interpolated by

$$\mathbf{X}_{,\alpha} = \sum_{I=1}^{n_{en}} N_{I,\alpha} \mathbf{X}_I \quad \mathbf{D}_{,\alpha} = \sum_{I=1}^{n_{en}} N_{I,\alpha} \mathbf{D}_I. \quad (3.23)$$

The other terms of the Reissner-Mindlin shell formulation are going to be approximated values and are denoted with $(\dots)^h$.

Starting from the solution variables \mathbf{u} , the same basis functions are used for their interpolation as for the description of the geometry

$$\mathbf{u}^h = \sum_{I=1}^{n_{en}} N_I \mathbf{u}_I. \quad (3.24)$$

The corresponding derivatives are computed analogously

$$\mathbf{u}_{,\alpha}^h = \sum_{I=1}^{n_{en}} N_{I,\alpha} \mathbf{u}_I. \quad (3.25)$$

The interpolation of the difference vector \mathbf{b}^h , see Eq. (3.3), and its derivative $\mathbf{b}_{,\alpha}^h$, see Eq. (3.4), requires the interpolated value of the rotational parameter $\boldsymbol{\omega}^h$ and its derivative $\boldsymbol{\omega}_{,\alpha}^h$

$$\mathbf{b}^h = \boldsymbol{\omega}^h \times \mathbf{D}, \quad \mathbf{b}_{,\alpha}^h = \boldsymbol{\omega}_{,\alpha}^h \times \mathbf{D} + \boldsymbol{\omega}^h \times \mathbf{D}_{,\alpha}. \quad (3.26)$$

On the other hand, the interpolated rotational parameter $\boldsymbol{\omega}^h$

$$\boldsymbol{\omega}^h = \sum_{I=1}^{n_{en}} N_I \boldsymbol{\omega}_I \quad (3.27)$$

can be reformulated in relation to the nodal rotations $\boldsymbol{\beta}_I$. For this purpose, the nodal transformation matrix \mathbf{T}_{3I} is introduced, which includes the nodal Cartesian system \mathbf{A}_{iI} of the reference configuration described in Section 3.3.1. Again, for a smooth surface the transformation matrix \mathbf{T}_{3I} consists only of two nodal basis vectors $\mathbf{A}_{\alpha I}$

$$\mathbf{T}_{3I} = [\mathbf{A}_{2I} \quad \mathbf{A}_{1I}]. \quad (3.28)$$

The third nodal basis vector \mathbf{A}_{3I} is not included in order to avoid zero energy modes which arise due to drilling rotations. The final formulation of the interpolated rotational parameter as well as its derivative reads

$$\boldsymbol{\omega}^h = \sum_{I=1}^{n_{en}} \mathbf{T}_{3I} N_I \boldsymbol{\beta}_I \quad \boldsymbol{\omega}_{,\alpha}^h = \sum_{I=1}^{n_{en}} \mathbf{T}_{3I} N_{I,\alpha} \boldsymbol{\beta}_I. \quad (3.29)$$

In this manner the interpolated variation of the shell strains, see Eq. (3.20), is given as

$$\delta \boldsymbol{\varepsilon}^h = \begin{bmatrix} \delta \varepsilon_{11}^h \\ \delta \varepsilon_{22}^h \\ 2\delta \varepsilon_{12}^h \\ \delta \kappa_{11}^h \\ \delta \kappa_{22}^h \\ 2\delta \kappa_{12}^h \\ \delta \gamma_1^h \\ \delta \gamma_2^h \end{bmatrix} = \begin{bmatrix} \mathbf{X}_{,1} \cdot \delta \mathbf{u}_{,1}^h \\ \mathbf{X}_{,2} \cdot \delta \mathbf{u}_{,2}^h \\ \mathbf{X}_{,1} \cdot \delta \mathbf{u}_{,2}^h + \mathbf{X}_{,2} \cdot \delta \mathbf{u}_{,1}^h \\ \mathbf{X}_{,1} \cdot \delta \mathbf{b}_{,1}^h + \mathbf{D}_{,1} \cdot \delta \mathbf{u}_{,1}^h \\ \mathbf{X}_{,2} \cdot \delta \mathbf{b}_{,2}^h + \mathbf{D}_{,2} \cdot \delta \mathbf{u}_{,2}^h \\ \mathbf{X}_{,1} \cdot \delta \mathbf{b}_{,2}^h + \mathbf{X}_{,2} \cdot \delta \mathbf{b}_{,1}^h + \mathbf{D}_{,1} \cdot \delta \mathbf{u}_{,2}^h + \mathbf{D}_{,2} \cdot \delta \mathbf{u}_{,1}^h \\ \mathbf{X}_{,1} \cdot \delta \mathbf{b}^h + \delta \mathbf{u}_{,1}^h \cdot \mathbf{D} \\ \mathbf{X}_{,2} \cdot \delta \mathbf{b}^h + \delta \mathbf{u}_{,2}^h \cdot \mathbf{D} \end{bmatrix}. \quad (3.30)$$

For a shorter notation the matrix \mathbf{B}_I is introduced, which provides a relation between the virtual strains and the variations of the nodal displacements and rotations

$$\delta \boldsymbol{\varepsilon}^h = \sum_{I=1}^{n_{en}} \mathbf{B}_I \delta \mathbf{v}_I \quad (3.31)$$

with

$$B_I = \begin{bmatrix} \mathbf{X}_{,1}^T N_{I,1} & 0 \\ \mathbf{X}_{,2}^T N_{I,2} & 0 \\ \mathbf{X}_{,1}^T N_{I,2} + \mathbf{X}_{,2}^T N_{I,1} & 0 \\ \mathbf{D}_{,1}^T N_{I,1} & \mathbf{X}_{,1}^T \mathbf{W}^T \mathbf{T}_{3I} N_{I,1} + \mathbf{X}_{,1}^T \mathbf{W}_{,1}^T \mathbf{T}_{3I} N_I \\ \mathbf{D}_{,2}^T N_{I,2} & \mathbf{X}_{,2}^T \mathbf{W}^T \mathbf{T}_{3I} N_{I,2} + \mathbf{X}_{,2}^T \mathbf{W}_{,2}^T \mathbf{T}_{3I} N_I \\ \mathbf{D}_{,1}^T N_{I,2} + \mathbf{D}_{,2}^T N_{I,1} & \mathbf{X}_{,1}^T \mathbf{W}^T \mathbf{T}_{3I} N_{I,2} + \mathbf{X}_{,1}^T \mathbf{W}_{,2}^T \mathbf{T}_{3I} N_I \\ & + \mathbf{X}_{,2}^T \mathbf{W}^T \mathbf{T}_{3I} N_{I,1} + \mathbf{X}_{,2}^T \mathbf{W}_{,1}^T \mathbf{T}_{3I} N_I \\ \mathbf{D}^T N_{I,1} & \mathbf{X}_{,1}^T \mathbf{W}^T \mathbf{T}_{3I} N_I \\ \mathbf{D}^T N_{I,2} & \mathbf{X}_{,2}^T \mathbf{W}^T \mathbf{T}_{3I} N_I \end{bmatrix}. \quad (3.32)$$

3.5 Adjusted approximation spaces against transverse shear locking

Transverse shear locking is a very common problem in the Finite Element Analysis. It is very profound in pure bending dominated problems and is intensified the thinner the structure gets. In these kind of problems the transverse shear strains are going to be zero, i.e., $\lim_{t \rightarrow 0} \gamma_\alpha \stackrel{!}{=} 0$. This condition is automatically satisfied in Kirchhoff-Love type formulations, however in Reissner-Mindlin type models this requirement causes problems. Looking at the presented shell formulation the resulting compatibility requirement for the interpolated transverse shear strains is computed as follows

$$\gamma_\alpha^h = \mathbf{X}_{,\alpha}^T \mathbf{W}^T \sum_{I=1}^{n_{en}} N_I \mathbf{T}_{3I} \beta_I + \mathbf{D}^T \sum_{I=1}^{n_{en}} N_{I,\alpha} \mathbf{u}_I \stackrel{!}{=} 0. \quad (3.33)$$

Normally, the same basis functions are used for the interpolation of the displacements u_i and the rotations β_α . However, that would mean that the first term of the condition, which includes the used basis functions and the second term, which includes the derivatives of the basis functions, being spline basis functions of one order lower, should together result in zero. It is clear that this mismatch in polynomial degrees hinders a proper fulfillment of Eq. (3.33). The problem is more visible when considering plate formulations, where the definition of the shear strains is much simpler

$$\gamma_\alpha^h = \sum_{I=1}^{n_{en}} N_I \beta_{\alpha I} + \sum_{I=1}^{n_{en}} N_{I,\alpha} u_{3I} = 0. \quad (3.34)$$

Thus, transverse shear locking is not a physical problem of the plate or shell formulation but a numerical problem. It leads to spurious shear strains which make the structure much stiffer than it actually is. The resulting deformation is going to be

smaller than it would have been in reality. Furthermore, the shear stress resultants are going to exhibit an oscillatory behavior, see Oesterle et al. (2016). In order to overcome this problem several methods have been suggested for the Finite Element Method and to some extent also for Isogeometric Analysis, see Section 3.2. Here, the method proposed by Beirão da Veiga et al. (2012a) for an isogeometric plate formulation is extended to the presented isogeometric shell formulation.

Beirão da Veiga et al. suggested that if the problem lies in using the same basis functions for u_i and β_α , then using different basis functions with compatible polynomial degrees for the relevant direction would solve the problem. However, this necessitates the use of separate control meshes for the displacements and the two rotations. An example for such a differentiation is given in Fig. 3.2 for a polynomial degree of $p_u = 3$ and $q_u = 2$ for the displacements and only one element. The meshes of the rotations β_1 and β_2 have a polynomial degree which is reduced by one in the relevant direction ($p_{\beta_1} = 2, q_{\beta_1} = 2$ for the β_1 mesh and $p_{\beta_2} = 3, q_{\beta_2} = 1$ for the β_2 mesh). The only value that is going to be the same for all three meshes is the number of elements. This choice is made in order to simplify numerical integration of the weak formulation.

It is important to mention that the starting geometry is the same for all three meshes. Only by applying different degrees of refinement, the new control meshes are created. Thus, the isogeometric concept, namely the direct use of the surface design model in analysis, still holds because the given geometry is not altered but only refined in different ways. A combination of the three meshes results in the so-called global mesh which includes all control points from all meshes, see Fig. 3.2. The total number of control points of the global mesh holds for $p_u, q_u \geq 2$

$$n^{ges} \cdot m^{ges} = (p_u + p_{\beta_1} + 2 \cdot n_{el} - 2) \cdot (q_u + q_{\beta_2} + 2 \cdot m_{el} - 2), \quad (3.35)$$

where n_{el}, m_{el} are the number of elements per direction. If $p_u = 1$ or $q_u = 1$, the equation would change to $n^{ges} = p_u + p_{\beta_1} + 2 \cdot n_{el}$ or $m^{ges} = q_u + q_{\beta_2} + 2 \cdot m_{el}$, respectively. However, the control points of the global mesh do not have the same degrees of freedom. Depending on which mesh they belong to, there are control points with one, three, four or five degrees of freedom. The total number of degrees of freedom for the global mesh is $n_{dofs}^{ges} = n_u \cdot m_u \cdot 3 + n_{\beta_1} \cdot m_{\beta_1} + n_{\beta_2} \cdot m_{\beta_2}$, where n_u, m_u are the number of control points per direction for the u mesh and $n_{\beta_1}, m_{\beta_1}, n_{\beta_2}, m_{\beta_2}$ for the β_1, β_2 mesh, respectively. This equation can be rewritten regarding the polynomial degrees and the number of elements as follows

$$n_{dofs}^{ges} = (p_u + n_{el}) \cdot (q_u + m_{el}) \cdot 5 - (q_u + m_{el} + p_u + n_{el}). \quad (3.36)$$

As it can be seen in Eq. (3.36), the shell formulation with the adjusted approximation spaces has $(q_u + m_{el} + p_u + n_{el})$ less degrees of freedom than its corresponding standard Reissner-Mindlin shell formulation. That means that the computational effort for

the solution of the weak form is lowered and at the same time, especially for lower polynomial degrees and number of elements, the results are more accurate due to the mechanism against transverse shear locking.

The maximal number of control points which have support on an element of the global mesh is calculated by

$$n_{en}^{ges} = (p_u + p_{\beta_1} + 2) \cdot (q_u + q_{\beta_2} + 2). \quad (3.37)$$

The $n_{en}^u = (p_u + 1) \cdot (q_u + 1)$ control points from the u mesh, as well as the $n_{en}^{\beta_1} = (p_{\beta_1} + 1) \cdot (q_{\beta_1} + 1)$ and $n_{en}^{\beta_2} = (p_{\beta_2} + 1) \cdot (q_{\beta_2} + 1)$ control points from the control meshes β_1, β_2 , respectively, that have support on the considered element are all included in the n_{en}^{ges} control points of the global mesh.

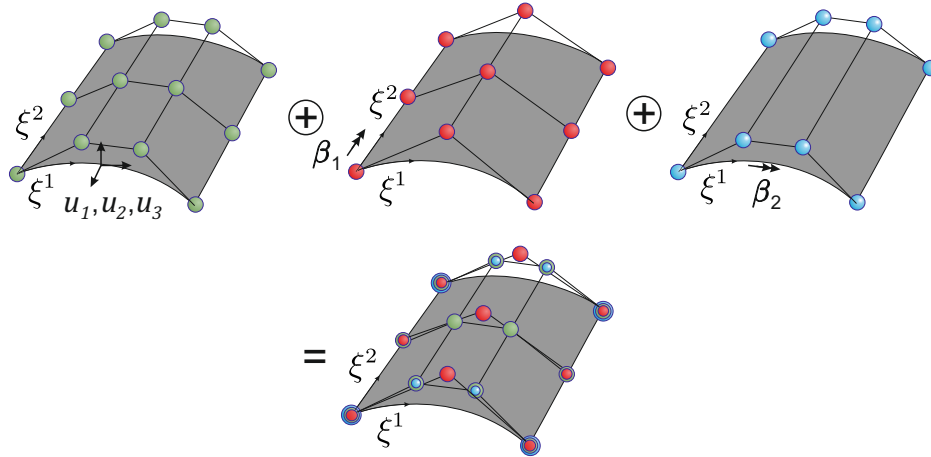


Figure 3.2: Adjusted approximation spaces for u_i and β_α and the resulting global mesh.

The global mesh is needed for the implementation of the weak formulation. In this manner, the shell strains (3.31) have to be rewritten in accordance to the new global mesh. The definition of the B_I matrix in (3.32) is conceived for a shell formulation which uses the same shape functions for all deformations. Now, for the purpose of employing different basis functions for the displacements and the two rotations, the B_I is split into three parts, i.e. $B_I = \begin{bmatrix} B_I^u & B_I^{\beta_1} & B_I^{\beta_2} \end{bmatrix}$, which correspond to the u_i (green), β_1 (red) and β_2 (blue) control mesh, respectively. B_I^u is a 8×3 matrix which includes the basis functions N_I^u from the displacement's control mesh, whereas $B_I^{\beta_1}$ and $B_I^{\beta_2}$ have the dimension 8×1 and contain the corresponding basis functions $N_I^{\beta_1}$, $N_I^{\beta_2}$ as well as the discrete nodal basis systems $A_{2I}^{\beta_1}$, $A_{1I}^{\beta_2}$ from the approximation spaces of the rotations.

$$B_I = \begin{bmatrix} \begin{matrix} X_{,1}^T N_{I,1}^u \\ X_{,2}^T N_{I,2}^u \\ X_{,1}^T N_{I,2}^u + X_{,2}^T N_{I,1}^u \\ D_{,1}^T N_{I,1}^u \end{matrix} & \begin{matrix} 0 \\ 0 \\ 0 \\ X_{,1}^T W^T A_{2I}^{\beta_1} N_{I,1}^{\beta_1} \\ + X_{,1}^T W^T A_{2I}^{\beta_1} N_I^{\beta_1} \\ X_{,2}^T W^T A_{2I}^{\beta_1} N_{I,2}^{\beta_1} \\ + X_{,2}^T W^T A_{2I}^{\beta_1} N_I^{\beta_1} \\ X_{,1}^T W^T A_{2I}^{\beta_1} N_{I,2}^{\beta_1} \\ + X_{,1}^T W^T A_{2I}^{\beta_1} N_I^{\beta_1} \\ X_{,2}^T W^T A_{2I}^{\beta_1} N_{I,1}^{\beta_1} \\ + X_{,2}^T W^T A_{2I}^{\beta_1} N_I^{\beta_1} \\ X_{,1}^T W^T A_{2I}^{\beta_1} N_I^{\beta_1} \\ X_{,2}^T W^T A_{2I}^{\beta_1} N_I^{\beta_1} \end{matrix} & \begin{matrix} 0 \\ 0 \\ 0 \\ X_{,1}^T W^T A_{1I}^{\beta_2} N_{I,1}^{\beta_2} \\ + X_{,1}^T W^T A_{1I}^{\beta_2} N_I^{\beta_2} \\ X_{,2}^T W^T A_{1I}^{\beta_2} N_{I,2}^{\beta_2} \\ + X_{,2}^T W^T A_{1I}^{\beta_2} N_I^{\beta_2} \\ X_{,1}^T W^T A_{1I}^{\beta_2} N_{I,2}^{\beta_2} \\ + X_{,1}^T W^T A_{1I}^{\beta_2} N_I^{\beta_2} \\ X_{,2}^T W^T A_{1I}^{\beta_2} N_{I,1}^{\beta_2} \\ + X_{,2}^T W^T A_{1I}^{\beta_2} N_I^{\beta_2} \\ X_{,1}^T W^T A_{1I}^{\beta_2} N_I^{\beta_2} \\ X_{,2}^T W^T A_{1I}^{\beta_2} N_I^{\beta_2} \end{matrix} \end{bmatrix}. \quad (3.38)$$

Accordingly, the virtual shell strains of the new global mesh read

$$\delta \varepsilon_I = B_I^u \delta u_I + B_I^{\beta_1} \delta \beta_{1I} + B_I^{\beta_2} \delta \beta_{2I}. \quad (3.39)$$

Considering Eq. (3.19), the approximation of the weak form for the new global control mesh has the form

$$G(v, \delta v) = \bigcup_{e=1}^{n_{el} \cdot m_{el}} \sum_{I=1}^{n_{en}^{ges}} \sum_{J=1}^{n_{en}^{ges}} \delta v_I^T \left(\int_{\Omega_e} \begin{bmatrix} B_I^{uT} C B_J^u & B_I^{uT} C B_J^{\beta_1} & B_I^{uT} C B_J^{\beta_2} \\ B_I^{\beta_1 T} C B_J^u & B_I^{\beta_1 T} C B_J^{\beta_1} & B_I^{\beta_1 T} C B_J^{\beta_2} \\ B_I^{\beta_2 T} C B_J^u & B_I^{\beta_2 T} C B_J^{\beta_1} & B_I^{\beta_2 T} C B_J^{\beta_2} \end{bmatrix} dA \cdot v_J - \right. \\ \left. \int_{\Omega_e} \begin{bmatrix} N_I^u & 0 & 0 & 0 & 0 \\ 0 & N_I^u & 0 & 0 & 0 \\ 0 & 0 & N_I^u & 0 & 0 \\ 0 & 0 & 0 & N_I^{\beta_1} & 0 \\ 0 & 0 & 0 & 0 & N_I^{\beta_2} \end{bmatrix} \cdot \begin{bmatrix} q_x^u \\ q_y^u \\ q_z^u \\ m_x^{\beta_1} \\ m_y^{\beta_2} \end{bmatrix} dA - \int_{\Gamma_e^N} \begin{bmatrix} N_I^u & 0 & 0 & 0 & 0 \\ 0 & N_I^u & 0 & 0 & 0 \\ 0 & 0 & N_I^u & 0 & 0 \\ 0 & 0 & 0 & N_I^{\beta_1} & 0 \\ 0 & 0 & 0 & 0 & N_I^{\beta_2} \end{bmatrix} \cdot \begin{bmatrix} f_x^u \\ f_y^u \\ f_z^u \\ \tilde{m}_x^{\beta_1} \\ \tilde{m}_y^{\beta_2} \end{bmatrix} ds \right) = 0. \quad (3.40)$$

The required Gauss points for the surface integrals in the weak formulation are chosen as the Gauss points of the u mesh, leading to a total number of $n_{gp} = (p_u + 1) \cdot (q_u + 1)$ Gauss points. Since the elements are the same for all meshes, using the Gauss points of the u mesh, which has the highest polynomial degrees, is also going to be compatible with the other meshes.

3.6 Numerical examples

Remarks. In the following examples, when referring to the shell formulation with adjusted approximation spaces (AAS shell), the polynomial degrees of the u mesh (p_u, q_u) are given. For the rotation meshes only the reduced polynomial degree in the corresponding direction, see Fig. 3.2, is given, i.e. $(p_{\beta_1}, q_{\beta_2})$. It is implied that the polynomial degrees of the rotation meshes in the other directions have the same value as the ones from the u mesh, i.e. $q_{\beta_1} = q_u$ and $p_{\beta_2} = p_u$. For the shell formulation of Dornisch et al. (ω -shell) the polynomial degrees p and q are given.

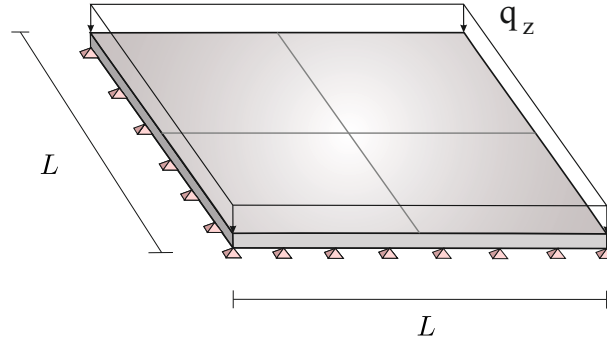
In the comparison of the relative error of the ω -shell with the AAS shell, the total number of equations for the solution, i.e. the total number of degrees of freedom, were taken as the reference value. That is because the shell with adjusted approximation spaces does not have all degrees of freedom in every control point as the ω -shell does, see Section 3.5. Thus, a comparison with respect to the number of control points or the number of elements would be insufficient.

3.6.1 Simply supported plate with biaxial bending

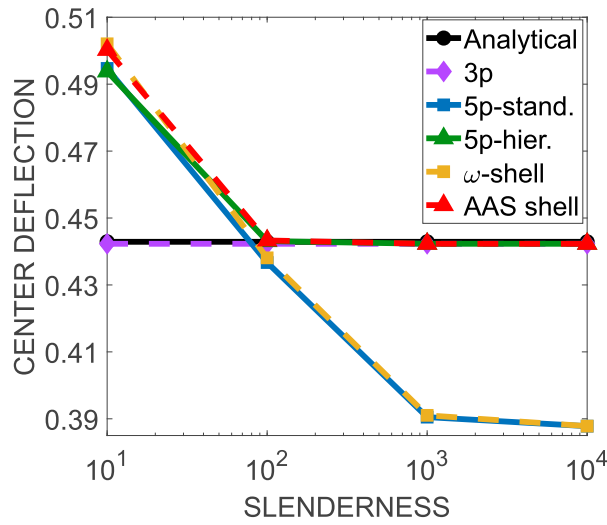
In the first example a simply supported plate of length $L = 10$ is considered which is subjected to a uniformly distributed load q_z leading to biaxial bending, see Fig. 3.3(a). The plate has an E-modulus of $E = 1000$ and a Poisson's ratio of $\nu = 0.3$. The analytical solution for the center deflection is taken from Timoshenko (1940) and has a value of $u_{3,max}^{an} = 0.442892$. It corresponds to the center deflection of a Kirchhoff-Love plate. Here, the dependency of the plate's center deflection is evaluated over the slenderness which includes the critical parameter, i.e. the thickness t . In order to get the same value for the center deflection regardless of the considered thickness, the unit load is scaled with t^3 . Different element types are used for the investigation, namely:

- **3p.** The isogeometric Kirchhoff-Love shell model proposed in Echter et al. (2013) with 3 independent parameters which correspond to the 3 mid-surface displacement components.
- **5p-stand.** The standard isogeometric 5-parameter shell model proposed in Echter et al. (2013) with 5 independent parameters which correspond to 3 mid-surface displacement components and 2 difference vector components.
- **5p-hier.** The isogeometric 5-parameter shell model proposed in Echter et al. (2013) with 5 independent parameters which correspond to 3 mid-surface displacement components and 2 hierarchic difference vector components. The hierarchic difference vector includes the shear deformations and is applied on the rotated director of the Kirchhoff-Love formulation.

- **ω -shell.** The isogeometric Reissner-Mindlin shell formulation proposed by Dornisch et al. (2013).
- **AAS shell.** The isogeometric Reissner-Mindlin shell formulation with adjusted approximation spaces for the displacements and the rotations proposed in this work.



(a)



(b)

Figure 3.3: (a) Simply supported plate subjected to a uniformly distributed load and (b) the center deflection with increasing slenderness.

The center deflections of the three first shell models are taken from the Dissertation of Echter (2013). For all element types a refinement of 10×10 elements with a polynomial degree of two in both directions, i.e. $p = q = 2$ is used (maximum C^1 -continuity).

As it can be seen in Fig. 3.3(b), the 3 parameter shell model coincides with the analytical solution for both the thick and the thin regime. This result is as expected since the

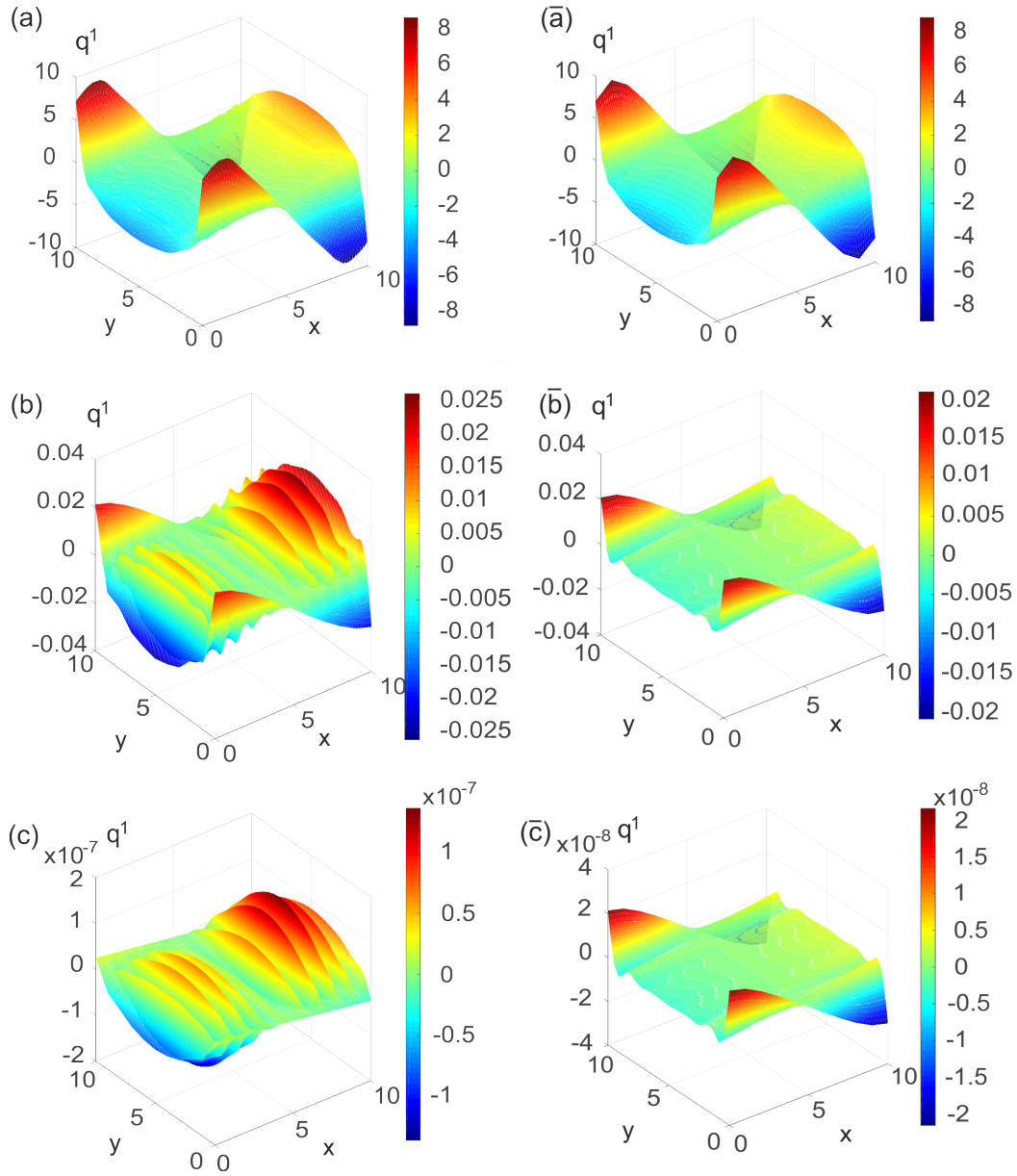


Figure 3.4: Shear stress resultant q^1 for slenderness $\frac{L}{t} = 10$ ((a) ω -shell, (\bar{a}) AAS shell), $\frac{L}{t} = 100$ ((b) ω -shell, (\bar{b}) AAS shell) and $\frac{L}{t} = 10000$ ((c) ω -shell, (\bar{c}) AAS shell).

3p model is based on the Kirchhoff-Love kinematics and does not consider any shear terms. The 5p-shell and the ω -shell elements, which both do not have any measures against transverse shear locking, yield agreeing results. Namely, in the thick regime the center deflection is higher than the analytical one, which is physically sound due to the additional shear terms which are included in the Reissner-Mindlin shell theory. However, in the thin regime instead of converging to the solution of the Kirchhoff-

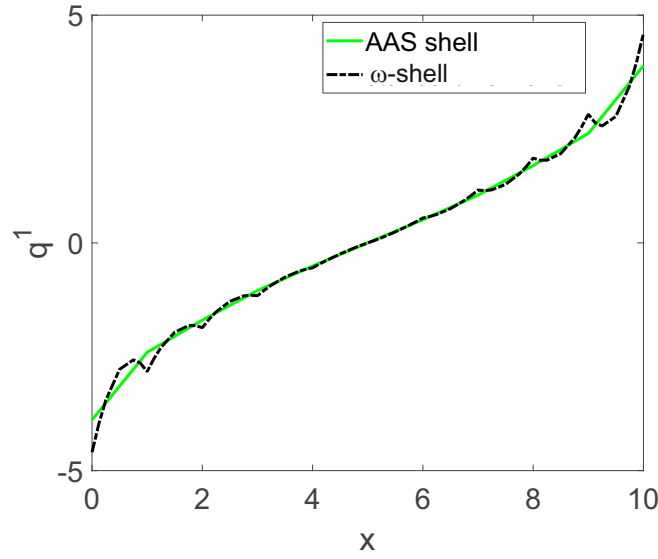


Figure 3.5: Shear stress resultant q^1 for slenderness $\frac{L}{t} = 10$ for $y = 5$.

Love plate, the deflection is underestimated. This behavior illustrates transverse shear locking, where an additional stiffness leads to reduced deformations. The 5p-hier shell and the ω -shell with adjusted approximation spaces do not exhibit such a behavior due to their anti-locking mechanisms. In these cases the results converge to the Kirchhoff-Love results as expected.

Another interesting aspect of transverse shear locking is its influence on the shear stresses that is more pronounced than for the displacements. This behavior was outlined in the work of Oesterle et al. (2016). In Fig. 3.4 the shear force q^1 is presented only for the ω -shell and the AAS shell. Three cases are considered, a plate with moderate thickness, $t = 1$ ((a) and (\bar{a})), a plate with $t = 0.1$ ((b) and (\bar{b})), and a plate in the thin regime with $t = 0.001$ ((c) and (\bar{c})). Since soft support is used, the high values of q^1 at the two boundary ends with $y = 0$ and $y = 10$ are legitimate and do not have anything to do with transverse shear locking. In Fig. 3.4(b) it can be seen that for the ω -shell the shear forces q^1 exhibit an oscillating behavior due to transverse shear locking. The maximum value of the oscillation has almost the same value as the shear forces at the boundaries due to soft support. In Fig. 3.4(c) it is shown that the oscillations become even more profound with increasing slenderness due to the intensification of the transverse shear locking phenomenon. In this case the maximum value of the oscillation exceeds the shear forces due to soft support by one magnitude, so in this scale the shear forces at the boundaries are not visible any more. Even for the thicker plate with $t = 1$, where the shear force looks fine, see Fig. 3.4(a), at a closer look some small oscillations still exist, see Fig. 3.5. On the other hand these

oscillations can not be found in the AAS shell model for all thicknesses (Fig. 3.4(ā), Fig. 3.4(b̄) and Fig. 3.4(c̄)). Analogous results are obtained if the other shear stress q^2 is considered.

3.6.2 Razzaque's skew plate

This example was proposed and studied by Razzaque (1973). It consists of a skew plate which is simply supported on two opposite edges, free on the other two and subjected to a uniformly distributed load $q_z = 1$, see Fig. 3.6(a). Here, the chosen length for the plate is $L = 10$ and the thickness is $t = 0.1$. The material parameters are given as $E = 10^6$ and $\nu = 0.31$. The analytical solution for the center deflection is taken from Razzaque (1973) and has the value $u_3^{an} = 0.7945 \frac{qL^4}{100D}$ with D the flexural rigidity. In this example, the AAS shell's performance for skew geometries is examined. The relative error of the center deflection of the ω -shell formulation and the AAS formulation over the number of equations is compared to the relative error of the 4-node Bathe/Dvorkin plate element, see Fig. 3.6(b) in double logarithmic scale. The Bathe/Dvorkin element is based on the Reissner-Mindlin theory and uses different interpolations for bending and transverse shear effects in the element stiffness matrix in order to avoid locking. Since the Bathe/Dvorkin element is a plate element and the relative error is evaluated in relation to the number of equations required for the solution, the plate version of the ω -shell and the AAS formulation is taken with $\mathbf{A}_i = \mathbf{e}_i$. Otherwise, a transparent comparison would not be possible, since the shell elements have automatically more degrees of freedom than the corresponding plate elements. The axes of Fig. 3.6(b) are given in double logarithmic scale. As it can be seen, the ω -plate element with a polynomial degree $p = q = 1$ and $p = q = 2$ shows strong locking effects, especially for a low number of elements. On the other hand, the plate formulation with adjusted approximation spaces and the Bathe/Dvorkin plate element have better results especially for a low number of elements and a constant convergence rate which indicates that they are locking free. The convergence rate of the Bathe/Dvorkin element is 1, whereas for the AAS element it is slightly higher with a value of 1.35. That is because Bathe/Dvorkin uses linear basis functions, whereas the AAS plate uses quadratic basis functions for the displacements and linear basis functions for the rotations. Thus, the AAS formulation performs slightly better than the Bathe/Dvorkin element. With higher number of elements the error of the ω -plate improves and if locking is sufficiently reduced the error gets smaller than for the other two formulations. That is because the ω formulation uses higher polynomial degrees for the displacements and rotations compared to the other two formulations and thus it should have a higher convergence rate if locking is reduced.

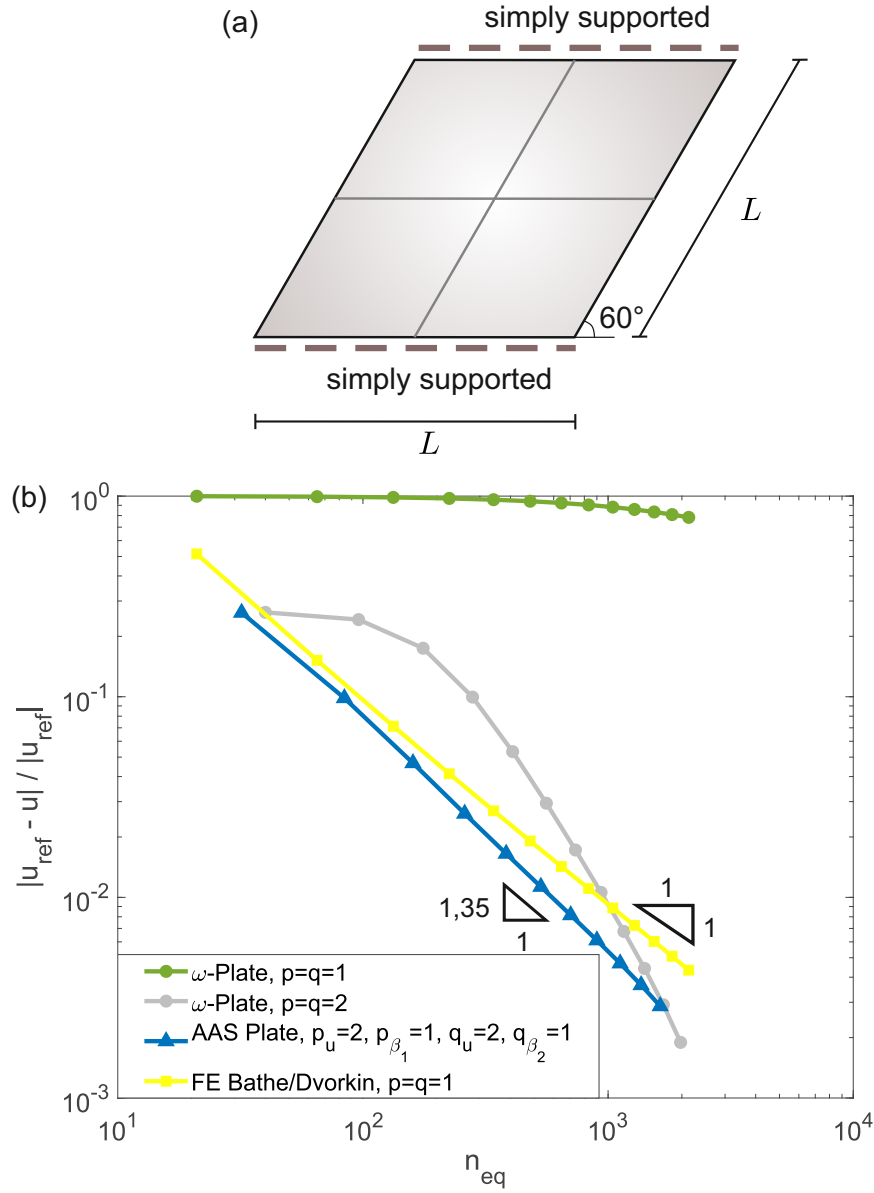


Figure 3.6: (a) Razzaques' skew plate and (b) the error of the center deflection over the number of equations.

3.6.3 Fully hard clamped square plate

The third example consists of a unitary square block $[0, 1]^2$ which has all four sides clamped, see Fig. 3.7(a). It is subjected to a body load, with the following definition:

$$\begin{aligned}
 q_z(x, y) = \frac{E}{12(1 - \nu^2)} & [12y(y - 1)(5x^2 - 5x + 1)(2y^2(y - 1)^2 + x(x - 1) \\
 & \times (5y^2 - 5y + 1)) + 12x(x - 1)(5y^2 - 5y + 1)(2x^2(x - 1)^2 \\
 & + y(y - 1)(5x^2 - 5x + 1))],
 \end{aligned} \tag{3.41}$$

see Fig. 3.7(b). The analytical solution of the deflection and the rotations is derived in Chinosi and Lovadina (1995) and is given for each point (x,y) of the plate as follows:

$$\begin{aligned}
 u_3(x, y) &= \frac{1}{3}x^3(x-1)^3y^3(y-1)^3 - \frac{2t^2}{5(1-\nu)}[y^3(y-1)^3x(x-1) \\
 &\quad \times (5x^2 - 5x + 1) + x^3(x-1)^3y(y-1)(5y^2 - 5y + 1)], \\
 \beta(x, y) &= \left(\frac{y^3(y-1)^3x^2(x-1)^2(2x-1)}{x^3(x-1)^3y^2(y-1)^2(2y-1)} \right). \quad (3.42)
 \end{aligned}$$

A linear elastic material law with Young's modulus $E = 1.092 \cdot 10^7$ and Poisson's ratio $\nu = 0.3$ is used. The thickness of the plate is set to $t = 10^{-3}$. The given example is examined in Beirão da Veiga et al. (2012a) for the plate formulation with adjusted approximation spaces. Here, the example is used to compare the shell formulation with adjusted approximation spaces to the ω -shell for different polynomial degrees.

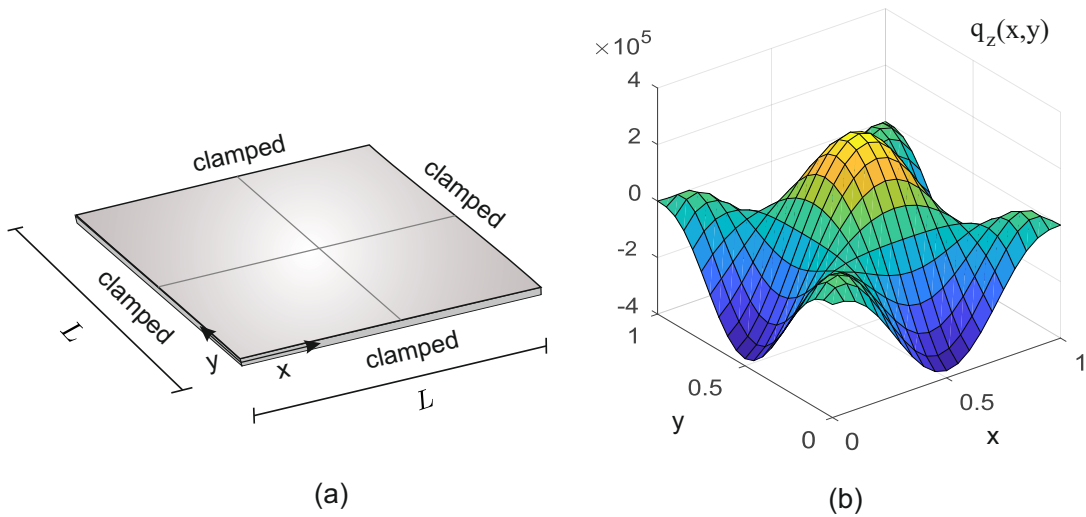


Figure 3.7: (a) Fully hard clamped square plate and (b) body load $q_z(x, y)$.

In Fig. 3.8 the error of the center deflection is illustrated as a function of the number of equations used for the solution, i.e. as a function of the total number of degrees of freedom. The diagrams are displayed in a double logarithmic scale. In order to have a substantive comparison, the polynomial degrees (p, q) and $(p+1, q+1)$ of the ω -shell are compared to the polynomial degrees $(p_u = p+1, q_u = q+1)$ and subsequently $(p_{\beta_1} = p, q_{\beta_1} = q+1)$, $(p_{\beta_2} = p+1, q_{\beta_2} = q)$ of the shell formulation with adjusted approximation spaces.

In this manner, the polynomial degrees $p = q = 1$ and $p = q = 2$ of the ω -shell show a very strong locking behavior which is more profound for a lower number of equations, i.e. a lower number of elements. On the other hand, the shell formulation with adjusted

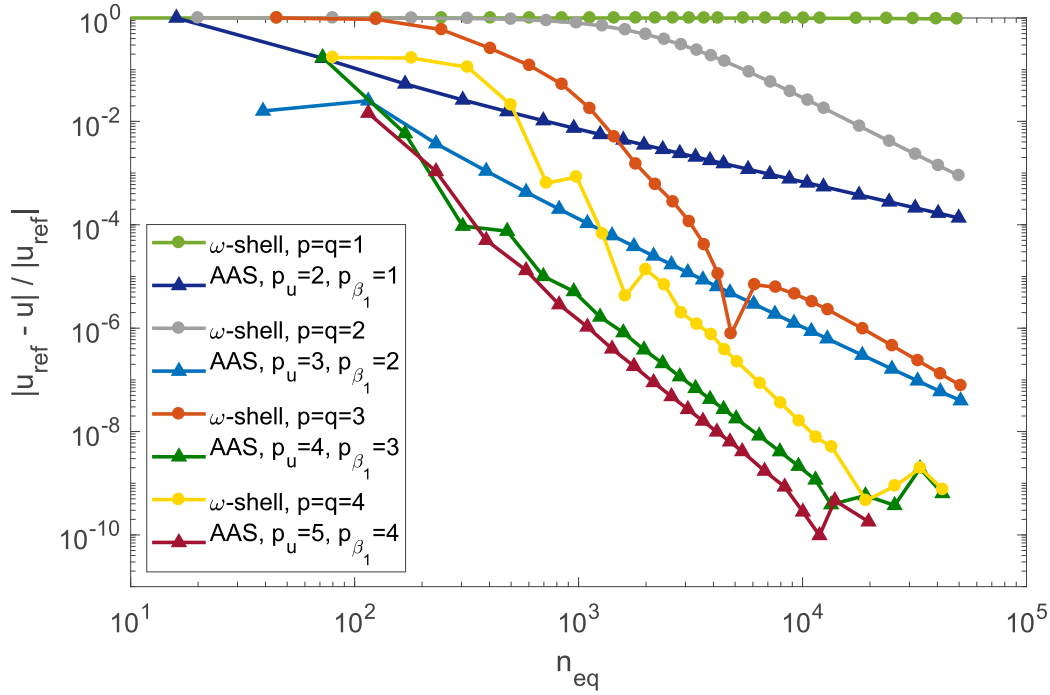


Figure 3.8: Error of the center deflection over the number of equations for the ω -shell and the AAS shell.

approximation spaces and $p_u = q_u = 2, p_{\beta_1} = 1, q_{\beta_2} = 1$ leads to significantly better results even for a low number of elements. For higher polynomial degrees, the ω -shell exhibits a similar behavior as before; for a low number of elements the displacements are strongly underestimated due to shear locking and with mesh refinement the locking effect is alleviated. The shell formulation with adjusted approximation spaces yields higher accuracy in all discretization ranges than the ω -shell formulation and its constant incline for all polynomial degrees shows that it is locking-free. It is interesting to see that even for the higher polynomial degrees the ω -shell formulation gets closer but never reaches the accuracy of the shell formulation with adjusted approximation spaces in contrast to the last example of the skew plate, see Section 3.6.2. As it was mentioned in Section 3.2, the choice of a higher polynomial degree for the ω -shell only alleviates the locking effect, it does not eliminate it. Here, even for a polynomial degree of $p = q = 4$ locking is still profound in the ω -shell.

3.6.4 Choice of shell examples

The asymptotic behavior of a shell model describes the stress and deformation state as the thickness tends to zero. Depending on the geometry, the boundary conditions and the loading, the shell problem is membrane dominated or bending dominated. In the

best case the convergence rate of a shell element should be independent of its thickness. Bending dominated problems, where pure bending is non-inhibited, are good tests for locking phenomena. In the case of bending dominated Reissner-Mindlin shells the membrane and shear energies tend to zero with decreasing thickness. Two bending dominated benchmark tests from literature, see Chapelle and Bathe (1998) and Lee and Bathe (2002), are presented in the following for the verification of the proposed anti-locking method. Here, no measures have been taken against membrane locking. So in the following examples, only the assessment of the adjusted approximation spaces to reduce transverse shear locking is considered. Membrane locking is still going to influence the results and its elimination should be the objective of research to follow.

3.6.4.1 Bending dominated test I - Pinched hemisphere

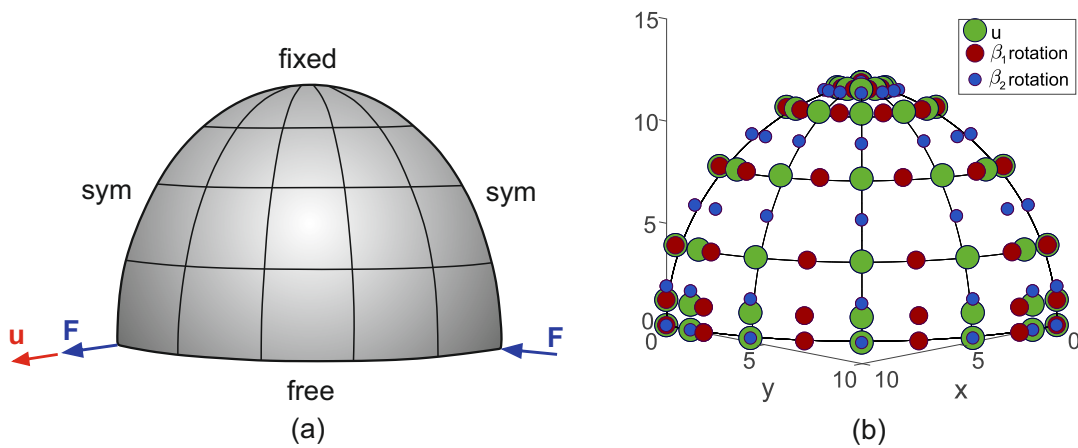


Figure 3.9: (a) Pinched hemisphere and (b) global mesh of pinched hemisphere for $p_u = q_u = 3$ and $n = m = 4$.

The first bending dominated test that is examined includes a hemisphere, subjected to a pair of equal but opposite point loads which are placed at antipodal points of the equator, see Fig. 3.9(a). As a boundary condition only the apex of the hemisphere is fixed in order to prevent rigid body motions and simultaneously to ensure a bending dominated behavior with decreasing thickness, see Chapelle and Bathe (1998). The edge along the equator is free. Due to symmetry only one quarter of the hemisphere is considered. This problem exhibits almost no membrane strains and is a challenging test for shell elements regarding their ability to avoid locking, see Bouclier et al. (2013a). Since large sections of this shell rotate almost as rigid bodies, it is also a good test for examining the formulation's ability to represent accurately these rotations about the normals to the shell surface, see Belytschko et al. (1985). Usually, the thickness for

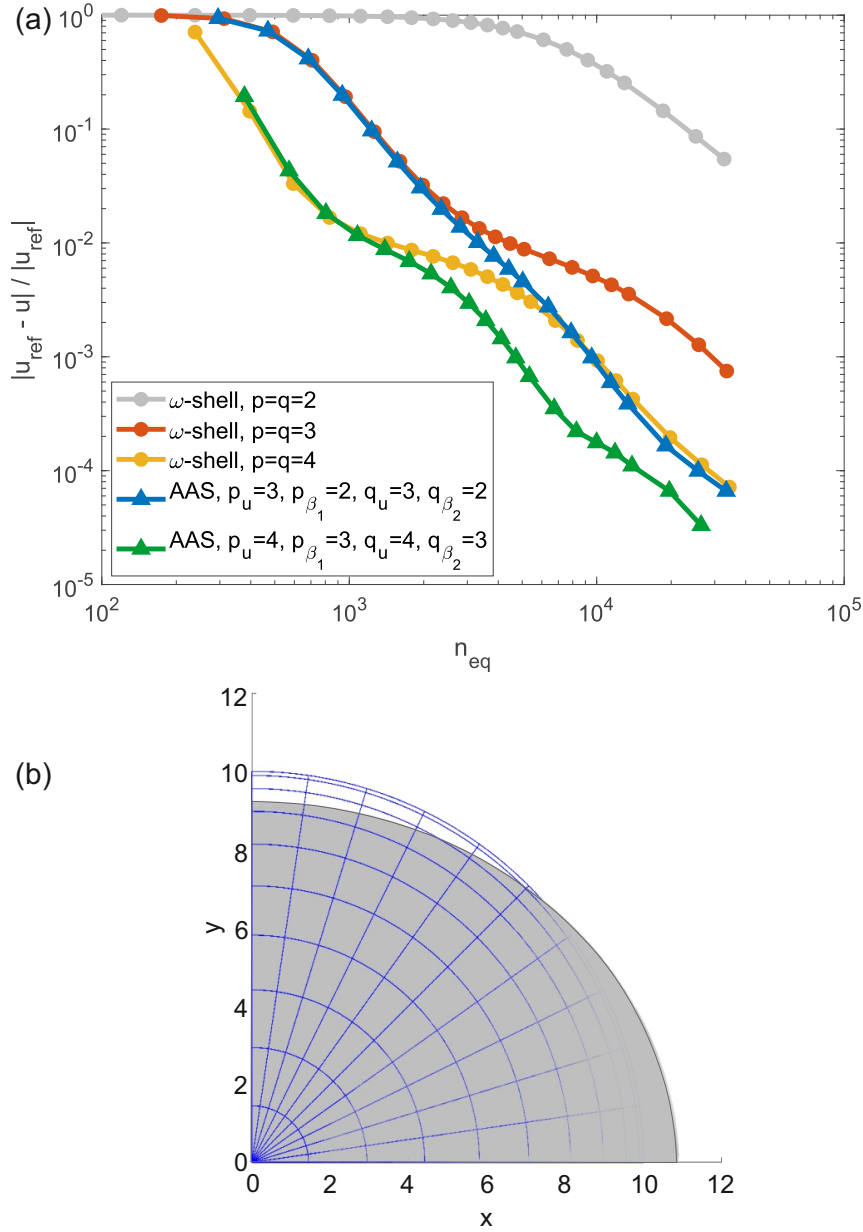


Figure 3.10: (a) The error over the number of equations for the ω -shell and the AAS shell and (b) initial mesh and deformed geometry with a scale factor 10 for the displacements

this problem is taken as $t = 0.04$, however, here a reduced thickness is considered with $t = 0.004$ in order to intensify the locking phenomenon. The displacement on which the focus lies on is at the point and in the direction of the loading, see Fig. 3.9(a). The global mesh of the hemisphere for $p_u = q_u = 3$ and $n = m = 4$ is shown in Fig. 3.9(b). As a reference solution the displacement calculated with a 80×80 mesh of ω -shell elements with $p = q = 6$ is considered. In contrast to the plate examples, in the

shell examples like this doubly curved surface, higher polynomial degrees are required in order to represent the geometry exactly. Thus, the ω -shell formulation starts with a polynomial degree of $p = q = 2$ and the AAS shell starts from $p_u = q_u = 3$, $p_{\beta_1} = 2$, $q_{\beta_2} = 2$. The error over the number of equations is represented in a double logarithmic scale in Fig. 3.10(a).

Comparing the ω -shell with $p = q = 2$ and $p = q = 3$ with the AAS shell with $p_u = q_u = 3$, $p_{\beta_1} = 2$, $q_{\beta_2} = 2$, it can be seen that for a low number of elements the AAS method is almost the same but still slightly better than the ω -shell with the higher polynomial degree $p = q = 3$. Furthermore, with a higher number of elements the difference between the ω -shell and the AAS shell is becoming very profound. So, in contrast to the plate examples, where the difference between the error norms is getting smaller with a higher number of elements, here the transverse shear locking becomes more visible. A reason for this is the membrane locking, which is more profound for a low number of elements, see Choi et al. (1998). Even for the ω -shell with $p = q = 4$, the relative error for a high number of elements is slightly bigger than for the AAS shell with $p_u = q_u = 3$, $p_{\beta_1} = 2$, $q_{\beta_2} = 2$. Going one step further and comparing higher polynomial degrees, namely the ω -shell with $p = q = 4$ and $p = q = 3$ with the AAS shell with $p_u = q_u = 4$, $p_{\beta_1} = 3$, $q_{\beta_2} = 3$, a similar behavior can be observed. However, the difference between the relative errors has slightly improved due to the higher polynomial degrees. The undeformed mesh in contrast to the deformed shape with a scale factor 10 is shown in Fig. 3.10(b).

3.6.4.2 Bending dominated test II - Partly clamped hyperbolic paraboloid

The partly clamped hyperbolic paraboloid was introduced in Chapelle and Bathe (1998) and recommended as a good test problem for the evaluation of the locking behavior of a shell element. It was further investigated in Bathe et al. (2000) and a more detailed asymptotic analysis for this example is given in Lee and Bathe (2002). The surface of the hyperbolic paraboloid is defined as $Z = X^2 - Y^2$; with $(X, Y) \in [(-L/2; L/2)]^2$. It is clamped along the edge $X = -L/2$ and subjected to its self-weight, see Fig. 3.11(a). The global mesh of the hyperbolic paraboloid for $p_u = q_u = 4$ and $n = m = 4$ is exemplarily shown in Fig. 3.11(b). Due to its symmetric geometry only one half of the shell is considered with respective symmetry boundary conditions along the side $Y = 0$. The main aim of this test is to examine the influence of the thickness on the convergence behavior of the shell elements, thus different slenderness values are considered, i.e. $t/L = 1/100$, $t/L = 1/1000$ and $t/L = 1/10000$. Since an analytical solution for this problem does not exist, the val-

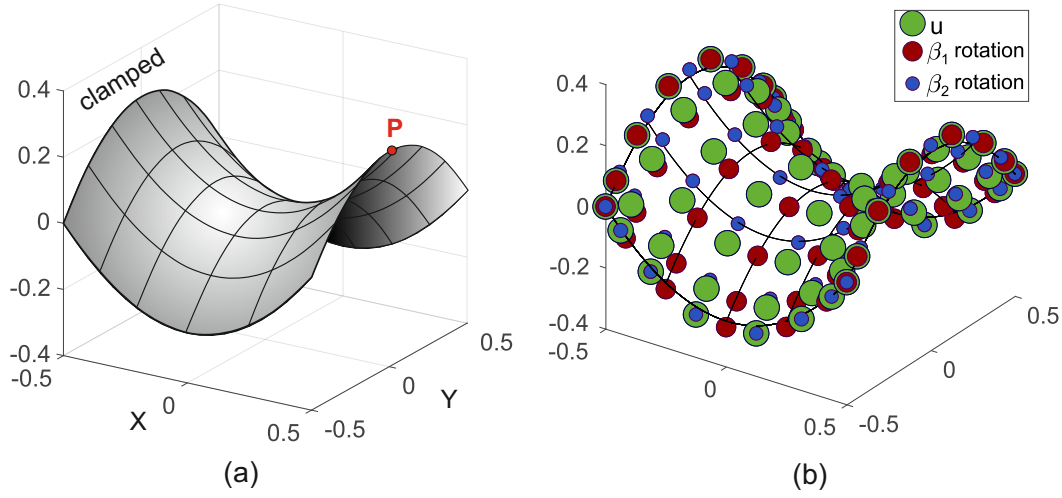


Figure 3.11: (a) Partly clamped hyperbolic paraboloid and (b) global mesh of hyperbolic paraboloid for $p_u = q_u = 4$ and $n = m = 4$.

t/L	Vertical displacement at $X = L/2, Y = 0$
1/100	-9.3521×10^{-5}
1/1000	-6.3974×10^{-3}
1/10000	-5.3049×10^{-1}

Table 3.1: Reference values for the vertical displacement at point $X = L/2, Y = 0$ using a 100×50 mesh of ω -shell elements with $p = q = 6$.

ues obtained at $X = L/2, Y = 0$ (point P) using a 100×50 mesh of ω -shell elements with $p = q = 6$ are used as reference solutions, see Table 3.1. The self-weight is proportional to the thickness and thus, the displacements scale as $1/t^2$, see Bathe et al. (2000).

The material parameters of this example are $E = 2 \cdot 10^{11}$, $\nu = 0.3$, $\rho = 8000$ and the length of the hyperbolic paraboloid is $L = 1$. In Fig. 3.12(a-c) the error of the vertical displacement of point P is given in relation to the number of equations used for the solution. The plots are in double logarithmic scale. For the thicker shell ($t = 0.01$, see Fig. 3.12(a)) the difference between the accuracy of the ω -shell and the shell with adjusted approximation spaces is small. For few elements the AAS element is slightly better than the ω -shell. On the other hand, for a large number of elements the ω -shell gets slightly better than the AAS shell because here the locking effect has already been alleviated and the ω -shell has a higher polynomial degree for the rotation compared to AAS. So in the first case, transverse shear locking has still not such a big influence. In the second case with $t = 0.001$, see Fig. 3.12(b), the difference between the elements is more visible. The AAS element with $p_u = q_u = 3$, $p_{\beta_1} = 2$, $q_{\beta_2} = 2$ leads to

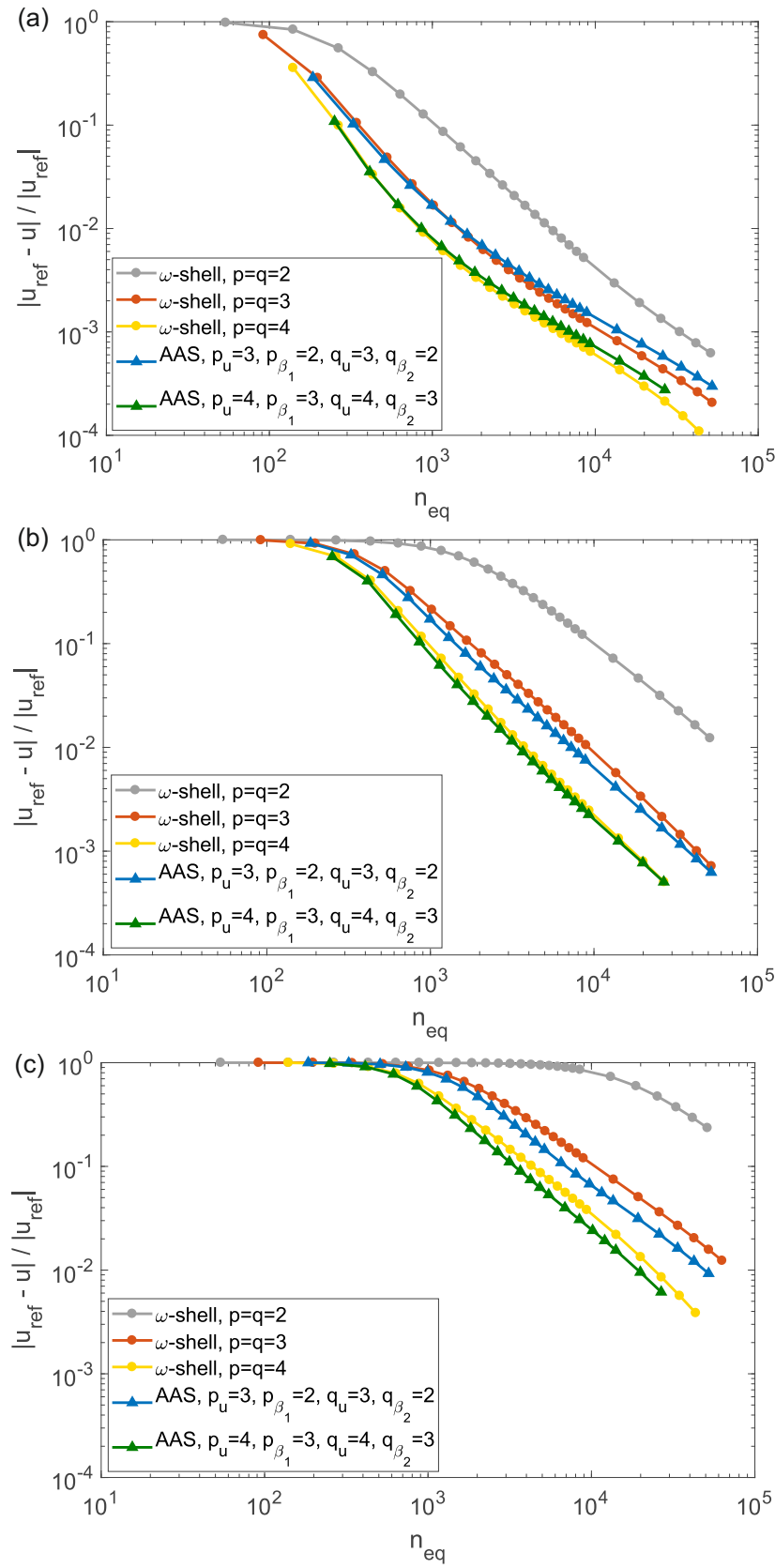


Figure 3.12: Convergence in the displacement $w(L/2,0)$ for $t/L=1/100$ (a), $t/L=1/1000$ (b) and $t/L=1/10000$ (c).

better results compared to the ω -shell with $p = q = 2$ and $p = q = 3$. Furthermore, the AAS element with $p_u = q_u = 4$, $p_{\beta_1} = 3$, $q_{\beta_2} = 3$, still shows a higher accuracy compared to the ω -shell element even though the locking effect is slightly alleviated due to higher polynomial degrees. However the biggest difference can be seen in the last case with $t = 0.0001$, see Fig. 3.12(c), where the transverse shear locking effect is more profound. Here, the deviation is clearly visible even for higher polynomial degrees. As it was also noticed in the last example of the pinched hemisphere in contrast to the plate examples, the difference between the ω -shell and the AAS shell is more profound the higher the number of elements gets due to membrane locking, which has a bigger influence for a low number of elements, see Choi et al. (1998). Now, looking at all the three diagrams, it is noticed that the convergence rate is decreasing (there is a shift in the convergence plot as t decreases), the thinner the shell gets. This is again due to the membrane locking which is getting more profound the thinner the shell gets.

3.7 Conclusions

In the current work, a method to treat transverse shear locking was presented in the context of an isogeometric Reissner-Mindlin shell formulation. The method uses adjusted approximation spaces for the displacements and the two rotations in order to ensure consistency in the interpolated terms of the strain formulation. It is generally applicable for any polynomial degree and no additional variables have to be introduced. Furthermore, it was shown that the method leads to less degrees of freedom in the system of equations than its corresponding standard Reissner-Mindlin shell formulation. Regarding computational time, it could be argued that the use of different meshes is going to increase the processing time. However, since locking is more intense for low polynomial degrees and a low number of elements the additional computational time is not profound in these cases and the improvement of the solution's accuracy is more significant. In addition, since the system of equations is reduced, it will lead again to a reduction of the computational time.

The method was tested for several plate problems and has shown a superior behavior in contrast to the ω -shell formulation, in which no anti-locking measures are considered. Especially for a low polynomial degree and a low number of elements, where transverse locking is more profound, the formulation with adjusted approximation spaces showed a higher accuracy with fewer degrees of freedom. Furthermore, compared to other elements that have mechanisms against locking, namely, the hierarchic shell formulation and the Bathe/Dvorkin element from the standard Finite Element Method, the proposed method shows very good results. Oscillations in the stress resultants due to

locking is also effectively eliminated. In addition, some bending dominated shell examples were investigated for the proposed method and the ω -shell formulation. As for the shell examples, the formulation with adjusted approximation spaces shows much better results than the ω -shell formulation, however for both formulations, membrane locking still has an influence on the results. Thus, an additional elimination of membrane locking and, in a second step, other locking effects is going to be the content of future work. In particular, the problem of membrane locking could be handled with existing methods, already mentioned in Section 3.2. One option could be the Assumed Natural Strain method which has successfully been implemented for the case of isogeometric solid-shell elements, see Caseiro et al. (2014). Furthermore, the Discrete Strain Gap method which was extended to an isogeometric Kirchhoff-Love shell in Echter et al. (2013) was able to remove membrane locking. Finally, mixed methods as used in Echter et al. (2013) and Oesterle et al. (2016) for a Kirchhoff-Love shell formulation and in Bouclier et al. (2013a) for a solid-shell formulation to eliminate locking could be extended to the proposed Reissner-Mindlin shell formulation.

Chapter 4

Two-field formulations for isogeometric Reissner-Mindlin plates and shells with global and local condensation

This chapter was published as:

Kikis, G. and Klinkel, S. (2022). Two-field formulations for isogeometric Reissner-Mindlin plates and shells with global and local condensation. *Computational Mechanics*, 69:1-21.

4.1 Abstract

In this paper, mixed formulations are presented in the framework of isogeometric Reissner-Mindlin plates and shells with the aim of alleviating membrane and shear locking. The formulations are based on the Hellinger-Reissner functional and use the stress resultants as additional unknowns, which have to be interpolated in appropriate approximation spaces. The additional unknowns can be eliminated by static condensation. In the framework of isogeometric analysis static condensation is performed globally on the patch level, which leads to a high computational cost. Thus, two additional local approaches to the existing continuous method are presented, an approach with discontinuous stress resultant fields at the element boundaries and a reconstructed approach which is blending the local control variables by using weights in order to compute the global ones. Both approaches allow for a static condensation on the element level instead of the patch level. Various numerical examples are investigated in

order to verify the accuracy and effectiveness of the different approaches and a comparison to existing elements that include mechanisms against locking is carried out.

4.2 Introduction

Isogeometric Analysis (IGA) was introduced by Hughes et al. (2005) with the aim of unifying the design and analysis process. This is achieved by using for both the same higher order basis functions that are common in CAD tools, such as Non-Uniform Rational B-splines (NURBS). Since then, isogeometric analysis has been successfully implemented in structural mechanics and many other fields, e.g. in fluid mechanics, see Gomez et al. (2010), contact mechanics, see Temizer et al. (2011) and fracture mechanics, see Kikis et al. (2021).

Especially in the context of shell structures, isogeometric analysis offers many advantages. The higher continuity of splines over the patch is essential for the correct computation of the shell's curvature and the surface's normal. Furthermore, free form structures can now be computed with a significantly lower computational cost. Thus, in the past years a lot of effort was put in integrating isogeometric analysis into the existing shell formulations. The first step was done with the Kirchhoff-Love shells, see Kiendl et al. (2009), Benson et al. (2011), Nguyen-Thanh et al. (2011) and Duong et al. (2017) and later with the Reissner-Mindlin shells in Uhm and Youn (2009), Benson et al. (2010b), Dornisch et al. (2013, 2016) and Kiendl et al. (2017) and the solid-shells in Hosseini et al. (2013, 2014b) and Bouclier et al. (2013a).

Even though splines are very advantageous due to their higher order and continuity, they suffer from the same locking effects as Lagrange shape functions, see Echter and Bischoff (2010). Locking leads to an artificial stiffening of the system, an underestimation of the deformation and oscillations in the stress resultants. Various methods have been proposed in order to eliminate these undesirable effects in the framework of isogeometric analysis. The easiest one is to use higher order shape functions, however, this approach does not eliminate locking completely and at the same time increases the computational cost, see Benson et al. (2010b), Echter and Bischoff (2010) and Bouclier et al. (2013b). An attempt to overcome locking effects on the theoretical level by using hierarchic formulations was made in the framework of Reissner-Mindlin and 3D shells in Long et al. (2012), Echter et al. (2013), Beirão Da Veiga et al. (2015) and Oesterle et al. (2016). Even though these formulations were able to avoid transverse shear and curvature thickness locking *ab initio*, additional methods had to be implemented for the elimination of membrane locking. In Kiendl et al. (2015b, 2018) the classical Timoshenko beam problem was reformulated to a single differential equation with only one primal variable in order to avoid shear locking by construction. A mixed displacement

method that avoids the geometrical locking effects ab initio was presented in Bieber et al. (2018).

In addition to these formulations, methods that have been valuable in the classical finite element analysis for the elimination of locking effects have been extended to isogeometric analysis, like the Assumed Natural Strain (ANS) method in Caseiro et al. (2014, 2015), the Discrete Shear Gap (DSG) approach in Echter and Bischoff (2010) and Echter et al. (2013) and the Enhanced Assumed Strain (EAS) method in Cardoso and Cesar de Sa (2012). Non-uniform integration techniques were implemented for isogeometric Reissner-Mindlin shells in Dornisch et al. (2016) and Adam et al. (2015) in order to overcome locking and increase the efficiency of the formulations. However, the latter method fails for general non-uniform knot vectors and is thus not relevant for industrial applications. Reduced integrated fields were applied for a solid-shell in Cardoso and Cesar de Sa (2014) in combination with a moving least square approach to project them back onto the fully integrated space. The use of adjusted approximation spaces for the displacements and the rotations in Reissner-Mindlin plates and shells was able to eliminate transverse shear locking, see Beirão da Veiga et al. (2012a) and Kikis et al. (2019).

The \bar{B} method, one of the most popular methods for the finite element analysis, was introduced for isogeometric analysis in Elguedj et al. (2008) along with an \bar{F} projection in order to alleviate locking in nearly incompressible linear and nonlinear elasticity and plasticity problems. Later, it was extended to straight and curved Timoshenko beams in Bouclier et al. (2012) and in Greco et al. (2017) to plane curved Kirchhoff rods. A first attempt to apply the \bar{B} method to isogeometric 2D solid shells was made in Bouclier et al. (2013b). As it was often stated in these works, the \bar{B} method within the framework of isogeometric analysis leads to a linear system where a matrix defined on the patch level has to be inverted and the resulting stiffness matrix is fully populated, which increases the computational cost. This led to the introduction of local \bar{B} formulations, where the \bar{B} -projection is applied locally and the global variables are obtained from the local ones using reconstruction algorithms. Such a local \bar{B} formulation was first introduced in Bouclier et al. (2013a) for a NURBS-based solid-shell. A local \bar{B} formulation based on the Bézier projection proposed by Thomas et al. (2015) was presented in Miao et al. (2018) to alleviate transverse shear locking in Timoshenko beams and volumetric locking in nearly incompressible elastic solids. In addition, Miao et al. presented a non-symmetric Bézier \bar{B} projection, where the variation of the assumed variables is discretized with the dual basis functions. This way, the assumed variables are directly condensed out without the need of an inversion and lead to a sparse stiffness matrix with a slightly higher bandwidth. This method was later applied to geometrically nonlinear Reissner-Mindlin shells in Zou et al. (2020). A much simpler reconstruction algorithm which is also based on the work of Thomas

et al. (2015) can be found in Greco et al. (2017, 2018) for plane curved Kirchhoff rods and Kirchhoff-Love shells. There the local variables are directly interpolated with local B-spline functions without a Bézier projection and transformation to the Bernstein basis. Local \bar{B} formulations where the locking strains or stresses are projected onto interpolation spaces with the lowest possible order for each element leading to different projection spaces for the inner, corner and boundary elements are presented in Hu et al. (2016, 2020). Antolin et al. (2017, 2020) used discontinuous polynomial spaces for the projection of the strains.

Mixed formulations, which are equivalent to the \bar{B} formulations for linear cases as stated in Bouclier et al. (2013a) and Simo and Hughes (1986), were implemented in the context of isogeometric analysis for a solid-shell in order to eliminate membrane, shear and thickness locking in linear, see Bouclier et al. (2013a) and geometrically nonlinear cases, see Bouclier et al. (2015). Echter et al. (2013) and Rafetseder and Zulehner (2019) used a mixed formulation to overcome membrane locking in hierarchical shells and Kirchhoff-Love shells, respectively. Mixed variational formulations for nearly incompressible solids were implemented in Taylor (2011) and Fahrendorf et al. (2020). However, as it is for the \bar{B} method, mixed methods involve static condensation on the patch level due to the high continuity of the shape functions in isogeometric analysis. This includes the inversion of a matrix on the patch level and leads to a fully populated stiffness matrix. In order to overcome these issues and reduce the computational cost, in this work, two approaches are presented based on the two-field Hellinger-Reissner variational principle which perform static condensation on the element level. In the first one, the stress fields are defined discontinuously (C^{-1}) across the element boundaries. The resulting stiffness matrix is sparse and has the same bandwidth as the standard displacement-based shell which additionally reduces the computational cost. The second approach is based on the reconstruction algorithm used by Greco et al. (2017, 2018) in the framework of a \bar{B} method. Here, it is reformulated for the mixed method with the stress resultants as additional unknowns and is extended to the case of Reissner-Mindlin plates and shells where membrane and transverse shear locking occur. The resulting stiffness matrix has a slightly higher bandwidth than the standard displacement-based formulations. Both methods can be applied for any polynomial degree. They are compared to the mixed formulation where static condensation is performed on the patch level.

The paper is organized as follows. In Section 4.3, the Reissner-Mindlin shell formulation from Dornisch et al. (2013) and Kikis et al. (2019) is briefly summarized. In Section 4.4, the isogeometric mixed formulation based on the Hellinger-Reissner variational principle is presented for alleviating membrane and shear locking. The two methods for performing static condensation on the element level are presented, and the existing approach, where static condensation is performed on the patch level is re-

called. In Section 4.5, the performance of the different approaches is compared on the basis of various numerical examples. Finally, in Section 4.6, conclusions are drawn and an outlook for future research is presented.

4.3 Reissner-Mindlin shell formulation

4.3.1 Kinematics and basis systems

The shell formulation presented in this section is based on the Reissner-Mindlin shell theory and can be found in Dornisch et al. (2013) and Kikis et al. (2019). It is derived from continuum mechanics and the shell structure is defined with respect to its mid-surface. In order to describe the thickness direction, the so-called director vector, see Fig. 4.1, is used. The director vector of the reference configuration \mathbf{D} coincides with the normal vector of the shell's surface, whereas the director vector of the current configuration is defined by a difference vector formulation

$$\mathbf{d} = \mathbf{D} + \mathbf{b}, \quad (4.1)$$

since only linear problems are considered. The difference vector reads

$$\mathbf{b} = \boldsymbol{\omega} \times \mathbf{D} = \mathbf{W}^T \boldsymbol{\omega} \quad \text{with} \quad \mathbf{W} = \text{skew}(\mathbf{D}) \quad (4.2)$$

and depends on the rotational parameter $\boldsymbol{\omega}$ of the shell's mid-surface and the reference director vector \mathbf{D} . Only small rotations are considered and the inextensibility condition in thickness direction is fulfilled in the sense of $|\mathbf{d}| \simeq |\mathbf{D}| = 1$.

Using the director vector, the reference position vector of an arbitrary point on the shell is given as

$$\tilde{\mathbf{X}}(\xi^i) = \mathbf{X}(\xi^\alpha) + \xi^3 \mathbf{D}(\xi^\alpha), \quad (4.3)$$

where $i = 1, 2, 3$, ξ^α with $\alpha = 1, 2$ are the two in-plane coordinates of the convected curvilinear coordinate system of the mid-surface, $-\frac{t}{2} \leq \xi^3 \leq \frac{t}{2}$ is the thickness coordinate and $\mathbf{X}(\xi^\alpha)$ is the position vector of the mid-surface in the reference configuration. In the same manner, the displacement vector $\tilde{\mathbf{u}}$ of an arbitrary point on the shell is defined as

$$\tilde{\mathbf{u}}(\xi^i) = \mathbf{u}(\xi^\alpha) + \xi^3 \mathbf{d}(\xi^\alpha), \quad (4.4)$$

where $\mathbf{u}(\xi^\alpha)$ is the displacement vector of the mid-surface. The current position vector $\mathbf{x}(\xi^\alpha)$ and the displacement vector $\mathbf{u}(\xi^\alpha)$ are linked to each other in the following way

$$\mathbf{x}(\xi^\alpha) = \mathbf{X}(\xi^\alpha) + \mathbf{u}(\xi^\alpha). \quad (4.5)$$

The covariant basis vectors \mathbf{G}_i of the shell are defined with respect to ξ^i as follows

$$\mathbf{G}_\alpha = \mathbf{X}_{,\alpha} + \xi^3 \mathbf{D}_{,\alpha}, \quad \mathbf{G}_3 = \mathbf{D}, \quad (4.6)$$

while the contravariant basis vectors \mathbf{G}^j form their dual basis system with $\mathbf{G}_i \cdot \mathbf{G}^j = \delta_i^j$ and δ_i^j the Kronecker delta symbol. However, an orthonormal basis system is needed for the constitutive relation, thus, a local basis system \mathbf{A}_i is introduced, see Fig. 4.1. It is defined with respect to the local Cartesian coordinate system θ^i and is computed as close as possible to the convected basis system using the lamina coordinate system, see Dornisch et al. (2013). In this sense, the displacement and position vectors in Eqs. (4.3-4.4) are now defined with respect to the new coordinate system θ^i .

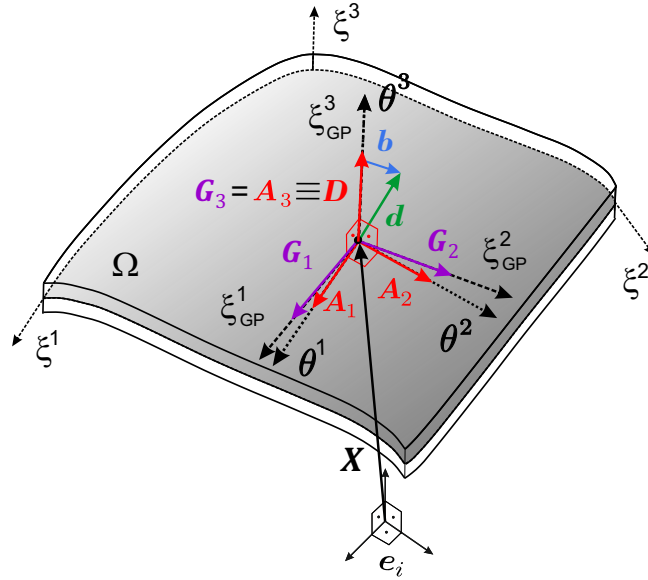


Figure 4.1: Basis systems and director vector at a point on the shell's mid-surface.

The definition of the Jacobian matrix \mathbf{J} is necessary for the computation of the derivatives with respect to the local Cartesian coordinate system as well as for the transformation of the stress resultant components in Section 4.4. Its entries $J_{\alpha\beta}$ are defined as

$$J_{\alpha\beta} = \mathbf{G}_\alpha \cdot \mathbf{A}_\beta. \quad (4.7)$$

Since only smooth surfaces are considered, the unknown deformation is summed up in the following deformation vector

$$\mathbf{v} = \begin{bmatrix} \mathbf{u} \\ \boldsymbol{\beta} \end{bmatrix} = [u_1 \quad u_2 \quad u_3 \quad \beta_1 \quad \beta_2]^T, \quad (4.8)$$

where u_i are the displacements and β_α the rotations. In the case of surfaces with kinks the third rotation β_3 should be considered additionally.

4.3.2 Strains and stresses

The strains and stresses are expressed with respect to the local Cartesian basis system \mathbf{A}_i and its dual basis system $\mathbf{A}^i = \mathbf{A}_i$. Since only linear problems are considered the linearized Green-Lagrange strain tensor is used and the strain tensor with respect to \mathbf{A}^i is defined as

$$\mathbf{E} = E_{ij} \mathbf{A}^i \otimes \mathbf{A}^j. \quad (4.9)$$

The components E_{ij} are split into the in-plane and transverse shear strains as follows

$$E_{\alpha\beta} = \varepsilon_{\alpha\beta} + \theta^3 \kappa_{\alpha\beta} + (\theta^3)^2 \rho_{\alpha\beta}, \quad (4.10)$$

$$2E_{\alpha 3} = \gamma_\alpha. \quad (4.11)$$

E_{33} is zero due to the inextensibility constraint. In Eq. (4.10) $\varepsilon_{\alpha\beta}$ denote the membrane strains

$$\varepsilon_{\alpha\beta} = \frac{1}{2} (\mathbf{X}_{,\alpha} \cdot \mathbf{u}_{,\beta} + \mathbf{X}_{,\beta} \cdot \mathbf{u}_{,\alpha}) \quad (4.12)$$

and $\kappa_{\alpha\beta}$ the curvatures

$$\kappa_{\alpha\beta} = \frac{1}{2} (\mathbf{X}_{,\alpha} \cdot \mathbf{b}_{,\beta} + \mathbf{X}_{,\beta} \cdot \mathbf{b}_{,\alpha} + \mathbf{D}_{,\alpha} \cdot \mathbf{u}_{,\beta} + \mathbf{D}_{,\beta} \cdot \mathbf{u}_{,\alpha}). \quad (4.13)$$

The second-order curvatures, which are denoted as

$$\rho_{\alpha\beta} = \frac{1}{2} (\mathbf{d}_{,\alpha} \cdot \mathbf{d}_{,\beta} - \mathbf{D}_{,\alpha} \cdot \mathbf{D}_{,\beta}) \quad (4.14)$$

are neglected here because only thin shells are considered and their contribution to the strain energy tends to zero. The shear strains γ_α in Eq. (4.11) are given as

$$\gamma_\alpha = \mathbf{X}_{,\alpha} \cdot \mathbf{b} + \mathbf{u}_{,\alpha} \cdot \mathbf{D}. \quad (4.15)$$

The different strain components are assembled in Voigt notation in the strain vector

$$\boldsymbol{\varepsilon} = [\varepsilon_{11} \quad \varepsilon_{22} \quad 2\varepsilon_{12} \quad \kappa_{11} \quad \kappa_{22} \quad 2\kappa_{12} \quad \gamma_1 \quad \gamma_2]^T. \quad (4.16)$$

The corresponding stress resultant vector in Voigt notation includes the membrane forces $n^{\alpha\beta}$, the bending moments $m^{\alpha\beta}$ and the shear forces q^α

$$\boldsymbol{\sigma} = [n^{11} \quad n^{22} \quad n^{12} \quad m^{11} \quad m^{22} \quad m^{12} \quad q^1 \quad q^2]^T. \quad (4.17)$$

Since a linear elastic material is considered, the relation between the stress resultants and the strains is defined as $\boldsymbol{\sigma} = \bar{\mathbf{D}} \cdot \boldsymbol{\varepsilon}$, where $\bar{\mathbf{D}}$ is the constitutive matrix, see Dornisch et al. (2016).

4.4 Isogeometric displacement-stress mixed method for alleviating membrane and shear locking

4.4.1 Hellinger-Reissner variational formulation

In contrast to classical displacement-based formulations, mixed formulations include as additional unknowns the stresses or strains (Hellinger–Reissner) or both the stresses and the strains (Hu–Washizu). The approximation spaces for these additional unknowns must be chosen accordingly, with the aim of alleviating locking effects. In this work, the Hellinger–Reissner functional is used within the framework of an isogeometric Reissner-Mindlin shell formulation, in order to alleviate membrane and shear locking.

The mixed formulation based on the Hellinger-Reissner principle from Hellinger (1914) and Reissner (1950) reads

$$\begin{aligned} G(\mathbf{v}, \boldsymbol{\sigma}, \delta \mathbf{v}, \delta \boldsymbol{\sigma}) &= \int_{\Omega} (\delta \boldsymbol{\varepsilon}^T \boldsymbol{\sigma} - \delta \mathbf{v}^T \bar{\mathbf{p}}_0) d\Omega + \int_{\Omega} \delta \boldsymbol{\sigma}^T (\boldsymbol{\varepsilon} - \bar{\mathbf{D}}^{-1} \boldsymbol{\sigma}) d\Omega \\ &\quad - \int_{\partial\Omega_{\sigma}} \delta \mathbf{v}^T \bar{\mathbf{t}}_0 d\Omega_{\sigma} = 0 \end{aligned} \quad (4.18)$$

with $\bar{\mathbf{p}}_0$ the surface loads, $\bar{\mathbf{t}}_0$ the boundary tractions and $\mathbf{v} = \begin{bmatrix} \mathbf{u} \\ \boldsymbol{\beta} \end{bmatrix} = [u_1, u_2, u_3, \beta_1, \beta_2]^T$ the deformation vector. The strains $\boldsymbol{\varepsilon}$ and their variations $\delta \boldsymbol{\varepsilon}$ are functions of the unknown displacements and rotations \mathbf{v} and their variations $\delta \mathbf{v}$, respectively. The formulation results from the principle of minimum complementary energy when employing Lagrangian multipliers in order to additionally include the equilibrium and traction boundary conditions in the expression. The Hellinger-Reissner functional leads to a saddle point type problem, thus, the existence of a unique solution and the stability of the system are only guaranteed when fulfilling additional conditions, see Andelfinger (1991). In particular, the Babuška-Brezzi condition (inf-sup condition), see Babuška and Aziz (1972) and Brezzi (1974), which ensures the stability of the system should be verified. Here, the condition was not examined, however, since the results obtained in the numerical examples in Section 4.5 were accurate and robust it is assumed that the condition is fulfilled. Nevertheless, in order to ensure the stability of the proposed mixed formulations in general, a mathematical verification of the condition should be carried out in future work. The corresponding variational formulation for a classical displacement-based approach of an isogeometric Reissner-Mindlin shell formulation can be found in Kikis et al. (2019).

The stress resultant components that are considered as additional unknowns and interpolated with adjusted approximation spaces are those that correspond to the occurring

locking effect. In other words, for shear locking the unknown stress resultants include $\boldsymbol{\sigma} = [q^1, q^2]$, for membrane locking $\boldsymbol{\sigma} = [n^{11}, n^{22}, n^{12}]$ and in the case where both locking effects occur, e.g. in shells, the unknowns include $\boldsymbol{\sigma} = [n^{11}, n^{22}, n^{12}, q^1, q^2]$.

In the following, the formulation is presented for the case shear and membrane locking occur. However, in the numerical examples of Section 4.5 all three versions have been implemented and used for the corresponding examples. The equations are then adjusted. Furthermore, in the case of shells, the bending parts could be also considered as additional unknowns. Here, this does not lead to a significant improvement of the results and increases the computational cost considerably. Thus, only the membrane and shear terms are considered. However, in cases where the membrane and bending terms are coupled the consideration of the bending terms as additional unknowns is mandatory, see Andelfinger (1991). They are then interpolated in the same manner as the membrane terms.

The Hellinger-Reissner variational formulation from Eq. (4.18) is now modified for the case where membrane and shear locking is expected

$$\begin{aligned} G(\mathbf{v}, \boldsymbol{\sigma}, \delta \mathbf{v}, \delta \boldsymbol{\sigma}) = & \int_{\Omega} \delta \boldsymbol{\varepsilon}_{\varepsilon\gamma}^T \boldsymbol{\sigma} \, d\Omega + \int_{\Omega} \delta \boldsymbol{\kappa}^T \bar{\mathbf{D}}^{\kappa} \boldsymbol{\kappa} \, d\Omega + \int_{\Omega} \delta \boldsymbol{\sigma}^T \boldsymbol{\varepsilon}_{\varepsilon\gamma} \, d\Omega \\ & - \int_{\Omega} \delta \boldsymbol{\sigma}^T (\bar{\mathbf{D}}^{\varepsilon\gamma})^{-1} \boldsymbol{\sigma} \, d\Omega - \int_{\Omega} \delta \mathbf{v}^T \bar{\mathbf{p}}_0 \, d\Omega - \int_{\partial\Omega_{\sigma}} \delta \mathbf{v}^T \bar{\mathbf{t}}_0 \, \partial\Omega_{\sigma} = 0. \end{aligned} \quad (4.19)$$

Here, $\boldsymbol{\varepsilon}_{\varepsilon\gamma}^T = [\varepsilon_{11}, \varepsilon_{22}, 2\varepsilon_{12}, \gamma_1, \gamma_2]$ are the corresponding strains to $\boldsymbol{\sigma}$ and $\boldsymbol{\kappa}^T = [\kappa_{11}, \kappa_{22}, 2\kappa_{12}]$ the curvatures. The strains $\boldsymbol{\varepsilon}_{\varepsilon\gamma}$, $\boldsymbol{\kappa}$ and their variations $\delta \boldsymbol{\varepsilon}_{\varepsilon\gamma}$, $\delta \boldsymbol{\kappa}$ are functions of the unknown displacements and rotations \mathbf{v} and their variations $\delta \mathbf{v}$, respectively. The isotropic linear elastic material tensor is also split into the part that corresponds to the membrane and transverse shear strains

$$\bar{\mathbf{D}}^{\varepsilon\gamma} = \begin{bmatrix} \frac{Et}{1-\nu^2} & \frac{Et\nu}{1-\nu^2} & 0 & 0 & 0 \\ \frac{Et\nu}{1-\nu^2} & \frac{Et}{1-\nu^2} & 0 & 0 & 0 \\ 0 & 0 & \frac{Et(1-\nu)}{2(1-\nu^2)} & 0 & 0 \\ 0 & 0 & 0 & \frac{Et\kappa_s}{2(1+\nu)} & 0 \\ 0 & 0 & 0 & 0 & \frac{Et\kappa_s}{2(1+\nu)} \end{bmatrix} \quad (4.20)$$

and the part that corresponds to the curvatures

$$\bar{\mathbf{D}}^{\kappa} = \begin{bmatrix} \frac{Et^3}{12(1-\nu^2)} & \frac{Et^3\nu}{12(1-\nu^2)} & 0 \\ \frac{Et^3\nu}{12(1-\nu^2)} & \frac{Et^3}{12(1-\nu^2)} & 0 \\ 0 & 0 & \frac{Et^3(1-\nu)}{24(1-\nu^2)} \end{bmatrix}, \quad (4.21)$$

where E is Young's modulus, ν is Poisson's ratio, t is the shell's thickness and $\kappa_s = \frac{5}{6}$ is the shear correction factor.

In the framework of isogeometric analysis, the appropriate shape functions for the stress resultant fields are, in the relevant direction, one order lower than the ones used for the interpolation of the deformation, see Table 4.1. There also exists the possibility to reduce the polynomial degree in both directions by one, see Bouclier et al. (2013a) and Antolin et al. (2020). However, this version is not considered here. The resulting approximation spaces for the different stress resultant components for a polynomial degree of $p = 3$ and $q = 2$ is depicted in Fig. 4.2. It should be noted that all approximation spaces have the same number of elements and the same number of Gauss points as the deformation mesh. However, the number of control points and their location is different for each approximation space.

$\mathbf{v}^h(\xi^1, \xi^2)$	$\Xi_1^p \otimes \Xi_2^q$	$\mathbf{N}^{p,q}$	$\{S_{\alpha_1}^p \otimes S_{\alpha_2}^q\}$
$n^{11,h}(\xi^1, \xi^2)$ and $q^{1,h}(\xi^1, \xi^2)$	$\Xi_1^{p-1} \otimes \Xi_2^q$	$\mathbf{N}^{p-1,q}$	$\{S_{\alpha_1-1}^{p-1} \otimes S_{\alpha_2}^q\}$
$n^{22,h}(\xi^1, \xi^2)$ and $q^{2,h}(\xi^1, \xi^2)$	$\Xi_1^p \otimes \Xi_2^{q-1}$	$\mathbf{N}^{p,q-1}$	$\{S_{\alpha_1}^p \otimes S_{\alpha_2-1}^{q-1}\}$
$n^{12,h}(\xi^1, \xi^2)$	$\Xi_1^{p-1} \otimes \Xi_2^{q-1}$	$\mathbf{N}^{p-1,q-1}$	$\{S_{\alpha_1-1}^{p-1} \otimes S_{\alpha_2-1}^{q-1}\}$

Table 4.1: Order of the shape functions for the deformation and stress resultants. $S_{\alpha_1}^p, S_{\alpha_2}^q$ are the one-dimensional B-spline spaces with degree p, q and α_1, α_2 continuous derivatives across interior knots, respectively.

Here, NURBS shape functions are used for the approximation of the deformation and the stress resultants, see Piegl and Tiller (1997) and Cottrell et al. (2009). The shape functions for the stress resultant components $\boldsymbol{\sigma} = [n^{11}, n^{22}, n^{12}, q^1, q^2]$ are summed up in the following way

$$\mathbf{N}_\sigma = \begin{bmatrix} \mathbf{N}^{p-1,q} & 0 & 0 & 0 & 0 \\ 0 & \mathbf{N}^{p,q-1} & 0 & 0 & 0 \\ 0 & 0 & \mathbf{N}^{p-1,q-1} & 0 & 0 \\ 0 & 0 & 0 & \mathbf{N}^{p-1,q} & 0 \\ 0 & 0 & 0 & 0 & \mathbf{N}^{p,q-1} \end{bmatrix},$$

where the color indicates the corresponding approximation space from Fig. 4.2 and p, q are the polynomial degrees of the deformations in the first and second direction. $\mathbf{N}^{p-1,q}$, $\mathbf{N}^{p,q-1}$ and $\mathbf{N}^{p-1,q-1}$ include the shape function's values at all control points $\mathbf{N}_I^{p-1,q}$, $\mathbf{N}_I^{p,q-1}$ and $\mathbf{N}_I^{p-1,q-1}$. This way, the stress resultants $\boldsymbol{\sigma}$ are defined with respect to the covariant basis \mathbf{G}_α . However, they need to be defined with respect to the local

Cartesian basis \mathbf{A}_β , thus, the transformation matrix \mathbf{T}_σ is introduced

$$\mathbf{T}_\sigma = \begin{bmatrix} J_{11}^2 & J_{21}^2 & 2J_{11}J_{21} & 0 & 0 \\ J_{12}^2 & J_{22}^2 & 2J_{12}J_{22} & 0 & 0 \\ J_{11}J_{12} & J_{21}J_{22} & J_{11}J_{22} + J_{21}J_{12} & 0 & 0 \\ 0 & 0 & 0 & J_{11} & J_{21} \\ 0 & 0 & 0 & J_{12} & J_{22} \end{bmatrix}, \quad (4.22)$$

where the entries of the Jacobian matrix $J_{\alpha\beta}$ are evaluated at the integration points and are defined in Eq. (4.7). The new resulting shape functions for the stress resultants read $\hat{\mathbf{N}}_\sigma = \mathbf{T}_\sigma \mathbf{N}_\sigma$. Finally, the interpolations of \mathbf{v} and $\boldsymbol{\sigma}$ are given in matrix notation as follows

$$\mathbf{v}^h = \mathbf{N}^{p,q} \hat{\mathbf{v}}, \quad (4.23)$$

$$\boldsymbol{\sigma}^h = \hat{\mathbf{N}}_\sigma \hat{\boldsymbol{\sigma}}, \quad (4.24)$$

where $\hat{\mathbf{v}}$ includes the 5 nodal degrees of freedom of all the control points in the deformation mesh and $\hat{\boldsymbol{\sigma}}$ includes the stress resultant components of all the control points in the different stress resultant meshes.

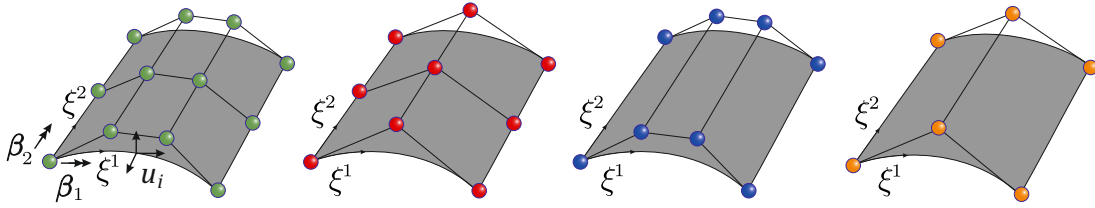


Figure 4.2: Approximation spaces for the deformation \mathbf{v} (green) and the stress resultant components n_{11} , q_1 (red), n_{22} , q_2 (blue) and n_{12} (orange)

Isogeometric analysis uses the same shape functions for the design and analysis which leads to an exact representation of the geometry. Thus, the interpolated values of \mathbf{X} and \mathbf{D} are not approximations but exact values and are denoted without $(\dots)^h$. In order to interpolate the difference vector \mathbf{b}^h , the interpolation of the rotational parameter $\boldsymbol{\omega}^h$ from Eq. (4.2) has to be calculated first. It depends on the nodal transformation matrix $\mathbf{T}_{3I} = [\mathbf{A}_{1I} \ \mathbf{A}_{2I}]$, which includes the nodal Cartesian system $\mathbf{A}_{\alpha I}$ at the I -th control point. These nodal values $\mathbf{A}_{\alpha I}$ are calculated using a method proposed by Dornisch et al. (2013). There, the nodal Cartesian basis systems are defined in a way that their interpolated values at any point of the surface coincide as well as possible with the basis system defined by the geometry. In this sense, the resulting interpolated rotational parameter reads

$$\boldsymbol{\omega}^h = \sum_{I=1}^{nen} \mathbf{T}_{3I} \mathbf{N}_I^{p,q} \boldsymbol{\beta}_I, \quad (4.25)$$

where nen is the number of shape functions that are non zero for a given element.

The strain-deformation matrices $B^{\varepsilon\gamma}$ and B^κ provide a relation between the strains and the nodal deformation

$$\varepsilon_{\varepsilon\gamma}^h = B^{\varepsilon\gamma} \hat{\mathbf{v}}, \quad (4.26)$$

$$\kappa^h = B^\kappa \hat{\mathbf{v}}. \quad (4.27)$$

Eqs. (4.26,4.27) are given in matrix notation and $B^{\varepsilon\gamma}$, B^κ include the values for all the control points $I = 1, n_{cp}$ of the deformation mesh

$$B_I^{\varepsilon\gamma} = \begin{bmatrix} \mathbf{X}_{,1}^T N_{I,1}^{p,q} & 0 \\ \mathbf{X}_{,2}^T N_{I,2}^{p,q} & 0 \\ \mathbf{X}_{,1}^T N_{I,2}^{p,q} + \mathbf{X}_{,2}^T N_{I,1}^{p,q} & 0 \\ \mathbf{D}_{,1}^T N_{I,1}^{p,q} & \mathbf{X}_{,1}^T \mathbf{W}^T \mathbf{T}_{3I} N_I^{p,q} \\ \mathbf{D}_{,2}^T N_{I,2}^{p,q} & \mathbf{X}_{,2}^T \mathbf{W}^T \mathbf{T}_{3I} N_I^{p,q} \end{bmatrix}, \quad (4.28)$$

$$B_I^\kappa = \begin{bmatrix} \mathbf{D}_{,1}^T N_{I,1}^{p,q} & \mathbf{X}_{,1}^T \mathbf{W}^T \mathbf{T}_{3I} N_{I,1}^{p,q} \\ \vdots & \vdots \\ \mathbf{D}_{,2}^T N_{I,2}^{p,q} & \mathbf{X}_{,2}^T \mathbf{W}^T \mathbf{T}_{3I} N_{I,2}^{p,q} \\ \vdots & \vdots \\ \mathbf{D}_{,1}^T N_{I,2}^{p,q} + \mathbf{D}_{,2}^T N_{I,1}^{p,q} & \mathbf{X}_{,1}^T \mathbf{W}^T \mathbf{T}_{3I} N_{I,2}^{p,q} \\ \vdots & \vdots \\ & + \mathbf{X}_{,1}^T \mathbf{W}_{,2}^T \mathbf{T}_{3I} N_I^{p,q} \\ & + \mathbf{X}_{,2}^T \mathbf{W}^T \mathbf{T}_{3I} N_{I,1}^{p,q} \\ & + \mathbf{X}_{,2}^T \mathbf{W}_{,1}^T \mathbf{T}_{3I} N_I^{p,q} \end{bmatrix}. \quad (4.29)$$

Inserting the interpolated values from Eqs. (4.23-4.24) and Eqs. (4.26-4.27) in Eq. (4.19) leads to the discrete weak form of the Hellinger-Reissner variational formulation

$$\begin{aligned} G^h(\hat{\mathbf{v}}, \hat{\boldsymbol{\sigma}}, \delta \hat{\mathbf{v}}, \delta \hat{\boldsymbol{\sigma}}) &= \int_{\Omega^h} \delta \hat{\mathbf{v}}^T (B^{\varepsilon\gamma})^T \hat{\mathbf{N}}_\sigma \hat{\boldsymbol{\sigma}} \, d\Omega^h + \int_{\Omega^h} \delta \hat{\mathbf{v}}^T (B^\kappa)^T \bar{\mathbf{D}}^\kappa B^\kappa \hat{\mathbf{v}} \, d\Omega^h \\ &+ \int_{\Omega^h} \delta \hat{\boldsymbol{\sigma}}^T \hat{\mathbf{N}}_\sigma^T B^{\varepsilon\gamma} \hat{\mathbf{v}} \, d\Omega^h - \int_{\Omega^h} \delta \hat{\boldsymbol{\sigma}}^T \hat{\mathbf{N}}_\sigma^T (\bar{\mathbf{D}}^{\varepsilon\gamma})^{-1} \hat{\mathbf{N}}_\sigma \hat{\boldsymbol{\sigma}} \, d\Omega^h - \int_{\Omega^h} \delta \hat{\mathbf{v}}^T (N^{p,q})^T \bar{\mathbf{p}}_0 \, d\Omega^h \\ &- \int_{\partial\Omega_\sigma^h} \delta \hat{\mathbf{v}}^T (N^{p,q})^T \bar{\mathbf{t}}_0 \, \partial\Omega_\sigma^h = 0. \end{aligned} \quad (4.30)$$

The linear system of equations that results from Eq. (4.30) and has to be solved is given as follows

$$\begin{bmatrix} \mathbf{K}_{vv} & \mathbf{K}_{v\sigma} \\ \mathbf{K}_{\sigma v} & -\mathbf{K}_{\sigma\sigma} \end{bmatrix} \begin{bmatrix} \hat{\mathbf{v}} \\ \hat{\boldsymbol{\sigma}} \end{bmatrix} = \begin{bmatrix} \mathbf{F} \\ \mathbf{0} \end{bmatrix} \quad (4.31)$$

with the different stiffness parts defined as

$$\mathbf{K}_{vv} = \int_{\Omega^h} (\mathbf{B}^\kappa)^T \bar{\mathbf{D}}^\kappa \mathbf{B}^\kappa d\Omega^h \quad (4.32)$$

$$\mathbf{K}_{v\sigma} = \int_{\Omega^h} (\mathbf{B}^{\varepsilon\gamma})^T \hat{\mathbf{N}}_\sigma d\Omega^h \quad (4.33)$$

$$\mathbf{K}_{\sigma v} = \int_{\Omega^h} \hat{\mathbf{N}}_\sigma^T \mathbf{B}^{\varepsilon\gamma} d\Omega^h \quad (4.34)$$

$$\mathbf{K}_{\sigma\sigma} = \int_{\Omega^h} \hat{\mathbf{N}}_\sigma^T (\bar{\mathbf{D}}^{\varepsilon\gamma})^{-1} \hat{\mathbf{N}}_\sigma d\Omega^h \quad (4.35)$$

and the force vector defined as

$$\mathbf{F} = \int_{\Omega^h} (\mathbf{N}^{p,q})^T \bar{\mathbf{p}}_0 d\Omega^h + \int_{\partial\Omega_\sigma^h} (\mathbf{N}^{p,q})^T \bar{\mathbf{t}}_0 \partial\Omega_\sigma^h. \quad (4.36)$$

Applying static condensation on the patch level, a new mixed stiffness matrix \mathbf{K}_{Mixed} can be defined

$$\underbrace{(\mathbf{K}_{vv} + \mathbf{K}_{v\sigma} \cdot \mathbf{K}_{\sigma\sigma}^{-1} \cdot \mathbf{K}_{\sigma v})}_{\mathbf{K}_{Mixed}} \cdot \bar{\mathbf{v}} = \mathbf{F}, \quad (4.37)$$

that has the same dimension as the stiffness matrix from the classical displacement-based formulation. This way, the unknowns to be calculated are again only the deformations. In the following three different approaches to perform the static condensation are presented.

4.4.2 Continuous approach

In the first approach, the approximation spaces for the stress resultant components $\hat{\sigma}$ are chosen to be one level of continuity lower than the approximation space of the deformation. In other words, the continuity of the deformation across an interior element boundary is C^{p-1} , while for the stress resultant components the continuity can take the value C^{p-2} depending on the direction. The high continuity of the NURBS shape functions, which is one of the advantages for using isogeometric analysis, is now an obstacle when doing the static condensation in Eq. (4.31). In the standard C^0 continuous finite element method, static condensation can be done on the element level since the stress resultant components are discontinuous across the element boundaries. However, in isogeometric analysis, due to the higher continuity, static condensation has to be performed on the patch level. Thus, the stiffness matrix components in Eqs. (4.32-4.35) are going to have the following dimension

- \mathbf{K}_{vv} has the dimension $(ncp_v \cdot ndf) \times (ncp_v \cdot ndf)$, where ncp_v is the total number of control points from the displacement/rotation mesh and $ndf = 5$ are the degrees of freedom per control point.
- $\mathbf{K}_{v\sigma}$ and $\mathbf{K}_{\sigma v}^T$ have the dimension $(ncp_v \cdot ndf) \times (ncp_s)$, where here ncp_s includes the total number of control points ncp_{11} , ncp_{22} , ncp_{12} from the stress resultant component meshes. Depending on the locking phenomena to be alleviated, ncp_s can take different values, as can be seen in Table 4.2.
- $\mathbf{K}_{\sigma\sigma}$ has the dimension $ncp_s \times ncp_s$.

ncp_s	Continuous	Discontinuous
Membrane locking	$ncp_{11} + ncp_{22} + ncp_{12}$	$nen_{11} + nen_{22} + nen_{12}$
Shear locking	$ncp_{11} + ncp_{22}$	$nen_{11} + nen_{22}$
Membrane and shear locking	$2ncp_{11} + 2ncp_{22} + ncp_{12}$	$2nen_{11} + 2nen_{22} + nen_{12}$

Table 4.2: Dimension ncp_s defined for the continuous and discontinuous approach as well as for different locking cases.

This way, also the stress resultant components $\hat{\sigma}$ are defined on the patch level

$$\hat{\sigma} = (\mathbf{K}_{\sigma\sigma})^{-1} \mathbf{K}_{\sigma v} \hat{v}, \quad (4.38)$$

where

$$\hat{\sigma}^T = [\mathbf{n}^{11}, \mathbf{n}^{22}, \mathbf{n}^{12}, \mathbf{q}^1, \mathbf{q}^2] \quad (4.39)$$

with $\mathbf{n}^{11} = [n_1^{11}, \dots, n_{ncp_{11}}^{11}]$, $\mathbf{n}^{22} = [n_1^{22}, \dots, n_{ncp_{22}}^{22}]$, $\mathbf{n}^{12} = [n_1^{12}, \dots, n_{ncp_{12}}^{12}]$, $\mathbf{q}^1 = [q_1^1, \dots, q_{ncp_{11}}^1]$ and $\mathbf{q}^2 = [q_1^2, \dots, q_{ncp_{22}}^2]$. The inversion of $\mathbf{K}_{\sigma\sigma}$ on the patch level requires a significantly higher computational time since the size of the matrix increases very quickly, see Table 4.2. Furthermore, the resulting stiffness matrix \mathbf{K}_{Mixed} is not a banded matrix anymore but a full one, which additionally increases the computational cost, see Section 4.4.5.

Since here only linear problems are considered, the continuous mixed formulation is equivalent to the global \bar{B} formulation firstly presented in Elguedj et al. (2008) and later used in Bouclier et al. (2013a) in the framework of an isogeometric NURBS-based solid-shell with the aim of alleviating membrane, shear and thickness locking. It was later extended to the case of large rotations and large displacements in Bouclier et al. (2015). Another continuous mixed formulation can be found in the work of Echter et al. (2013), where it was applied to a hierarchic family of shells and in the work of Rafetseder and Zulehner (2019), where it was implemented to an isogeometric Kirchhoff-Love shell. In both approaches, the aim was to alleviate membrane locking.

Advantages: The results are in general more accurate than for the following two approaches as it will be seen in Section 4.5.

Disadvantages: Higher computational cost since $\mathbf{K}_{\sigma\sigma}$ is inverted on the patch level and the resulting stiffness matrix is full.

4.4.3 Discontinuous approach

In the discontinuous approach, the shape functions for the stress resultant components are again chosen with one order lower in the relevant direction than the shape functions for the deformations. However, this time, in order to enable static condensation on the element level, the continuity between internal element boundaries is reduced so that the elements are discontinuous again. This is achieved by repeating the internal entries of the knot vector until a continuity of C^{-1} is reached. A discontinuous stress resultant field for the component n^{11} and q^1 is depicted in Fig. 4.3 in comparison to the corresponding continuous deformation field.

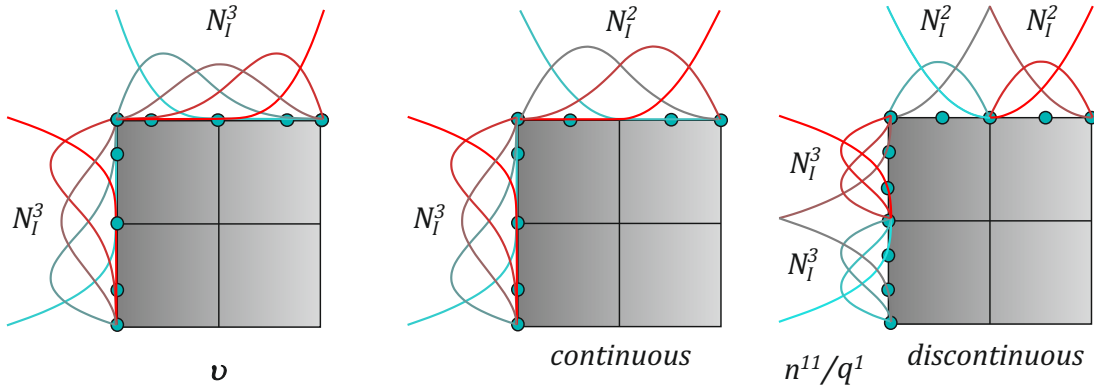


Figure 4.3: Shape functions of n^{11}/q^1 for the continuous and the discontinuous approaches in comparison to the shape functions of the deformation v ($p = q = 3$, 2×2 elements).

Eqs. (4.32-4.35) are now defined on the element level, thus, the integrals are computed within the element limits, i.e. $\int_{\Omega_e} d\Omega_e$. The stiffness matrix components have the following dimension

- \mathbf{K}_{vv} has the dimension $(nen_v \cdot ndf) \times (nen_v \cdot ndf)$, where $nen_v = (p+1) \cdot (q+1)$ is the number of nonzero shape functions for an element in the deformation mesh.
- $\mathbf{K}_{v\sigma}$ and $\mathbf{K}_{\sigma v}^T$ have the dimension $(nen_v \cdot ndf) \times (ncp_s)$, where ncp_s includes the number of nonzero shape functions $nen_{11} = p \cdot (q+1)$, $nen_{22} = (p+1) \cdot q$, $nen_{12} = p \cdot q$ for an element in the stress resultant component meshes. Again, ncp_s varies based on the locking phenomena that have to be alleviated, see Table 4.2.

- $K_{\sigma\sigma}$ has the dimension $ncp_s \times ncp_s$.

The stress resultant components $\hat{\sigma}^e$ are now defined on the element level

$$\hat{\sigma}^e = (K_{\sigma\sigma}^e)^{-1} K_{\sigma v}^e \hat{v}^e, \quad (4.40)$$

where $e = 1, \text{numel}$ and

$$\hat{\sigma}^{eT} = [\mathbf{n}^{11}, \mathbf{n}^{22}, \mathbf{n}^{12}, \mathbf{q}^1, \mathbf{q}^2] \quad (4.41)$$

with $\mathbf{n}^{11} = [n_1^{11}, \dots, n_{nen_{11}}^{11}]$, $\mathbf{n}^{22} = [n_1^{22}, \dots, n_{nen_{22}}^{22}]$, $\mathbf{n}^{12} = [n_1^{12}, \dots, n_{nen_{12}}^{12}]$, $\mathbf{q}^1 = [q_1^1, \dots, q_{nen_{11}}^1]$ and $\mathbf{q}^2 = [q_1^2, \dots, q_{nen_{22}}^2]$. The inversion of $K_{\sigma\sigma}^e$ is now computationally much cheaper than for the continuous approach and the resulting stiffness matrix K_{Mixed} has the same bandwidth of $2 \cdot p + 1$ as the displacement-based formulation, which additionally reduces the computational cost, see Section 4.4.5. However, due to the discontinuity of the stress resultant fields, locking is not completely eliminated, as will be shown in Section 4.5.

In the framework of the \bar{B} method, a discontinuous approach was presented in Greco et al. (2017) for plane curved Kirchhoff rods in order to alleviate membrane locking. However, there, the assumed strain field is not directly implemented discontinuously from the beginning. The strains are computed on the element level using a local L^2 -projection or a collocation method where only the control variables which have an influence on the given element are considered. Across the element boundaries the continuity of the shape functions for the assumed strains are still one continuity lower than the ones for the displacements. This way the formulation becomes quasi discontinuous. Discontinuous local basis functions as the ones presented here were used in Caseiro et al. (2014) in the context of an Assumed Natural Strain method for solid shell NURBS-based elements and in Antolin et al. (2020) again for isogeometric solid shells. Furthermore, Antolin et al. (2017) chose for the projection space of the volumetric strain piecewise discontinuous polynomials, however, they were built on a coarser mesh than the displacements.

Advantages: Static condensation can be performed on the element level. The resulting stiffness matrix is banded and has the same bandwidth as the displacement-based formulation. Thus, the computational cost is low.

Disadvantages: The discontinuity of the stress resultants seems to reduce the accuracy of the results. Larger input file due to the additional control points.

4.4.4 Reconstructed approach

In order to achieve a low computational cost as in the discontinuous approach while maintaining a high accuracy as in the continuous approach, a reconstruction algorithm

is implemented. Reconstruction algorithms have been introduced mainly in the framework of the \bar{B} method when using local approaches. One of these algorithms is presented in the work of Greco et al. (2018) for a B-spline based isogeometric Kirchhoff-Love shell with the aim of alleviating membrane locking. There, the assumed membrane strains are first defined with a local L^2 - projection and later reconstructed by blending the local control variables using weights in order to get the global ones. Even though this method is based on the algorithm proposed by Thomas et al. (2015) it is much simpler and easier to implement. In Thomas' method, first, Bézier extraction is applied to project the spline basis functions onto the Bernstein basis of each element. In a next step, the Bézier local control points are converted to spline control points using an element reconstruction operator and then weighted in order to compute the global spline control values. On the other hand, Greco et al. directly interpolates the local variables with local B-spline functions and later blends them using the same weights proposed by Thomas.

The Bézier projection algorithm from Thomas was also implemented in the framework of the \bar{B} method in order to alleviate transverse shear locking in Timoshenko beams and volumetric locking in nearly incompressible solids in Miao et al. (2018). There, a non-symmetric Bézier \bar{B} -projection method was additionally proposed where the variation of the assumed variables is discretized with the dual basis that correspond to the spline basis functions. This way, the assumed variables are condensed out using the orthogonality property of the Bézier dual bases and an inversion of a matrix is not necessary anymore. This method was extended to a geometrically nonlinear isogeometric Reissner-Mindlin shell element to alleviate shear and membrane locking in the work of Zou et al. (2020). Another reconstruction algorithm that could be compared to the one proposed in this work is the local \bar{B} formulation presented in the work of Bouclier et al. (2013a) for a NURBS-based solid-shell to alleviate membrane, shear and thickness locking. A local least squares method is applied to each element and afterwards the resulting local variables are smoothed over the global structure using the average of the shared local degrees of freedom, as it is proposed in the work of Mitchell et al. (2011) and Govindjee et al. (2012). However, the weights proposed by Thomas are more exact compared to the ones proposed by Govindjee and lead to more accurate results as stated in Thomas et al. (2015). Here, the procedure presented by Greco et al. (2018) is adopted to the mixed formulation with stress resultants as additional unknowns and is then extended to the case of the Reissner-Mindlin shell.

As in the continuous approach, the stress resultant fields are in the relevant direction one order and one level of continuity lower than the deformation field. However, static condensation is still performed on the element level, as in the discontinuous approach.

Thus, the stress resultant components $\hat{\sigma}^e$ are defined for each element as

$$\hat{\sigma}^e = (\mathbf{K}_{\sigma\sigma}^e)^{-1} \mathbf{K}_{\sigma v}^e \hat{v}^e, \quad (4.42)$$

where $e = 1, \text{numel}$ and

$$\hat{\sigma}^{e^T} = [\mathbf{n}^{11}, \mathbf{n}^{22}, \mathbf{n}^{12}, \mathbf{q}^1, \mathbf{q}^2] \quad (4.43)$$

with $\mathbf{n}^{11} = [n_1^{11}, \dots, n_{nen_{11}}^{11}]$, $\mathbf{n}^{22} = [n_1^{22}, \dots, n_{nen_{22}}^{22}]$, $\mathbf{n}^{12} = [n_1^{12}, \dots, n_{nen_{12}}^{12}]$, $\mathbf{q}^1 = [q_1^1, \dots, q_{nen_{11}}^1]$ and $\mathbf{q}^2 = [q_1^2, \dots, q_{nen_{22}}^2]$.

In order to reconstruct again a continuous stress resultant field on the patch level, the local stress resultant control variables are blended with a weighted average as follows

$$n_{I,rec}^{\alpha\beta} = \sum_{e \in D_I} n_{I,e}^{\alpha\beta} w_{I,e}^{\alpha\beta} \quad (4.44)$$

$$q_{I,rec}^\alpha = \sum_{e \in D_I} q_{I,e}^\alpha w_{I,e}^{\alpha\alpha}, \quad (4.45)$$

where D_I includes the elements where the I -th NURBS shape function is not zero. The weights $w_{I,e}^{\alpha\beta}$ are specified according to the work of Thomas et al. (2015) as the volume included by the graph of the I -th shape function defined on the element e divided by the volume included by the graph of the I -th shape function defined on the whole patch:

$$w_{I,e}^{11} = \frac{\int_{\hat{\Omega}^e} N_{I,e}^{p-1,q} d\hat{\Omega}^e}{\int_{\hat{\Omega}} N_I^{p-1,q} d\hat{\Omega}}, \quad w_{I,e}^{22} = \frac{\int_{\hat{\Omega}^e} N_{I,e}^{p,q-1} d\hat{\Omega}^e}{\int_{\hat{\Omega}} N_I^{p,q-1} d\hat{\Omega}} \quad (4.46)$$

$$w_{I,e}^{12} = \frac{\int_{\hat{\Omega}^e} N_{I,e}^{p-1,q-1} d\hat{\Omega}^e}{\int_{\hat{\Omega}} N_I^{p-1,q-1} d\hat{\Omega}} \quad (4.47)$$

$$\sum_{e \in D_e} w_{I,e}^{\alpha\beta} = 1, \quad (4.48)$$

where $\hat{\Omega}$ is the parametric domain of the patch while $\hat{\Omega}^e$ is the parametric domain of the element e . In comparison, the weights proposed in the local least squares method of Mitchell et al. (2011) and Govindjee et al. (2012) are defined as the average of the shared local degrees of freedom

$$w_{I,e}^{11} = \frac{1}{n_I^{11}}, \quad w_{I,e}^{22} = \frac{1}{n_I^{22}}, \quad w_{I,e}^{12} = \frac{1}{n_I^{12}} \quad (4.49)$$

$$\sum_{e \in D_e} w_{I,e}^{\alpha\beta} = 1, \quad (4.50)$$

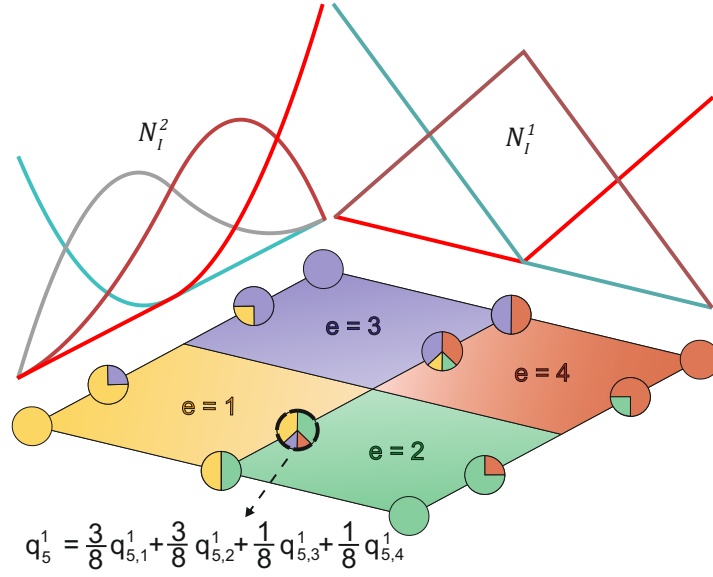


Figure 4.4: Control points of the stress resultant component q^1 with polynomial degrees $p = 1$, $q = 2$ and 2×2 elements and their weights w^{11} for each element according to Thomas et al. (2015). The reconstruction of q^1 for the 5th control point is demonstrated.

where n_I^{11} , n_I^{22} , n_I^{12} are the number of elements in the support of the I -th shape function.

The reconstructed stress resultant components $\hat{\sigma}^{rec}$, which include again the control variables of the whole patch are used for the definition of \mathbf{K}_{Mixed} in Eq. (4.37). An example for the reconstruction algorithm is given for a plate in Fig. (4.4). There the control points of the stress resultant component q^1 with polynomial degrees $p = 1$, $q = 2$ and 2×2 elements are depicted with their weights w^{11} for each element. The reconstruction of q^1 for the 5th control point is demonstrated. The same example is in addition illustrated in Fig. 4.5 for the case that the weights of Mitchell et al. (2011) and Govindjee et al. (2012) are used, see Eq. (4.49).

The dimension of the stiffness matrix components in Eqs. (4.32-4.35) are now partly defined as in the continuous method and partly as in the discontinuous method. $\mathbf{K}_{\sigma\sigma}$ and $\mathbf{K}_{\sigma v}$ are defined as in the discontinuous method on the element level. Thus, the computational cost for the inversion of $\mathbf{K}_{\sigma\sigma}$ is low. On the other hand $\mathbf{K}_{v\sigma}$ is defined as in the continuous method on the patch level. This way, the resulting stiffness matrix \mathbf{K}_{Mixed} is not symmetric anymore. However, \mathbf{K}_{Mixed} is again a banded matrix with a bandwidth slightly higher than in the discontinuous case, which additionally reduces the computational time, see Section 4.4.5. The exact value of the bandwidth is $6 \cdot p - 3$ as stated in Bouclier et al. (2013a).

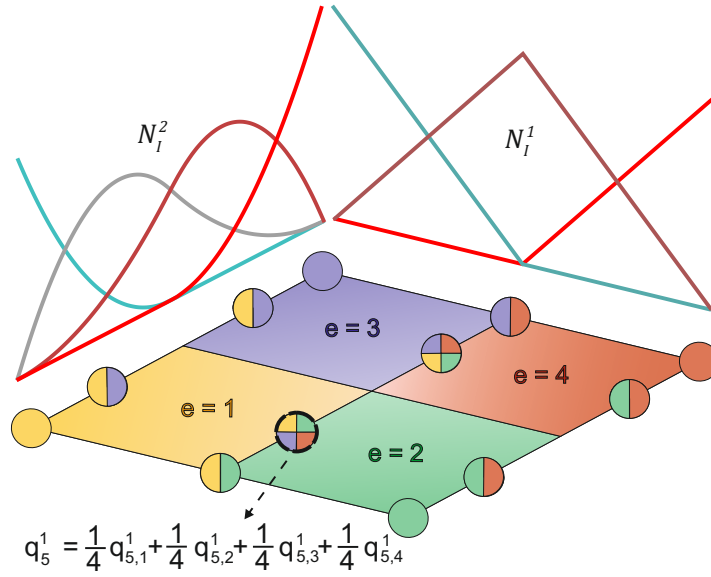


Figure 4.5: Control points of the stress resultant component q^1 with polynomial degrees $p = 1$, $q = 2$ and 2×2 elements and their weights w^{11} for each element according to Mitchell et al. (2011) and Govindjee et al. (2012). The reconstruction of q^1 for the 5th control point is demonstrated.

Advantages: Accuracy almost as good as for the continuous approach, see Section 4.5. The inversion of $\mathbf{K}_{\sigma\sigma}$ is done on the element level which reduces the computational cost. The resulting stiffness matrix is banded which reduces the computational cost compared to the continuous method.

Disadvantages: The weights for the reconstruction algorithm have to be defined beforehand and stored. The resulting stiffness matrix is not symmetric anymore. Loss of physical meaning since Betti-Maxwell's theorem is not valid anymore.

4.4.5 Computational time

In the previous sections, while describing the advantages and disadvantages of the different approaches to the static condensation, the computational time was often mentioned as an argument. In this section the computational cost is discussed in more detail. In particular, the computational time for the inversion of the $\mathbf{K}_{\sigma\sigma}$ matrix, the computation of \mathbf{K}_{Mixed} and the solution of the equations is going to be the main focus since they can increase rapidly depending on the approach that is used.

The computational complexity for the inversion of an $n \times n$ matrix, based on the Gauss-Jordan elimination algorithm is $O(n^3)$. There also exist other algorithms which are slightly better concerning the computational time, for instance the Strassen algo-

rithm ($O(n^{2.807})$) or the Coppersmith-Winograd algorithm ($O(n^{2.376})$), see Petković and Stanimirović (2009). In the framework of this comparison, only algorithms for the direct inversion of a matrix are considered. Preconditioned iterative solvers or multi-grid solvers are not taken into account, since their application to shell problems is often problematic and not straightforward, see e.g. Gee et al. (2005) and Saint-Georges et al. (1999). Here, the Gauss-Jordan elimination algorithm is used for the inversion. The dimension of $\mathbf{K}_{\sigma\sigma}$ is $ncp_s \times ncp_s$, where ncp_s was defined for the continuous and the discontinuous method as well as for different locking effects in Table 4.2. It can be seen that for the continuous approach where ncp_s depends on the number of control points from the different stress resultant meshes, the dimension of $\mathbf{K}_{\sigma\sigma}$ and thus the computational time increases rapidly when increasing the number of elements. On the other hand, for the discontinuous and the reconstructed approach, where static condensation is performed on the element level, the dimension of the $\mathbf{K}_{\sigma\sigma}$ matrix is constant for a fixed polynomial degree, regardless of the number of elements. Thus, in this case the total cost for the inversion increases linearly with an increasing number of elements $numel$ (if t_1 the computational time for the inversion of $\mathbf{K}_{\sigma\sigma}$ for one element, the total time for the inversions is $numel \cdot t_1$).

The computation of the new mixed stiffness matrix \mathbf{K}_{Mixed} in Eq. (4.37) requires the matrix multiplication of $\mathbf{K}_{\sigma\sigma}^{-1}$, $\mathbf{K}_{\sigma v}$ and $\mathbf{K}_{v\sigma}$. The computational complexity for the multiplication of two $(n \times m)$ and $(m \times k)$ matrices is, when using the simplest algorithm, $O(nmk)$. Thus, if the matrices are defined on the patch level as in the continuous approach, the computational cost for computing \mathbf{K}_{Mixed} is a lot higher than for the discontinuous approach where they are defined on the element level. The reconstructed approach, as defined in Section 4.4.4, is going to be in between the continuous and the discontinuous approach since $\mathbf{K}_{\sigma\sigma}^{-1}$ and $\mathbf{K}_{\sigma v}$ are defined on the element level whereas $\mathbf{K}_{v\sigma}$ is defined on the patch level.

The resulting stiffness matrix for the continuous, discontinuous and reconstructed approach have the same dimension, however, in the first case the stiffness matrix is full, while in the last two cases the stiffness matrix is banded, see Section 4.5.4. This has an influence on the computational time for the solution of the equations. In particular, fast solvers like the pardiso solver, where only the non zero entries of the matrix are stored and used and which are running parallel can not be applied when the matrix is full. This additionally increases the total computational time for the continuous approach.

Regarding the question which of these operations is going to dominate the total computational time and which computational complexity should be expected for each method, the following has been observed:

- Mixed Continuous method: The operations that dominate in the mixed continuous method are the inversion of $\mathbf{K}_{\sigma\sigma}$ and the computation of $\mathbf{K}_{v\sigma}(\mathbf{K}_{\sigma\sigma})^{-1}\mathbf{K}_{\sigma v}$

on the patch level. The expected computational complexity is going to be a combination of the computational complexities of these operations, i.e. $O(ncp_s^3) + O((ncp_v \cdot ndf) \cdot ncp_s^2) + O((ncp_v \cdot ndf)^2 \cdot ncp_s)$ with ncp_s as defined in Table 4.2 for the continuous method. The values ncp_s and ncp_v depend on the polynomial degrees p, q and the number of elements per direction nel_x, nel_y , i.e. the total number of elements $numel = nel_x \cdot nel_y$. In the case where the polynomial degrees are fixed and the number of elements is increased, the computational complexity can be rewritten depending on $numel$ as $O(numel^3)$. This cubic increase of the computational time when the number of elements is increased is going to be demonstrated in Section 4.5.4 for the case of a pinched cylinder. In Table 4.3 the computational complexity is defined additionally for the case that the number of elements and the polynomial degree q are constant while the polynomial degree p is changing.

- **Mixed Discontinuous method:** The operations that dominate the total time are the inversion of $\mathbf{K}_{\sigma\sigma}^e$ and the computation of $\mathbf{K}_{v\sigma}^e (\mathbf{K}_{\sigma\sigma}^e)^{-1} \mathbf{K}_{\sigma v}^e$ on the element level. Since these operations are carried out for each element, the computational complexity is going to be a combination of $numel \cdot O(ncp_s^3) + numel \cdot O((nen_v \cdot ndf) \cdot (ncp_s)^2) + numel \cdot O((nen_v \cdot ndf)^2 \cdot ncp_s)$, with ncp_s as defined in Table 4.2 for the discontinuous method. This time ncp_s as well as nen_v only depend on the polynomial degrees p, q . In the case where the polynomial degrees are fixed and the number of elements is increased, the computational complexity is going to be $O(numel)$. This linear increase in computational time when increasing the number of elements is going to be observed in Section 4.5.4 for the case of a pinched cylinder. The computational complexity for the case where the polynomial degree q and the number of elements $numel$ is fixed and only p is changing is given in Table 4.3.
- **Mixed Reconstructed method:** Since in the mixed reconstructed method the inversion of $\mathbf{K}_{\sigma\sigma}^e$ and the matrix multiplication $(\mathbf{K}_{\sigma\sigma}^e)^{-1} \mathbf{K}_{\sigma v}^e$ are carried out on the element level, the computational time which is going to dominate is from the matrix multiplication on the patch level in order to compute \mathbf{K}_{Mixed} . The computational complexity for this is $O((ncp_v \cdot ndf)^2 \cdot ncp_s)$, where ncp_s is defined as for the continuous method in Table 4.2. Thus, ncp_s and ncp_v depend on the polynomial degrees p, q and the number of elements $numel$. In the case where the polynomial degrees are fixed and the number of elements is increased, the computational complexity can be rewritten depending on $numel$ as $O(numel^3)$. This is also shown in Section 4.5.4 for the case of a pinched cylinder. In Table 4.3 the complexity is additionally defined for the case that $numel$ and q are constant and p is changing.

It is important to notice that the computational complexity only describes how the computational time is going to grow as the input grows. The actual value of the computational time for each method depends on the example. A case study is given in Sec. 4.5.4 for the pinched cylinder. Furthermore, the computational cost should always be considered in relation to the accuracy of a method as shown in Section 4.5.4.

	$numel$ changing, p, q constant	p changing, $numel, q$ constant
Mixed Continuous	$O(numel^3)$	$O(p^3)$
Mixed Discontinuous	$O(numel)$	$O(p^3)$
Mixed Reconstructed	$O(numel^3)$	$O(p^3)$

Table 4.3: Computational complexity of the three methods for two different cases.

4.5 Numerical examples

In this section, the presented mixed formulation with its different ways of performing the static condensation is tested and compared to other existing models. The elements and their corresponding abbreviations which are going to be used in the examples are summarized in the following

- **ω -shell.** The isogeometric 5-parameter Reissner-Mindlin shell formulation proposed by Dornisch et al. (2013). It does not include any measures against locking.
- **Mixed Conti.** Mixed continuous formulation presented in Section 4.4.2.
- **Mixed Discont.** Mixed Discontinuous formulation presented in Section 4.4.3.
- **Mixed Recon.** Mixed reconstructed formulation as presented in Section 4.4.4.
- **AAS shell.** The isogeometric Reissner-Mindlin shell formulation with adjusted approximation spaces for the displacements and the rotations proposed in Kikis et al. (2019). The polynomial degrees p_u, q_u correspond to the displacements u_i while the rotations β_α are interpolated with one order lower polynomials in the relevant direction.
- **Pian/Sumihara.** 4 node plane stress element based on the work of Pian and Sumihara (1984), which uses a mixed formulation.

4.5.1 Cook's membrane

In the first example Cook's membrane, see Cook (1974), is examined which has been widely used as a benchmark example to evaluate, among other things, the sensitivity

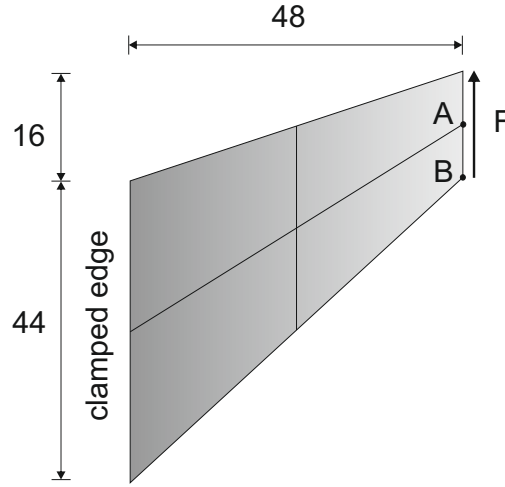


Figure 4.6: Cook's membrane. Geometry and loading.

of an element to geometric distortions. It was also investigated in the original work of Pian and Sumihara (1984). Cook's membrane consists of a tapered panel which is clamped at one edge and subjected to a uniformly distributed shear load on the opposite edge, see Fig. 4.6. The material parameters are given as follows: $E = 1$, $\nu = 0.33333$, $t = 1$. The total load on the right side has the value $F = 1$. Here, the plane stress version of Cook's membrane is considered.

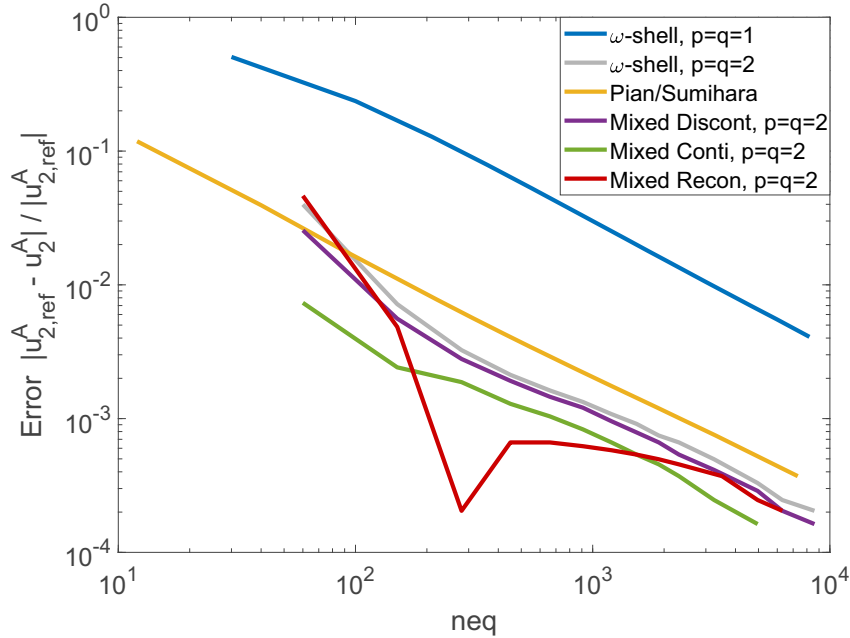


Figure 4.7: Cook's membrane. Error of the deflection at Point A over the number of equations.

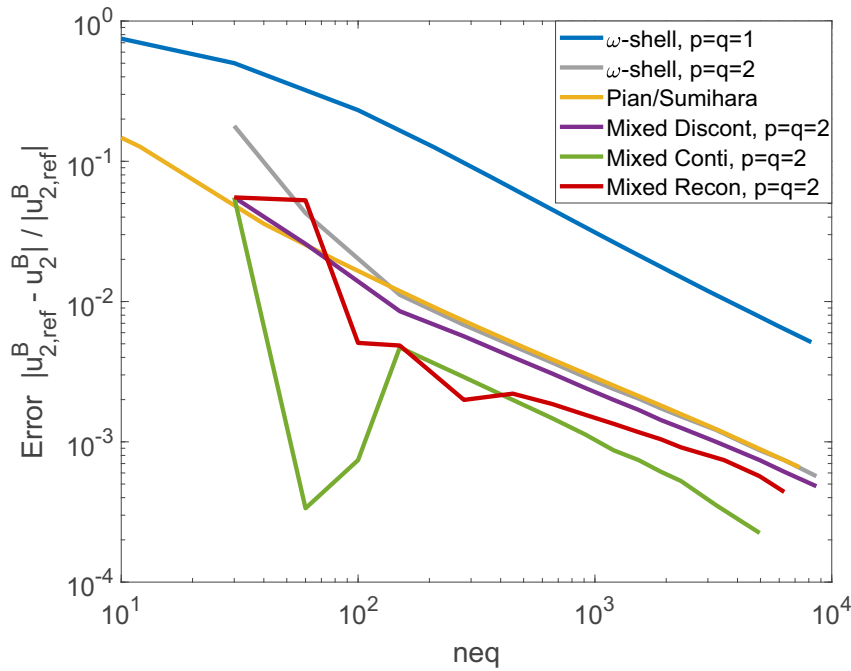


Figure 4.8: Cook's membrane. Error of the deflection at Point B over the number of equations.

The deflection of the panel is examined at two different points, the middle point A of the right edge and the lower point B of the right edge as shown in Fig. 4.6. As a reference solution, the result of Pian/Sumihara's element is considered with a refinement of 200×200 elements and has a value of $u_{2,ref}^A = 23.9659$, $u_{2,ref}^B = 23.2162$, respectively. The total number of equations neq for the solution includes the total number of degrees of freedom related to displacements and rotations. It is the same for the mixed formulations, since the additional degrees of freedom related to the stress resultants are condensed out. As expected, a significant improvement is observed when using the Pian/Sumihara compared to the ω -shell with $p = q = 1$, see Fig. 4.7 and Fig. 4.8. For $p = q = 2$ the ω -shell has better results than the Pian/Sumihara element, which uses linear basis functions. However, both formulations are surpassed by the mixed formulations presented in this work. Namely, Mixed Discont with $p = q = 2$ is already slightly better than the ω -shell in both points A and B. Even more accurate are Mixed Conti and Mixed Recon with $p = q = 2$. Kinks that occur in their error distributions in Figs. 4.7 and 4.8, arise because the deflection first converges from above, then crosses the reference solution to converge again from below. Overall, the mixed formulations, especially Mixed Conti and Mixed Recon, lead to very satisfying results.

4.5.2 Clamped plate with point load

In this example a rectangular plate is considered which is clamped at all edges and subjected to a point load at the center. The material parameters are given as: $E = 1 \cdot 10^4$, $\nu = 0.3$. The plate has a length of $L = 100$ and a thickness of $t = 0.1$ and the point load at the center of the plate has a value of $F = 16.367 \cdot 10^{-3}$, see Fig. 4.9. Due to symmetry only one quarter of the plate is modeled. Here, shear locking is expected and the aim is to validate the ability of the presented mixed formulations to alleviate this effect in comparison to another proven approach, the AAS shell, which includes adjusted approximation spaces for the interpolation of the displacements and the rotations, see Kikis et al. (2019). For this purpose, first, the error of the center deflection is evaluated for the polynomial degrees $p = q = 2$ and $p = q = 3$. The analytical solution is set, according to the Kirchhoff-Love theory, to $u_{3,ref} = 1$, see Timoshenko (1940). All figures have been plotted in double logarithmic scale.

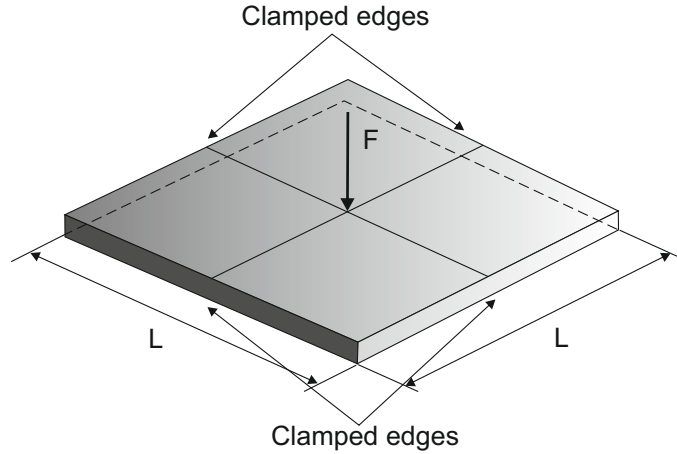


Figure 4.9: Clamped plate. Geometry and loading.

In the case of $p = q = 2$ transverse shear locking is very profound. This is visible in Fig. 4.10, where the ω -shell is underestimating the deflection, leading to a high error especially for a low number of elements. The AAS shell on the other hand is much more accurate and has a constant convergence rate which indicates that it is locking free. Regarding the mixed methods, Mixed Discont is showing a slight locking behavior for a low number of elements, which is quickly overcome when increasing the elements. However, its performance is still significantly better than the ω -shell's. The best results are obtained with Mixed Conti and Mixed Recon, which both have a constant convergence rate. Another interesting point is that the three mixed approaches have the same starting point, since the formulations are identical for a single-element mesh.

In the second case, where the polynomial degree is increased to $p = q = 3$, a slightly different behavior can be observed, see Fig. 4.11. The ω -shell does not exhibit locking as profound as in the first case since the increase of the polynomial degree is a way to reduce locking, see Section 4.2. Mixed Discont, which was significantly better than the ω -shell for $p = q = 2$ is now only slightly improving the results. The AAS shell is again able to overcome locking as well as Mixed Conti and Mixed Recon. The latter two methods exhibit again the best behavior and their results lie very close together.

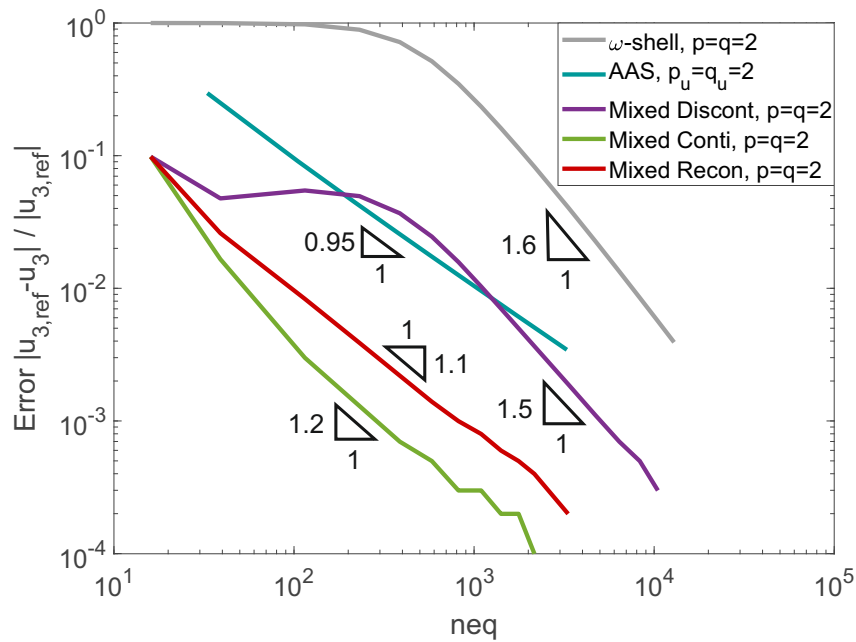


Figure 4.10: Clamped plate. Error of the center deflection over the number of equations for $p = q = 2$.

In conclusion, even though for a low polynomial degree Mixed Discont delivers good results, for higher polynomial degrees it seems that the discontinuity of the stress resultant fields hinders the complete elimination of locking. Another interesting observation that can be made is that the convergence rate of the AAS shell is lower than for all the other methods. This is due to the fact that while the polynomial degrees p_u, q_u of the displacements are the same as for the other methods, the rotations β_1, β_2 are interpolated, in the relevant direction, with one polynomial degree less. This slows down the convergence of the method compared to the others.

As it was outlined in the work of Oesterle et al. (2016), locking does not only distort the results of the displacements but also the stresses. Its effect is even more severe

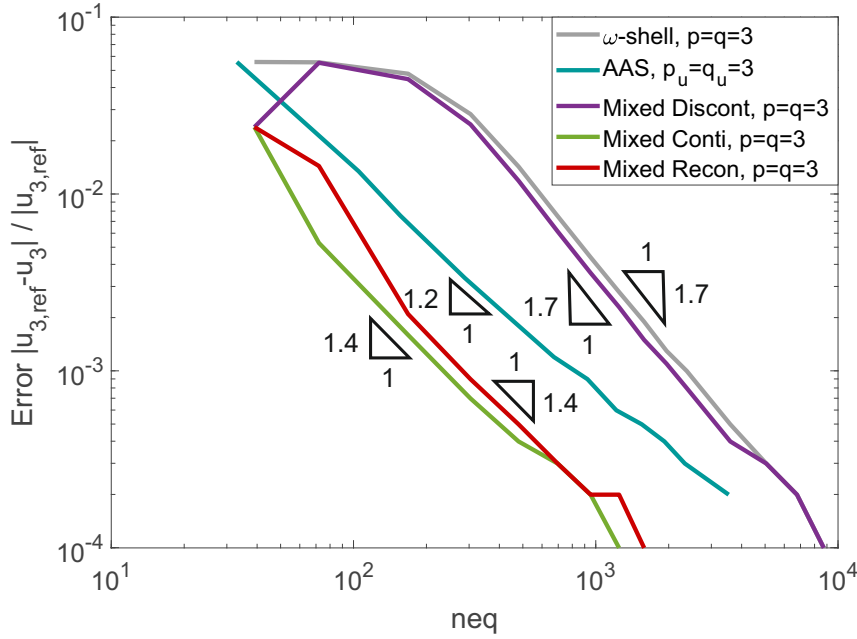


Figure 4.11: Clamped plate. Error of the center deflection over the number of equations for $p = q = 3$.

and visible for the stresses since oscillations occur with high amplitudes. This phenomenon is now examined for the different element types. In Figs. 4.12(a-e) the shear force q^1 is presented for the different methods with $p = q = 2$ and 10×10 elements. In Fig. 4.12(a) it can be seen that for the ω -shell the shear force q^1 exhibits a strong oscillating behavior due to locking. The amplitudes of the oscillations have even higher values than the shear force at the center of the plate where the point load is applied. On the other hand, the AAS shell in Fig. 4.12(b) successfully eliminates these oscillations. Regarding the mixed methods, Mixed Discont reduces the amplitudes of the oscillations, which are now more concentrated around the center of the plate, see Fig. 4.12(c). This makes sense since Mixed Discont was not able to completely eliminate transverse shear locking for the center deflection, see Fig. 4.10. Mixed Conti and Mixed Recon which led to the best results when considering the center deflection, eliminate almost all oscillations as seen in Figs. 4.12(d) and (e). However, compared to the AAS shell there are still some minor oscillations visible across the midlines.

4.5.3 Cylindrical shell strip

In this example a cylindrical shell strip that is clamped at one edge and subjected to a constant line load \hat{q} at the other is investigated, see Fig. 4.13. The material parameters

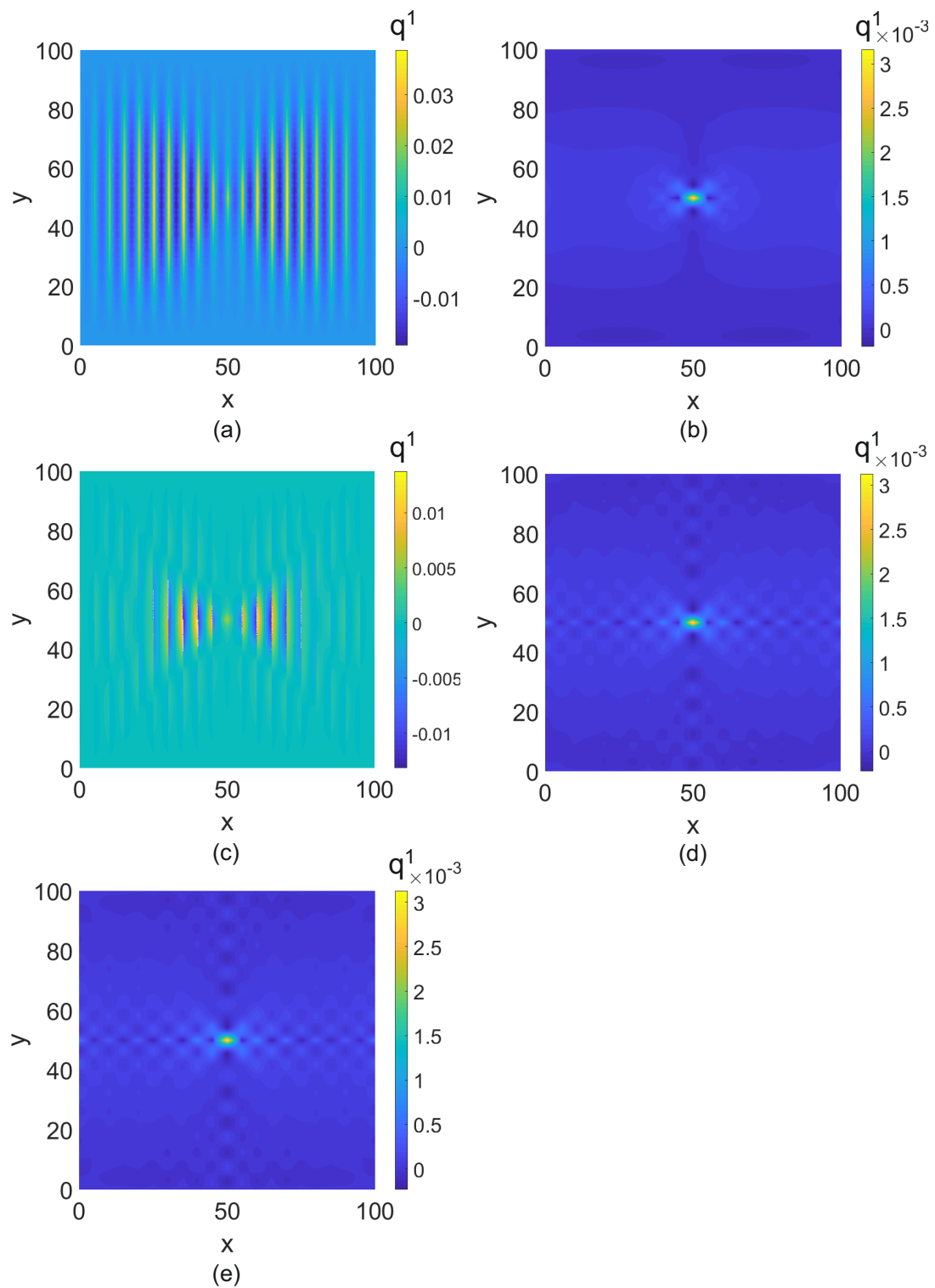


Figure 4.12: Clamped plate. Shear stress resultant q^1 for the (a) ω -shell, (b) AAS shell (c) Mixed Discont (d) Mixed Conti (e) Mixed Recon with $p = q = 2$ and 10×10 elements.

are $E = 1000$ and $\nu = 0$. The shell strip has a radius of $R = 10$ and a width of $b = 1$. The radial displacement u_{1P} is computed for different slenderness values R/t . Here, both membrane and transverse shear locking are expected. These locking effects depend strongly on the slenderness of the shell, i.e. they are more pronounced the thinner the structure is. Thus, locking is going to be more pronounced for higher slenderness values. A reference solution based on Bernoulli beam theory yields $u_{ref} = 0.9451$. The applied line load $\hat{q} = 0.1$ is scaled with t^3 in order to receive the same reference solution independent of the slenderness. The geometry is refined with 10 elements in circumferential direction and 1 element in axial direction.

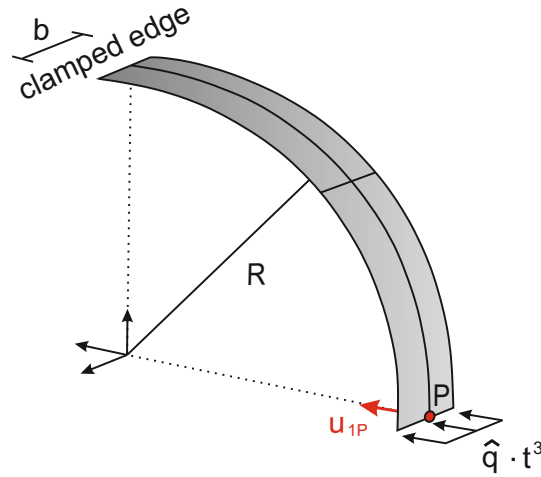


Figure 4.13: Cylindrical shell strip. Geometry and loading.

In Fig. 4.14 the results are computed for the different element types. As can be seen, the ω -shell, which first matches the reference solution for a slenderness of $R/t = 10$, quickly exhibits locking behavior, which is worse the thinner the shell gets. To be more specific, for the case of $p = q = 2$ the radial displacement is strongly underestimated and reaches almost the value 0 for a slenderness of $R/t = 10000$. An improvement is visible when using the higher polynomial degree $p = 3$, however, locking is still present and visible for an increasing slenderness. On the other hand, Mixed Discont with $p = q = 2$ significantly improves the results compared to the ω -shell, though locking is not completely eliminated, as can be seen for a higher slenderness. When using a higher polynomial degree $p = 3$ Mixed Discont shows a slight improvement in the results which is more visible for the highest slenderness, however, it does not reach such significant differences to the ω -shell as for $p = 2$. Hence, as it was also observed for the previous example where only shear locking occurred, Mixed Discont should be preferred when using lower polynomial degrees. The higher the polynomial degree the smaller the improvement of the solution compared to the ω -shell. The AAS

shell, which includes a mechanism to eliminate shear locking but has nothing against membrane locking is also illustrated for a polynomial degree $p_u = 3$, $q_u = 2$ for the displacements. As can be seen, for low and medium slenderness values its behavior is very similar to the one of the ω -shell and Mixed Discont. However, for the highest slenderness the displacement is strongly underestimated since membrane locking is more profound. Mixed Conti and Mixed Recon successfully eliminate transverse shear and membrane locking and lead to the correct displacement regardless of the slenderness.

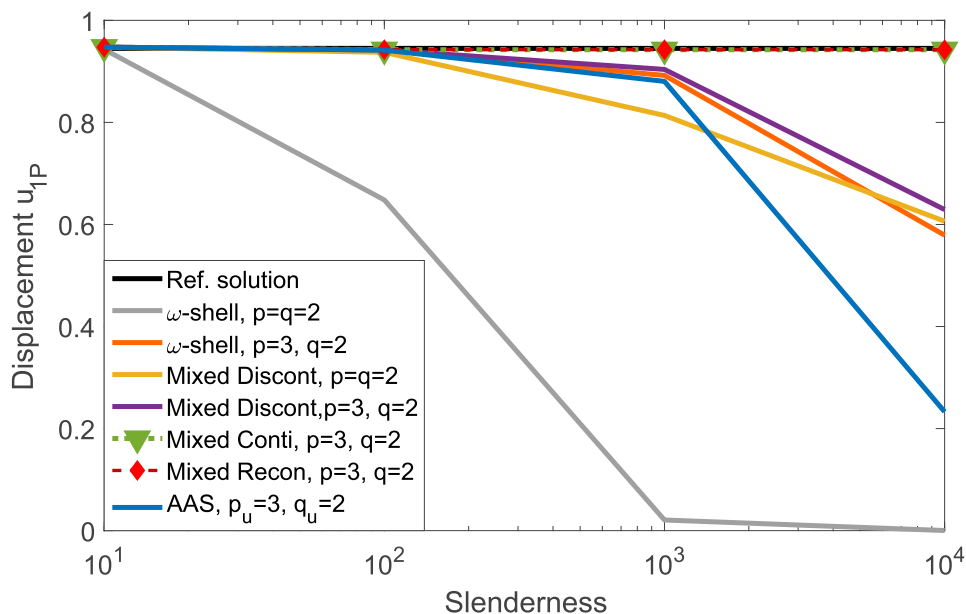


Figure 4.14: Cylindrical shell strip. Radial displacement u_{1P} with increasing slenderness.

4.5.4 Pinched Cylinder

This example is part of the shell obstacle course of Belytschko et al. (1985) and is a good test to validate the performance of an element in the case of inextensional bending modes and complex membrane states. This numerical benchmark consists of a cylinder with a radius of $R = 300$, a length of $L = 600$ and a thickness $t = 3$. The material parameters are given as $E = 3 \cdot 10^6$, $\nu = 0.3$. The cylinder has at both ends a rigid diaphragm and is subjected to a point load $F = 1$ in radial direction. Due to symmetry only one eighth of the geometry is used, see Fig. 4.15. The reference solution $u_{ref} = -1.82889 \cdot 10^{-5}$ is obtained by a computation with 100×100 elements of polynomial order $p = q = 4$.

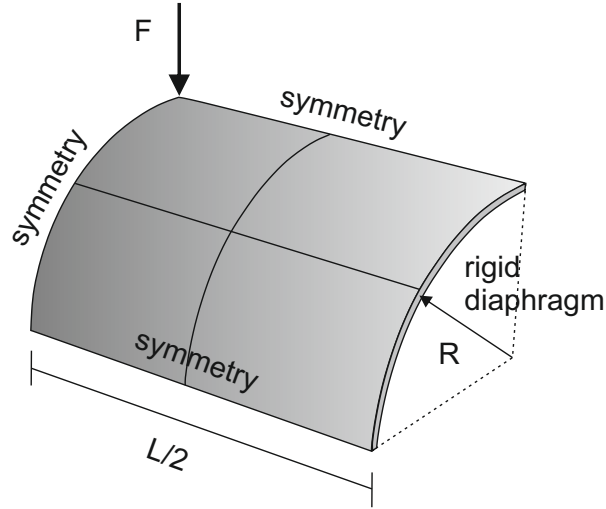


Figure 4.15: Pinched cylinder. Geometry and loading.

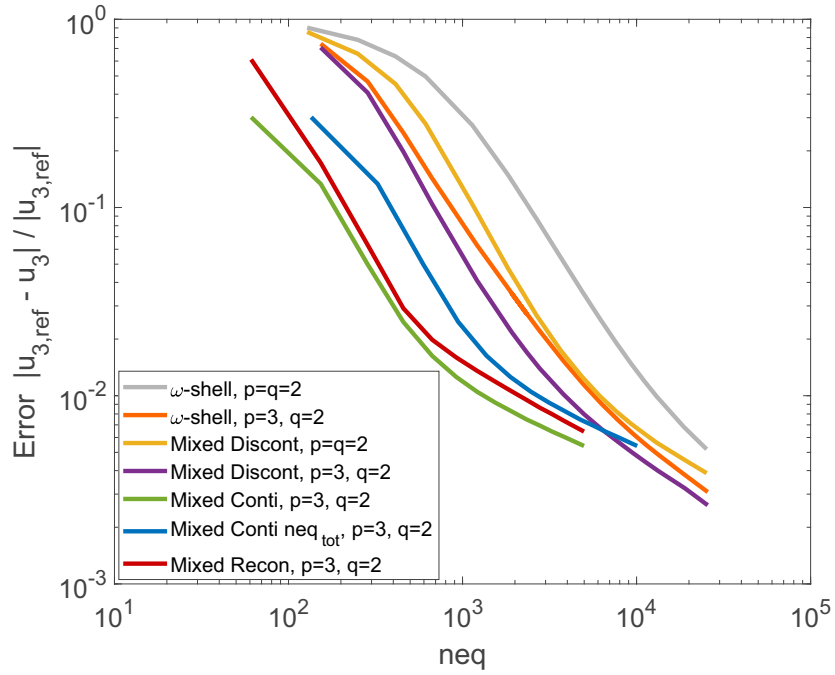


Figure 4.16: Pinched Cylinder. Error of deflection in load direction over the number of equations.

As in the previous example, membrane and shear locking are expected. This example is used to show again the ability of the proposed methods to alleviate these locking effects and in addition to take a closer look on the computational cost of each method. In Fig. 4.16 the error of the deflection under the point load is shown for a varying number

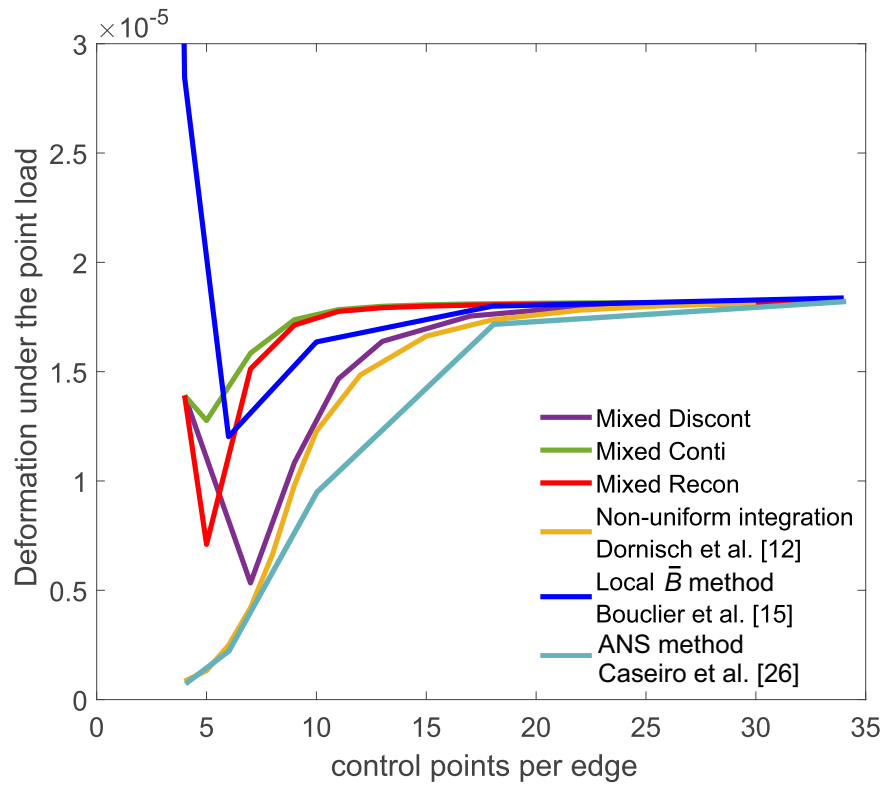


Figure 4.17: Pinched Cylinder. Comparison of the deformation convergence behavior of the mixed methods to other methods against locking.

of equations neq in double logarithmic scale. As expected, the ω -shell strongly underestimates the deflection, especially for the lower polynomial degree $p = q = 2$. Again, the solution can be improved to a certain extent when increasing the polynomial degree to $p = 3, q = 2$. Mixed Discont, on the other hand, significantly improves the results compared to the ω -shell. Even for the polynomial degree $p = 3, q = 2$ the improvement is clearly visible and much greater than, i.e. in the case of the clamped plate, since here, in addition to the transverse shear locking, membrane locking is alleviated. Mixed Conti and Mixed Recon lead to the best results and lie very close together. Here, in addition to the mixed continuous method with static condensation, the case of the mixed continuous method is depicted when no static condensation is performed and the full system of equations is solved with the stress resultants as additional unknowns. In this case the total number of equations is $neq_{tot} = neq + 2 \cdot ncp_{11} + 2 \cdot ncp_{22} + ncp_{12}$, where ncp_{11} is the number of control points of the stress resultant components n^{11} and q^1 , ncp_{22} the number of control points of n^{22} and q^2 and ncp_{12} is the number of control points of n^{12} . The curve is shifted to the right and is in between Mixed Recon and Mixed Discont.

A comparison of the mixed methods proposed in this work with other existing methods against locking is depicted in Fig. 4.17. The chosen methods are the Non-uniform integration technique from Dornisch et al. (2016), the local \bar{B} method presented in Bouclier et al. (2013a) and the ANS method from Caseiro et al. (2014). The focus lies on the deformation under the point load when considering an increasing number of control points per edge. As can be seen in Fig. 4.17, Mixed Discont lies very close to the Non-uniform integration method from Dornisch et al. (2016), which uses a carefully chosen set of integration points in order to reduce locking. Both methods have a better convergence behavior than the ANS method from Caseiro et al. (2014). More accurate results are achieved by the local \bar{B} method from Bouclier et al. (2013a), which uses a local least-squares method for each element and afterwards applies the weights proposed by Mitchell et al. (2011) and Govindjee et al. (2012) in order to reconstruct the global variables from the local ones. However, this method is not accurate enough for a very low number of control points per edge. The best results are achieved by Mixed Conti and Mixed Recon. However, it should be mentioned here that the methods from Dornisch et al., Bouclier et al. and Caseiro et al. use in both directions quadratic basis functions. On the other hand, the mixed methods proposed here use quadratic basis functions in the axial direction whereas in circumferential direction cubic basis functions are applied. For these methods the control points per edge in Fig. 4.17 are the ones from the edge with cubic basis functions.

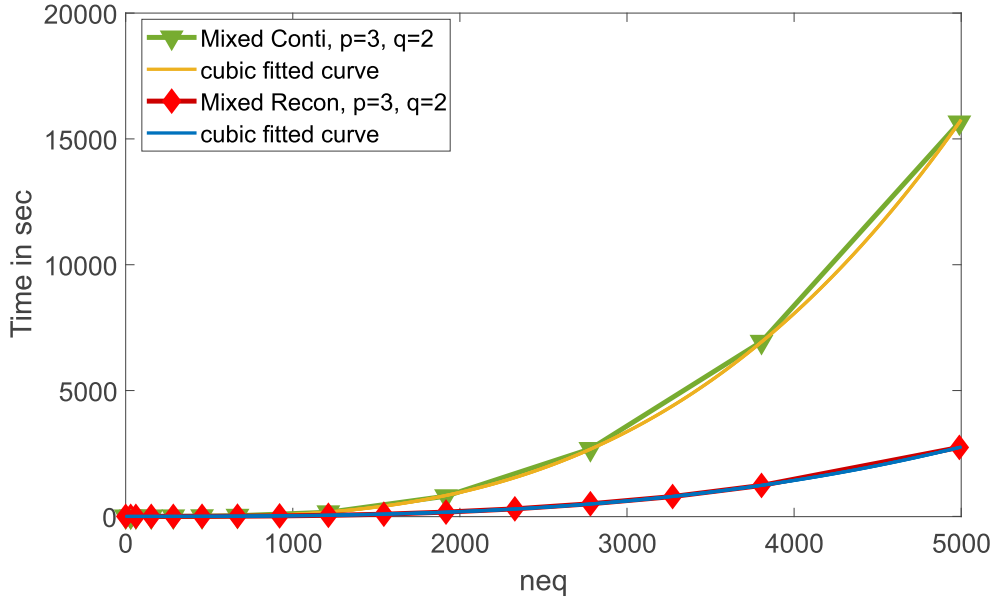


Figure 4.18: Total time in the case of Mixed Conti and Mixed Recon.

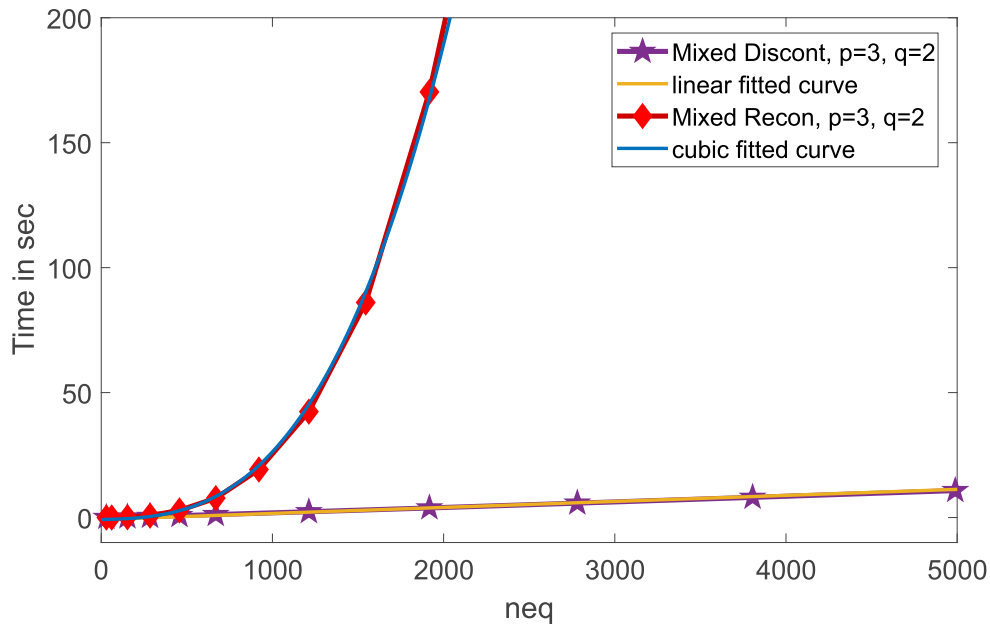


Figure 4.19: Total time in the case of Mixed Discont and the Mixed Recon.

Regarding the computational cost of Mixed Conti, Mixed Discont and Mixed Recon, a comparison is made in Figs. 4.18 and 4.19 for $p = 3$, $q = 2$. The computational time which is considered here includes a) the time for inversion of $\mathbf{K}_{\sigma\sigma}$ b) the time for the computation of \mathbf{K}_{Mixed} c) the time for triangular decomposition d) the time for the solution of the equations. Time is defined in CPU seconds on one core of an Intel®Core™ i7-3520M CPU (Core™i7 vPro™).

In Fig. 4.18, first, a comparison of the total computational time over the number of equations neq is made between Mixed Conti and Mixed Recon. It can be seen that Mixed Conti has a rapid, almost cubic increase of the computational time when neq increases. This is in line with the observations made in Section 4.4.5. There it was mentioned that a cubic computational complexity should be expected in the case where the polynomial degrees are fixed and the number of elements is increased. Here it is also observed, as expected, that the resulting stiffness matrix is full, see Fig. 4.21.

On the other hand, the computational time for Mixed Recon increases much slower than for Mixed Conti. The reason for this is again explained in Section 4.4.5 with reference to the reduced matrix dimension of $\mathbf{K}_{\sigma\sigma}$ and $\mathbf{K}_{\sigma v}$. Furthermore, the resulting stiffness matrix is banded, as it is shown in Fig. 4.22, which additionally reduces the overall computational time. The best time, however, is obtained with Mixed Discont, see Fig. 4.19. There, an almost linear increase of the computational time over neq is depicted. This is due to the performance of the static condensation and the definition of \mathbf{K}_{Mixed} on the element level, which leads to a constant dimension of $\mathbf{K}_{\sigma\sigma}$, $\mathbf{K}_{\sigma v}$ and

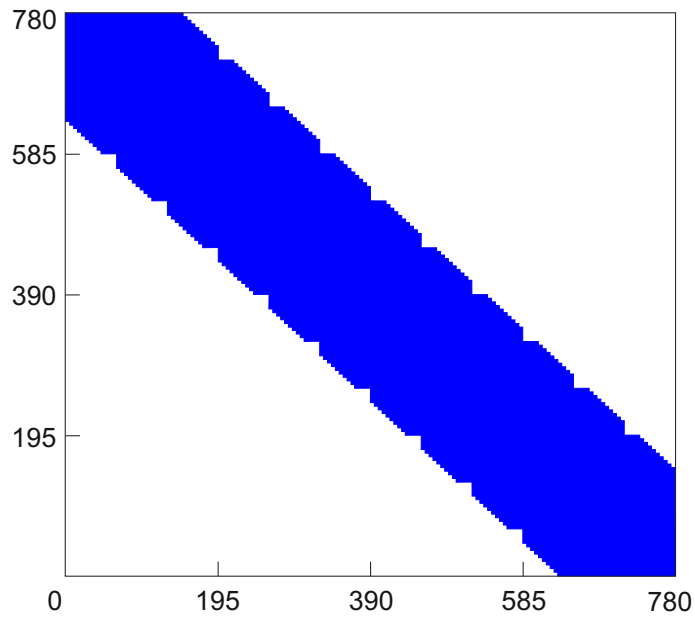


Figure 4.20: Pinched cylinder. Sparsity pattern of stiffness matrix in the displacement-based method (ω -shell) and the mixed discontinuous method (Mixed Discont) for $p = 3$, $q = 2$ and 10×10 elements.

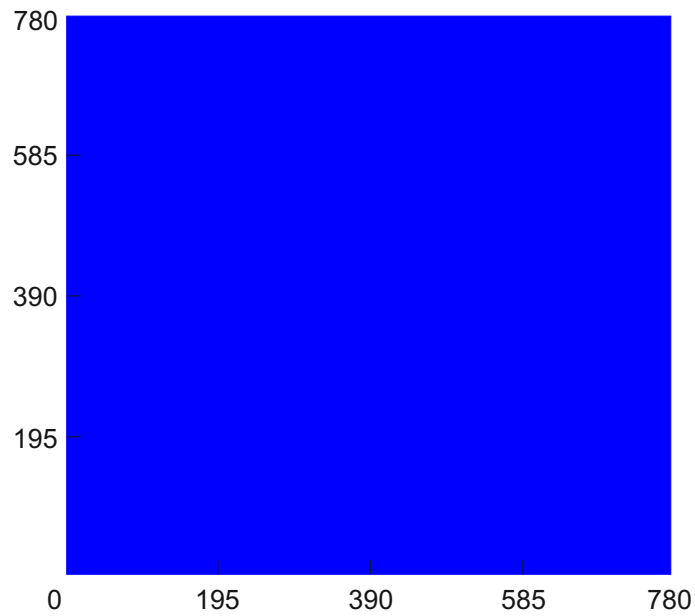


Figure 4.21: Pinched cylinder. Sparsity pattern of stiffness matrix in the mixed continuous method (Mixed Conti) for $p = 3$, $q = 2$ and 10×10 elements.

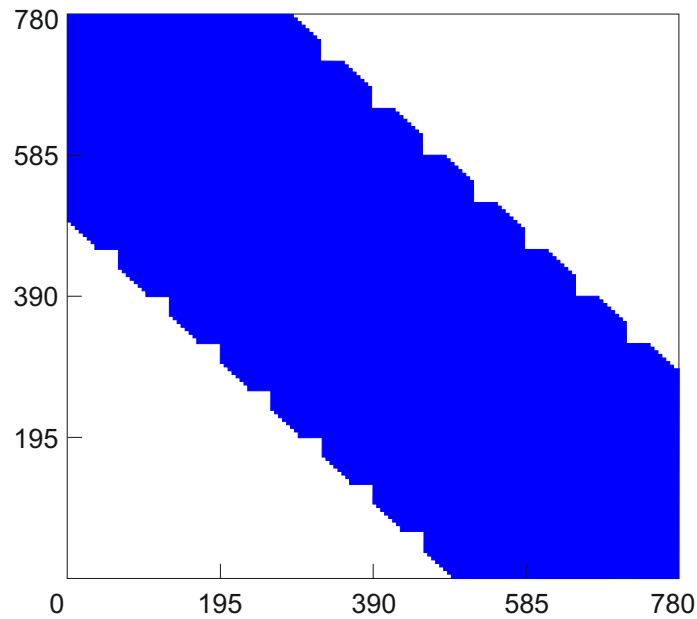


Figure 4.22: Pinched cylinder. Sparsity pattern of stiffness matrix in the mixed reconstructed method (Mixed Recon) for $p = 3$, $q = 2$ and 10×10 elements.

$K_{v\sigma}$ regardless of the number of elements, see Section 4.4.5. In addition, the resulting stiffness matrix is banded and has the same bandwidth as the standard displacement-based method (ω -shell), see Fig. 4.20.

Considering now Fig. 4.16 and Figs. 4.18, 4.19 at the same time, it can be seen that in order to achieve a desired accuracy as fast as possible, it is often better to use Mixed Recon than Mixed Conti, especially for a higher neq . On the other hand, if a very large neq is considered it is even advisable to use Mixed Discont, since it is going to reduce the computational time significantly.

Here, the time depicted in Figs. 4.18, 4.19 should provide an idea on the increase of the computational time for the three different approaches. Of course, depending on how efficient the code is programmed and on the system that is used, the values for the time can slightly vary. However, the relation between the three different approaches should stay the same.

4.5.5 Partly clamped hyperbolic paraboloid

In the last example, the partly clamped hyperbolic paraboloid which was introduced in Chapelle and Bathe (1998) and further investigated e.g. in Bathe et al. (2000), is considered. The geometry of the hyperbolic paraboloid is given as $Z = X^2 - Y^2$ with $(X, Y) \in [(-L/2, L/2)]^2$. The edge $X = -L/2$ is clamped and the structure is

subjected to its self-weight, see Fig. 4.23. Due to symmetry only one half of the shell is considered with respective symmetry boundary conditions along $Y = 0$. The thickness of the shell is $t = 0.0001$ and the length is set to $L = 1$. The material parameters are $E = 2 \cdot 10^{11}$, $\nu = 0.3$ and $\rho = 8000$. The thinnest version of this shell is chosen since it is expected that locking is going to be more severe for this case.

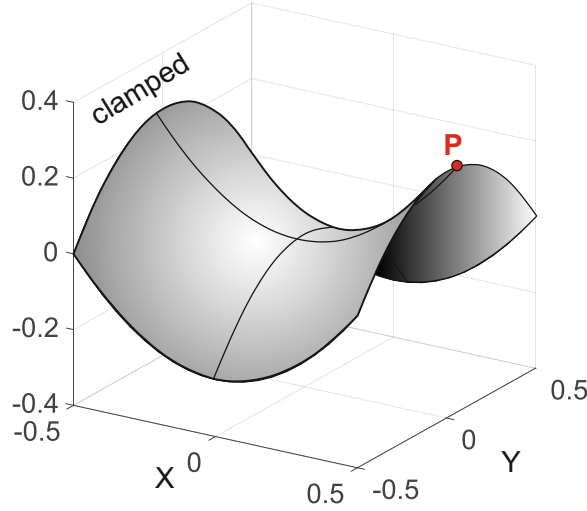


Figure 4.23: Partly clamped hyperbolic paraboloid. Geometry and boundary conditions.

The aim of this example is to evaluate the two superior mixed methods, i.e. Mixed Conti and Mixed Recon, for the case of a double curved surface. In Fig. 4.24 the error of the vertical displacement at point P ($X = 0.5$, $Y = 0$, $Z = 0.25$) is depicted in relation to the number of equations. The plot is given in double logarithmic scale. As a reference solution, the vertical displacement obtained at point P using a 100×50 mesh of ω -shell elements with $p = q = 6$ is used ($u_{3,ref} = -5.3049 \cdot 10^{-1}$). As it can be seen, the ω -shell with polynomial degrees $p = q = 2$ and $p = q = 3$ strongly underestimates the displacement, especially for a low number of elements, due to membrane and shear locking. The AAS shell, which alleviates transverse shear locking, only improves the results for a higher number of elements since for a low number membrane locking is still profound. On the other hand, Mixed Conti and Mixed Recon strongly improve the results for a low and moderate number of elements, which indicates that both membrane and shear locking have been alleviated. However, the convergence rate of the mixed methods is lower than for the other formulations, creating a point of intersection from where the other methods lead to better results. In addition, for a high number of elements the error curves of the mixed methods seem to flatten. The reason for this is that the matrix $\mathbf{K}_{\sigma\sigma}$, which has to be inverted, is, in this example, ill-conditioned. This has an influence on the results especially for a high

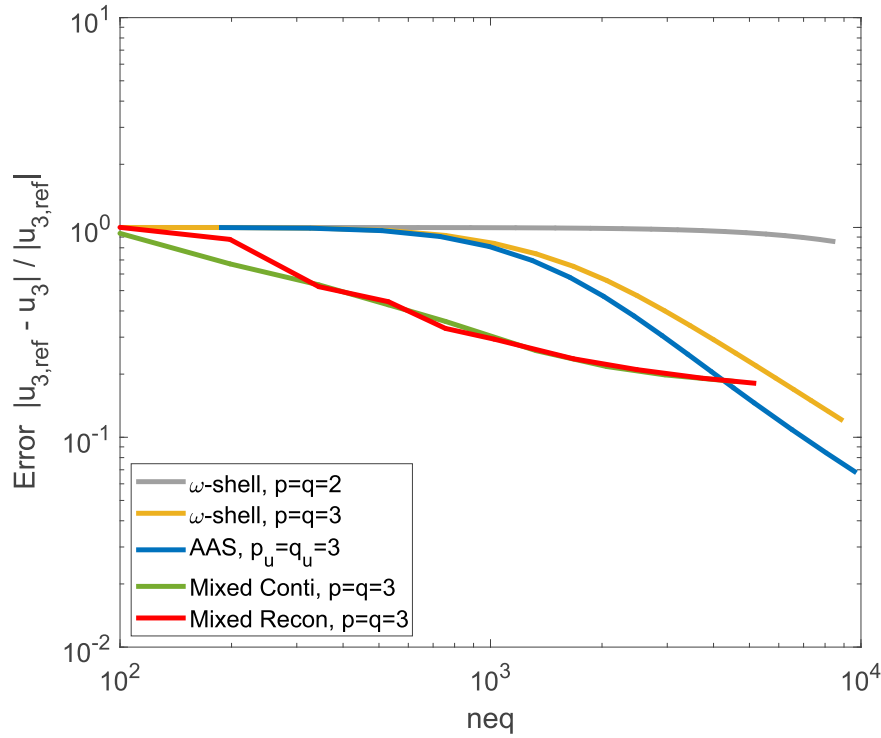


Figure 4.24: Partly clamped hyperbolic paraboloid. Error of the displacement at point P over the number of equations.

number of elements. This behavior is not observed e.g. for the mixed and the local \bar{B} method presented in Bouclier et al. (2013a) for a solid-shell, where thicker versions of this example were examined and a better convergence behavior was observed. The choice of a thicker shell does not improve the results. A combination of Mixed Conti or Mixed Recon for membrane locking and AAS for transverse shear locking could at least reduce this problematic and should be examined in future work.

4.6 Conclusion

In this work, a displacement-stress mixed method is presented in the framework of an isogeometric Reissner-Mindlin shell formulation in order to alleviate membrane and shear locking. The method was derived using the Hellinger-Reissner functional and by choosing appropriate approximation spaces for the different stress resultant components. One main issue which was discussed here, is the performance of the static condensation. Three different approaches were presented, a continuous approach which performs static condensation on the patch level, a discontinuous approach which performs static condensation on the element level and a reconstructed approach which

tries to combine the advantages of the previous two approaches and uses weights for the local control variables in order to get blended global ones. The advantages and disadvantages for using each approach were outlined.

Several numerical examples were investigated in order to test the accuracy and efficiency of the different approaches. They range from a simple panel subjected to an in-plane loading to a plate and shell examples. Depending on the example, different stress resultant components were considered as additional unknowns for the mixed formulation. A comparison to existing elements with mechanisms against locking was additionally carried out. It was shown that the mixed discontinuous approach, while leading to good results for low polynomial degrees, does not improve the results as much for higher polynomial degrees. It seems that the discontinuity of the stress resultant fields hinders the alleviation of locking in those cases. On the other hand, the mixed continuous and the mixed reconstructed approaches surpassed in terms of accuracy every other formulation that was examined here. However, considering the computational effort for the continuous approach which leads to a full stiffness matrix and is computed on the patch level, the use of the reconstructed approach which leads to a banded stiffness matrix and is computed partly on the element level should be considered.

An extension of the proposed mixed formulation to nonlinear problems with large deformations is going to be the focus of future work.

Chapter 5

Phase-field model of brittle fracture in Reissner-Mindlin plates and shells

This chapter was published as:

Kikis, G., Ambati, M., De Lorenzis, L., and Klinkel, S. (2021). Phase-field model of brittle fracture in Reissner-Mindlin plates and shells. *Computer Methods in Applied Mechanics and Engineering*, 373:113490.

Disclosure of the individual authors' contributions to the article:

G. Kikis and M. Ambati implemented the phase-field model of brittle fracture into the isogeometric Reissner-Mindlin shell formulation and created a user element in Matlab. M. Ambati and L. De Lorenzis provided the existing solid and Kirchhoff-Love shell user elements in Matlab. G. Kikis performed the first, second and fourth numerical example with the isogeometric Reissner-Mindlin shell element, the solid element and the Kirchhoff-Love element. M. Ambati performed the simulations for the third numerical example. G. Kikis reviewed the relevant existing literature, wrote the article, interpreted and compared the results. M. Ambati, L. De Lorenzis and S. Klinkel gave conceptual advice, contributed to the discussion of the results, read the article and gave valuable suggestions for improvement. All authors approved the publication of the final version of the manuscript.

5.1 Abstract

In this paper, a phase-field model is presented for the description of brittle fracture in a Reissner-Mindlin plate and shell formulation. The shell kinematics as well as the phase-field variable are described on the mid-surface of the structure. Non-Uniform Rational B-Spline basis functions are used for the discretization of both the

displacement/rotations and the phase-field. The spectral decomposition for the tension-compression split is applied on the total strain tensor, which varies through the thickness. Thus, the plane stress condition has to be enforced numerically. Various numerical examples are presented in order to verify the accuracy and effectiveness of the method and a detailed comparison to existing formulations is performed.

5.2 Introduction

Shells are found in various forms in nature and have been adopted in engineering due to their favorable mechanical features. They span wide areas without the need of additional support and their geometrical form leads to an optimal load-carrying behavior with a high stiffness. Many applications of shell structures are found in architectural and civil engineering, mechanical engineering and marine engineering, thus, the correct numerical analysis of shells is of great importance. Almost fifteen years ago, isogeometric analysis was introduced by Hughes et al. (2005) with the aim of unifying the design and analysis process by using for both the same higher order basis functions from CAD tools, i.e. Non-Uniform Rational B-Spline (NURBS) shape functions. Regarding shells, the higher continuity of these functions allows the correct computation of the curvature as well as the normal of the shell surface and reduces significantly the computational cost. Thus, isogeometric analysis has been applied to Kirchhoff-Love shell formulations, in Kiendl et al. (2009), Benson et al. (2011), Nguyen-Thanh et al. (2011) and Duong et al. (2017), in the framework of Reissner-Mindlin shell formulations, in Uhm and Youn (2009), Benson et al. (2010b), Dornisch et al. (2013, 2016) and Kiendl et al. (2017) and solid shells in Hosseini et al. (2013, 2014b), Bouclier et al. (2013a, 2015) and Caseiro et al. (2015). Later on, blended shells were introduced in Benson et al. (2013), as well as a hierarchic family of shells in Echter et al. (2013) and a shear deformable rotation free shell formulation in Oesterle et al. (2016).

A crucial aspect of shells is their fracture behavior. When considering brittle fracture, where failure occurs abruptly without any visible indications, the correct description of crack initiation and propagation is of great interest, see Kobayashi and Onoue (1943). However, due to the complex interaction of shell geometry, shell kinematics and material constitutive law, the correct description of its fracture behavior is not an easy task. In general, fracture processes can be described discontinuously by discrete crack surfaces, or continuously, i.e. the cracked medium is still considered as a continuum. One discontinuous approach, which has been widely used due to its simplicity, especially in cases where the crack path is known, is the cohesive zone modeling approach. In this model, interface or generalized contact cohesive elements are implemented, either from the beginning or adaptively, and many applications of it in the framework

of shell elements can be found e.g. in Cirak et al. (2005), Zavattieri (2006), Rabczuk and Areias (2008) and Becker et al. (2011) and in later years in combination with isogeometric analysis, e.g. in Dimitri et al. (2014).

In order to allow for arbitrary crack paths, independent of the mesh, the extended finite element method (XFEM) was developed based on the partition of unity method. It uses additional approximation fields for the displacements and if needed for the director in order to describe the discontinuities. XFEM has been applied to Kirchhoff-Love type shells in Areias et al. (2006), Areias and Belytschko (2006) and Song and Belytschko (2009), to solid-like shell formulations for modeling through-the-thickness cracks in Areias and Belytschko (2005), Larsson et al. (2011) and Mostofizadeh et al. (2013) and to a Reissner-Mindlin based plate in Dolbow et al. (2000). In the context of isogeometric analysis, a Kirchhoff-Love based, see Nguyen-Thanh et al. (2015), and a Reissner-Mindlin based, see Benson et al. (2010a), extended isogeometric element formulation were introduced for modeling fracture in shells. Another method, which can compute mesh-independent crack propagation and has proven to be very similar to XFEM approaches, is the phantom node method. Overlapping elements are used at the cracked regions, which are employed by the so-called phantom nodes. Applications of this method can be found in Chau-Dinh et al. (2012), Ahmed et al. (2012) and Lua et al. (2016). A continuum-based phantom node method combined with a molecular statics model is presented in Budarapu et al. (2017), creating an adaptive multiscale method for solid shells. Multi-level models have also been used in the framework of debonding between the levels of composite structures, see Kocaman et al. (2020). The problem with discontinuous approaches in general is that diffuse ductile damage, as it is encountered e.g. in metals, cannot be computed and thus they have mainly been applied to brittle fracture.

Another group of methods which are used for the description of fracture are the so called continuum approaches. Here, the crack is not described as a discontinuity in the structure, but instead the material is still seen as a continuum, however, with weakened mechanical properties at the cracked areas. Various approaches of this type have been introduced, among others in Areias et al. (2011) and Woelke and Abboud (2012), in connection with meshfree formulations in Ren and Li (2012) and Caleyron et al. (2012) and based on the gradient-enhanced damage approach in Hosseini et al. (2014a), Nguyen et al. (2012) and Pigazzini et al. (2019). However, general continuum approaches may have difficulties in properly describing surface decohesion and crack propagation after the softening and damage localization phase.

An approach that can be regarded as a gradient damage model enjoying especially useful mathematical properties is the phase-field method. It was firstly introduced in Bourdin et al. (2000, 2008) and since then has been extensively investigated for brittle, see Ambati et al. (2015b), and ductile fracture, see Alessi et al. (2018), for the case of

solids. The main idea is to introduce a continuous crack phase-field that defines the transition between the cracked and uncracked material leading to a regularized representation of the crack. The model contains a length parameter, and has been proven to converge (in the Γ -convergence sense) to the variational formulation of the classical Griffith's theory of brittle fracture, see Griffith and Taylor (1921) and Francfort and Marigo (1998), when this parameter tends to zero. Phase-field models have the advantage of naturally describing crack initiation, propagation, merging and branching without the need of remeshing or additional criteria. The elastic strain energy density is reduced using a degradation function which depends on the phase-field. The degradation function is either applied on the entire elastic strain energy density or only on the part that corresponds to tension. In the latter case, a previous split of the elastic strain energy density into its tensile and compressive parts is required.

Regarding plates and shells a few recent works can be found. A first attempt of combining the phase-field method with Kirchhoff-Love shell formulations was conducted by Ulmer et al. (2012). There, the separation of the elastic strain energy density into its membrane and bending parts is proposed with a spectral decomposition of the membrane part. The membrane tensile part and the entire bending part is then degraded. This formulation, however, can lead to unphysical crack behavior in certain loading conditions, see Kiendl et al. (2016). Amiri et al. (2014) later proposed an isotropic model with a degradation of the full strain energy density by the phase-field. However, this formulation is going to lead to fracture in both tensile and compressive areas, which is unphysical. Kiendl et al. (2016) tried to overcome these defiances of the previous two approaches by using an anisotropic phase-field formulation, where the spectral decomposition is applied on the total strain energy, without any classification in the different strain terms. Regarding solid-shell formulations, Ambati and De Lorenzis (2016) used a phase-field model for the description of brittle and ductile fracture in shells with small rotations and displacements. Furthermore, Reinoso et al. (2017) used a phase-field model for brittle fracture in shells with large deformations in combination with a monolithic approach. Finally, Areias et al. (2016) applied independent phase-fields for the lower and for the upper face of the shell, in order to describe correctly bending-dominated problems. The effect of transverse shear deformations, using Reddy's third-order shear deformation theory and a hybrid phase-field fracture model, on the fracture process in thick plates was studied very recently in Raghu et al. (2020). Combining the phase-field fracture approach with a Reissner-Mindlin shell formulation has not been attempted so far.

In this work, a phase-field model of brittle fracture is developed for an isogeometric Reissner-Mindlin shell formulation based on Dornisch et al. (2013) and Kikis et al. (2019). Reissner-Mindlin shell formulations have the advantage that they are applicable for both thin and thick shells, since they take into account shear deformations.

The paper is organized as follows. In Section 5.3, the formulation of the isogeometric Reissner-Mindlin shell from Dornisch et al. (2013) and Kikis et al. (2019) is recalled in some detail. In Section 5.4, a 3D phase-field model is presented. In Section 5.5, existing phase-field models of brittle fracture for plate and shell formulations are recapitulated and the phase-field model to be used in this work is illustrated. In Section 5.6, the verification of the presented model is performed on the basis of various numerical examples. Finally, in Section 5.7, conclusions are drawn and future research directions are presented.

5.3 Reissner-Mindlin shell formulation

The Reissner-Mindlin theory is adopted for the present shell formulation. It is based on the isogeometric shell model proposed in Dornisch et al. (2013) and Kikis et al. (2019). A concise description of this theory is presented below.

5.3.1 Kinematics and basis systems

The shell is derived from continuum mechanics and degraded to its mid-surface. The thickness direction is then described using the so-called director vector, see Fig. 5.1. The director vector \mathbf{D} of the reference configuration coincides with the normal vector \mathbf{N} of the shell surface and has the length $|\mathbf{D}(\xi^\alpha)| = 1$. The current director vector \mathbf{d} can be updated by a difference vector formulation, since only linear problems are considered

$$\mathbf{d} = \mathbf{D} + \mathbf{b}. \quad (5.1)$$

The difference vector

$$\mathbf{b} = \boldsymbol{\omega} \times \mathbf{D} = \mathbf{W}^T \cdot \boldsymbol{\omega} \quad \text{with} \quad \mathbf{W} = \text{skew}(\mathbf{D}) \quad (5.2)$$

is defined as the vector cross product of the rotational parameter of the shell mid-surface $\boldsymbol{\omega}$ and the reference director vector. The inextensibility condition in thickness direction is fulfilled since small rotations are considered and thus $|\mathbf{d}| \simeq |\mathbf{D}| = 1$. In this sense, the displacement $\tilde{\mathbf{u}}$ of an arbitrary point on the shell can be described as follows

$$\tilde{\mathbf{u}}(\xi^i) = \mathbf{u}(\xi^\alpha) + \xi^3 \mathbf{d}(\xi^\alpha), \quad (5.3)$$

where $\mathbf{u}(\xi^\alpha)$ is the displacement vector on the mid-surface, ξ^a with $\alpha = 1, 2$ are the parametric coordinates and $-\frac{t}{2} \leq \xi^3 \leq \frac{t}{2}$ is the thickness coordinate. The current position vector $\mathbf{x}(\xi^\alpha)$ of an arbitrary point on the shell mid-surface is obtained, depending

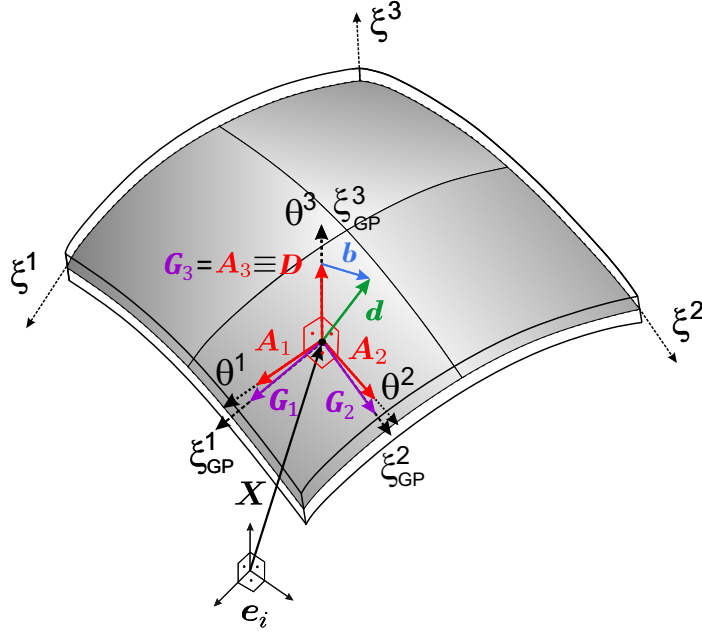


Figure 5.1: Basis systems and director vector at a Gauss point.

on the displacement vector $\mathbf{u}(\xi^\alpha)$, as

$$\mathbf{x}(\xi^\alpha) = \mathbf{X}(\xi^\alpha) + \mathbf{u}(\xi^\alpha), \quad (5.4)$$

where $\mathbf{X}(\xi^\alpha)$ is the position vector in the reference configuration.

In the given shell formulation, the definition of two different basis systems is necessary. The first one is the well known covariant basis system defined as

$$\mathbf{G}_\alpha = \mathbf{X}_{,\alpha} + \xi^3 \mathbf{D}_{,\alpha}, \quad \mathbf{G}_3 = \mathbf{D}, \quad (5.5)$$

with the corresponding contravariant basis vectors derived with the use of the Kronecker Delta, $\mathbf{G}_i \cdot \mathbf{G}^j = \delta_i^j$. However, in the constitutive relation an orthonormal basis system is necessary, so a second local basis system \mathbf{A}_i is defined with the corresponding local Cartesian coordinate system θ_i . It is computed at the Gauss points as close as possible to the convected basis system using the lamina coordinate system. In this sense, the displacement and position vectors in Eq. (5.3) and Eq. (5.4) are now defined with respect to θ_i . In addition to \mathbf{A}_i , the corresponding nodal Cartesian system \mathbf{A}_{iI} at the control points is needed for the interpolation of the rotational parameter ω^h

$$\omega^h = \sum_{I=1}^{n_{en}} \mathbf{T}_{3I} N_I \beta_I. \quad (5.6)$$

As it can be seen, the interpolation depends on the nodal rotations β_I and a nodal transformation matrix \mathbf{T}_{3I} , which includes the nodal Cartesian system \mathbf{A}_{iI} . In the

case of a smooth surface, the transformation matrix \mathbf{T}_{3I} consists only of two nodal basis vectors $\mathbf{A}_{\alpha I}$, thus, $\mathbf{T}_{3I} = [\mathbf{A}_{2I} \ \mathbf{A}_{1I}]$. The third nodal basis vector \mathbf{A}_{3I} can be neglected in order to avoid zero energy modes which occur due to drilling rotations. Dornisch et al. (2013) proposed a method where the nodal basis systems are defined so that their interpolated values at any point of the surface coincide as well as possible with the basis systems defined by the geometry.

The three unknown displacements u_i and the two unknown rotations β_i form the deformation vector

$$\mathbf{v} = \begin{bmatrix} \mathbf{u} \\ \boldsymbol{\beta} \end{bmatrix} = [u_1 \ u_2 \ u_3 \ \beta_1 \ \beta_2]^T. \quad (5.7)$$

Again, only two rotations are taken into account because only smooth surfaces are being considered. In other cases, i.e. for surfaces with kinks, the third rotation is indispensable.

5.3.2 Total strains

In the shell formulation, the linearized version of the Green-Lagrange strain tensor is used, since only linear problems are considered

$$\tilde{\boldsymbol{\varepsilon}} = \tilde{\varepsilon}_{ij} \mathbf{G}^i \otimes \mathbf{G}^j, \quad (5.8)$$

with the covariant components

$$\tilde{\varepsilon}_{ij} = \frac{1}{2}(\mathbf{G}_i \cdot \tilde{\mathbf{u}}_{,j} + \mathbf{G}_j \cdot \tilde{\mathbf{u}}_{,i}). \quad (5.9)$$

However, since the strains and stresses have to be expressed in a dual basis system, a transformation to the local Cartesian basis system \mathbf{A}_i is mandatory. The strains in Eq. (5.8) are now defined as

$$\boldsymbol{\varepsilon} = \varepsilon_{ij} \mathbf{A}^i \otimes \mathbf{A}^j, \quad (5.10)$$

with \mathbf{A}^i being the contravariant dual basis vectors defined as $\mathbf{A}^i = \mathbf{A}_i$. The components ε_{ij} can be split into the in-plane and transverse shear strains as follows

$$\varepsilon_{\alpha\beta} = \varepsilon_{\alpha\beta}^m + \theta^3 \kappa_{\alpha\beta} + (\theta^3)^2 \rho_{\alpha\beta} \quad (5.11)$$

$$2\varepsilon_{\alpha 3} = \gamma_{\alpha}, \quad (5.12)$$

where $\varepsilon_{\alpha\beta}^m$ denote the membrane strains

$$\varepsilon_{\alpha\beta}^m = \frac{1}{2}(\mathbf{X}_{,\alpha} \cdot \mathbf{u}_{,\beta} + \mathbf{X}_{,\beta} \cdot \mathbf{u}_{,\alpha}), \quad (5.13)$$

$\kappa_{\alpha\beta}$ represents the curvature of the shell

$$\kappa_{\alpha\beta} = \frac{1}{2}(\mathbf{X}_{,\alpha} \cdot \mathbf{b}_{,\beta} + \mathbf{X}_{,\beta} \cdot \mathbf{b}_{,\alpha} + \mathbf{D}_{,\alpha} \cdot \mathbf{u}_{,\beta} + \mathbf{D}_{,\beta} \cdot \mathbf{u}_{,\alpha}) \quad (5.14)$$

and γ_α are the shear strains

$$\gamma_\alpha = \mathbf{X}_{,\alpha} \cdot \mathbf{b} + \mathbf{u}_{,\alpha} \cdot \mathbf{D}. \quad (5.15)$$

The second-order curvatures

$$\rho_{\alpha\beta} = \frac{1}{2}(\mathbf{d}_{,\alpha} \cdot \mathbf{d}_{,\beta} - \mathbf{D}_{,\alpha} \cdot \mathbf{D}_{,\beta}) \quad (5.16)$$

are neglected since only moderate thick plates are considered within the Reissner-Mindlin theory. The derivatives $(\dots)_{,\alpha}$ and $(\dots)_{,\beta}$ are defined with respect to the coordinate system θ^i . They are computed by a transformation of the derivatives with respect to the convected basis system

$$(\dots)_{,\alpha} = J_{\alpha\beta}^{-1} \frac{\partial(\dots)}{\partial \xi^\beta} \quad (5.17)$$

with $J_{\alpha\beta} = \frac{\partial \theta^\beta}{\partial \xi^\alpha} = \mathbf{G}_\alpha \cdot \mathbf{A}_\beta$ being the components of the Jacobian matrix. The resulting linear shell strains can be rearranged in Voigt notation in the strain vector

$$\hat{\boldsymbol{\varepsilon}} = [\varepsilon_{11}^m \quad \varepsilon_{22}^m \quad 2\varepsilon_{12}^m \quad \kappa_{11} \quad \kappa_{22} \quad 2\kappa_{12} \quad \gamma_1 \quad \gamma_2]^T. \quad (5.18)$$

5.3.3 Strain energy density and stress resultants

The strain energy density of the shell formulation considering the plane stress condition ($\sigma_{33} = 0$) is given as follows

$$\psi_e = \frac{1}{2}\lambda \text{tr}^2(\boldsymbol{\varepsilon}) + \mu \text{tr}(\boldsymbol{\varepsilon}^2) - \frac{\lambda^2}{2(\lambda + 2\mu)} \text{tr}^2(\boldsymbol{\varepsilon}), \quad (5.19)$$

with λ and μ as the Lamé constants. An integration of the strain energy density over the thickness direction θ^3 gives the strain energy surface density Ψ_e , which describes the strain energy per unit area of the mid-surface

$$\Psi_e = \int_{-h/2}^{h/2} \psi_e(\theta^3) d\theta^3. \quad (5.20)$$

As long as ψ_e is defined by Eq. (5.19), depending on the linearized strain tensor $\boldsymbol{\varepsilon}$, the integral can be calculated analytically.

As the total strains were split into the membrane, bending and shear terms, the total strain energy per unit area of the mid-surface can be divided into the corresponding

three terms $\Psi_e = \Psi_e^m(\boldsymbol{\varepsilon}^m) + \Psi_e^b(\boldsymbol{\kappa}) + \Psi_e^t(\boldsymbol{\gamma}^t)$. They are defined through an analytical integration of the strain energy density ψ_e over the thickness and a subsequent split into the parts that depend on $\boldsymbol{\varepsilon}^m$, $\boldsymbol{\kappa}$ and $\boldsymbol{\gamma}^t$ as follows

$$\Psi_e^m(\boldsymbol{\varepsilon}^m) = h \left(\frac{1}{2} \lambda \text{tr}^2(\boldsymbol{\varepsilon}^m) + \mu \text{tr}((\boldsymbol{\varepsilon}^m)^2) - \frac{\lambda^2}{2(\lambda + 2\mu)} \text{tr}^2(\boldsymbol{\varepsilon}^m) \right) \quad (5.21)$$

$$\Psi_e^b(\boldsymbol{\kappa}) = \frac{h^3}{12} \left(\frac{1}{2} \lambda \text{tr}^2(\boldsymbol{\kappa}) + \mu \text{tr}(\boldsymbol{\kappa}^2) - \frac{\lambda^2}{2(\lambda + 2\mu)} \text{tr}^2(\boldsymbol{\kappa}) \right) \quad (5.22)$$

$$\Psi_e^t(\boldsymbol{\gamma}^t) = h\alpha_s\mu \text{tr}((\boldsymbol{\gamma}^t)^2), \quad (5.23)$$

where $\boldsymbol{\gamma}^t$ is computed as $\gamma_{\alpha\beta}^t = \delta_{\alpha\beta} \frac{\gamma_\alpha}{2}$ with $\delta_{\alpha\beta}$ as the Kronecker Delta.

The stress tensor of the shell is defined as the derivative of the strain energy density

$$\boldsymbol{\sigma} = \frac{\partial \psi_e(\boldsymbol{\varepsilon})}{\partial \boldsymbol{\varepsilon}} = \lambda \text{tr}(\boldsymbol{\varepsilon}) \mathbf{I} + 2\mu \boldsymbol{\varepsilon} - \frac{\lambda^2}{\lambda + 2\mu} \text{tr}(\boldsymbol{\varepsilon}) \mathbf{I}. \quad (5.24)$$

The corresponding stress resultants are defined through the integration of the stress tensor components over the thickness

$$n^{\alpha\beta} = \int_{-h/2}^{h/2} \sigma^{\alpha\beta} \mu_G d\theta^3 \quad (5.25)$$

$$m^{\alpha\beta} = \int_{-h/2}^{h/2} \sigma^{\alpha\beta} \mu_G \theta^3 d\theta^3 \quad (5.26)$$

$$q^\alpha = \int_{-h/2}^{h/2} \sigma^{\alpha 3} \mu_G d\theta^3, \quad (5.27)$$

where $n^{\alpha\beta}$ are the membrane forces, $m^{\alpha\beta}$ the bending moments and q^α the shear forces. The determinant of the shifter tensor μ_G is set to $\mu_G = 1$, since it is assumed that the basis vectors \mathbf{G}_i are constant over the thickness, see Dornisch et al. (2013). The integration over the thickness can still be computed analytically here and leads to the following definition of the stress resultants depending on their corresponding strains

$$\mathbf{n} = h \left(\lambda \text{tr}(\boldsymbol{\varepsilon}^m) \mathbf{I} + 2\mu \boldsymbol{\varepsilon}^m - \frac{\lambda^2}{\lambda + 2\mu} \text{tr}(\boldsymbol{\varepsilon}^m) \mathbf{I} \right) \quad (5.28)$$

$$\mathbf{m} = \frac{h^3}{12} \left(\lambda \text{tr}(\boldsymbol{\kappa}) \mathbf{I} + 2\mu \boldsymbol{\kappa} - \frac{\lambda^2}{\lambda + 2\mu} \text{tr}(\boldsymbol{\kappa}) \mathbf{I} \right) \quad (5.29)$$

$$\mathbf{q} = 2h\alpha_s\mu \boldsymbol{\gamma}^t. \quad (5.30)$$

Analogously to the strain vector $\hat{\boldsymbol{\varepsilon}}$, a stress tensor in Voigt notation is derived

$$\hat{\boldsymbol{\sigma}} = [n^{11} \quad n^{22} \quad n^{12} \quad m^{11} \quad m^{22} \quad m^{12} \quad q^1 \quad q^2]^T. \quad (5.31)$$

5.4 Phase-field model of brittle fracture

Griffith and Taylor (1921) described the propagation of cracks as the counteract of the structure's bulk energy and the surface energy. In other words, a crack will only grow if the released strain energy exceeds a critical value, necessary to form a new crack surface. A generalization of Griffith's theory of brittle fracture was proposed by Francfort and Marigo (1998) in the variational framework. Here, the free energy functional in a quasi-static case is given by

$$E(\boldsymbol{\varepsilon}, \Gamma) = \int_{\Omega} \psi_e(\boldsymbol{\varepsilon}) d\Omega + G_c \int_{\Gamma} d\Gamma, \quad (5.32)$$

where $\psi_e(\boldsymbol{\varepsilon})$ is the elastic strain energy density function, $\boldsymbol{\varepsilon}$ is the strain tensor, G_c is the material fracture toughness and Γ is the set of crack surfaces. In this way, crack initiation, propagation and branching is governed naturally by the minimization problem. However, since the displacement field becomes discontinuous when cracks appear, a numerical implementation of the model is not straightforward. In order to enable an adequate numerical implementation of the model, Bourdin et al. (2000, 2008) and Bourdin (2007) proposed a regularized version of variational formulation (5.32) as

$$E_{l_0}(\boldsymbol{\varepsilon}, s) = \int_{\Omega} (g(s)\psi_e(\boldsymbol{\varepsilon}) + \psi_s(s, \nabla s)) d\Omega, \quad (5.33)$$

where

$$\psi_s(s, \nabla s) = G_c \left(\frac{1}{4l_0} (1 - s)^2 + l_0 |\nabla s|^2 \right) \quad (5.34)$$

is the fracture energy density function.

The formulation depends now on a smoothly distributed field variable s , which takes values between 1 (for an undamaged material) and 0 (for a totally broken material). The regularization parameter $l_0 > 0$ has the dimension of a length and describes the transition zone between cracked and uncracked material. Bourdin et al. (2008) proved the Γ -convergence of the formulation, which means that when the length parameter l_0 tends to zero, the model Γ -converges to Griffith's theory of brittle fracture (Eq. (5.32)). The total elastic strain energy density function $\psi_e(\boldsymbol{\varepsilon})$ is reduced through the degradation function $g(s) > 0$, which couples the phase-field with the elastic field. The degradation function computed according to Miehe et al. (2010a) reads

$$g(s) = (1 - \eta)s^2 + \eta. \quad (5.35)$$

Here, the positive dimensionless parameter $\eta \ll 1$ represents a residual stiffness factor. It is chosen as small as possible in order to circumvent the full degradation of the

strain energy density and at the same time avoid ill-posedness at a fully broken state $s = 0$. This formulation, where the entire strain is degraded, is referred to as “isotropic model”. Since there is no distinction between the contributions from tension and compression in the model, cracks can occur in regions with compression, which leads to an unphysical behavior.

In order to overcome this problem and, in addition, to avoid crack interpenetration in compression, “anisotropic models” have been proposed. In these models, the elastic strain energy density is split into tensile and compressive parts in order to degrade only the parts that come from tension. The split can be achieved by separating the strain energy in a spherical and a deviatoric part and accounting for the sign of the volumetric strain, as it was done by Amor et al. (2009). The degradation function is then applied only to the strain energy part related to expansion and shear. In this work, the energy split based on a spectral decomposition of the strain tensor according to the work of Miehe et al. (2010b,a) is adopted. The spectral decomposition of the strain is given by

$$\boldsymbol{\varepsilon} = \sum_{i=1}^3 \varepsilon_i \mathbf{n}_i \otimes \mathbf{n}_i, \quad (5.36)$$

where $\{\varepsilon_i\}_{i=1,2,3}$ are the principal strains and $\{\mathbf{n}_i\}_{i=1,2,3}$ the principal strain directions. The positive and negative principal strain tensor components are then defined as

$$\boldsymbol{\varepsilon}^{\pm} = \sum_{i=1}^3 \langle \varepsilon_i \rangle^{\pm} \mathbf{n}_i \otimes \mathbf{n}_i, \quad (5.37)$$

where $\langle \varepsilon_i \rangle^{\pm} = (\varepsilon_i \pm |\varepsilon_i|)/2$. An additive decomposition of the strain tensor $\boldsymbol{\varepsilon} = \boldsymbol{\varepsilon}^+ + \boldsymbol{\varepsilon}^-$, and of the strain energy density function $\psi_e = \psi_e^+ + \psi_e^-$ in tensile and compressive parts is then performed.

The free energy functional based on the “anisotropic” model is then computed as follows

$$E_{l_0}(\boldsymbol{\varepsilon}, s) = \int_{\Omega} (g(s)\psi_e^+(\boldsymbol{\varepsilon}) + \psi_e^-(\boldsymbol{\varepsilon}) + \psi_s(s, \nabla s)) d\Omega. \quad (5.38)$$

The stress tensor is degraded in a similar fashion

$$\boldsymbol{\sigma}(\boldsymbol{\varepsilon}, s) = g(s) \frac{\partial \psi_e^+(\boldsymbol{\varepsilon})}{\partial \boldsymbol{\varepsilon}} + \frac{\partial \psi_e^-(\boldsymbol{\varepsilon})}{\partial \boldsymbol{\varepsilon}} = g(s) \boldsymbol{\sigma}^+(\boldsymbol{\varepsilon}) + \boldsymbol{\sigma}^-(\boldsymbol{\varepsilon}). \quad (5.39)$$

In the absence of volume loads, the minimization problem of the functional in Eq. (5.38) leads to the following Euler-Lagrange equations, which represent the strong form of the governing equations

$$\operatorname{div} \boldsymbol{\sigma} = \mathbf{0} \quad (5.40)$$

$$\left(\frac{4l_0(1-\eta)\psi_e^+}{G_c} + 1 \right) s - 4l_0^2 \Delta s = 1 \quad (5.41)$$

with the following Dirichlet and Neumann boundary conditions

$$\boldsymbol{v} = \bar{\boldsymbol{v}} \text{ on } \partial\mathcal{B}_0^{\bar{\boldsymbol{v}}} \quad (5.42)$$

$$\boldsymbol{\sigma} \cdot \boldsymbol{N} = \bar{\boldsymbol{t}} \text{ on } \partial\mathcal{B}_0^{\bar{\boldsymbol{t}}} \quad (5.43)$$

$$\nabla s \cdot \boldsymbol{N} = 0 \text{ on } \partial\mathcal{B}_0, \quad (5.44)$$

where $\partial\mathcal{B}_0$ the boundary of the body and $\partial\mathcal{B}_0^{\bar{\boldsymbol{v}}}$ and $\partial\mathcal{B}_0^{\bar{\boldsymbol{t}}}$ denote the boundary of the body with prescribed displacements $\bar{\boldsymbol{v}}$ and boundary tractions $\bar{\boldsymbol{t}}$, respectively.

The two coupled balance equations (5.40) and (5.41) include the quasi-static stress equilibrium and a gradient-type phase-field evolution equation. The first equation can be seen as the macroscopic equilibrium condition. The second, which defines the evolution of the phase-field can be seen as the microscopic balance. There exist two main approaches for the solution of the two balance equations, the monolithic and the staggered approach. In the monolithic approach the unknown displacement and crack phase-field are calculated simultaneously, which reduces the computational effort, see Gerasimov and De Lorenzis (2016). Here, however, a staggered approach is implemented where the two equations are algorithmically decoupled and solved alternately, see e.g. Miehe et al. (2010b) and Ambati et al. (2015b). In other words, at each load increment, the weak formulation of the first equation is solved in order to get the unknown variable \boldsymbol{v} while s is held constant. Next \boldsymbol{v} is held constant while the weak formulation of the phase-field evolution equation is solved. The procedure is repeated until convergence is reached. The advantage of the staggered scheme is that it has proven to be very robust.

In the second balance equation Eq. (5.41), ψ_e^+ can be replaced by a history value \mathcal{H} which represents the maximum positive elastic strain energy density that has been calculated up to the given pseudo time step in the loading process

$$\mathcal{H}(t) := \max_{\tau \in [0, t]} \psi_e^+(\tau). \quad (5.45)$$

In this way, the irreversibility condition of the crack during loading and unloading is enforced and an algorithmic decoupling of the system of equations is enabled, see the work of Miehe et al. (2010a).

5.5 Phase-field fracture models combined with plate and shell formulations

5.5.1 Existing approaches

Phase-field models of fracture were applied to the special cases of plates and shells only in a few investigations thus far. Here, a brief recapitulation of the existing ap-

proaches is presented. In connection with Kirchhoff-Love shell formulations, the first two approaches can be found in the works of Amiri et al. (2014) and Ulmer et al. (2012). Amiri et al. (2014) proposed to degrade the full strain energy density by the phase-field just as it is done in the isotropic model, see Section 5.4. Thus, the free energy functional is written analogously to Eq. (5.33) in the following way

$$E_{l_0}(\boldsymbol{\varepsilon}^m, \boldsymbol{\kappa}, s) = \int_A (g(s) \Psi_e(\boldsymbol{\varepsilon}^m, \boldsymbol{\kappa}) + \Psi_s(s, \nabla s)) dA, \quad (5.46)$$

where A is now the mid-surface while the integration through the thickness is included in Ψ_e and Ψ_s . However, as it was mentioned before, this kind of formulation leads to cracks in regions where there is only compression, something that is unphysical.

On the other hand, Ulmer et al. (2012) proposed to separate the elastic strain energy density into its membrane and bending parts, as it was shown in Eq. (5.21) and Eq. (5.22). The membrane part is split again into its tensile and compressive contributions by a spectral decomposition of $\boldsymbol{\varepsilon}^m$, whereby only the tensile term is degraded in the free energy functional. The bending part is not split and it is degraded entirely by the phase-field. The corresponding free energy functional reads

$$E_{l_0}(\boldsymbol{\varepsilon}^m, \boldsymbol{\kappa}, s) = \int_A (g(s) (\Psi_e^{m+}(\boldsymbol{\varepsilon}^m) + \Psi_e^b(\boldsymbol{\kappa})) + \Psi_e^{m-}(\boldsymbol{\varepsilon}^m) + \Psi_s(s, \nabla s)) dA. \quad (5.47)$$

The problem with this formulation, as it was pointed out in Kiendl et al. (2016), is that it does not consider the dependency of the total strain on a combination of both membrane and bending strains. This means that if, for instance, bending and compression is applied in a way that the total strain is compressive everywhere, the model would still lead to fracture. Furthermore, since the model does not consider a split of the bending energy into tensile and compressive parts, it would behave, in the case of pure bending, basically in the same way as an isotropic model, potentially leading to an unphysical behavior.

Kiendl et al. (2016) solved the issues of the previous approaches by using a phase-field formulation where the spectral decomposition is applied to the total strain energy, as it is done in the anisotropic formulation, without considering a classification into the different strain terms. In other words, crack propagation is driven by the tensile part of the strain energy surface density which depends on both the membrane and bending strains

$$E_{l_0}(\boldsymbol{\varepsilon}^m, \boldsymbol{\kappa}, s) = \int_A (g(s) \Psi_e^+(\boldsymbol{\varepsilon}^m, \boldsymbol{\kappa}) + \Psi_e^-(\boldsymbol{\varepsilon}^m, \boldsymbol{\kappa}) + \Psi_s(s, \nabla s)) dA. \quad (5.48)$$

On the other hand, Areias et al. (2016) applied two independent phase-fields, one for the lower and one for the upper face of the shell in order to properly describe bending-dominated problems.

To the best of the author's knowledge, a combination of an isogeometric degenerated Reissner-Mindlin shell formulation with the phase-field model of fracture has not been attempted yet. In the following we present such a combination for the case of brittle fracture. As a starting point, the formulation of Kiendl et al. (2016), which has been used very successfully for the description of brittle fracture in Kirchhoff-Love shells, is adopted and extended to the isogeometric Reissner-Mindlin shell formulation from Dornisch et al. (2013) and Kikis et al. (2019).

5.5.2 Phase-field model of brittle fracture for the Reissner-Mindlin shell formulation

The goal here is to implement the anisotropic phase-field model of brittle fracture with a spectral decomposition of the strain tensor from Section 5.4 to the isogeometric Reissner-Mindlin shell formulation presented in Section 5.3. In order to achieve this, the approach proposed in Kiendl et al. (2016) is now extended to the case of the Reissner-Mindlin shell formulation. First, since only the mid-surface of the shell is considered the strain energy functional defined in Eq. (5.38) can be rewritten in the following way

$$E_{l_0}(\boldsymbol{\varepsilon}, s) = \int_A (g(s) \Psi_e^+(\boldsymbol{\varepsilon}) + \Psi_e^-(\boldsymbol{\varepsilon}) + \Psi_s(s, \nabla s)) dA, \quad (5.49)$$

where $\Psi_e^\pm(\boldsymbol{\varepsilon})$ are the positive and negative parts of the strain energy surface density, defined as

$$\Psi_e^\pm = \int_{-h/2}^{h/2} \psi_e^\pm(\theta^3) d\theta^3. \quad (5.50)$$

In contrast to the definition given in Eq. (5.20), here the integral cannot be determined analytically anymore. It has to be performed numerically at the integration points through the thickness. The phase-field variable s is defined only on the mid-surface of the shell, see Fig. 5.2. The split of the strain energy density into tensile and compressive contributions reads

$$\psi_e^\pm(\theta^3) = \frac{1}{2} \lambda (\langle \text{tr}(\boldsymbol{\varepsilon}(\theta^3)) \rangle^\pm)^2 + \mu \text{tr} \left(\left((\boldsymbol{\varepsilon}(\theta^3))^\pm \right)^2 \right). \quad (5.51)$$

The split is applied to the total strain tensor and not separately to the membrane, bending and shear terms of Eq. (5.21-5.23). In the same sense, the tensile and compressive terms of the stress tensor are defined as

$$\boldsymbol{\sigma}^\pm(\theta^3) = \lambda \langle \text{tr}(\boldsymbol{\varepsilon}) \rangle^\pm \mathbf{I} + 2 \mu \boldsymbol{\varepsilon}^\pm, \quad (5.52)$$

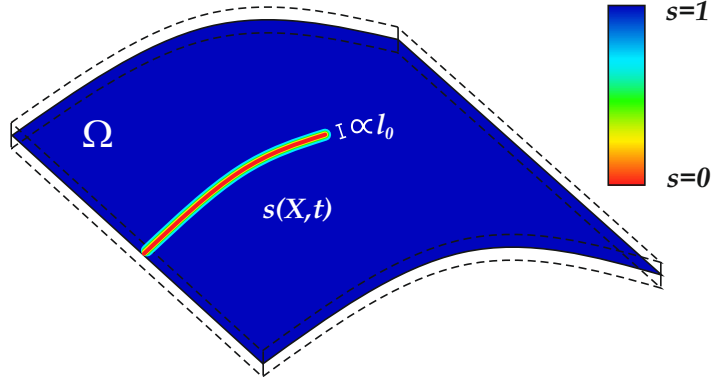


Figure 5.2: Phase-field for a degenerated Reissner-Mindlin shell formulation.

where \mathbf{I} is the identity tensor with respect to the local Cartesian space. It is important to note that these definitions Eq. (5.51-5.52) as well as the material tangent tensors $\mathbb{C}(\boldsymbol{\varepsilon}, s) = \frac{\partial \boldsymbol{\sigma}(\boldsymbol{\varepsilon}, s)}{\partial \boldsymbol{\varepsilon}}$ have to be modified for the shell model in order to enforce the plane stress condition, which is usually considered in dimensionally reduced structural models. In the presented Reissner-Mindlin shell formulation, it is assumed that the transverse normal strain ε_{33} is zero due to the inextensibility condition. In addition, the normal stresses σ_{33} have to be zero in order to avoid artificial stiffening effects due to an unbalance of ε_{33} and σ_{33} for non-zero Poisson's ratios. This condition is usually referred to as the plane stress condition, even though $\sigma^{i3} \neq 0$. It should be noted here that the plane stress condition is a classical assumption for thin shells since in this case the dominating quantities are the in plane and the transverse shear stresses. The thickness direction insignificantly contributes to the load transfer. Thus, effects where the normal stresses σ_{33} play a crucial role, for instance in Reinoso et al. (2016), where wrinkling and buckling-induced delamination in thermal barrier coatings is examined, are excluded here. Normally, the plane stress condition could be fulfilled easily by removing ε_{33} and σ_{33} from the constitutive law by static condensation and having in the end only five strain and stress components. However, in this case ε_{33} is needed for the spectral decomposition of the strain tensor $\boldsymbol{\varepsilon}$. To be more specific, in order to perform the spectral decomposition of the total strain tensor in Eq. (5.36), first, the eigenvalue problem

$$(\boldsymbol{\varepsilon} - \varepsilon_i \cdot \mathbf{I}) \cdot \mathbf{n}_i = 0 \quad (5.53)$$

is solved at each integration point through the thickness, with $\boldsymbol{\varepsilon}$ being the total strain tensor with respect to the local Cartesian system, see Eq. (5.10). Its components $\varepsilon_{\alpha\beta}$, $\varepsilon_{\alpha 3}$ are defined in Eq. (5.11) and Eq. (5.12) respectively and for the computation of ε_{33} the plane stress condition has to be enforced numerically. Here, a local algorithm with quadratic convergence based on the work of Klinkel and Govindjee (2002), as

well as on the work of Ambati et al. (2018), is used in order to fulfill the zero stress condition at each integration point. Namely, an additional Newton-Raphson iteration is applied inside the thickness integration loop in order to define the normal strain ε_{33} for which the normal stress is zero, see Appendix A. For each thickness integration point a spectral decomposition of the total strain (including normal strain) is applied and the following condition is enforced

$$\sigma_{i+1}^{33} = \sigma_i^{33} + \frac{\partial \sigma_i^{33}}{\partial \varepsilon_{33}^i} (\varepsilon_{33}^{i+1} - \varepsilon_{33}^i) \stackrel{!}{=} 0. \quad (5.54)$$

Thus, the newly calculated strain is defined as

$$\varepsilon_{33}^{i+1} = \varepsilon_{33}^i - (\mathbb{C}_i^{3333})^{-1} \sigma_i^{33} \quad (5.55)$$

until the stress σ_i^{33} obtains a value which is smaller than a given tolerance. In addition, the material tangent modulus is required for the global Newton-Raphson iteration. The incremental vector representation of the 3D constitutive law reads

$$\begin{pmatrix} d\sigma^{\alpha k} \\ d\sigma^{33} \end{pmatrix} = \begin{pmatrix} \mathbb{C}^{\alpha k \gamma l} & \mathbb{C}^{\alpha k 33} \\ \mathbb{C}^{33 \gamma l} & \mathbb{C}^{33 33} \end{pmatrix} \begin{pmatrix} d\varepsilon_{\gamma l} \\ d\varepsilon_{33} \end{pmatrix}. \quad (5.56)$$

The material tangent is condensed with $d\sigma^{33} = 0$ in order to obtain the tangent modulus for the global Newton-Raphson scheme, which fulfills the plane stress condition. Inserting the second equation of (5.56) in the first one leads to the following tangent modulus of the element formulation

$$d\sigma^{\alpha k} = \hat{\mathbb{C}}^{\alpha k \gamma l} d\varepsilon_{\gamma l} \quad \text{with} \quad \hat{\mathbb{C}}^{\alpha k \gamma l} = \mathbb{C}^{\alpha k \gamma l} - \mathbb{C}^{\alpha k 33} (\mathbb{C}^{33 33})^{-1} \mathbb{C}^{33 \gamma l}. \quad (5.57)$$

The stress resultants are then computed according to Eq. (5.25-5.27) as follows

$$\mathbf{n}(\varepsilon^m, \boldsymbol{\kappa}, s) = \int_{-h/2}^{h/2} (g(s) \boldsymbol{\sigma}^+(\varepsilon^m, \boldsymbol{\kappa}) + \boldsymbol{\sigma}^-(\varepsilon^m, \boldsymbol{\kappa})) d\theta^3 \quad (5.58)$$

$$\mathbf{m}(\varepsilon^m, \boldsymbol{\kappa}, s) = \int_{-h/2}^{h/2} (g(s) \boldsymbol{\sigma}^+(\varepsilon^m, \boldsymbol{\kappa}) + \boldsymbol{\sigma}^-(\varepsilon^m, \boldsymbol{\kappa})) \theta^3 d\theta^3 \quad (5.59)$$

$$\mathbf{q}(\boldsymbol{\gamma}^t, s) = \int_{-h/2}^{h/2} (g(s) \boldsymbol{\sigma}^+(\boldsymbol{\gamma}^t) + \boldsymbol{\sigma}^-(\boldsymbol{\gamma}^t)) d\theta^3. \quad (5.60)$$

In contrast to Section 5.3, the integration over the thickness for Eq. (5.50) and Eq. (5.58-5.60) cannot be computed analytically here, due to the spectral decomposition of the strain tensor ε . Instead, a numerical integration is necessary. For each thickness integration point a spectral decomposition of the total strain is applied and the corresponding stress tensor $\boldsymbol{\sigma}^\pm$ and the strain energy density Ψ_e^\pm are computed. In

this way, the proposed approach, where fracture is described using a single phase field which is constant over the thickness, leads to a nonlinear distribution of σ and Ψ_e over the thickness, see Kiendl et al. (2016).

The strong form of the two balance equations, see Eq. (5.40) and Eq. (5.41), is used as the basis to formulate the weak form by integration and multiplication with appropriate test functions. In the end, the following two minimization subproblems result

$$\int_A \mathbf{n} : \delta \boldsymbol{\varepsilon}^m + \mathbf{m} : \delta \boldsymbol{\kappa} + \mathbf{q} : \delta \boldsymbol{\gamma}^t dA - \int_A \delta \mathbf{v}^T \bar{\mathbf{p}}_0 dA - \int_{\Gamma_0^N} \delta \mathbf{v}^T \bar{\mathbf{t}}_0 ds = 0 \quad (5.61)$$

$$\int_A \left(\frac{4 l_0 (1 - \eta) \mathcal{H}}{h G_c} + 1 \right) s \delta s dA + 4 l_0^2 \int_A \nabla s \cdot \nabla \delta s dA = \int_A \delta s dA, \quad (5.62)$$

where $\bar{\mathbf{p}}_0$ are the surface loads and $\bar{\mathbf{t}}_0$ the boundary tractions. The variation of the shell strains is defined as

$$\delta \boldsymbol{\varepsilon}_{\alpha\beta}^m = \frac{1}{2} (\mathbf{X}_{,\alpha} \cdot \delta \mathbf{u}_{,\beta} + \mathbf{X}_{,\beta} \cdot \delta \mathbf{u}_{,\alpha}) \quad (5.63)$$

$$\delta \boldsymbol{\kappa}_{\alpha\beta} = \frac{1}{2} (\mathbf{X}_{,\alpha} \cdot \delta \mathbf{b}_{,\beta} + \mathbf{X}_{,\beta} \cdot \delta \mathbf{b}_{,\alpha} + \mathbf{D}_{,\alpha} \cdot \delta \mathbf{u}_{,\beta} + \mathbf{D}_{,\beta} \cdot \delta \mathbf{u}_{,\alpha}) \quad (5.64)$$

$$\delta \boldsymbol{\gamma}_\alpha = \mathbf{X}_{,\alpha} \cdot \delta \mathbf{b} + \delta \mathbf{u}_{,\alpha} \cdot \mathbf{D}. \quad (5.65)$$

The variables of the shell formulation as well as the phase-field variable s are discretized using NURBS shape functions, see Piegl and Tiller (1997) and Cottrell et al. (2009). A detailed NURBS-based isogeometric shell discretization and implementation can be found in Dornisch et al. (2013) and Kikis et al. (2019). As it was mentioned in Section 5.4 a staggered approach is used for the solution of the two weak governing equations. Due to the split of the total strain tensor, the first equation is non-linear and the Newton-Raphson scheme has to be applied. On the other hand, the equation of evolution of the phase-field is linear.

5.6 Numerical examples

In this section, the proposed phase-field model applied to the isogeometric Reissner-Mindlin shell is tested and a comparison to existing models is performed. Namely, a Kirchhoff-Love shell and a solid are additionally examined and the differences between the shell types are investigated. The elements that are used in the examples are summarized here with their corresponding abbreviations

- **Solid** The standard 3D solid element with one element in thickness direction and three integration points through the thickness, which uses an anisotropic model for the description of fracture processes.

- **KL shell** The isogeometric Kirchhoff-Love shell formulation proposed in Kiendl et al. (2016), which applies the spectral decomposition on the total strain and uses then an anisotropic model of brittle fracture. In order to stay consistent with the Solid formulation, 3 integration points are taken in the thickness direction.
- **RM shell** The proposed approach for the isogeometric Reissner-Mindlin shell formulation from Dornisch et al. (2013) and Kikis et al. (2019). The spectral decomposition is applied to the total strain energy which includes the membrane, bending and shear parts. As in Solid and KL shell, three integration points are considered to perform numerical thickness integration.

In Reissner-Mindlin shell formulations, an issue that arises is locking. It leads to an artificial stiffening of the system, an underestimation of the deformations and oscillations in the stress resultants. This phenomenon is intensified with a decreasing shell thickness, i.e. at the Kirchhoff limit. In the context of isogeometric analysis, different methods were proposed to alleviate these undesirable effects, such as using adjusted approximation spaces for the displacements and rotations, increasing the order of the shape functions, using non-uniform integration or the Assumed Natural Strain (ANS) method to mention a few, see also Kikis et al. (2019). The two main locking effects that occur in the present Reissner-Mindlin shell formulation are the transverse shear locking (for the plates and shell examples) and the membrane locking (only for the shell example). However, since polynomial degree $p = 2$ is used, locking is already reduced compared to linear Lagrange shape functions. Furthermore, due to the required high refinement in the fracture area, a huge number of elements is used, which additionally reduces the transverse shear locking. In the end, comparing in the following examples the linear part before crack initiation, where locking should already occur, no significant differences are visible for the different shell types. This means that no severe locking occurs and the different formulations converge to the same solution. Therefore, in the following examples, locking effects are not investigated in any more detail. However, locking is not entirely eliminated and the implementation of a method that fully removes locking would be an interesting topic for future work.

As it was shown in Fig. 5.2, in the contour plots of the crack phase-field, blue denotes an intact material ($s = 1$) and red a fully cracked material ($s = 0$).

5.6.1 Beam with transverse loading and different boundary conditions

The first example consists of a rectangular plate which has no initial crack. Different boundary conditions are chosen, i.e. in the first case the beam is clamped at one edge

and in the second case it is simply supported at both edges, see Fig. 5.3 and Fig. 5.6 respectively. It is subjected in both cases to a uniformly distributed transverse loading. The material parameters are given as follows: $E = 10 \times 10^9 \text{ N/mm}^2$, $\nu = 0$, $G_c = 3 \text{ N/mm}$ and $l_0 = 0.01 \text{ mm}$. The plate has a length $L = 10 \text{ mm}$ and a width $W = 2 \text{ mm}$, while different thicknesses are considered in order to investigate the influence of transverse shear on the fracture behavior. The KL shell and the RM shell described at the beginning of Section 5.6 are compared for this purpose. For the calculations, the plate is divided into a total of 7701 elements for the clamped version and 7225 elements for the simply supported version, with a local refinement at the clamped edge or at the middle of the plate where the crack is expected to form, in order to fulfill the requirement of $h/l_0 = 1/10$. Arc-length control is adopted for the simulation until failure occurs.

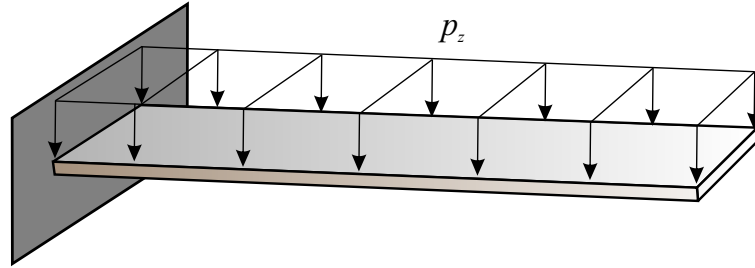


Figure 5.3: Clamped beam with transverse loading.



Figure 5.4: Crack phase-field at final fracture stage.

Due to the plate's length to width ratio and since $\nu = 0$, the problem could also be seen as a beam problem. When considering Bernoulli beams, which basically correspond to the Kirchhoff-Love theory, the results are reasonable up to a thickness to length ratio of $\frac{1}{10}$. For higher values, the transverse shear has a greater influence and the use of the Timoshenko theory, which corresponds here to the Reissner-Mindlin theory, is preferable. In the first case of the clamped beam this behavior is visible in the load-displacement curves in Fig. 5.5. The focus here lies on the norm of the total displacement vector, which is given as $U_{\text{norm}} = \sqrt{\frac{\hat{\mathbf{u}}^T \hat{\mathbf{u}}}{n_{\text{cp}}}}$ where $\hat{\mathbf{u}}$ is the vector of the control point displacements and n_{cp} is the total number of control points. For a

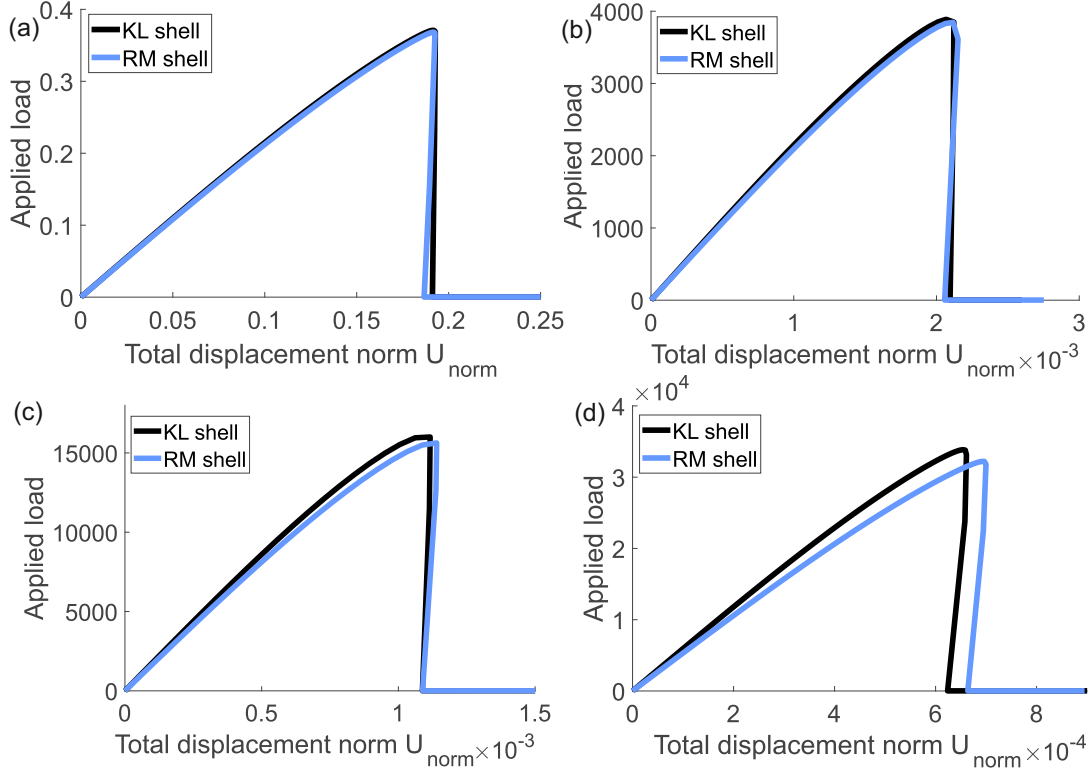


Figure 5.5: Load-displacement curves for the clamped beam with a thickness of (a) $t = 0.01$, (b) $t = 1$, (c) $t = 2$, (d) $t = 3$.

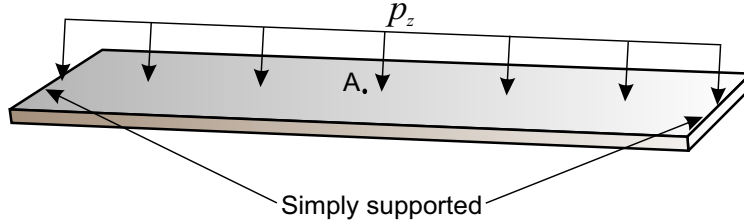


Figure 5.6: Simply supported beam with transverse loading.

thickness to length ratio smaller than or equal to $\frac{1}{10}$ the load-displacement curves of the KL shell and the RM shell are almost identical, see Fig. 5.5(a) and Fig. 5.5(b). As soon as the thickness increases, deviations regarding the maximum applied load and the total displacement are visible, see Fig. 5.5(c) and Fig. 5.5(d). This effect intensifies for thicker beams, leading to very clear differences in Fig. 5.5(d). The deformations for the RM shell are higher due to the consideration of the additional transverse shear deformations. On the other hand, the maximum applied load before failure of the RM shell is lower due to the shear terms considered in the phase-field formulation. A snap-back behavior is visible for both the KL shell and the RM shell. This could be

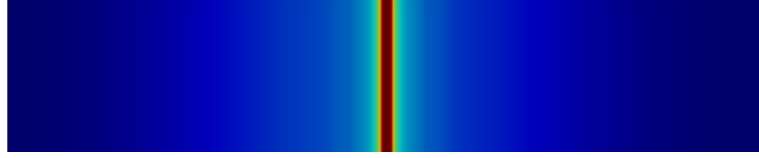


Figure 5.7: Crack phase-field of simply supported beam at final fracture stage.

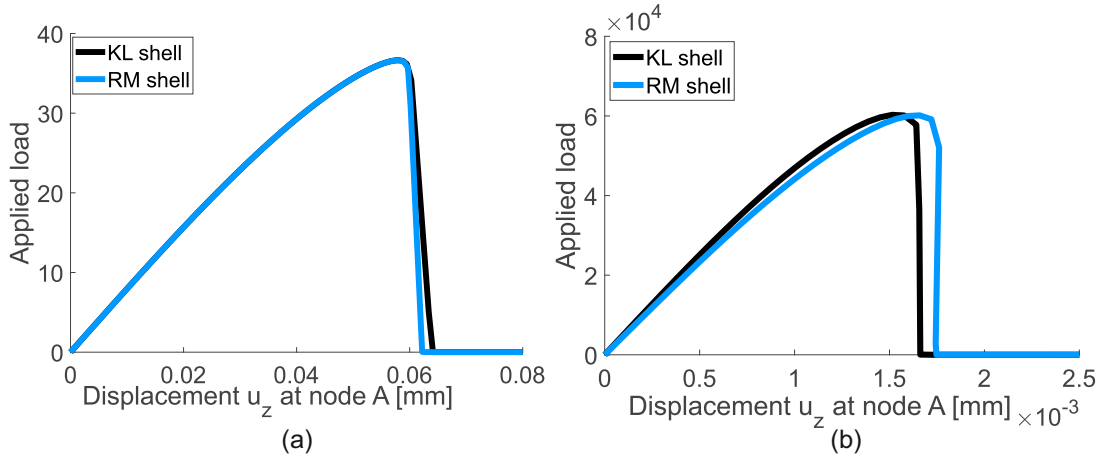


Figure 5.8: Load-displacement curves for the simply supported beam with a thickness of (a) $t = 0.05$, (b) $t = 2$.

explained as follows: in the beginning, the beam's curvature is increasing since it is clamped on one side and subjected to the uniformly distributed load. However, as soon as the crack forms at the clamped edge, it has no moment anymore and the curvature of the beam decreases again. Since in the load-displacement distribution the total displacement norm U_{norm} is considered, i.e. the displacements of all points of the beam, a reduction of the deformation in total after crack initiation is reasonable. The crack phase-field shows a similar pattern for both element types and is illustrated for the final fracture stage in Fig. 5.4. In the case of the simply supported beam a similar behavior is observed, i.e. for thin plates the KL shell and the RM shell have almost identical results while for thicker shells differences are observed especially regarding the displacement since the KL shell does not consider the transverse shear deformations, see Fig. 5.8(a-b). Here the focus lied on the vertical displacement u_z at point A in Fig. 5.6. The crack phase-field for the final fracture stage is given in Fig. 5.7.

5.6.2 Square plate with changing surface load

In the following, a square plate without initial cracks that is simply supported along its boundary is examined. The plate is subjected to a pressure loading which is ap-

plied on an area of $a \times a$, see Fig. 5.9. The material parameters are given as follows: $E = 190 \times 10^3 \text{ N/mm}^2$, $\nu = 0.29$, $G_c = 0.295 \text{ N/mm}$ and $l_0 = 0.02 \text{ mm}$. This example is known from literature, e.g. Areias et al. (2011) and Kiendl et al. (2016) for the case of $a = L$, i.e. when the load is applied to the whole plate. Here, however, different values for a , i.e. $a \in \{L, \frac{L}{2}, \frac{L}{4}, \frac{L}{6}, \frac{L}{8}, \frac{L}{10}\}$ are considered in order to demonstrate the influence of the shear terms on the fracture procedure. Namely, when $a < L$ a jump in the transverse load occurs and the shear forces are going to be high close to this discontinuity boundary. This phenomenon should influence the results of the RM shell and the Solid which consider shear deformations in contrast to the KL shell. The thickness of the plate is chosen to $t = 0.02 \text{ mm}$ in order to allow a reasonable comparison to the KL shell element. Due to symmetry only one quarter of the plate is considered for the calculations and discretized uniformly with a number of 7225 elements, i.e. $\frac{h}{l_0} = 0.6$. The simulation is performed using arc-length control.

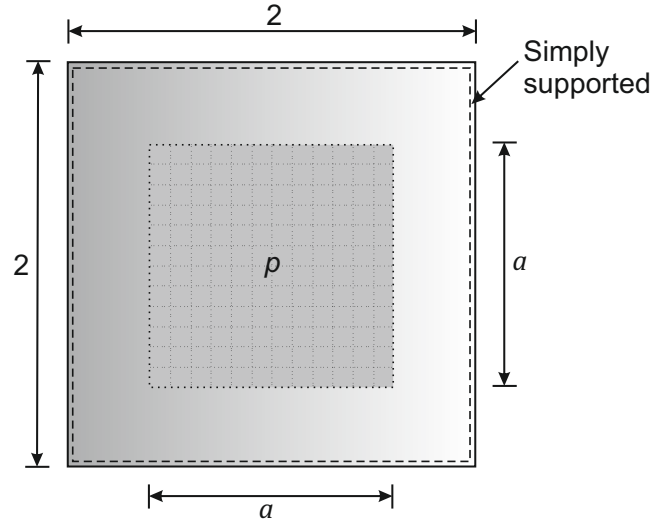


Figure 5.9: Simply supported plate subjected to transverse loading with changing area.

In the case of $a = L$, the expected crack path, according to Areias et al. (2011) and Kiendl et al. (2016), starts with four cracks at the center of the plate which propagate towards its corners. As soon as the cracks reach the boundary, the plate is divided into four separate triangular plates and complete failure occurs. The crack path for the other load cases is the same, however the crack is propagating slower the smaller a is. This is expected, since, for decreasing a , the maximum bending moments and shear forces become more concentrated close to the center of the plate. So, the crack initiation is going to occur fast in the middle of the plate, however, as the crack propagates along the diagonals the internal forces reduce significantly and the propagation is going to slow down. In Fig. 5.10(a) and Fig. 5.10(b) the crack phase-field is depicted at different

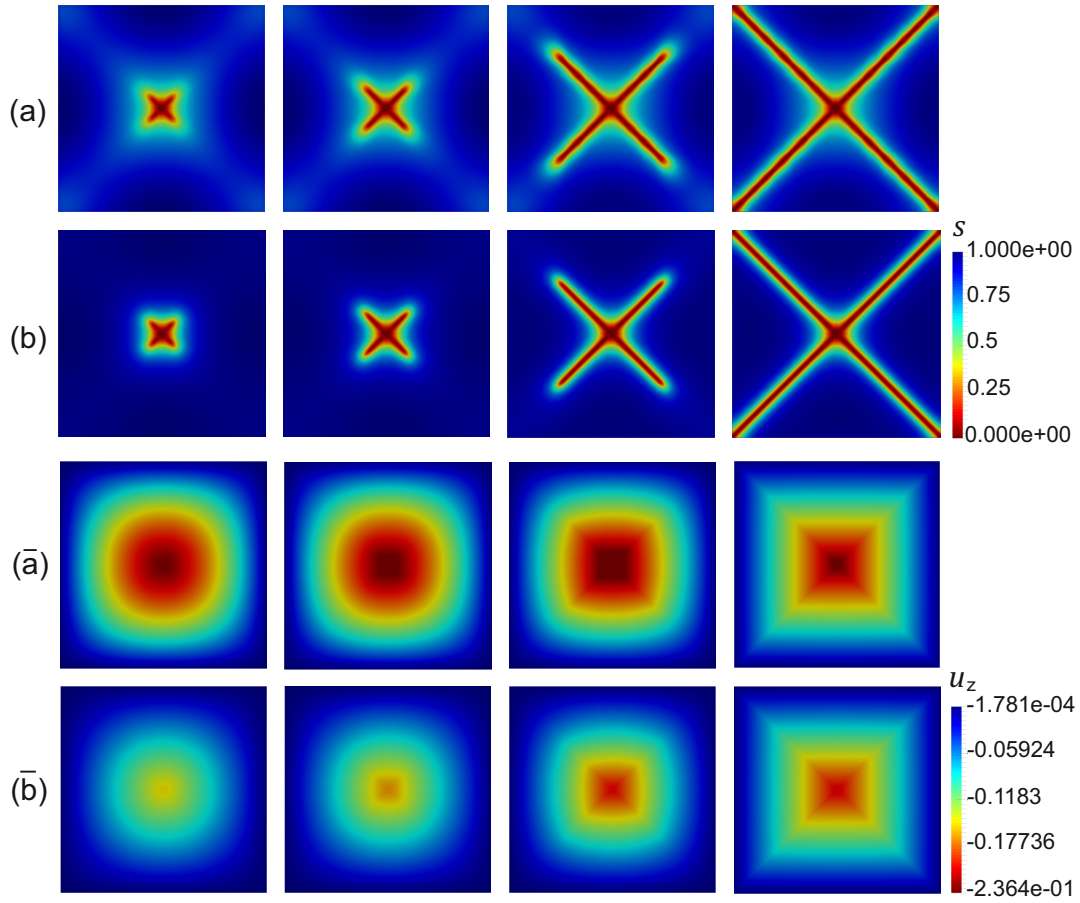


Figure 5.10: Simply supported plate. Crack phase-field and deflection at various fracture stages for a transverse load with (a),(ā) $a = L$ and (b),(b̄) $a = \frac{L}{10}$, respectively.

fracture stages for a transverse load with $a = L$ and $a = \frac{L}{10}$, respectively. In the case of $a = L$ it is visible that even at the first stage, when the crack is initiated at the center, the rest of the plate has already weakened along its diagonals, since there the value of s is less than 1. So, the crack has already a given path to follow where the stiffness of the structure is lowered. On the other hand, for the case of $a = \frac{L}{10}$ the damage is limited close to the cracks and the rest of the plate is more or less undamaged. In Fig. 5.10(ā) and Fig. 5.10(b̄) the contour plot of the deflection is depicted for the same fracture stages and with $a = L$ and $a = \frac{L}{10}$, respectively. The same scale was used for both cases in order to emphasize the differences in the values of the deflection. At the first stage, where the crack is very small at the center and the curvature of the plate is still more or less smooth, the deflection has the characteristic contour plot as it is known from the uncracked plate. The stiffness of the structure decreases as the crack propagates which leads to higher deformations. At the last stage, the crack has fully propagated and the kinks in the plate are visible in the contour plot of the deflection.

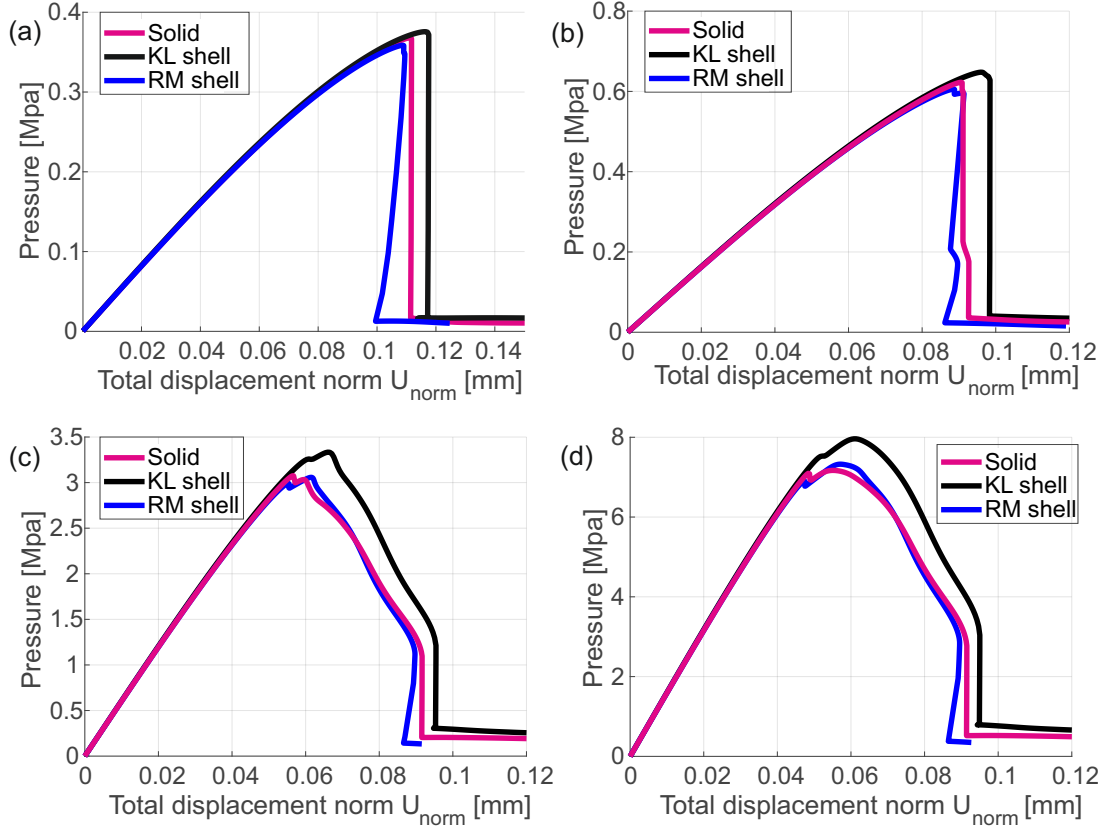


Figure 5.11: Simply supported plate. Load-displacement curves for a transverse load with (a) $a = L$, (b) $a = L/2$, (c) $a = L/6$, (d) $a = L/10$.

In Fig. 5.11 the pressure-total displacement norm curves are exemplarily given for the cases of $a \in \{L, \frac{L}{2}, \frac{L}{6}, \frac{L}{10}\}$. The observations made above are visible in the load-displacement curves, especially the delay in the propagation of the cracks. For the cases where $a < L$, the crack forms at the center (first kink in the curve), slowly grows uniformly around the center (no further significant reduction of the stiffness, the curve continues) before starting propagating along the diagonals (stiffness reduces again, second kink). The curves of the RM shell and the Solid show very good agreement, especially for the cases where $a < L$. On the other hand, the KL shell is always overestimating the maximum applicable load before crack initiation. This is reasonable since strong shearing occurs at the load boundaries, however, the KL shell does not consider shear terms in the phase-field formulation. Another interesting observation regarding the RM shell is a slight snap back behavior, i.e. a more brittle behavior, which is not occurring in the other two element types. The reason for this could be the choice of the load increment for the arc-length control. Here, it has the same value for all three element types for reasons of consistency, however, it depends on the degrees

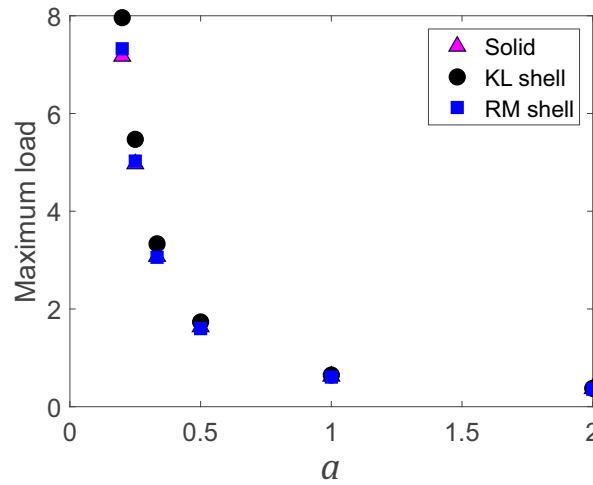


Figure 5.12: Simply supported plate. Maximum load for (a) $a = L$, (b) $a = L/2$, (c) $a = L/6$, (d) $a = L/10$.

of freedom and since the RM shell has two additional degrees of freedom, namely the two rotations, it should be modified. Another reason could be that all three element types have a snap back behavior, which is however only visible for the RM shell due to the chosen parameters. In Fig. 5.12, the maximum applicable pressure is depicted for the six different load cases. An almost exponential increase in the limit load with decreasing a can be observed for all element types. However, it is also visible that although the limit loads of the RM shell and the Solid are almost equal for all cases, the difference to the KL shell grows gradually with decreasing a due to the absence of the shear deformations.

5.6.3 Annular plate

In this example an annular plate which is simply supported at the inner and the outer edges is considered, see e.g. Ambati and De Lorenzis (2016) and Kiendl et al. (2016). The plate is subjected to a uniformly distributed transverse load and is firstly examined as initially uncracked and later with four small initial circumferential cracks, see Fig. 5.13(a) and Fig. 5.13(b), respectively. In the latter case the ability of the phase-field formulation to correctly describe crack interaction and merging is investigated. The material parameters read: $E = 10.92 \times 10^7 \text{ N/mm}^2$, $G_c = 3 \text{ N/mm}$ and $l_0 = 0.01 \text{ mm}$, $\nu = 0$ and the plate has a thickness of $t = 0.01 \text{ mm}$. Due to symmetry, the calculation is performed only on one quarter of the geometry. The plate is discretized with 8670 elements for the initially uncracked case and with 7395 elements for the case with initial cracks. In the expected crack propagation region an additional

local mesh refinement is applied for both cases with $h/l_0 = 1/10$. The simulation is performed using arc-length control.

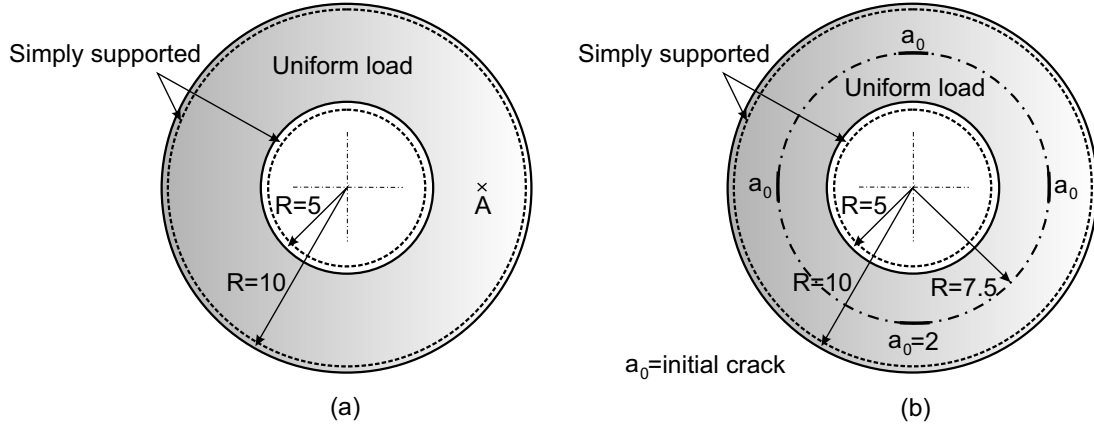


Figure 5.13: Annular plate. Geometry and boundary conditions, (a) without initial cracks and (b) with initial cracks.

In the case of the initially uncracked plate, a circumferential crack develops close to the middle of the annulus, see Fig. 5.15(a) for the RM shell and the Solid. In Fig. 5.15(b) the crack phase-field is depicted for the deformed state, where it can be seen that for the Solid the plate is totally cracked along the thickness direction. A slight loss of symmetry for the RM shell could result from the use of the rotations as additional degrees of freedom at each interpolation point. The load-displacement curves for both cases are depicted in Fig. 5.14. The load-displacement curves of the three different element types are compared for the initially uncracked plate in Fig. 5.14(a). A slight

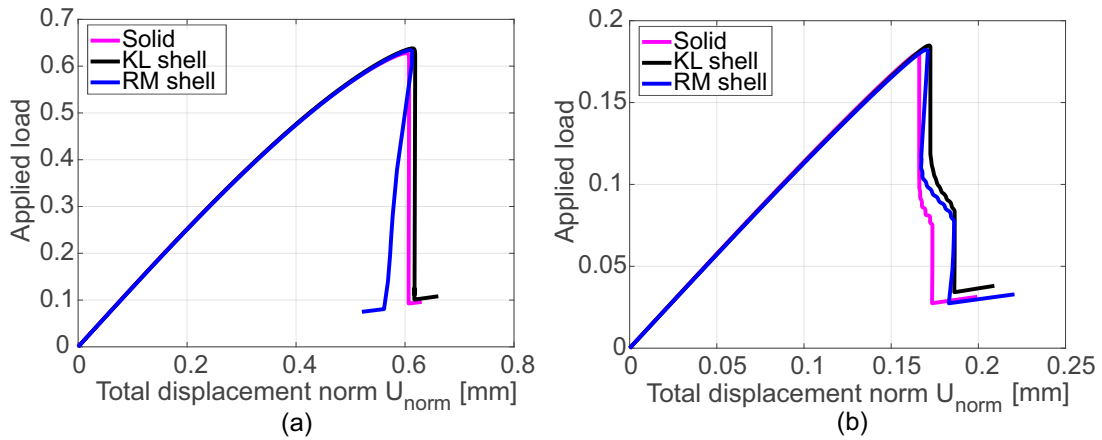


Figure 5.14: Annular plate. Load-displacement curves, (a) without initial cracks and (b) with initial cracks.

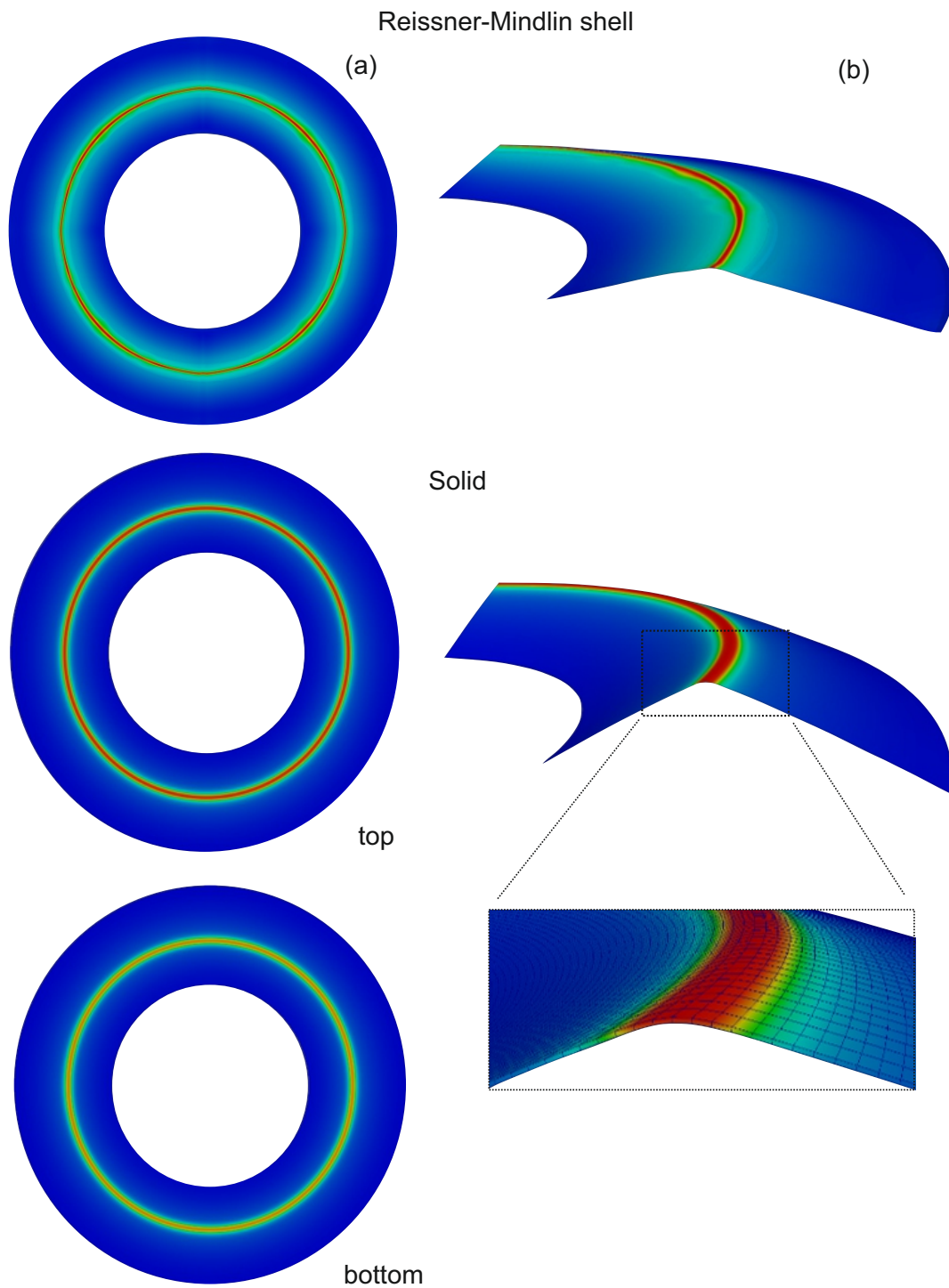


Figure 5.15: Annular plate without initial cracks. Crack phase-field at final fracture stage, on the undeformed (a) and the deformed configuration (b). Comparison between RM shell and Solid.

snap back behavior is visible for the RM shell, as it was previously observed in the example with the square plate. The reasons for this behavior are the same, namely, since the RM shell has two additional degrees of freedom the load increment for the arc-length control should be chosen differently compared to the other two elements. However, it is also possible that the snap back behavior occurs for all three elements but is only visible for the RM shell due to the chosen parameters. In the case of the plate with four initial cracks, a good agreement between the three element types is observed, see Fig. 5.14(b). The load-displacement curve of the RM shell is between those of the Solid and the KL shell. The crack path evolves from the four initial cracks and propagates along the circumferential direction of the plate until a closed circumferential crack is formed. Small oscillations observed in all three element types could be a result of interlocking between the elements where the load carrying behavior goes from the bending-dominated state to the membrane-dominated state. The results confirm that the proposed phase-field approach is able to naturally describe the interaction and merging of different cracks.

5.6.4 Pressurized cylinder with initial crack

In the last example two shell setups are investigated in order to verify the good performance of the Reissner-Mindlin element for shell structures. In the first case, a cylindrical shell under internal pressure is considered as shown in Fig. 5.17, see also Kiendl et al. (2016) and Ambati and De Lorenzis (2016). The cylinder has a longitudinal crack at the center and is fixed at both ends in X and Y direction. The material parameters read: $E = 70 \times 10^3 \text{ N/mm}^2$, $G_c = 1.5 \text{ N/mm}$ and $l_0 = 0.05 \text{ mm}$, $\nu = 0.3$ and the cylinder has a thickness of $t = 0.125 \text{ mm}$. The spatial discretization of the model comprises 9180 elements and an a priori local refinement of the mesh at the area where the crack is expected to propagate is performed with $h/l_0 = 1/125$. Because of symmetry only one quarter of the cylinder is modeled. The main intention of the present example is to perform a comparison of the results of the KL shell element to the RM shell element. The thickness of the cylinder is relatively small, which makes a comparison valid. Due to the internal pressure, the initial crack is going to propagate longitudinally along the cylinder height. The crack path is presented for different stages in Fig. 5.18. The elements where $s < 0.05$ are removed (only for visualization purposes). Arc-length control is adopted for the application of the inner pressure until failure.

In the second case, the same cylinder is considered, however, reinforced with two tear straps along its circumference, as shown in Fig. 5.19. This example is well-known in the literature, see Areias and Belytschko (2005), Kiendl et al. (2016), Ambati and De Lorenzis (2016) and Areias et al. (2016) and is based on experiments carried out

by Keesecker et al. (2003). The model is discretized with 28980 elements and the local refinement of the mesh is performed with $h/l_0 = 1/60$. An interesting aspect of this example is the "flapping" behavior, i.e. the crack turning when reaching the tear straps. At the beginning the initial crack is going to propagate axially, however, when reaching the tear straps, the crack deviates to the circumferential direction and continues its path along the straps. This behavior is observed in Fig. 5.20, where the crack path is presented for different stages. Thus, the presented model is able to fully capture the flapping behavior. In Fig. 5.16 the applied pressure over the norm of the total displacement is shown for the cylinder with and without tear straps. A very good agreement is observed between the KL shell and the RM shell for both cases. Small oscillations can be observed for both shell types as it was already seen in the case of the annular plate, see Section 5.6.3. Again, a reason for that could be an interlocking of the elements in the transition zone between the membrane-dominated (without crack) and the bending-dominated state (with crack). The corresponding diagrams of the Pressure-Total displacement norm for a solid-shell is provided in Kiendl et al. (2016), showing an overall good agreement between the results of the KL shell and the solid-shell.

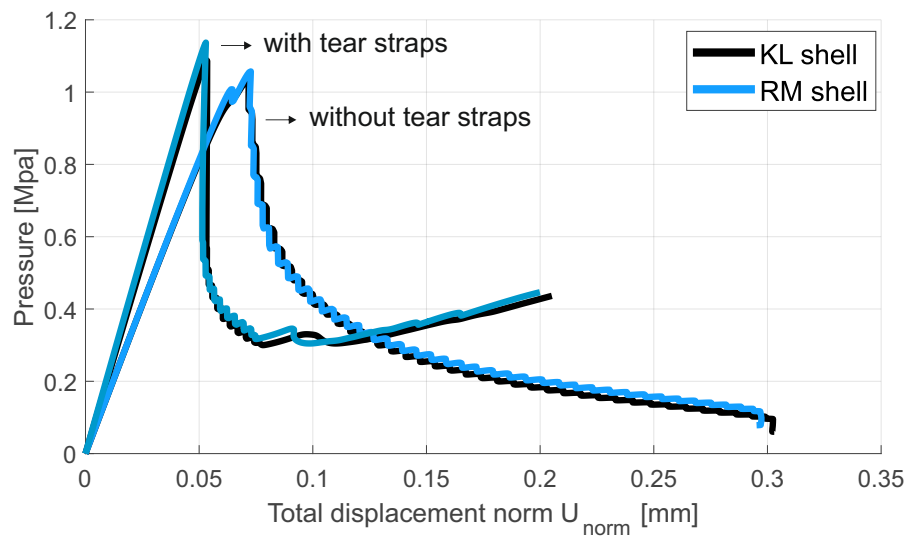


Figure 5.16: Pressure-norm of the total displacement curves for pressurized cylinder with initial crack.

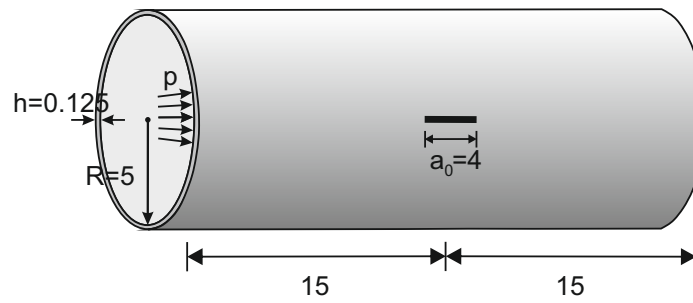


Figure 5.17: Geometry and loading of the cylinder with initial crack.

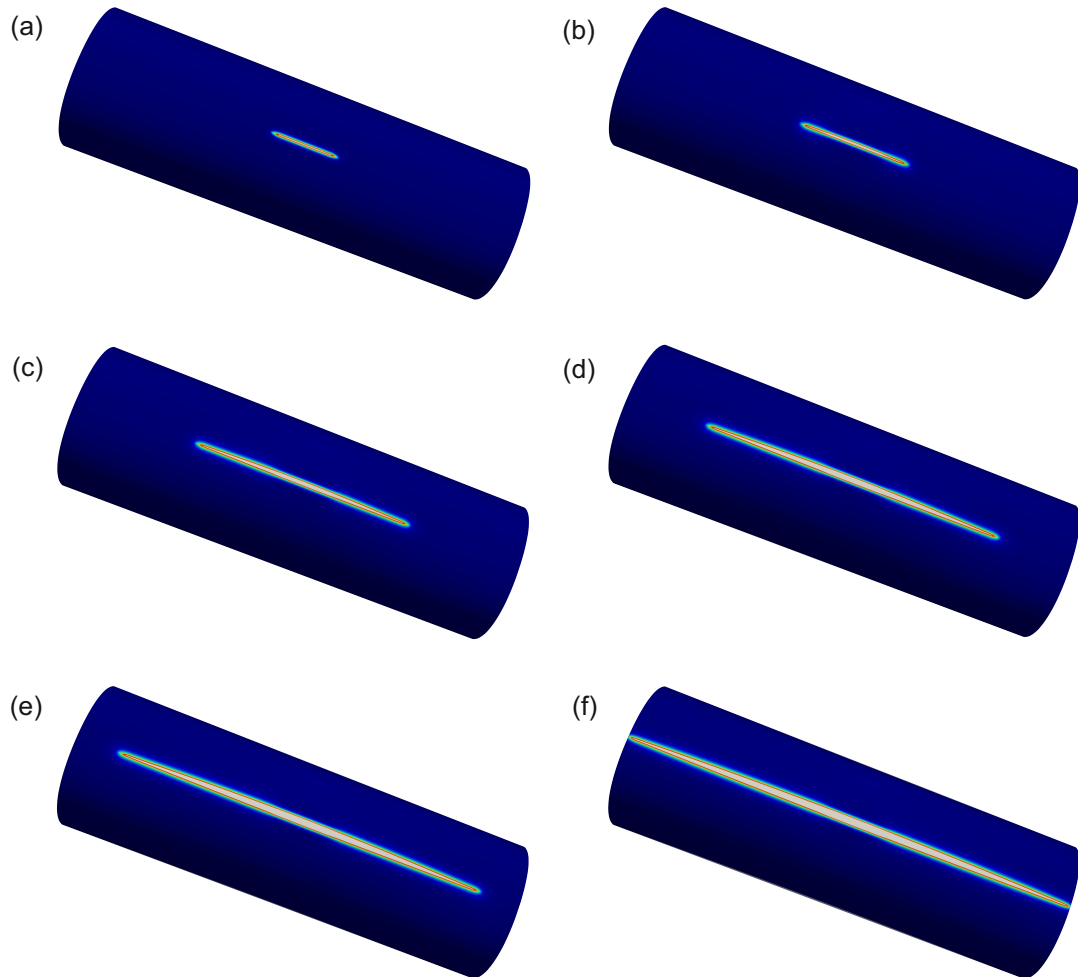


Figure 5.18: Pressurized cylinder without tear straps. (a-f) Crack phase-field at different fracture stages.

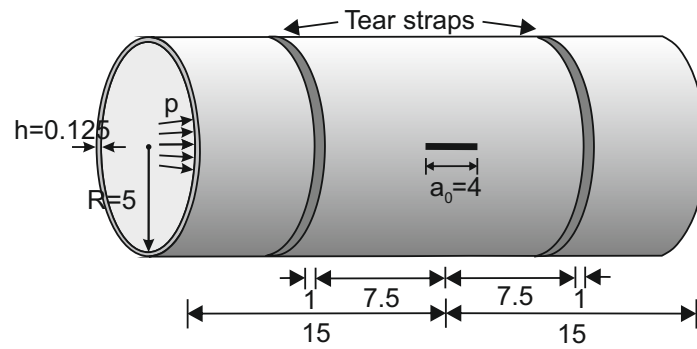


Figure 5.19: Geometry and loading of the cylinder with initial crack and tear straps.

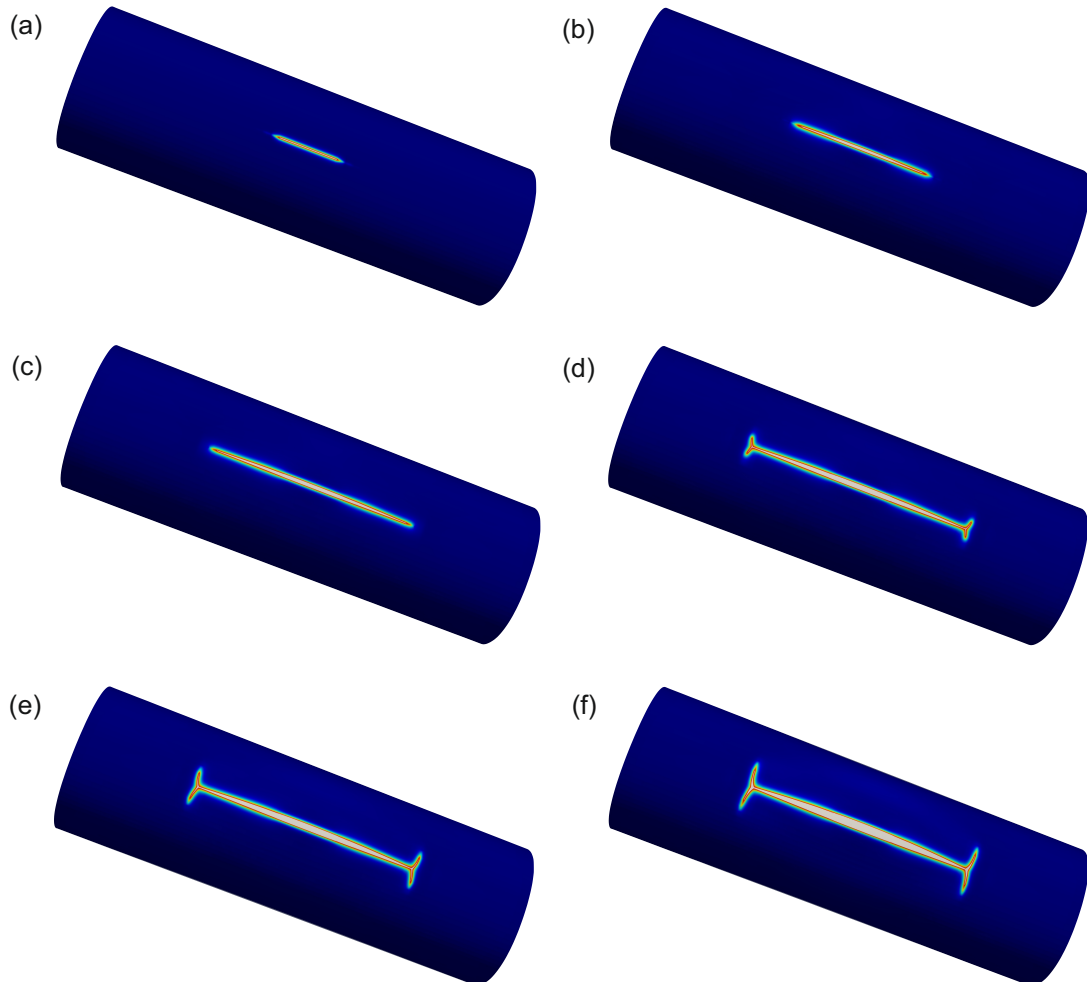


Figure 5.20: Pressurized cylinder with tear straps. (a-f) Crack phase-field at different fracture stages.

5.7 Conclusion

In this work, a phase-field model of brittle fracture was presented for the application to plate and shell structures. An isogeometric Reissner-Mindlin shell formulation was adopted from Dornisch et al. (2013) and Kikis et al. (2019) in order to make the formulation applicable for both thick and thin plates/shells. According to this formulation both the displacement/rotation fields as well as the phase-field are only defined on the mid-surface. The thickness direction is described with the help of the director vector. Regarding the formulation of the brittle phase-field model, the focus lied on the correct description of crack initiation, propagation and merging in the context of the degenerated plate/shell formulation with its corresponding Reissner-Mindlin kinematics. For this purpose, the phase-field model that was successfully applied in the work of Kiendl et al. (2016) to the case of Kirchhoff-Love plates and shells was here extended to the more general case of thick plates/shells. The spectral decomposition for the tension-compression split was again applied on the total strain, which changes over the thickness, without considering a decomposition into the membrane, curvature and shear terms first. In this way, unphysical fracture in compressed regions is avoided. On the other hand, the spectral decomposition of the total strain can only be applied if the plane stress condition is enforced numerically. A local algorithm which was proposed in the work of Klinkel and Govindjee (2002) was used in order to fulfill the zero stress condition in each integration point. The ability of the proposed brittle phase-field model to correctly describe fracture in plates and shells has been proven on the basis of various numerical examples. Furthermore, the results obtained by the Reissner-Mindlin shell formulation have been compared to those delivered by a 3D solid element and the Kirchhoff-Love shell formulation by Kiendl et al. (2016). A good agreement between all three element types could be observed. Pronounced differences between the Reissner-Mindlin and the Kirchhoff-Love shell were visible for cases where the transverse shear deformations played an important role, since they are not considered in the Kirchhoff-Love shell formulation. Thus, when shearing is crucial the phase-field model in combination with the Reissner-Mindlin shell formulation leads to more accurate results. Furthermore, in moderate thick plates and shells it is computationally more efficient to consider a Reissner-Mindlin shell formulation rather than a solid element. In addition, the performance of the proposed method for the cases of shell structures could be verified. In particular the "flapping" behavior of a reinforced cylinder was fully captured by the present model. Further extensions of the proposed method to nonlinear shell formulations as well as other fracture types, e.g. ductile fracture and fatigue are going to be the focus of future work. In addition, a comparison to other fracture models like GFEM or XFEM could highlight the benefits of the phase-field formulation compared to other existing models. Finally, a future goal

is to verify the numerical model based on experimental data.

Chapter 6

Outlook and conclusion

6.1 Summary and concluding points

This work is concerned with the treatment of locking effects in thin plates and shells within the framework of isogeometric analysis and the development of a phase-field model of brittle fracture for the application to plate and shell structures. An isogeometric Reissner-Mindlin shell formulation is used since it allows for the description of both thin and thick plates and shells. The geometry is described by the mid-surface using NURBS shape functions and for the thickness direction a director vector is used. In addition to the three displacements, two rotational degrees of freedom are defined since only smooth surfaces are considered.

First, a method to treat transverse shear locking in plates and shells has been introduced. Adjusted approximation spaces are used for the displacements and the two rotations in order to ensure consistency in the interpolated terms of the strain formulation. Namely, the two rotations are interpolated in the relevant direction with one degree lower shape functions than the displacements. In the framework of plates, the method has shown superior behavior compared to a standard Reissner-Mindlin shell formulation where no measures against locking have been taken. In particular in cases where transverse shear locking is more pronounced, i.e. for lower polynomial degrees, the proposed method has a higher accuracy with fewer degrees of freedom. In addition, the method has been compared to other well-known approaches that eliminate locking and showed that it is a competitive alternative. Except for the underestimation of the deformation, the other undesirable effect of locking that is solved using adjusted approximation spaces are the oscillations in the stress resultants. Regarding shell structures, transverse shear locking is eliminated and the remaining defiances in the results are due to the additional presence of membrane locking in shells. An advantage of this method is that no additional variables have to be introduced and it is generally ap-

plicable for any polynomial degree. Furthermore, it has been shown that compared to the standard Reissner-Mindlin shell formulation without any measures against locking, this method leads to a system of equations with less degrees of freedom.

A displacement-stress mixed method has been presented in order to alleviate both membrane and transverse shear locking in thin plates and shells in the framework of isogeometric analysis. The method is derived using a two-field Hellinger-Reissner variational principle where the stress resultants are considered as additional unknowns. Appropriate approximation spaces for the interpolation of the stresses that are related to locking had to be chosen. Namely, in the relevant direction, one order lower splines are chosen for the stresses compared to the deformation. The main focus lied on the implementation of the static condensation, which is performed in mixed formulations in order to eliminate the additional unknowns from the system of equations. Three different approaches have been presented. The first one is the standard approach where static condensation is performed on the patch level due to the high continuity of splines. This leads to the inversion of a matrix on the patch level and a fully populated stiffness matrix, which on the other hand increases the computational cost. Thus, two local approaches have been proposed that perform the static condensation on the element level. In the first one the stress resultants are defined discontinuously (C^{-1}) across the element boundaries, thus, leading to a sparse stiffness matrix that has the same bandwidth as the standard displacement-based shell. This method showed good results for low polynomial degrees, however, it did not improve the results greatly for higher polynomial degrees. This indicates that the discontinuity in the stress resultant fields hinders the complete elimination of locking. Thus, a second approach has been proposed that uses weights for the local control variables in order to get blended global ones. This method is based on the reconstruction algorithm used for \bar{B} formulations in Greco et al. (2017, 2018). The mixed reconstructed approach shows a high accuracy, close to the results of the global approach which is performed on the patch level. However, since it is computed partly on the element level and leads to a banded stiffness matrix it reduces the computational cost compared to the global approach. The advantages and disadvantages of each approach have been outlined in detail and a comparison to existing formulations with measures against locking has been carried out and showed the superiority of the mixed continuous and mixed reconstructed approach.

A phase-field model has been presented for the description of brittle fracture in isogeometric Reissner-Mindlin plates and shells. A special focus lied on the incorporation of the transverse shear strains in the model in order to allow for fracture due to transverse shear deformations. For this reason the phase-field model presented in Kiendl et al. (2016) for Kirchhoff-Love plates and shells was extended to the general case of thick plates and shells with Reissner-Mindlin kinematics. A continuous crack phase-field is introduced that is defined on the shell mid-surface and describes the transition be-

tween the cracked and uncracked material. In order to avoid any unphysical fracture in compressed regions, the spectral decomposition for the tension-compression split was applied on the total strain which changes over the thickness. Thus, the application of the plane stress condition is not straightforward anymore, i.e. it can not be applied by a simple elimination of the thickness normal strain and thickness normal stress from the constitutive law but has to be enforced numerically. For this purpose a local algorithm with quadratic convergence proposed in the work of Klinkel and Govindjee (2002) and Ambati et al. (2018) was used in order to enforce the zero stress condition in each integration point through the thickness. The ability of the proposed brittle phase-field model to correctly describe crack initiation, propagation and merging has been proven on the basis of different numerical examples considering plate and shell structures. A comparison of the proposed model to the existing 3D solid element and the Kirchhoff-Love shell element by Kiendl et al. (2016) showed a good agreement. In cases where shearing played an important role in the fracture behavior, the Reissner-Mindlin shell and the 3D solid had very similar results while noticeable differences were visible in the Kirchhoff-Love shell, since in the latter transverse shear deformations are not considered. Furthermore, the "flapping" behavior that is observed in the case of a reinforced cylinder was fully captured by the presented model.

6.2 Outlook

The proposed methods to treat locking effects in plates and shells, including adjusted approximation spaces and global or local mixed formulations, have been successfully tested for geometrically linear problems. In a next step, their extension to geometrical and material nonlinear problems is of great interest. In the case of geometrically nonlinear problems, an orthogonal rotation that is described by the Rodrigues' tensor could be used to define the director vector in the current configuration as it has been proposed in Dornisch et al. (2016). There, various concepts for the interpolation of the current director vector have been introduced and examined. In the framework of the global and local mixed formulations an extension to the Hu-Washizu variational principle should be carried out, where in addition to the stress resultants, the strains are considered as unknowns and interpolated in carefully chosen approximation spaces. In contrast to the Hellinger-Reissner variational principle, the Hu-Washizu has the advantage of reducing the computational cost when considering nonlinear problems. In addition, a detailed investigation of the Babuška-Brezzi condition should be carried out for the mixed formulations. Here it was assumed that the condition is fulfilled because the obtained results were accurate and robust. However, in order to ensure the stability of the system in general, the condition should be verified mathematically.

Regarding fracture in isogeometric Reissner-Mindlin plate and shell analysis, an extension of the presented phase-field model to other types of fracture, such as ductile fracture or fatigue should be the focus of future work. For this purpose, a nonlinear Reissner-Mindlin shell formulation as the one presented in Dornisch et al. (2016) should be implemented. In the framework of ductile fracture, the phase-field model presented in Ambati et al. (2015a) and Ambati and De Lorenzis (2016) could be adopted to isogeometric Reissner-Mindlin plate and shell formulations. There, the total free energy functional additionally includes the plastic strain energy density function which depends on a hardening variable. In this case, instead of a spectral decomposition of the elastic strain energy density, a decomposition into the volumetric and deviatoric contributions is more suitable. Furthermore, a detailed investigation of locking effects in the framework of fracture should be carried out in the future. In a first step, the anti-locking mechanisms presented in this thesis for transverse shear and membrane locking should be combined with the phase-field model. Furthermore, other locking effects that are interesting for fracture should be examined and mechanisms to treat them should be implemented. A comparison of the presented phase-field model to other fracture models like GFEM or XFEM could highlight the benefits of this model. Finally, a future goal is the verification of the numerical model based on experimental data.

Appendix A

Local plane stress algorithm

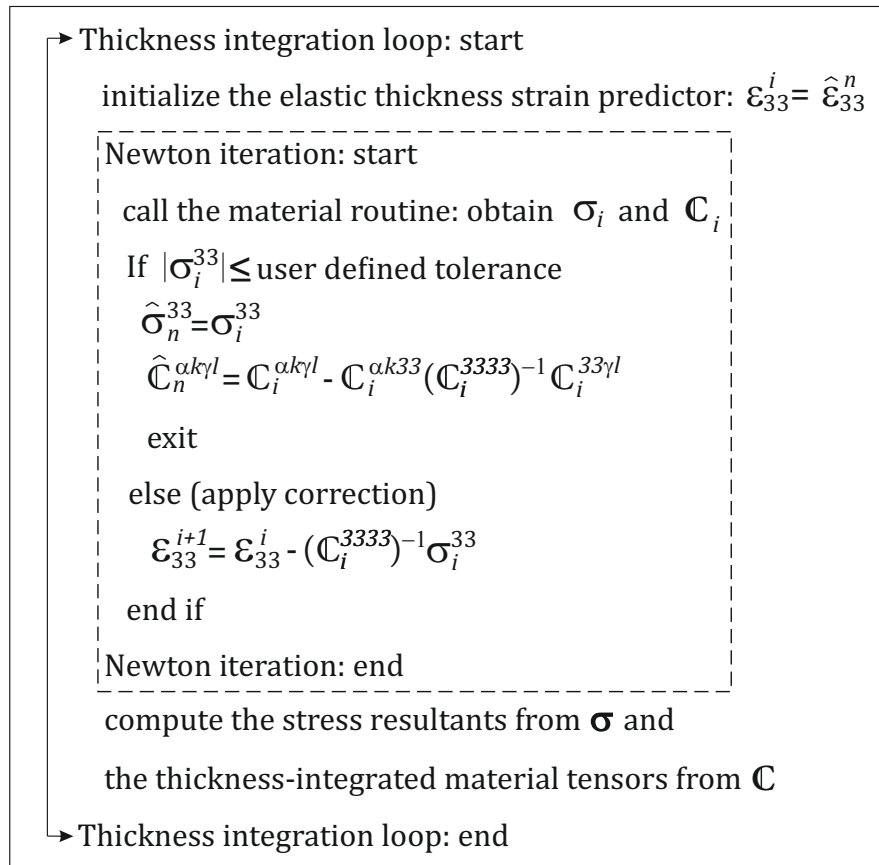


Figure A.1: Local plane stress algorithm.

Bibliography

- Adam, C., Bouabdallah, S., Zarroug, M., and Maitournam, H. (2014). Improved numerical integration for locking treatment in isogeometric structural elements, Part I: Beams. *Computer Methods in Applied Mechanics and Engineering*, 279:1–28.
- Adam, C., Bouabdallah, S., Zarroug, M., and Maitournam, H. (2015). Improved numerical integration for locking treatment in isogeometric structural elements. Part II: Plates and shells. *Computer Methods in Applied Mechanics and Engineering*, 284:106–137.
- Ahmed, A., van der Meer, F. P., and Sluys, L. J. (2012). A geometrically nonlinear discontinuous solid-like shell element (DSLSE) for thin shell structures. *Computer Methods in Applied Mechanics and Engineering*, 201-204:191–207.
- Alessi, R., Ambati, M., Gerasimov, T., Vidoli, S., and De Lorenzis, L. (2018). *Comparison of Phase-Field Models of Fracture Coupled with Plasticity*, pages 1–21. Springer International Publishing.
- Ambati, M. and De Lorenzis, L. (2016). Phase-field modeling of brittle and ductile fracture in shells with isogeometric NURBS-based solid-shell elements. *Computer Methods in Applied Mechanics and Engineering*, 312:351–373.
- Ambati, M., Gerasimov, T., and De Lorenzis, L. (2015a). Phase-field modeling of ductile fracture. *Computational Mechanics*, 55:1017–1040.
- Ambati, M., Gerasimov, T., and De Lorenzis, L. (2015b). A review on phase-field models of brittle fracture and a new fast hybrid formulation. *Computational Mechanics*, 55:383–405.
- Ambati, M., Kiendl, J., and De Lorenzis, L. (2018). Isogeometric Kirchhoff-Love shell formulation for elasto-plasticity. *Computer Methods in Applied Mechanics and Engineering*, 340:320–339.
- Amiri, F., Millán, D., Shen, Y., Rabczuk, T., and Arroyo, M. (2014). Phase-field modeling of fracture in linear thin shells. *Theoretical and Applied Fracture Mechanics*, 69:102–109.

- Amor, H., Marigo, J.-J., and Maurini, C. (2009). Regularized formulation of the variational brittle fracture with unilateral contact: Numerical experiments. *Journal of the Mechanics and Physics of Solids*, 57:1209–1229.
- Andelfinger, U. (1991). *Untersuchungen zur Zuverlässigkeit hybrid-gemischter Finiter Elemente für Flächentragwerke*. Ph.D. thesis, Institute for Structural Mechanics - University of Stuttgart.
- Antolin, P., Bressan, A., Buffa, A., and Sangalli, G. (2017). An isogeometric method for linear nearly-incompressible elasticity with local stress projection. *Computer Methods in Applied Mechanics and Engineering*, 316:694–719.
- Antolin, P., Kiendl, J., Pingaro, M., and Reali, A. (2020). A simple and effective method based on strain projections to alleviate locking in isogeometric solid shells. *Computational Mechanics*, 65:1621–1631.
- Areias, P., Garção, J., Pires, E. B., and Barbosa, J. I. (2011). Exact corotational shell for finite strains and fracture. *Computational Mechanics*, 48:385–406.
- Areias, P., Rabczuk, T., and Msekh, M. A. (2016). Phase-field analysis of finite-strain plates and shells including element subdivision. *Computer Methods in Applied Mechanics and Engineering*, 312:322–350.
- Areias, P. M. A. and Belytschko, T. (2005). Non-linear analysis of shells with arbitrary evolving cracks using XFEM. *International Journal for Numerical Methods in Engineering*, 62:384–415.
- Areias, P. M. A. and Belytschko, T. (2006). Analysis of Finite Strain Anisotropic Elastoplastic Fracture in Thin Plates and Shells. *Journal of Aerospace Engineering*, 19:259–270.
- Areias, P. M. A., Song, J. H., and Belytschko, T. (2006). Analysis of fracture in thin shells by overlapping paired elements. *Computer Methods in Applied Mechanics and Engineering*, 195:5343–5360.
- Auricchio, F., Beirão da Veiga, L., Kiendl, J., Lovadina, C., and Reali, A. (2013). Locking-free isogeometric collocation methods for spatial Timoshenko rods. *Computer Methods in Applied Mechanics and Engineering*, 263:113–126.
- Babu, C. R. and Prathap, G. (1986). A linear thick curved beam element. *International Journal for Numerical Methods in Engineering*, 23:1313–1328.
- Babu, C. R., Subramanian, G., and Prathap, G. (1987). Mechanics of field-consistency in finite element analysis-a penalty function approach. *Computers & Structures*, 25:161–173.

- Babuška, I. and Aziz, A. (1972). *The Mathematical Foundations of the Finite Element Method with Applications to Partial Differential Equations*, chapter Survey Lectures on the Mathematical Foundations of the Finite Element Method, pages 3–362. Academic Press, New York.
- Bathe, K.-J., Iosilevich, A., and Chapelle, D. (2000). An evaluation of the MITC shell elements. *Computers & Structures*, 75:1–30.
- Becker, G., Geuzaine, C., and Noels, L. (2011). A one field full discontinuous Galerkin method for Kirchhoff-Love shells applied to fracture mechanics. *Computer Methods in Applied Mechanics and Engineering*, 200:3223–3241.
- Beirão da Veiga, L., Buffa, A., Lovadina, C., Martinelli, M., and Sangalli, G. (2012a). An isogeometric method for the Reissner-Mindlin plate bending problem. *Computer Methods in Applied Mechanics and Engineering*, 209-212:45–53.
- Beirão Da Veiga, L., Hughes, T. J. R., Kiendl, J., Lovadina, C., Niiranen, J., Reali, A., and Speleers, H. (2015). A locking-free model for Reissner-Mindlin plates: Analysis and isogeometric implementation via NURBS and triangular NURPS. *Mathematical Models and Methods in Applied Sciences*, 25:1519–1551.
- Beirão da Veiga, L., Lovadina, C., and Reali, A. (2012b). Avoiding shear locking for the Timoshenko beam problem via isogeometric collocation methods. *Computer Methods in Applied Mechanics and Engineering*, 241-244:38–51.
- Belytschko, T., Stolarski, H., Liu, W. K., Carpenter, N., and Ong, J. S. J. (1985). Stress projection for membrane and shear locking in shell finite elements. *Computer Methods in Applied Mechanics and Engineering*, 51:221–258.
- Benson, D. J., Bazilevs, Y., De Luycker, E., Hsu, M.-C., Scott, M., Hughes, T. J. R., and Belytschko, T. (2010a). A generalized finite element formulation for arbitrary basis functions: From isogeometric analysis to XFEM. *International Journal for Numerical Methods in Engineering*, 83:765–785.
- Benson, D. J., Bazilevs, Y., Hsu, M.-C., and Hughes, T. J. R. (2010b). Isogeometric shell analysis: The Reissner-Mindlin shell. *Computer Methods in Applied Mechanics and Engineering*, 199:276–289.
- Benson, D. J., Bazilevs, Y., Hsu, M.-C., and Hughes, T. J. R. (2011). A large deformation, rotation-free, isogeometric shell. *Computer Methods in Applied Mechanics and Engineering*, 200:1367–1378.

- Benson, D. J., Hartmann, S., Bazilevs, Y., Hsu, M.-C., and Hughes, T. J. R. (2013). Blended isogeometric shells. *Computer Methods in Applied Mechanics and Engineering*, 255:133–146.
- Bieber, S., Oesterle, B., Ramm, E., and Bischoff, M. (2018). A variational method to avoid locking-independent of the discretization scheme. *International Journal for Numerical Methods in Engineering*, 114:801–827.
- Bischoff, M. (1999). *Theorie und Numerik einer dreidimensionalen Schalenformulierung*. PhD thesis, Institut für Baustatik der Universität Stuttgart.
- Bouclier, R., Elguedj, T., and Combescure, A. (2012). Locking free isogeometric formulations of curved thick beams. *Computer Methods in Applied Mechanics and Engineering*, 245-246:144–162.
- Bouclier, R., Elguedj, T., and Combescure, A. (2013a). Efficient isogeometric NURBS-based solid-shell elements: Mixed formulation and \bar{B} -method. *Computer Methods in Applied Mechanics and Engineering*, 267:86–110.
- Bouclier, R., Elguedj, T., and Combescure, A. (2013b). On the development of NURBS-based isogeometric solid shell elements: 2D problems and preliminary extension to 3D. *Computational Mechanics*, 52:1085–1112.
- Bouclier, R., Elguedj, T., and Combescure, A. (2015). An isogeometric locking-free NURBS-based solid-shell element for geometrically nonlinear analysis. *International Journal for Numerical Methods in Engineering*, 101:774–808.
- Bourdin, B. (2007). Numerical implementation of the variational formulation for quasi-static brittle fracture. *Interfaces and Free Boundaries*, 9:411–430.
- Bourdin, B., Francfort, G. A., and Marigo, J.-J. (2000). Numerical experiments in revisited brittle fracture. *Journal of the Mechanics and Physics of Solids*, 48:797–826.
- Bourdin, B., Francfort, G. A., and Marigo, J.-J. (2008). The Variational Approach to Fracture. *Journal of elasticity*, 91:5–148.
- Brezzi, F. (1974). On the existence, uniqueness and approximation of saddle-point problems arising from Lagrangian multipliers. *ESAIM: Mathematical Modelling and Numerical Analysis - Modélisation Mathématique et Analyse Numérique*, 8:129–151.
- Budarapu, P., Reinoso, J., and Paggi, M. (2017). Concurrently coupled solid shell-based adaptive multiscale method for fracture. *Computer Methods in Applied Mechanics and Engineering*, 319:338–365.

- Caleyron, F., Combescure, A., Faucher, V., and Potapov, S. (2012). Dynamic simulation of damage-fracture transition in smoothed particles hydrodynamics shells. *International Journal for Numerical Methods in Engineering*, 90:707–738.
- Cardoso, R. P. R. and Cesar de Sa, J. M. A. (2012). The enhanced assumed strain method for the isogeometric analysis of nearly incompressible deformation of solids. *International Journal for Numerical Methods in Engineering*, 92:56–78.
- Cardoso, R. P. R. and Cesar de Sa, J. M. A. (2014). Blending moving least squares techniques with NURBS basis functions for nonlinear isogeometric analysis. *Computational Mechanics*, 53:1327–1340.
- Caseiro, J. F., Valente, R. A. F., Reali, A., Kiendl, J., Auricchio, F., and Alves de Sousa, R. J. (2014). On the Assumed Natural Strain method to alleviate locking in solid-shell NURBS-based finite elements. *Computational Mechanics*, 53:1341–1353.
- Caseiro, J. F., Valente, R. A. F., Reali, A., Kiendl, J., Auricchio, F., and Alves de Sousa, R. J. (2015). Assumed Natural Strain NURBS-based solid-shell element for the analysis of large deformation elasto-plastic thin-shell structures. *Computer Methods in Applied Mechanics and Engineering*, 284:861–880.
- Chapelle, D. and Bathe, K.-J. (1998). Fundamental considerations for the finite element analysis of shell structures. *Computers & Structures*, 66:19–36.
- Chau-Dinh, T., Zi, G., Lee, P.-S., Rabczuk, T., and Song, J.-H. (2012). Phantom-node method for shell models with arbitrary cracks. *Computers & Structures*, 92-93:242–256.
- Chinosi, C. and Lovadina, C. (1995). Numerical analysis of some mixed finite element methods for Reissner-Mindlin plates. *Computational Mechanics*, 16:36–44.
- Choi, D., Palma, F. J., Sanchez-Palencia, E., and Vilariño, M. A. (1998). Membrane locking in the finite element computation of very thin elastic shells. *RAIRO, Modélisation Math. Anal. Numér.*, 32:131–152.
- Cirak, F., Ortiz, M., and Pandolfi, A. (2005). A cohesive approach to thin-shell fracture and fragmentation. *Computer Methods in Applied Mechanics and Engineering*, 194:2604–2618.
- Cook, R. D. (1974). Improved two-dimensional finite element. *Journal of the Structural Division*, 100:1851–1863.
- Cottrell, J. A., Hughes, T. J. R., and Bazilevs, Y. (2009). *Isogeometric Analysis: Toward Integration of CAD and FEA*. Wiley, Chichester.

- Daderot (2014). Exhibit in the Fernbank Museum of Natural History, Atlanta, Georgia, USA. CC0, via Wikimedia Commons. https://commons.wikimedia.org/wiki/File:Nautilus_pompilius_-_Fernbank_Museum_of_Natural_History_-_DSC00294.JPG.
- Dimitri, R., De Lorenzis, L., Wriggers, P., and Zavarise, G. (2014). NURBS- and T-spline-based isogeometric cohesive zone modeling of interface debonding. *Computational Mechanics*, 54:369–388.
- Dolbow, J., Moës, N., and Belytschko, T. (2000). Modeling fracture in Mindlin-Reissner plates with the extended finite element method. *International Journal of Solids and Structures*, 37:7161–7183.
- Dornisch, W. (2015). *Interpolation of Rotations and Coupling of Patches in Isogeometric Reissner-Mindlin Shell Analysis*. PhD thesis, Chair of Structural Analysis and Dynamics - RWTH Aachen.
- Dornisch, W. and Klinkel, S. (2014). Treatment of Reissner-Mindlin shells with kinks without the need for drilling rotation stabilization in an isogeometric framework. *Computer Methods in Applied Mechanics and Engineering*, 276:35–66.
- Dornisch, W., Klinkel, S., and Simeon, B. (2013). Isogeometric Reissner-Mindlin shell analysis with exactly calculated director vectors. *Computer Methods in Applied Mechanics and Engineering*, 253:491–504.
- Dornisch, W., Müller, R., and Klinkel, S. (2016). An efficient and robust rotational formulation for isogeometric Reissner-Mindlin shell elements. *Computer Methods in Applied Mechanics and Engineering*, 303:1–34.
- Duong, T. X., Roohbakhshan, F., and Sauer, R. A. (2017). A new rotation-free isogeometric thin shell formulation and a corresponding continuity constraint for patch boundaries. *Computer Methods in Applied Mechanics and Engineering*, 316:43–83.
- Echter, R. (2013). *Isogeometric analysis of shells*. PhD thesis, Institute for Structural Mechanics - University of Stuttgart.
- Echter, R. and Bischoff, M. (2010). Numerical efficiency, locking and unlocking of NURBS finite elements. *Computer Methods in Applied Mechanics and Engineering*, 199:374–382.
- Echter, R., Oesterle, B., and Bischoff, M. (2013). A hierarchic family of isogeometric shell finite elements. *Computer Methods in Applied Mechanics and Engineering*, 254:170–180.

- Elguedj, T., Bazilevs, Y., Calo, V. M., and Hughes, T. J. R. (2008). $\bar{\mathbf{B}}$ and $\bar{\mathbf{F}}$ projection methods for nearly incompressible linear and non-linear elasticity and plasticity using higher-order NURBS elements. *Computer Methods in Applied Mechanics and Engineering*, 197:2732–2762.
- Fahrendorf, F., Morganti, S., Reali, A., Hughes, T. J. R., and De Lorenzis, L. (2020). Mixed stress-displacement isogeometric collocation for nearly incompressible elasticity and elastoplasticity. *Computer Methods in Applied Mechanics and Engineering*, 369:113112.
- Francfort, G. A. and Marigo, J.-J. (1998). Revisiting brittle fracture as an energy minimization problem. *Journal of the Mechanics and Physics of Solids*, 46:1319–1342.
- Gee, M., Ramm, E., and Wall, W. A. (2005). Parallel multilevel solution of nonlinear shell structures. *Computer Methods in Applied Mechanics and Engineering*, 194(21):2513–2533.
- Gerasimov, T. and De Lorenzis, L. (2016). A line search assisted monolithic approach for phase-field computing of brittle fracture. *Computer Methods in Applied Mechanics and Engineering*, 312:276–303.
- Gomez, H., Hughes, T. J. R., Nogueira, X., and Calo, V. M. (2010). Isogeometric analysis of the isothermal Navier-Stokes-Korteweg equations. *Computer Methods in Applied Mechanics and Engineering*, 199(25):1828–1840.
- Govindjee, S., Strain, J., Mitchell, T. J., and Taylor, R. L. (2012). Convergence of an efficient local least-squares fitting method for bases with compact support. *Computer Methods in Applied Mechanics and Engineering*, 213–216:84–92.
- Greco, L. and Cuomo, M. (2016). An isogeometric implicit G^1 mixed finite element for Kirchhoff space rods. *Computer Methods in Applied Mechanics and Engineering*, 298:325–349.
- Greco, L., Cuomo, M., and Contrafatto, L. (2018). A reconstructed local $\bar{\mathbf{B}}$ formulation for isogeometric Kirchhoff-Love shells. *Computer Methods in Applied Mechanics and Engineering*, 332:462–487.
- Greco, L., Cuomo, M., Contrafatto, L., and Gazzo, S. (2017). An efficient blended mixed B-spline formulation for removing membrane locking in plane curved Kirchhoff rods. *Computer Methods in Applied Mechanics and Engineering*, 324:476–511.

- Griffith, A. A. and Taylor, G. I. (1921). VI. The phenomena of rupture and flow in solids. *Philosophical Transactions of the Royal Society of London. Series A, Containing Papers of a Mathematical or Physical Character*, 221:163–198.
- Hellinger, E. (1914). *Enzyklopädie der Mathematischen Wissenschaften*, chapter Die Allgemeinen Ansätze der Mechanik der Kontinua, pages 601–694. Teubner, Leipzig.
- Hosseini, S., Remmers, J. J. C., and de Borst, R. (2014a). The incorporation of gradient damage models in shell elements. *International Journal for Numerical Methods in Engineering*, 98:391–398.
- Hosseini, S., Remmers, J. J. C., Verhoosel, C. V., and de Borst, R. (2013). An isogeometric solid-like shell element for nonlinear analysis. *International Journal for Numerical Methods in Engineering*, 95:238–256.
- Hosseini, S., Remmers, J. J. C., Verhoosel, C. V., and de Borst, R. (2014b). An isogeometric continuum shell element for non-linear analysis. *Computer Methods in Applied Mechanics and Engineering*, 271:1–22.
- Hu, P., Hu, Q., and Xia, Y. (2016). Order reduction method for locking free isogeometric analysis of Timoshenko beams. *Computer Methods in Applied Mechanics and Engineering*, 308:1–22.
- Hu, Q., Xia, Y., Natarajan, S., Zilian, A., Hu, P., and Bordas, S. P. A. (2020). Isogeometric analysis of thin Reissner-Mindlin shells: locking phenomena and B-bar method. *Computational Mechanics*, 65:1323–1341.
- Hughes, T. J. R. (2000). *The finite element method: Linear static and dynamic finite element analysis*. Dover Publications, Mineola, reprinted edition edition.
- Hughes, T. J. R., Cottrell, J. A., and Bazilevs, Y. (2005). Isogeometric analysis: CAD, finite elements, NURBS, exact geometry and mesh refinement. *Computer Methods in Applied Mechanics and Engineering*, 194:4135–4195.
- Ishaquddin, M., Raveendranath, P., and Reddy, J. N. (2012). Flexure and torsion locking phenomena in out-of-plane deformation of Timoshenko curved beam element. *Finite Elements in Analysis and Design*, 51:22–30.
- Keesecker, A. L., Dávila, C. G., Johnson, E. R., and Starnes, J. H. (2003). Crack path bifurcation at a tear strap in a pressurized shell. *Computers & Structures*, 81:1633–1642.

- Kiendl, J., Ambati, M., Lorenzis, L. D., Gomez, H., and Reali, A. (2016). Phase-field description of brittle fracture in plates and shells. *Computer Methods in Applied Mechanics and Engineering*, 312:374–394.
- Kiendl, J., Auricchio, F., Beirão da Veiga, L., Lovadina, C., and Reali, A. (2015a). Iso-geometric collocation methods for the Reissner-Mindlin plate problem. *Computer Methods in Applied Mechanics and Engineering*, 284:489–507.
- Kiendl, J., Auricchio, F., Hughes, T. J. R., and Reali, A. (2015b). Single-variable formulations and isogeometric discretizations for shear deformable beams. *Computer Methods in Applied Mechanics and Engineering*, 284:988–1004.
- Kiendl, J., Auricchio, F., and Reali, A. (2018). A displacement-free formulation for the Timoshenko beam problem and a corresponding isogeometric collocation approach. *Meccanica*, 53:1403–1413.
- Kiendl, J., Bazilevs, Y., Hsu, M.-C., Wüchner, R., and Bletzinger, K.-U. (2010). The bending strip method for isogeometric analysis of Kirchhoff-Love shell structures comprised of multiple patches. *Computer Methods in Applied Mechanics and Engineering*, 199:2403–2416.
- Kiendl, J., Bletzinger, K.-U., Linhard, J., and Wüchner, R. (2009). Isogeometric shell analysis with Kirchhoff-Love elements. *Computer Methods in Applied Mechanics and Engineering*, 198:3902–3914.
- Kiendl, J., Hsu, M.-C., Wu, M. C. H., and Reali, A. (2015c). Isogeometric Kirchhoff-Love shell formulations for general hyperelastic materials. *Computer Methods in Applied Mechanics and Engineering*, 291:280–303.
- Kiendl, J., Marino, E., and De Lorenzis, L. (2017). Isogeometric collocation for the Reissner-Mindlin shell problem. *Computer Methods in Applied Mechanics and Engineering*, 325:645–665.
- Kikis, G., Ambati, M., De Lorenzis, L., and Klinkel, S. (2021). Phase-field model of brittle fracture in Reissner-Mindlin plates and shells. *Computer Methods in Applied Mechanics and Engineering*, 373:113490.
- Kikis, G., Dornisch, W., and Klinkel, S. (2019). Adjusted approximation spaces for the treatment of transverse shear locking in isogeometric Reissner-Mindlin shell analysis. *Computer Methods in Applied Mechanics and Engineering*, 354:850–870.
- Kirchhoff, G. (1850). Über das Gleichgewicht und die Bewegung einer elastischen Scheibe. *Journal für die reine und angewandte Mathematik*, 40:51–88.

- Klinkel, S. and Govindjee, S. (2002). Using finite strain 3D-material models in beam and shell elements. *Engineering Computations*, 19:902–921.
- Kobayashi, H. and Onoue, H. (1943). Brittle fracture of Liberty Ships. Technical Report 100, Failure Knowledge Database.
- Kocaman, E., Chen, B., and Pinho, S. (2020). A floating connector element formulation for multi-level modelling of composite structures. *Composite Structures*, 251:112532.
- Larsson, R., Mediavilla, J., and Fagerström, M. (2011). Dynamic fracture modeling in shell structures based on XFEM. *International Journal for Numerical Methods in Engineering*, 86:499–527.
- Lee, P.-S. and Bathe, K.-J. (2002). On the asymptotic behavior of shell structures and the evaluation in finite element solutions. *Computers & Structures*, 80:235–255.
- Leonetti, L., Liguori, F., Magisano, D., and Garcea, G. (2018). An efficient isogeometric solid-shell formulation for geometrically nonlinear analysis of elastic shells. *Computer Methods in Applied Mechanics and Engineering*, 331:159–183.
- Long, Q., Bornemann, P. B., and Cirak, F. (2012). Shear-flexible subdivision shells. *International Journal for Numerical Methods in Engineering*, 90:1549–1577.
- Love, A. E. H. (1888). The Small Free Vibrations and Deformation of a Thin Elastic Shell. *Philosophical Transactions of the Royal Society of London*, 179:491–546.
- Lua, J., Zhang, T., Fang, E., and Song, J.-H. (2016). Explicit phantom paired shell element approach for crack branching and impact damage prediction of aluminum structures. *International Journal of Impact Engineering*, 87:28–43.
- Miao, D., Borden, M. J., Scott, M. A., and Thomas, D. C. (2018). Bézier $\bar{\mathbf{B}}$ projection. *Computer Methods in Applied Mechanics and Engineering*, 335:273–297.
- Miehe, C., Hofacker, M., and Welschinger, F. (2010a). A phase field model for rate-independent crack propagation: Robust algorithmic implementation based on operator splits. *Computer Methods in Applied Mechanics and Engineering*, 199:2765–2778.
- Miehe, C., Welschinger, F., and Hofacker, M. (2010b). Thermodynamically consistent phase-field models of fracture: Variational principles and multi-field FE implementations. *International Journal for Numerical Methods in Engineering*, 83:1273–1311.

- Mindlin, R. D. (1951). Influence of rotatory inertia and shear on flexural motions of isotropic elastic plates. *Journal of Applied Mechanics*, 18:31–38.
- Mitchell, T. J., Govindjee, S., and Taylor, R. L. (2011). *Recent Developments and Innovative Applications in Computational Mechanics*, chapter A Method for Enforcement of Dirichlet Boundary Conditions in Isogeometric Analysis, pages 283–293. Springer, Berlin.
- Mostofizadeh, S., Fagerström, M., and Larsson, R. (2013). Dynamic crack propagation in elastoplastic thin-walled structures: Modelling and validation. *International Journal for Numerical Methods in Engineering*, 96:63–86.
- NASA (2002). Atlantis carrying the S1 Truss segment. NASA, Public domain, via Wikimedia Commons. https://commons.wikimedia.org/wiki/File:STS-112_Atlantis_carrying_S1_truss.jpg.
- Nguyen, A. D., Stoffel, M., and Weichert, D. (2012). A gradient-enhanced damage approach for viscoplastic thin-shell structures subjected to shock waves. *Computer Methods in Applied Mechanics and Engineering*, 217-220:236–246.
- Nguyen-Thanh, N., Kiendl, J., Nguyen-Xuan, H., Wüchner, R., Bletzinger, K.-U., Bazilevs, Y., and Rabczuk, T. (2011). Rotation free isogeometric thin shell analysis using PHT-splines. *Computer Methods in Applied Mechanics and Engineering*, 200:3410–3424.
- Nguyen-Thanh, N., Valizadeh, N., Nguyen, M. N., Nguyen-Xuan, H., Zhuang, X., Areias, P., Zi, G., Bazilevs, Y., De Lorenzis, L., and Rabczuk, T. (2015). An extended isogeometric thin shell analysis based on Kirchhoff-Love theory. *Computer Methods in Applied Mechanics and Engineering*, 284:265–291.
- Oesterle, B., Ramm, E., and Bischoff, M. (2016). A shear deformable, rotation-free isogeometric shell formulation. *Computer Methods in Applied Mechanics and Engineering*, 307:235–255.
- Oesterle, B., Sachse, R., Ramm, E., and Bischoff, M. (2017). Hierarchic isogeometric large rotation shell elements including linearized transverse shear parametrization. *Computer Methods in Applied Mechanics and Engineering*, 321:383–405.
- Paul, K., Zimmermann, C., Mandadapu, K. K., Hughes, T. J. R., Landis, C. M., and Sauer, R. A. (2020). An adaptive space-time phase field formulation for dynamic fracture of brittle shells based on LR NURBS. *Computational Mechanics*, 65:1039–1062.

- Petković, M. D. and Stanimirović, P. S. (2009). Generalized matrix inversion is not harder than matrix multiplication. *Journal of Computational and Applied Mathematics*, 230(1):270–282.
- Pian, T. H. H. and Sumihara, K. (1984). Rational approach for assumed stress finite elements. *International Journal for Numerical Methods in Engineering*, 20(9):1685–1695.
- Piegl, L. and Tiller, W. (1997). *The NURBS Book*. Monographs in Visual Communications, second edition. Springer, Berlin.
- Pigazzini, M. S., Kamensky, D., van Iersel, D. A. P., Alaydin, M. D., Remmers, J. J. C., and Bazilevs, Y. (2019). Gradient-enhanced damage modeling in Kirchhoff-Love shells: Application to isogeometric analysis of composite laminates. *Computer Methods in Applied Mechanics and Engineering*, 346:152–179.
- Proserpio, D., Ambati, M., De Lorenzis, L., and Kiendl, J. (2020). A framework for efficient isogeometric computations of phase-field brittle fracture in multipatch shell structures. *Computer Methods in Applied Mechanics and Engineering*, 372:113363.
- Proserpio, D., Ambati, M., De Lorenzis, L., and Kiendl, J. (2021). Phase-field simulation of ductile fracture in shell structures. *Computer Methods in Applied Mechanics and Engineering*, 385:114019.
- Rabczuk, T. and Areias, P. (2008). A meshfree thin shell for arbitrary evolving cracks based on an extrinsic basis. In *Computer Modeling in Engineering & Sciences*, volume 16, pages 115–130.
- Rafetseder, K. and Zulehner, W. (2019). A new mixed approach to Kirchhoff-Love shells. *Computer Methods in Applied Mechanics and Engineering*, 346:440–455.
- Raghu, P., Rajagopal, A., Jalan, S. K., and Reddy, J. N. (2021). Modeling of brittle fracture in thick plates subjected to transient dynamic loads using a hybrid phase field model. *Meccanica*, 56:1269–1286.
- Raghu, P., Rajagopal, A., and Reddy, J. N. (2020). Thermodynamically Consistent Variational Approach for Modeling Brittle Fracture in Thick Plates by a Hybrid Phase Field Model. *Journal of Applied Mechanics*, 87:021002.
- Razzaque, A. (1973). Program for triangular bending elements with derivative smoothing. *International Journal for Numerical Methods in Engineering*, 6:333–343.
- Reinoso, J., Paggi, M., and Linder, C. (2017). Phase field modeling of brittle fracture for enhanced assumed strain shells at large deformations: formulation and finite element implementation. *Computational Mechanics*, 59:981–1001.

- Reinoso, J., Paggi, M., and Rolfes, R. (2016). A computational framework for the interplay between delamination and wrinkling in functionally graded thermal barrier coatings. *Computational Materials Science*, 116:82–95.
- Reissner, E. (1944). On the Theory of Bending of Elastic Plates. *Journal of Mathematics and Physics*, 23(1-4):184–191.
- Reissner, E. (1950). On a Variational Theorem in Elasticity. *Journal of Mathematics and Physics*, 29(1-4):90–95.
- Ren, B. and Li, S. (2012). Modeling and simulation of large-scale ductile fracture in plates and shells. *International Journal of Solids and Structures*, 49:2373–2393.
- Rogers, D. F. (2001). *An introduction to NURBS with historical perspective*. Academic Press, San Diego.
- Saint-Georges, P., Warzee, G., Notay, Y., and Beauwens, R. (1999). Problem-dependent preconditioners for iterative solvers in FE elastostatics. *Computers & Structures*, 73(1):33–43.
- Simo, J. C. and Fox, D. D. (1989). On a stress resultant geometrically exact shell model. Part I: Formulation and optimal parametrization. *Computer Methods in Applied Mechanics and Engineering*, 72:267–304.
- Simo, J. C. and Hughes, T. J. R. (1986). On the Variational Foundations of Assumed Strain Methods. *Journal of Applied Mechanics*, 53:51–54.
- Song, J.-H. and Belytschko, T. (2009). Dynamic fracture of shells subjected to impulsive loads. *Journal of Applied Mechanics*, 76(5):051301.
- Sydney (2017). The Sydney Opera House in Sydney, Australia. Taken from Circular Quay in 2017. CC0, via Wikimedia Commons. [https://commons.wikimedia.org/wiki/File:Sydney_Opera_House_\(2017\).jpg](https://commons.wikimedia.org/wiki/File:Sydney_Opera_House_(2017).jpg).
- Taylor, R. L. (2011). Isogeometric analysis of nearly incompressible solids. *International Journal for Numerical Methods in Engineering*, 87:273–288.
- Temizer, İ., Wriggers, P., and Hughes, T. J. R. (2011). Contact treatment in isogeometric analysis with NURBS. *Computer Methods in Applied Mechanics and Engineering*, 200(9):1100–1112.
- Thai, C. H., Nguyen-Xuan, H., Nguyen-Thanh, N., Le, T.-H., Nguyen-Thoi, T., and Rabczuk, T. (2011). Static, free vibration, and buckling analysis of laminated composite Reissner-Mindlin plates using NURBS-based isogeometric approach. *International Journal for Numerical Methods in Engineering*, 91:571–603.

- Thomas, D. C., Scott, M. A., Evans, J. A., Tew, K., and Evans, E. J. (2015). Bézier projection: A unified approach for local projection and quadrature-free refinement and coarsening of NURBS and T-splines with particular application to isogeometric design and analysis. *Computer Methods in Applied Mechanics and Engineering*, 284:55–105.
- Timoshenko, S. (1940). *Theory of Plates and Shells*. Engineering Societies monograph. McGraw-Hill.
- Uhm, T.-K. and Youn, S.-K. (2009). T-spline finite element method for the analysis of shell structures. *International Journal for Numerical Methods in Engineering*, 80:507–536.
- Ulmer, H., Hofacker, M., and Miehe, C. (2012). Phase field modeling of fracture in plates and shells. *PAMM*, 12:171–172.
- U.S. GPO (1947). The Design and Methods of Construction of Welded Steel Merchant Vessels. Public domain, via Wikimedia Commons. <https://commons.wikimedia.org/wiki/File:TankerSchenectady.jpg?uselang=de#file>.
- Ventsel, E. and Krauthammer, T. (2001). *Thin Plates and Shells - Theory, Analysis and Applications*. CRC Press.
- Woelke, P. B. and Abboud, N. N. (2012). Modeling fracture in large scale shell structures. *Journal of the Mechanics and Physics of Solids*, 60:2044–2063.
- Zavattieri, P. (2006). Modeling of Crack Propagation in Thin-Walled Structures Using a Cohesive Model for Shell Elements. *Journal of Applied Mechanics*, 73:948–958.
- Zou, Z., Scott, M. A., Miao, D., Bischoff, M., Oesterle, B., and Dornisch, W. (2020). An isogeometric Reissner-Mindlin shell element based on Bézier dual basis functions: Overcoming locking and improved coarse mesh accuracy. *Computer Methods in Applied Mechanics and Engineering*, 370:113283.

Schriftenreihe
des Lehrstuhls für Baustatik und Baudynamik
der RWTH Aachen

Verzeichnis der bisher erschienenen Dissertationen/Habilitationen:

- 98/1: Ruth Feill, Zum Einfluss frequenzabhängiger aerodynamischer Beiwerte auf das Antwortverhalten schlanker Strukturen unter stochastischer Windbelastung, 1998.
- 00/1: Uwe Weitkemper, Zur numerischen Untersuchung seismisch erregter Hochbauten mit Aussteifungssystemen aus Stahlbetonwandscheiben, 2000.
- 00/2: Carsten Könke, Schädigungssimulationsverfahren zur Lebensdauerabschätzung von Tragwerken, 2000.
- 01/1: Sam-Young Noh, Beitrag zur numerischen Analyse der Schädigungsmechanismen von Naturzugkühltürmen, 2001.
- 02/1: Hamid Sadegh-Azar, Schnellbewertung der Erdbebengefährdung von Gebäuden, 2002.
- 02/2: Falko Schube, Beitrag zur numerischen Simulation des Wirbelsäulenverhaltens eines Kraftfahrers infolge durch Straßenunebenheiten induzierter Ganzkörperschwingungen, 2002.
- 03/1: Jörg Rocco Wagner, Seismisch belastete Schüttgutsilos, 2003.
- 04/1: Arno Grunendahl, Beitrag zur numerischen Simulationen des sitzenden Menschen zur Beurteilung der Auswirkung von Ganzkörperschwingungen, 2004.
- 04/2: Wolfram Kuhlmann, Gesamtkonzept zur Ermittlung der seismischen Vulnerabilität von Bauwerken am Beispiel unterirdischer Rohrleitungen, 2004.
- 06/1: Iman Karimi, Risk Management of Natural Disasters: A Fuzzy-Probabilistic Methodology and its Application to Seismic Hazard, 2006.
- 06/2: Stefan Holler, Dynamisches Mehrphasenmodell mit hypoplastischer Materialformulierung der Feststoffphase, 2006.
- 06/3: Michael Mistler, Verformungsbasiertes seismisches Bemessungskonzept für Mauerwerksbauten, 2006.

- 07/1: Ines Kalker, Numerische Simulation von unbewehrten und textilverstärkten Mauerwerksscheiben unter zyklischer Belastung, 2007.
- 07/2: Philippe Renault, Bewertungsverfahren zur Beurteilung der Erdbebensicherheit von Brückenbauwerken, 2007.
- 08/1: Frank Peiffer, Framework for adaptive multi-scale simulation of textile reinforced concrete, 2008.
- 08/2: Martin Konrad, Effect of multifilament yarn crack bridging on uniaxial behavior of textile reinforced concrete, 2008.
- 09/1: Britta Holtschoppen, Beitrag zur Auslegung von Industrieanlagen auf seismische Belastungen, 2009.
- 10/1: Andreas Gömmel, Modellbildung und Fluid-Struktur-Interaktion in der Biomechanik am Beispiel der menschlichen Phonation, 2010.
- 10/2: Christoph Gellert, Nichtlinearer Nachweis von unbewehrten Mauerwerksbauten unter Erdbebeneinwirkung, 2010.
- 11/1: Jakub Jerabek, Numerical Framework for Modeling of Cementitious Composites at the Meso-Scale, 2011.
- 12/1: Timo Schmitt, Zusammenhänge zwischen makroseismischen Intensitäten und Antwortspektren, Erdbebendauer und Bauwerksvulnerabilität, 2012.
- 12/2: Jaime Campbell, Numerical Model of Nonlinear Analysis of Masonry Walls, 2012.
- 13/1: Jin Park, Makroelemente für unbewehrte Mauerwerkswandscheiben unter Erdbebeneinwirkung, 2013.
- 13/2: Hannah Norda, Beitrag zum statischen nichtlinearen Erdbebennachweis von unbewehrten Mauerwerksbauten unter Berücksichtigung einer und höherer Modalformen, 2013.
- 01 (2013): Okayay Altay, Flüssigkeitsdämpfer zur Reduktion periodischer und stochastischer Schwingungen turmartiger Bauwerke, 2013, ISBN: 978-3-946090-01-4.
- 02 (2015): Francesca Taddei, Numerical Investigation of Soil-Structure Interaction for Onshore Wind Turbines Grounded on a Layered Soil, 2015, ISBN: 978-3-946090-00-7.

- 03 (2015): Wolfgang Dornisch, Interpolation of Rotations and Coupling of Patches in Isogeometric Reissner–Mindlin Shell Analysis, 2015, ISBN: 978-3-946090-02-1.
- 04 (2015): Konstantinos Mykoniou, Dynamic analysis of multiple liquid-storage tanks, 2015, ISBN: 978-3-946090-03-8.
- 05 (2015): Benedikt Kohlhaas, Ein Finite-Elemente-Modell zur Analyse des Verhaltens von Formgedächtnisfaserkompositen mit beliebiger Mikrostruktur, 2015, ISBN: 978-3-946090-04-5.
- 06 (2016): Lin Chen, Numerical Models for the Analysis of Soil, Structure and Their Interaction, 2016, ISBN: 978-3-946090-05-2.
- 07 (2016): Julia Rosin, Seismische Auslegung von Tankbauwerken, 2016, ISBN: 978-3-946090-06-9.
- 08 (2019): Sreelakshmy Rajan, Probabilistic Seismic Safety Analysis of Multicomponent Systems, 2019, ISBN: 978-3-946090-07-6.
- 09 (2020): Maximilian Praster, Entwicklung eines adaptiven FE2 Ansatzes zur Simulation von thermomechanisch beanspruchten Faser-Matrix-Kompositen, 2020, ISBN: 978-3-9460901-08-3.
- 10 (2020): Margarita Chasapi, Nonlinear Formulations and Coupling of Patches for Isogeometric Analysis of Solids in Boundary Representation, 2020, ISBN: 978-3-946090-09-0.
- 11 (2021): Philipp Michel, Boden-Bauwerk-Fluid-Interaktion flüssigkeitsgefüllter Tankbauwerke auf nachgiebigen, vielfach geschichteten Böden unter seismischer Einwirkung, 2021, ISBN: 978-3-946090-10-6.
- 12 (2021): Okyay Altay, Structural Vibration Control with Semi-Active and Shape Memory Alloy Based Systems, 2021, ISBN: 978-3-946090-11-3.
- 13 (2021): Niklas Boesen, Trag- und Verformungsverhalten von unbewehrten Mauerwerksscheiben unter Berücksichtigung der Interaktion mit der Gebäudestruktur, 2021, ISBN: 978-3-946090-12-0.
- 14 (2022): Simon Schleiter, Entwicklung einer numerischen Methode zur Identifikation von Bauwerk-Dämpfer-Systemparametern, 2022, ISBN: 978-3-946090-13-7.

Lebenslauf

Name	Georgia Kikis
Geburtsdatum	13. Juli 1990
Geburtsort	Kozani - Griechenland
09/2005 – 06/2008	Besuch des 1. Lyzeum Kozani (gymnasiale Oberstufe)
06/2008	Griechisches Abitur
10/2008 – 09/2009	Bachelorstudium der Mathematik Technische Universität München
10/2009 – 04/2013	Bachelorstudium des Bauingenieurwesens Karlsruher Institut für Technologie
04/2013	Bachelor of Science
04/2013 – 05/2015	Masterstudium des Bauingenieurwesens mit Schwerpunkt Konstruktiver Ingenieurbau Rheinisch-Westfälische Technische Hochschule Aachen
05/2015	Master of Science
06/2015 – 09/2020	Wissenschaftliche Mitarbeiterin Lehrstuhl für Baustatik und Baudynamik Rheinisch-Westfälische Technische Hochschule Aachen



Abstract

This work is concerned with the treatment of locking effects in the framework of an isogeometric Reissner-Mindlin shell formulation and the correct description of brittle fracture in Reissner-Mindlin plates and shells using a phase-field model. The geometry is described by the mid-surface of the structure with Non-Uniform Rational B-Spline (NURBS) basis functions that are common in CAD tools in combination with a director vector field. The focus lies on two locking effects, namely, transverse shear locking and membrane locking that lead to an artificial stiffening of the system and oscillations in the stress resultants. In a first step, adjusted approximation spaces are defined for the two rotations in order to eliminate transverse shear locking in plates and shells. In a second step, a displacement-stress mixed method based on the Hellinger-Reissner variational principle is proposed in order to alleviate both membrane and transverse shear locking. The stress resultants that are related to these locking effects are interpolated with carefully chosen basis functions. Two local approaches that enable static condensation on the element level are proposed. Furthermore, a phase-field model for the description of brittle fracture in isogeometric Reissner-Mindlin plates and shells is developed. A phase-field, which is defined on the shell mid-surface and interpolated with NURBS basis functions, is used to describe the transition between cracked and uncracked material. A special focus lies on the incorporation of the transverse shear strains in the phase-field model in order to enable fracture due to transverse shear deformations in thick plates and shells.